Strangeness Production at COSY-ANKE: pp → ppϕ

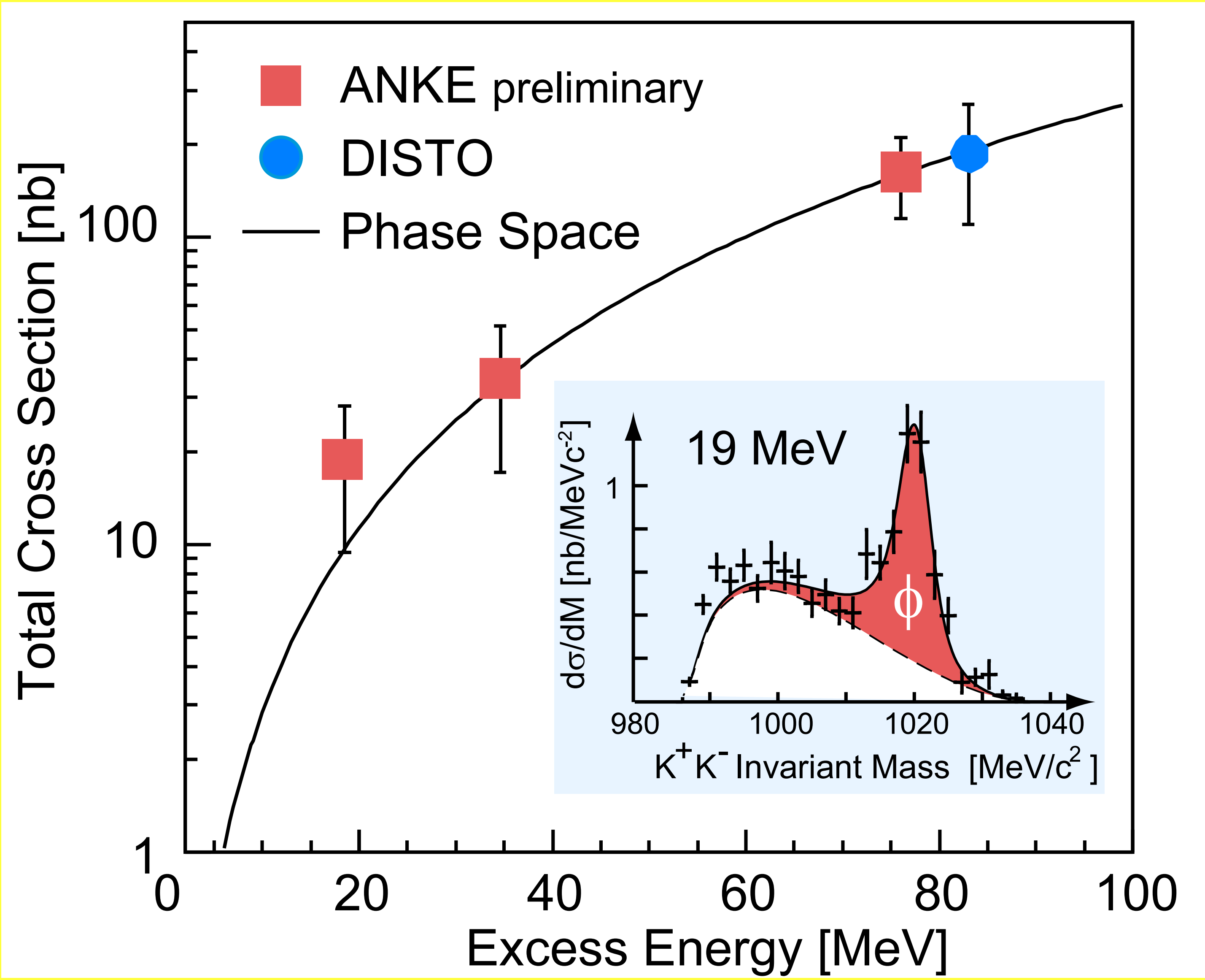

Annual Report 2004

Institut für Kernphysik / COSY

Cover picture:
The reaction $pp \to pp\phi$ has been studied with the ANKE spectrometer at excess energies Q = 19, 35, and 76 MeV by detecting the K^+K^- decay mode of the ϕ-meson. At each of these excess energies about 200-400 ϕ mesons have been identified. The total ϕ cross sections from ANKE are shown together with a data point from DISTO. The insert shows the invariant K^+K^- mass distribution for the lowest measured energy. The ϕ peak is on top of a broad distribution from non-resonant kaon production, while the background from misidentified particles is less than 4% (cf. page 3).

Preface

The year 2004 had been marked by events and activities that will be of strategic relevance for our institute. In February our institute was reviewed together with the GSI within the framework of the "Program Oriented Funding", which represents a new paradigm for science funding of the Helmholtz centres. This evaluation took place at the GSI, scrutinizing the Research Program "Physics of Hadrons and Nuclei", which is part of the Research Field "Structure of Matter".

As the major recommendations of this council, an "on-site" and "in-depth" review of the future activities of the institute, especially with respect to our close collaboration with GSI within the FAIR-project was proposed as well as to present a full proposal for the transfer of WASA from Uppsala to COSY to a dedicated review committee. The HGF-Senate has decided to postpone/defer any decision on budgets for the years 2006 to 2009 until the findings of the on-site review, which will take place in April 2005, are available.

The WASA proposal has been critically examined in October 2004 by an extended program advisory committee. It concluded unanimously that this detector in connection with COSY would constitute an outstanding physics opportunity and that the proposed physics program has unquestionably strategic relevance.

The institute has significantly intensified its engagement in the FAIR-project, which will set the stage for the mid- and long-term perspective in hadron physics. In collaboration with other partners our institute has taken on a leading role in the consortium that is planning, designing (and later building) the "High Energy Storage Ring" (HESR) of FAIR. In 2004 the IKP has played a prominent role in the timely completion of the Technical Reports for HESR, PANDA, PAX and FLAIR.

As outlined in our PoF-application, the institute has the following strategy for its future position within the scientific portfolio of the Helmholtz organisation (HGF):

- Scientific exploitation of COSY and its experimental facilities:
  - Hadron physics with hadronic probes
  - Preparatory investigations for the FAIR project of GSI (Darmstadt)
- Involvement in FAIR:
  - Planning, designing and building of HESR, the "High Energy Storage Ring" for anti-protons
  - Contributions to antiproton experiments and corresponding detector systems (PANDA, PAX, FLAIR)

It is evident that the timescale for the transition from COSY to HESR needs to be intertwined with the actual realization of the FAIR-project. As a result of an intense discussion within CANU (COSY Association of Networking Universities), it was agreed that COSY will be an indispensable experimental facility for the intervening period in order to sustain a viable hadron physics community. An efficient migration of the CANU-user community to the HESR is only conceivable if experimental activities can continue nearly seamlessly.

As mentioned above, we intend to transfer WASA (currently installed at CELSIUS of TSL, Uppsala, Sweden) to COSY — a corresponding Memorandum-of-Understanding between Uppsala University and FZJ was signed in December. As significant resources will be allocated to the HESR, PANDA, and other activities related to the FAIR-project, WASA — together with ANKE and TOF — will be the only detector systems operated at COSY in the near future. We already phased out nuclear spectroscopy and JESSICA during the past year.

As in the years before we had meetings of our international advisory committees, the IKP-Beirat and PAC for the COSY experimental program. I would like to take the opportunity to thank all of its members for their valuable advice and constructive discussions.

We also have had retirements of colleagues in 2004; I would like to mention: Prof. Detlev Filges and Prof. Kurt Kilian, long-term director of IKP I. I want to express our deep thanks to all retirees for their work and contributions as well as our best wishes for their future. We are very pleased to have successors for two retired directors (J. Speth, K. Kilian):

- Prof. Ulf-G. Meißner, holding a chair at the "Helmholtz Institut für Strahlen- und Kernphysik" at the "Rheinische Friedrich-Wilhelms Universität Bonn", who had acted as provisional director of the IKP-theory since 2003, took over as director in October.
- Prof. James Ritman from the "Justus-Liebig Universität Gießen", holding now a chair at the "Ruhr-Universität Bochum", is the new head of IKP I since September.

A hearty welcome and all the best to the new leadership and to all other new staff members of IKP. In closing, I would like to thank all colleagues, collaborators, friends from within the institute, the Research Center (FZJ) — in particular ZAM, ZAT and ZEL — and national and international universities and institutions for their support and dedication that was key to make COSY a world class facility and the IKP a center for hadron physics with hadronic probes.

Jülich, February 2005 Hans Ströher

Contents

1 Cover **i**

Titlepage **i**

Preface **iii**

2 Experimental Hadron Physics **1**

2.1 Experiments at COSY . . . 1
2.1.1 ϕ-meson production in pp collisions close to threshold . . . 2
2.1.2 The ϕ-meson production pn collisions . . . 3
2.1.3 Investigation of the $a_0(980)/f_0(980)$ resonances in pp and pn interactions with ANKE . . . 4
2.1.4 The reaction $pp \rightarrow d\pi^+\eta$ measured at ANKE . . . 5
2.1.5 $K^-\alpha$ scattering length the problem of K^--helium bound states and the reaction $dd \rightarrow \alpha K^+K^-$ . . . 6
2.1.6 Evidence of an excited hyperon state in $pp \rightarrow pK^+Y^{0*}$ . . . 7
2.1.7 Deuteron polarimetry at ANKE . . . 8
2.1.8 Cell tests at ANKE . . . 9
2.1.9 A New Geant4 based Simulation Framework for ANKE . . . 10
2.1.10 Drift chamber with a C-shaped frame . . . 11
2.1.11 A method to disentangle single meson and multi-pion production rates in the missing mass spectra of the quasi-free $pn \rightarrow pnX$ reactions . . . 12
2.1.12 Bremsstrahlung radiation in the Deuteron-Proton Collision . . . 13
2.1.13 Two-proton correlation function for the $pp \rightarrow pp\eta$ reaction . . . 14
2.1.14 The analysis status of the $\vec{p}p \rightarrow pp\eta$ reaction at $Q = 10$ MeV . . . 15
2.1.15 Status of the analysis of the $pn \rightarrow pn\eta$ reaction . . . 16
2.1.16 Determination of the COSY beam polarization by means of the COSY-11 setup . . . 17
2.1.17 Development of the COSY-11 simulation program for the study of the $dp \rightarrow dp\eta$ reaction . . . 18
2.1.18 Investigation of the $pd \rightarrow {}^3He\eta'$ production at COSY-11 . . . 19
2.1.19 Energy and momentum resolution of the COSY-11 neutron detector . . . 20
2.1.20 Excitation function of the $pp \rightarrow ppK^+K^-$ reaction near threshold . . . 21
2.1.21 Study of the reaction $np \rightarrow pp\pi^-$ for excess energies < 100 MeV above threshold . . . 22
2.1.22 Simulation of the detection efficiency of $pK^\circ\Sigma^+$ with a polarized target at COSY-TOF . . . 23
2.1.23 Detection of the η signal in the missing mass spectrum of $pp \rightarrow ppX$ . . . 24
2.1.24 The analysis framework TOFROOT for online and offline analysis . . . 25
2.1.25 Resolution and efficiency of the straw tube tracker for COSY-TOF . . . 26
2.1.26 The $p-n$-reaction studies via FSI . . . 27
2.1.27 Evaporation of composite particles from the spallation of Au by energetic protons . . . 28
2.1.28 Preequilibrium mechanism of the spallation of Au by energetic protons . . . 29
2.1.29 Isoptope Identification with Hybrid BCD-Si Telescope . . . 30
2.1.30 Detailed studies on a cryogenic methane-hydrate moderator . . . 31
2.1.31 Discrepancies between simulation and experiment due to total reflected neutrons . . . 32
2.1.32 Comparison of the wavelength dependent time-of-flight spectra of Methane Methan-Hydrate and Ice at $T = 20$ K . . . 33
2.1.33 Simulations for production of mesons via quasi-free proton-neutron scattering at the WASA 4π-detector . . . 34
2.1.34 Investigation of the η'-proton interaction at the COSY-11 and WASA-at-COSY facilities . . . 35
2.1.35 Detection possibilities of the quasi-free $pn \rightarrow pn\eta'$ reaction at the WASA detector . . . 36
2.1.36 Simulation of the reaction $pp \rightarrow d\pi^+\eta$ for WASA . . . 37
2.2 Experiments at External Facilities . . . 38
2.2.1 Usability of permanent magnets as Ioffe trap at ATRAP . . . 39
2.2.2 Charged particle cloud in a combined Penning/Ioffe trap . . . 40
2.2.3 High resolution spectroscopy of the Kβ transition in muonic hydrogen . . . 41
2.2.4 The resolution function of a Bragg spectrometer at pionic hydrogen energies . . . 42
2.2.5 Study of the breathing mode of the nucleon in high energy proton-proton scattering . . . 43

3 Theoretical Physics **44**
3.1 Hyperon-Nucleon Interaction in Chiral Effective Field Theory . . . 45
3.2 Accuracy test of FSI approaches for extracting scattering lengths . . . 46
3.3 New results on the limit for the with of the exotic $\Theta^+(1540)$ resonance . . . 47
3.4 Analysis of $\Theta^+(1540)$ production in K^+-Xe collisions . . . 48
3.5 Some aspects of Θ parity determination in the reaction $\gamma N \to \Theta^+\bar{K} \to NK\bar{K}$ . . . 49
3.6 Consistent analysis of the reactions $\gamma p \to p\eta'$ and $pp \to pp\eta'$ . . . 50
3.7 Bounds on bound η^3He system . . . 51
3.8 Flatté-like distributions and the $a_0(980)/f_0(980)$ mesons . . . 52
3.9 Spectrum and decays of kaonic hydrogen . . . 53
3.10 Partial-wave analysis for $\vec{p}\vec{p} \to pp\pi^\circ$ . . . 54
3.11 ω Production in pp Collisions . . . 55
3.12 Infrared regularization for spin-1 fields . . . 56
3.13 Orthonormalization procedure for chiral effective nuclear field theory . . . 57
3.14 Baryon masses in cut-off regularized chiral perturbation theory and application to lattice results . . . 58
3.15 Chiral extrapolations of baryon masses for unquenched three-flavor lattice simulations . . . 59
3.16 High precision calculation of the two-nucleon system in chiral effective field theory . . . 60
3.17 Isospin dependence of the three-nucleon force . . . 61
3.18 Universal Properties of the Four-Nucleon System . . . 62
3.19 Universal Properties of the Four-Boson System with Short-Range Interactions . . . 63
3.20 The Four-Boson System with Short-Range Interactions in two Dimensions . . . 64
3.21 Nucleon-Nucleon Potential in Finite Nuclei . . . 65
3.22 Ultraperipheral Collisions at Relativistic Heavy Ion Collisiders and Production of QED Pairs at RHIC . . . 66
3.23 Recent Developments in Electromagnetic Dissociation with Fast Heavy Ions . . . 67
3.24 Effective-Range Approach and Scaling Laws for Electromagnetic Strength in Neutron Halo Nuclei . . . 68
3.25 The Trojan-Horse Method: Investigation of the Threshold Region . . . 69
3.26 Near threshold enhancement of the $p\bar{p}$ mass spectrum in J/Ψ decay . . . 70
3.27 Radiative tritium β-decay and the neutrino mass . . . 71
3.28 Radiative neutron β-decay in effective field theory . . . 72

4 Accelerator Division **73**
4.1 SPINCOSY: Spin manipulation of vector and tensor polarized beams stored in COSY . . . 74
4.2 Characteristic Features of Electron Cooling at COSY . . . 77
4.3 Influence of Electron Beam Neutralization on the Stability of Electron-Cooled Ion Beams . . . 78
4.4 Stable Longitudinal Collective Modes in an Intense Electron Cooled Proton Beam . . . 79
4.5 Luminosity Considerations for Internal and External Experiments at COSY . . . 80
4.6 Beam Profile Measurements by Light Radiation of Excited Gas Atoms . . . 82
4.7 Modern Acceleration Cavities for Particle Rings . . . 83
4.8 Magnets Alignment and New Installations . . . 86
4.9 Synchronisation of Function Generators at COSY . . . 87
4.10 Overheating Protection And Monitoring System For The Electromagnetic Extraction Septum . . . 88
4.11 Operation of the injector cyclotron and the ion sources at COSY/Jülich . . . 89
4.12 Velocity measurements of the pulsed atomic hydrogen beam of the COSY polarized ion source . . . 91
4.13 Magnetic spectrograph BIG KARL . . . 93
4.14 Radiation Protection . . . 94
4.15 Pulsed operation of the superconducting HWRs The frequency-shift . . . 95
4.16 Warm measurements of the superconducting Half-Wave Resonators . . . 96
4.17 Cold measurements of the superconducting Half-Wave Resonators . . . 97

5 Preparations for FAIR **98**
5.1 Study of strangeness-2 baryonic states at FLAIR . . . 99
5.2 The design of the micro-vertex detector for the PANDA experiment . . . 100
5.3 R&D work (2005–2008) for the high-energy storage ring . . . 101
5.4 Polarized Beams in the High-Energy Storage Ring . . . 102
5.5 Perturbation of the HESR lattice due to the Electron Cooling Insertion . . . 103
5.6 Studies of the Effect of Longitudinal Impedances on the HESR . . . 104
5.7 Radiation protection at HESR . . . 105

6 Technical Developments **107**
6.1 First Polarization Measurement of Hydrogen Atoms Effusing from a Storage Cell into the Lamb-Shift Polarimeter and the Removal of the Components of the Polarized Target to COSY . . . 108
6.2 Observation of hydrogen and nitrogen pellets at the ANKE pellet target . . . 109
6.3 Polarized target for the TOF detector . . . 110
6.4 Gold fingers cryogenic target for external COSY experiments . . . 112
6.5 Residual gas analysis in the TOF high vacuum tank . . . 113
6.6 Studies for an external cryotarget for WASA at COSY . . . 114
6.7 Laboratory for Semiconductor Detectors . . . 115
6.8 Two-Dimensional Microstrip Germanium Detector for X-Ray Spectroscopy of Highly-Charged Heavy Ions . . . 116
6.9 Large-Volume Si(Li) Orthogonal-Strip Detectors for Compton-Effect-Based Instruments . . . 117
6.10 Electronics laboratory . . . 118
6.11 ZEL-IKP developments for Detection Systems . . . 119

A Councils **120**
A.1 Scientific Council . . . 120
A.2 Program Advisory Committee . . . 120

B Personnel **121**
B.1 Technical and Administrative Staff . . . 123

C Publications 2004 **124**

D Beam Time at COSY 2004 **132**

E List of Authors **136**

2 Experimental Hadron Physics

2.1 Experiments at COSY

ϕ-meson production in pp collisions close to threshold

M. Hartmann, Y. Maeda and I. Keshelashvili

The reaction $pp \to pp\phi$ has been studied with the ANKE spectrometer [1, 2] at excess energies of ε=76 MeV, 35 MeV and 19 MeV by detecting the K^+K^- decay mode of the ϕ-meson. At each energy about 200-300 ϕ-mesons were identified. First preliminary total cross sections for ϕ production are deduced at each energy [3].
Figure. 1 (a,b) shows the efficiency corrected K^+K^- invariant mass distributions at ε=35 MeV and ε=19 MeV. The ϕ cross section at ε=76 MeV (Fig. 1 (c)) is close to the DISTO data point [4]. Figure 1 (c) shows the total ϕ cross sections also for the two lower excess energies. The lines are the theoretical predictions by Tsushima and Nakayama [5] for different model parameters including the unknown ϕNN coupling constant. Within this theoretical framework our preliminary result at ε=19 MeV would suggest a weak ϕNN coupling constant. For comparision, a phase-space calculation normalized to the DISTO result is shown by the solid line in Fig. 2 (a).

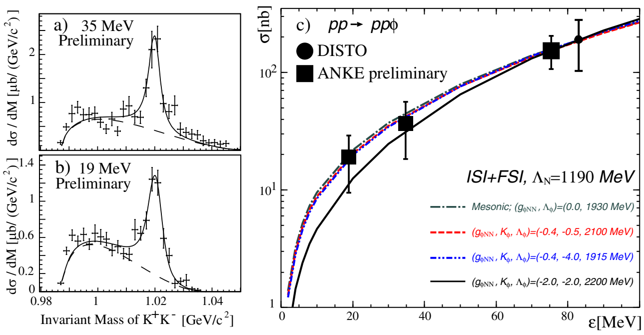

Fig. 1: (a) and (b) show the efficiency corrected K^+K^- invariant mass distribution at excess energies of 35 MeV and 19 MeV. The dashed curves are the non-resonant contributions based on four-body phase space. The solid line is the sum of non-resonant contribution and ϕ-meson production including the detector resolution. In (c) the total ϕ cross sections from ANKE are shown together with the DISTO point. The error bars indicate the systematical uncertainties. The lines are predictions from Ref. [5].

In addition to the information on the energy dependence of the ϕ production close to threshold the final result from ANKE will also provide the ϕ/ω cross section ratio below the DISTO measurements in combination with the existing SPES-III [6] and COSY-TOF [7] result on ω-production. The Okubo-Zweig-Iizuka (OZI) rule [8] states that processes with disconnected quark lines in the initial or final state are suppressed. Accordingly, the production of ϕ-mesons from initial non-strange states is expected to be substantially suppressed relative to ω-meson production. The cross-section ratio for ϕ- and ω-meson production under similar kinematical conditions should then be in the order of $R_{OZI}=\sigma_\phi/\sigma_\omega=\tan^2\alpha_V=4.2\times10^{-3}$ [9], where $\alpha_V=3.7^\circ$ is the deviation from the ideal $\phi-\omega$ mixing angle [10]. However, one may expect that a certain amount of hidden strangeness in the nucleon would manifest itself in a reaction cross section that significantly exceeds the limit given by the OZI rule. This question has lead to a large experimental activity involving different hadronic reactions. In specific channels in $\bar{p}p$ annihilation [11, 12, 13] enhancements of $R_{\phi/\omega}$ by up to two orders of magnitude have been observed. A systematic analysis of the ϕ to ω cross-section ratio in pp collisions and πN interactions as well as in mesonic and radiative decays have been performed by Sibirtsev and Cassing [14]. Almost all of the existing data give a ϕ-to-ω ratio of $3\times R_{OZI}$. Only the ratio derived from ϕ-meson production measured at DISTO at an excess energy of 83 MeV shows a 7 times larger value than R_{OZI}.

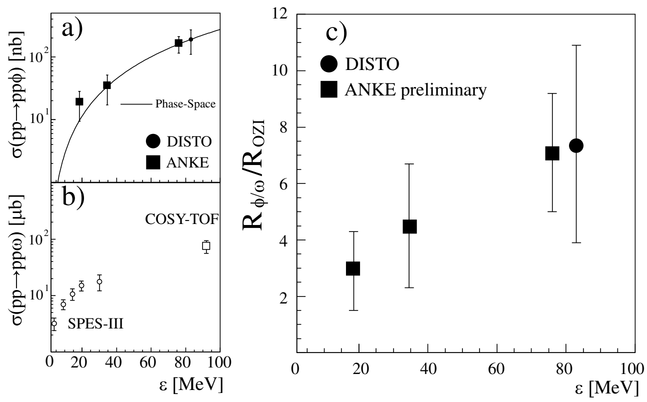

Fig. 2: (a) and (b) show the total cross section for the ϕ and ω production in pp collisions, respectively. In (c) the ϕ to ω cross section ratios normalized by R_{OZI} are shown.

In Fig. 2(b) the existing $pp \to pp\omega$ data from SPES-III [6] and COSY-TOF [7] are presented for comparison. The enhanced ϕ-to-ω ratio at $\varepsilon\approx$80 MeV is confirmed by the ANKE cross section. The ANKE ϕ-to-ω ratio at an excess energy ε=19 MeV is $3\times R_{OZI}$ and thus significantly smaller than at the DISTO excess energy (Fig. 2 (c)).

References:

[1] S. Barsov et al., Nucl. Instr. Meth. A **462** (2001) 364.
[2] M. Hartmann et al., Annual report 2002, Berichte des Forschungszentrums Jülich Jül-**4052**, ISSN 0944-2952 (2003) chapter 1.
[3] Hartmann et al., Presented at the conference BARYONS 2004. To be published in Nucl. Phys. A.
[4] F. Balestra et al., Phys. Rev. C **63** (2001) 024004.
[5] K. Tsushima and K. Nakayama, Phys. Rev. C **68** (2003) 034612.
[6] F. Hibou et al., Rev. Lett. **83** (1999) 492.
[7] S.Abd El-Samad et al., Phys. Lett. B **522** (2001) 16.
[8] S. Okubo, Phys. Lett. **5** (1963) 165; G. Zweig, CERN report **TH-401** (1964); J. Iizuka, Prog. Theor Phys. Suppl. **38** (1966) 21.
[9] H.J. Lipkin, Phys. Lett. B **60** (1976) 371.
[10] Particle Data Group, Eur. Phys. J. C **3**, 1 (1998).
[11] J. Reifenrother et al., Phys. Lett. B **267** (1991) 299 .
[12] V.G. Ablev et al., Phys. Lett. B **334** (1994) 237.
[13] C. Amsler et al., Phys. Lett. B **346** (1995) 363.
[14] A. Sibirtsev, W. Cassing, Eur. Phys. J. A **7** (2000) 407.

The ϕ-meson production in pn collisions

Y. Maeda, M. Hartmann and I. Keshelashvili

In February 2004, first data of the reaction $pn \to d\phi$ have been collected at the ANKE facility COSY Jülich. The experiment $pd \to dK^+K^-p_s$ has been performed at the proton beam energy T_p=2.65 GeV using a deuterium cluster-jet target [1]. The K^+ and K^- mesons as well as the deuteron are selected by TOF information, whereas the spectator proton p_s is not observed. In the K^+K^-d missing mass spectrum shown in Fig.1 (a), a clear signal at the proton mass is seen. The estimated background below the proton signal is less than 5%. Figure 1 (b) shows the K^+K^- invariant mass spectrum for the events inside the proton mass region of (a). The spectrum shows a strong peak at the ϕ-meson mass above the non-resonant K^+K^- production contribution. The peak contains about 1200 events. In the current state of analysis, 60% of the collected data are considered.

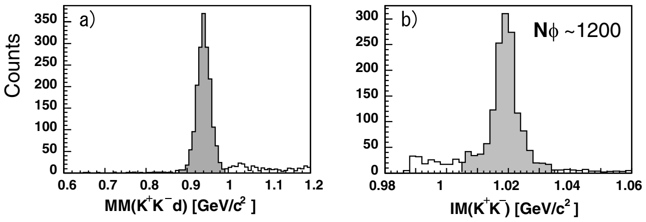

Fig. 1: a) Missing proton mass spectrum for the reaction $pd \to dK^+K^-p_s$. The shadowed region shows the cut for the missing proton. b) shows the K^+K^- invariant mass spectrum. The shadow region shows the ϕ-meson cut.

Assuming that the reaction $pd \to d\phi p_s$ is due to the interaction between beam proton and the target neutron, the proton in the final state is a spectator. The kinematics of the reaction $pn \to d\phi$ can be determined by the spectator momentum on event-by-event basis. Figure 2 shows the excess energy spectrum of the reaction $pn \to d\phi$ for selected ϕ events. In Fig.3 (a), invariant mass spectra of K^+K^- are shown for three excess energy regions up to 70 MeV. The statistical significance of the neutron data should be sufficient to extract the energy dependence of the cross section. For comparison, in the right part (b) the pp data from ANKE are displayed for three fixed excess energies of 19, 35 and 76 MeV [2]. For the neutron target the ratio of non-resonant $K\bar{K}$ to ϕ-meson production is much smaller than for pp reaction. This may indicate that the cross section of the reaction $pn \to d\phi$ is much larger than of the reaction $pp \to pp\phi$. The further analysis is in progress.

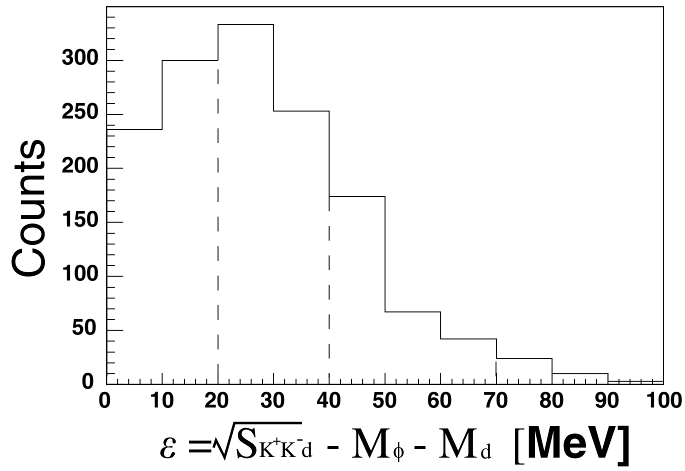

Fig. 2: The excess energy spectrum of the reaction $pn \to d\phi$. $\sqrt{S_{K^+K^-d}}$ is the c.m. energy. M_ϕ and M_d is the mass of the ϕ-meson and the deuteron, respectively. Dashed lines separate three different excess energy regions shown in Fig.3 (a).

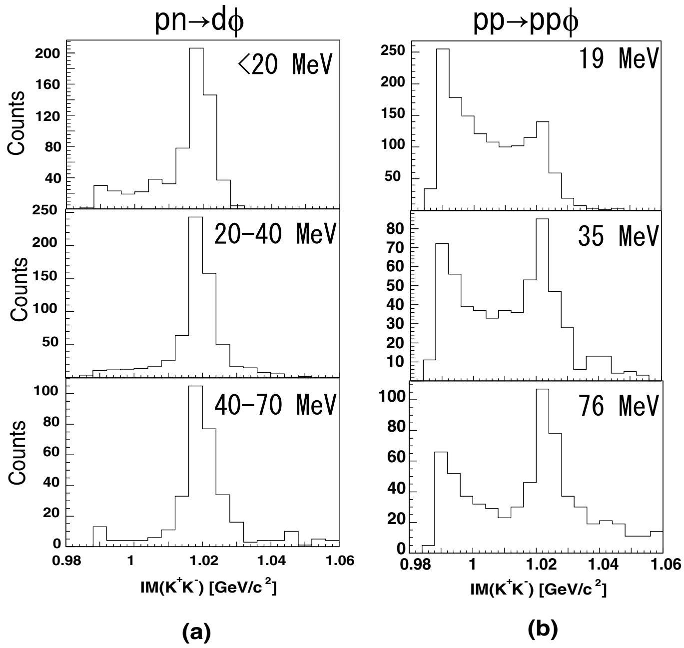

Fig. 3: (a) K^+K^- invariant mass spectra of the reaction $pn \to d\phi$ at three excess energy regions. (b) K^+K^- invariant mass spectra of the reaction $pp \to pp\phi$ at three fixed excess energies. The excess energies are indicated in the figures.

References:

[1] M. Büscher *et al.*, COSY Proposal No.92.

[2] M.Hartmann *et al.*, Ann. Rep. 2004 of IKP, (2005).

Investigation of the $a_0(980)/f_0(980)$ resonances in pp and pn interactions with ANKE*

A.Dzyuba[a], M.Büscher, P.Fedorets[b], V.Kleber[c], V.Koptev[a], M.Nekipelov[a]

The production of the light scalar resonances $a_0/f_0(980)$ in hadronic interactions is being investigated with the ANKE spectrometer, where their decays into $K\bar{K}$ can be observed. Final goal of these studies, which will be later supplemented by measurements of the non-strange decays with WASA, is to learn about the nature of these states and about isospin violating processes in the a_0/f_0 system [1].

The first ANKE experiments have been performed for pp collisions at beam energies $T_p = 2.65$ GeV (2001) [2] and $T_p = 2.83$ GeV (2002), and for pn collisions, using a deuterium cluster-jet target, at $T_p = 2.65$ GeV (2004) [3].

For the $pp \to dK^+\bar{K}^0$ data at $T_p = 2.83$ GeV the analysis is almost completed. The reaction has been identified by detecting dK^+ pairs using TOF and energy loss information, and cutting on the $\bar{K}^0$ peak in the dK^+ missing mass spectra. Moreover, the momentum resolution could be improved by a factor of two by using Runge-Kutta tracking instead of a polynomial method (Fig. 1).

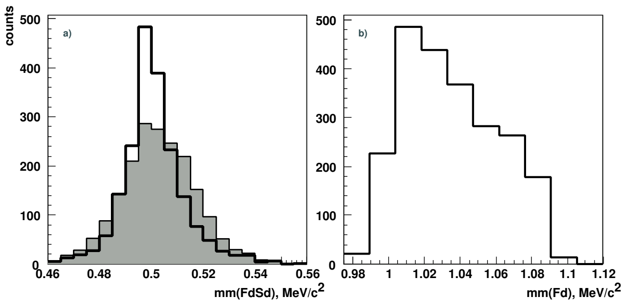

Fig. 1: a) dK^+ missing mass using two momentum reconstruction methods, polynomial (shaded histogram) and Runge-Kutta (solid line). b) Deuteron missing mass obtained with the Runge-Kutta algorithm.

Due to the increased phase-space volume as compared to the 2.65 GeV data, zero elements in the acceptance matrices have appeared (lower part of Fig. 2). This makes a model independent acceptance correction, as used for $T_p = 2.65$ GeV, impossible.

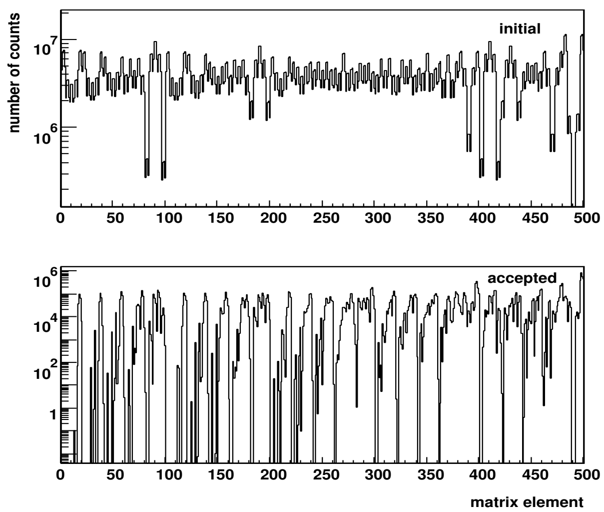

Fig. 2: Acceptance matrix of ANKE. For a description of the method see Ref. [2].

In order to calculate the total cross section for the higher energy a model described in Ref. [4] has been used as input for simulations. The integrated luminosity has been determined from pp elastic scattering. The preliminary value of the total cross section of the reaction $pp \to dK^+\bar{K}^0$ is in the range 200–300 nb, the statistical and systematic unsertainties amount to 20–30% of this value.

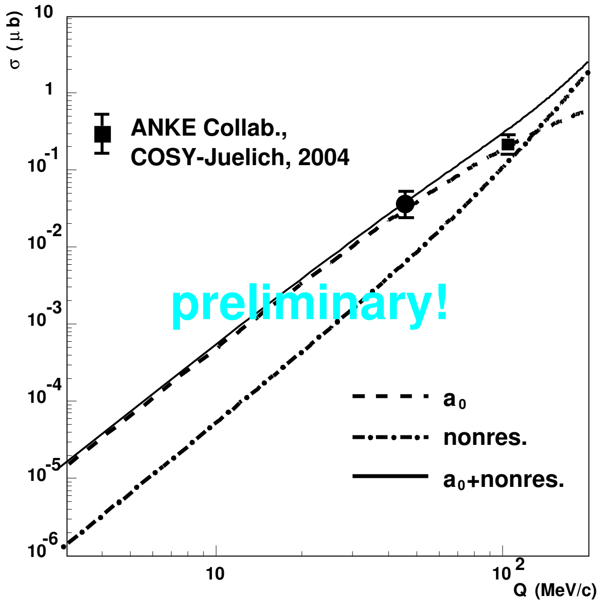

Fig. 3: Total cross-section for the reaction $pp \to dK^+\bar{K}^0$. The error bars represent the statistical and systematic uncertainties. The data point at the lower energy is taken from Ref. [2], the lines correspond to the model from Ref. [4].

A preliminary analysis of the pn-experiment for a_0/f_0 production in the reaction $pn \to da_0/f_0 \to dK^+K^-$ is available. Since all final particles — besides spectator protons which do not take part in the reaction — have been detected by ANKE, the K^+K^- invariant-mass spectrum should reveal an enhancement at low masses corresponding to the a_0/f_0. However, only a ϕ-meson (which also decays to K^+K^-) peak is clearly seen in this spectrum [5]. The enhancement in the low mass region may either be produced via the a_0/f_0 resonances or is caused by background from misidentified particles.

References:

[1] Proposal "WASA at COSY", nucl-ex/0411038.
[2] V.Kleber et al., Phys. Rev. Lett. **91**, 172304 (2003).
[3] M.Büscher et al., COSY Proposal No.92.
[4] V.Grishina et al., Eur. Phys. J. A **21**, 507–520 (2004).
[5] Y.Maeda et al., contribution to this annual report.

[a] PNPI, Gatchina, Russia
[b] ITEP, Moscow, Russia
[c] IKP, Universität zu Köln, Germany
* supported by DFG, FFE

The reaction $pp \to d\pi^+\eta$ measured at ANKE*

P. Fedorets[a], M. Büscher, V.P. Chernyshev[a], V.Yu. Grishina[b], V. Kleber[d], L.A. Kondratyuk[a], V.P. Koptev[c], A.E. Kudryavtsev[a], V.E. Tarasov[a]

$a_0^+(980)$-resonance production has been studied for the first time with ANKE in January 2001 at a beam energy of $T = 2.65$ GeV in the reaction $pp \to da_0^+$ with subsequent decays $a_0^+ \to K^+\bar{K}^0$ [1] and $a_0^+ \to \pi^+\eta$. The total cross sections for the $\pi^+\eta$ channel have been deduced for a_0^+ and for non-resonant $\pi^+\eta$ production from a model dependent analysis [2]. The results of a model independent analysis of the reaction $pp \to d\pi^+\eta$ are presented here.

The reaction $pp \to d\pi^+\eta$ has been measured by detecting in coincidence the two charged final particles. Subsequently, the reaction has been identified by selecting the η peak in the $mm(pp,d\pi^+)$ missing mass spectrum. The missing mass distributions $mm(pp,d)$ and $mm(pp,d\pi^+)$ for the selected $d\pi^+$ pairs [3] are presented in Fig. 1. In the $(pp,d\pi^+)$ missing mass distribution a clear peak is observed around $m(\eta) = 547$ MeV/c^2 with about 6200 events. The peak sits on top of a smooth background from multi-pion production $pp \to d\pi^+(n\pi)$ $(n \geq 2)$ [4]. After selecting the mass range $(530-560)$ MeV/c^2 around the η peak the missing mass spectrum $mm(pp,d)$ exhibits a shoulder at 980 MeV/c^2 (Fig. 1b, dotted), where the peak from the $a_0^+(980)$ resonance is expected.

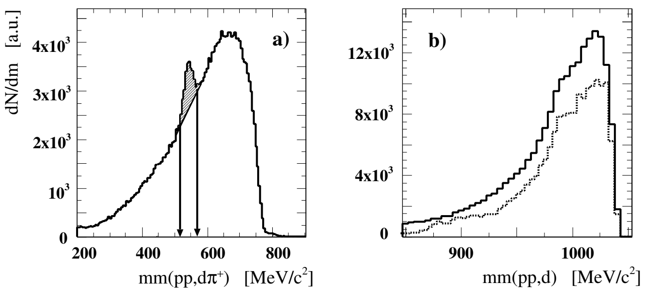

Fig. 1: Missing mass distributions (a) $mm(pp,d\pi^+)$, (b) $mm(pp,d)$ for the reaction $pp \to d\pi^+X$. The dotted histogram in $mm(pp,d)$ (scaled by factor 6) corresponds to the selected area around the η peak ($530-560$ MeV/c^2) in $mm(pp,d\pi^+)$ (indicated by arrows).

With the limited phase-space coverage of ANKE a partial wave decomposition, as it was performed in Ref. [1], is not possible in this case. Only differential cross sections of the reaction $pp \to d\pi^+\eta$ could be determined model independently. For this purpose two regions of phase space have been selected, where the acceptance of ANKE is 100% for this reaction. Six variables in the lab. system have been chosen for describing these rectangular areas: the vertical (θ_y) and horizontal (θ_x) angles and momenta of the two detected particles. The angles are defined as $tan(\theta_y) = p_y/p_z$, $tan(\theta_x) = p_x/p_z$. Figure 2 shows the missing mass distributions $mm(pp,d\pi^+)$, which correspond to the selected regions of phase space. The number of events under the η peak have been determined by fitting the missing mass spectra $mm(pp,d\pi^+)$ by the sum of a Gaussian distribution and a 3rd order polynomial. The results for the differential cross sections are shown in Table 1.

To summarize, the differential production cross section $d^4\sigma/d\Omega_d d\Omega_{\pi^+} dp_d dp_{\pi^+}$ for the reaction $pp \to d\pi^+\eta$ has been determined model independently for two regions of phase space. Both a_0^+ and non-resonant $\pi^+\eta$ productions contribute. For the momentum range $p_d = (1.4-1.6)$ GeV/c the non-resonant $\pi^+\eta$ production should be dominant, because this momentum range corresponds to low masses of the $\pi^+\eta$ system, where the a_0^+ production is suppressed.

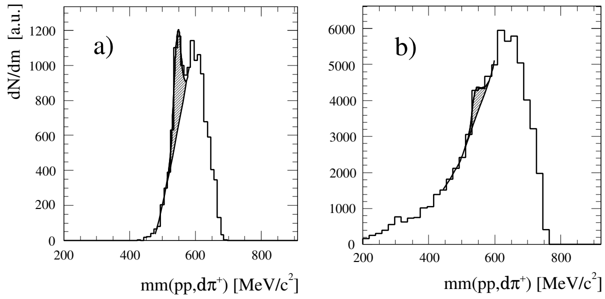

Fig. 2: Missing mass distribution $mm(pp,d\pi^+)$ for the selected regions of phase space: the momentum ranges $p_d = (1.4-1.6)$ GeV/c (a) and $p_d = (1.8-2.7)$ GeV/c (b).

$d^4\sigma/d\Omega_d d\Omega_{\pi^+} dp_d dp_{\pi^+}$ (μb/sr^2(GeV/c)^2)	variables, lab. system		
	θ_y (deg.)	θ_x (deg.)	p (GeV/c)
$71 \pm 6_{stat} \pm 20_{sys}$	deuteron variables		
	$(-3,+3)$	$(-3.5,+3.5)$	$(+1.4,+1.6)$
	pion variables		
	$(-4,+4)$	$(-11,-3)$	$(+0.65,+0.95)$
$30 \pm 4_{stat} \pm 9_{sys}$	deuteron variables		
	$(-3,+3)$	$(-6,-2)$	$(+1.8,2.7)$
	pion variables		
	$(-4,+4)$	$(-11,-3)$	$(+0.65,+0.95)$

Table 1: Differential production cross sections for the reaction $pp \to d\pi^+\eta$ for two regions of phase space where the acceptance of ANKE is 100% for this reaction.

References:

[1] V. Kleber *et al.*, Phys. Rev. Lett. **91**, 172304 (2003).
[2] P. Fedorets *et al.*, IKP Annual Report 2003
[3] V. Kleber *et al.*, IKP Annual Report 2001
[4] P. Fedorets *et al.*, IKP Annual Report 2002

[a]ITEP, Moscow, Russia
[b]INR, Moscow, Russia
[c]PNPI, Gatchina, Russia
[d]IKP, Universität zu Köln, Germany
*Supported by grants COSY-FFE-41520733, ISTC-1966, DFG-436RUS-113/733,787, RFBR02-02-16349, DFG-RFBR03-02-04013, 02-02-04001

$K^-\alpha$ scattering length, the problem of K^--helium bound states and the reaction $dd \to \alpha K^+ K^-$

V. Yu. Grishina[a], L.A. Kondratyuk[b], A.A. Sibirtsev, M. Büscher, S. Krewald, U.-G. Meißner[c] and F.P. Sassen

Exotic few-body nuclear systems with a $\bar{K}$-meson as a constituent have been studied by Akaishi and Yamazaki [1]. They proposed a phenomenological $\bar{K}N$ potential model, which reproduces K^-p and K^-n scattering lengths from Ref. [2], kaonic-hydrogen atom data, and properties (mass and width) of the $\Lambda(1405)$ resonance. The $\bar{K}N$ interaction in this model is characterized by a strong attraction in the $I=0$ channel, which causes the few-body systems to form dense nuclear objects. As a result, the nuclear ground states of a K^- in (pp), ^{3}He, ^{4}He and ^{8}Be were predicted to be discrete states with binding energies of 48, 108, 86 and 113 MeV and widths 61, 20, 34 and 38 MeV, respectively. Recently a strange tribaryon $S^0(3115)$ with a width of less than 21 MeV/c^2 has been found in the ^{4}He(stopped K^-,p) reaction [3]. This state may be interpreted as a candidate of a neutral deeply bound state $(\bar{K}NNN)^{Z=0}$ with $I=1, I_z=-1$. However, the $S^0(3115)$ is about 100 MeV lighter than the predicted state for which $Z=2, I_z=+1$ is expected. Therefore, further searches for bound kaonic nuclear states as well as new data on the interactions of $\bar{K}$ mesons with lightest nuclei are needed.

Up to now the s-wave $K^-\alpha$ scattering length $A(K^-\alpha)$ has not been measured and theoretical calculations of this quantity are not available. Here we present first calculations of $A(K^-\alpha)$ within the Multiple Scattering Approach (MSA). To calculate the s-wave $K^-\alpha$ scattering length as well as the FSI enhancement factor we use the Foldy–Brueckner adiabatic approach based on the multiple scattering (MS) formalism (see Ref. [4]). This method has already been used for the calculation of the enhancement factor for, *e.g.*, the reactions $pd \to {}^3\mathrm{He}\eta$ [5], and $pn \to d\eta$ [6] and $pp \to d\bar{K}^0K^+$ [7].

The calculations of $A(K^-\alpha)$ have been performed for four sets of parameters for the $\bar{K}N$ scattering length taken from Table I of Ref. [8]: K-matrix fit (Set 1), separable fit (Set 2), constant scattering length fit (CSL) from Dalitz–Deloff (Set 3) and CSL fit from Conboy (Set 4). The results of our calculations are presented in the right column of Table 1. They are very similar for Sets 1–3 giving the real (imaginary) parts of $A(K^-\alpha)$ in the range $-1.8\ldots-1.9$ fm ($0.9\ldots0.98$ fm). The results for Set 4 are different: Re $A(K^-\alpha)=-2.24$ fm and Im $A(K^-\alpha)$=1.58 fm.

	$a_0(\bar{K}N)$[fm]	$a_1(\bar{K}N)$[fm]	$A(K^-\alpha)$[fm]
Set 1	$-1.59+i0.76$	$0.26+i0.57$	$-1.80+i0.90$
Set 2	$-1.61+i0.75$	$0.32+i0.70$	$-1.87+i0.95$
Set 3	$-1.57+i0.78$	$0.32+i0.75$	$-1.90+i0.98$
Set 4	$-1.03+i0.95$	$0.94+i0.72$	$-2.24+i1.58$

Table 1: Different sets of the $\bar{K}N$ scattering lengths $a_I(\bar{K}N)$ $(I=0,1)$ taken from Ref. [8] to calculate the scattering length $A(K^-\alpha)$ (right column).

Unitarizing the constant scattering length approach we can reconstruct the $\bar{K}\alpha$ amplitude in the zero range approximation

$$f_{\bar{K}\alpha}(q) = \left((A_{\bar{K}\alpha})^{-1} - ik\right)^{-1}, \tag{1}$$

where $k=k_{\bar{K}\alpha}$ is the relative momentum of the $K^-\alpha$ system. The denominator of the amplitude has a zero at a complex energy

$$E^* = E_R - \frac{1}{2}i\Gamma_R = \frac{k^2}{2\mu}, \tag{2}$$

where E_R and Γ_R are the binding energy and width of a $K^-\alpha$ resonance. For Set 1 and Set 4 we found $E^*=(-6.7-\frac{1}{2}i18)$ MeV and $E^*=(-2.1-\frac{1}{2}i11.4)$ MeV, respectively. Note that assuming a strongly attractive phenomenological $\bar{K}N$ potential Akaishi and Yamazaki [1] found a deeply bound $\bar{K}\alpha$ state: $E^*=(-86-\frac{1}{2}i34)$ MeV. Having a very similar $\bar{K}N$ scattering length (as given by Set 1) our approach predicts a loosely bound state. It is not clear whether medium effects might be so strong that they drastically change the $\bar{K}\alpha$ scattering length predicted by the multiple scattering approach with the vacuum value of the $\bar{K}N$ scattering amplitude. In any case it is very importnat to measure the s-wave $\bar{K}\alpha$ scattering length. Note that in the limit of small absorption, *i.e.* when the imaginary part of $A_{\bar{K}\alpha}$ goes to zero, the real part of the scattering length should be much larger for the case of a loosely bound state as compared to the case of a deeply bound state. Such a situation is supported by the calculations within the zero range approximation (ZRA) (even in the presence of absorption) where in the case of a deeply bound state we find: $A(\bar{K}\alpha)=-0.07+i0.72$ fm. We expect that the ZRA can be applied for the description of the amplitude which is generated by the short range potential used in Ref.[1].

The reaction

$$dd \to \alpha K^- K^+ \tag{3}$$

provides an interesting tool to study $I=0$ resonances in the K^-K^+ sector . At the same time near threshold it is sensitive to the to $K^-\alpha$ final state interaction.We analyzed the $K^-\alpha$ FSI effect in the reaction $dd \to \alpha K^+K^-$ and found that the measurement of the $K^-\alpha$ mass distribution in the reaction $dd \to \alpha K^+K^-$ near threshold may provide a new possibility to determine the s-wave $K^-\alpha$ scattering length.

References:

[1] Y. Akaishi and T. Yamazaki, Phys. Rev. C **65** 044005 (2002).

[2] A.D. Martin, Nucl.Phys. B**179** 33 (1981).

[3] T. Suzuki et.al, Phys. Lett B **597** 263 (2004).

[4] M. L. Goldberger and K. M. Watson, Collision Theory, John Wiley and Sons, Inc., New York, London, Sidney (1964).

[5] G. Fäldt and C. Wilkin, Nucl. Phys. A **587**, 769 (1995).

[6] V.Yu. Grishina et al., Phys.Lett. B **475**, 9 (2000).

[7] V.Yu. Grishina, L.A. Kondratyuk, M. Büscher and W. Cassing Eur. Phys. J. A **21** 507 (2004); nucl-th/0402093.

[8] R. C. Barrett, A. Deloff, Phys. Rev. C **60**, 025201 (1999).

[a]INR, Moscow, Russia
[b]ITEP, Moscow, Russia
[c]HISKP, Universität Bonn, Germany

Evidence of an excited hyperon state in $pp \to pK^+Y^{0*}$

I. Zychor[a], V. Koptev[b], M. Büscher, A. Dzyuba, I. Keshelashvili, V. Kleber[c], R. Koch, S. Krewald, Y. Maeda, S. Mikirtichyants[b], M. Nekipelov, H. Ströher for the ANKE collaboration

The reaction $pp \to pK^+Y$ has been studied with the ANKE spectrometer to investigate heavy hyperon production. The missing mass spectra $MM(pK^+)$ have been analyzed and compared with extensive Monte Carlo simulations. Indications for a hyperon resonance $Y^{0*}(1480)$ have been found.

The measurements were performed at a proton beam momentum of 3.65 GeV/c incident on a a hydrogen cluster–jet target. The average luminosity during the measurements was $L = (1.38 \pm 0.15) \times 10^{31}\,\mathrm{s}^{-1}\,\mathrm{cm}^{-2}$.

At the COSY beam momentum of 3.65 GeV/c hyperons Y with masses up to 1540 MeV/c^2 can be produced in the reaction $pp \to pK^+Y$. A final state comprising a proton, a positively charged kaon, a pion of either charge and an unidentified residue X was investigated in the reaction $pp \to pK^+Y \to pK^+\pi^\pm X^\mp$.

The missing mass spectrum in the reaction $pp \to pK^+\pi^+X^-$ consists of a flat plateau with a peak at approximately 1195 MeV. The peak corresponds to the decay $Y \to \pi^+\Sigma^-(1197)$. In the charge–mirrored $pp \to pK^+\pi^-X^+$ case, the π^- may originate from different sources, *e.g.* a decay with the $\Sigma^+(1189)$ or a secondary decay of $\Lambda \to p\pi^-$, arising from the major background reaction $pp \to pK^+\Lambda \to pK^+\pi^-p$. Protons from this reaction can be easily rejected by cutting $MM(pK^+\pi^-)$ around the proton mass. Nevertheless the missing mass distribution for the (π^-X^+)-final state is more complicated.

If only events around the Σ mass are selected, then the missing mass $MM(pK^+)$ spectrum in the reaction $pp \to pK^+\pi^+X^-$ shows two peaks, see upper part in Fig. 1. One of them corresponds to the contribution of $\Sigma^0(1385)$ and $\Lambda(1405)$ hyperons. The second peak is located at a mass $\sim$1480 MeV/c^2. In the π^-X^+ case, the distribution also peaks at 1480 MeV/c^2, lower part in Fig. 1.

We have tried to explain the measured missing mass $MM(pK^+)$ spectra by the production of hyperon resonances and non-resonant contributions. Detailed Monte Carlo simulations have been performed including the production of well established excited hyperons ($\Sigma^0(1385), \Lambda(1405)$ and $\Lambda(1520)$) and non-resonant contributions like $pp \to pK^+\pi X$ and $pp \to pK^+\pi\pi X$, X denotes any hyperon which could be produced in the experiment. From the comparison of measured and simulated missing mass distributions it turned out that it is necessary to include another excited hyperon Y^{0*} with a mass $M(Y^{0*}) = (1480 \pm 15)$ MeV/c^2 and a width $\Gamma(Y^{0*}) = (60 \pm 15)$ MeV/c^2.

In summary, we have found indications in proton–proton collisions at 3.65 GeV/c for a neutral hyperon resonance Y^{0*} decaying into π^+X^- and π^-X^+ final states. Since it is neutral, it can be either a Λ or Σ hyperon. The production cross section is of the order of few hundred nanobarns. It seems to be difficult to integrate a $Y^{0*}(1480)$ hyperon within the existing classification of 3q-baryons [1, 2]. On the basis of available data we cannot decide whether it is a 3–quark baryon or an exotic state, although some preference towards its exotic nature may be deduced from theoretical considerations [3, 4, 5, 6, 7, 8].

Further studies are required to determine its quantum numbers. At ANKE, using a deuterium cluster target and spectator proton tagging, one can search for the charged Y^{-*} hyperon in the reaction $pn \to pK^+Y^{-*} \to pK^+\pi^-X^0$. The investigation of Y^* decays with photons in the final state is foreseen with the WASA detector at COSY [9].

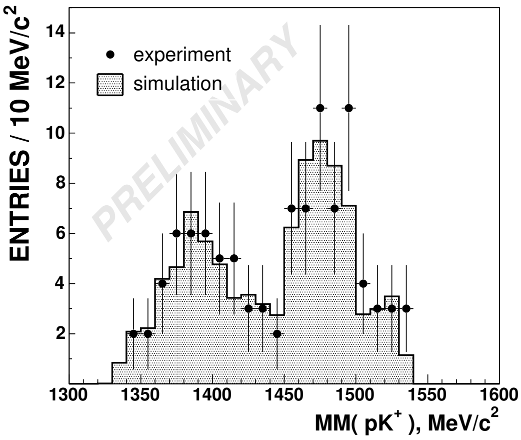

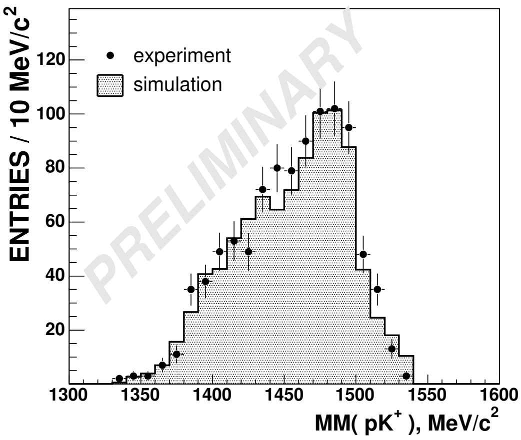

Fig. 1: Experimental and simulated missing mass $MM(pK^+)$ spectra for the reaction $pp \to pK^+\pi^+X^-$(upper) and $pp \to pK^+\pi^-X^+$(lower). The shaded histogram shows the fitted Monte Carlo simulations.

References:

[1] U. Loehring *et al.*, Eur. Phys. J. A **10**, 447 (2001)
[2] S. Capstick and N. Isgur, Phys. Rev. D **34**, 2809 (1986)
[3] H. Högaasen and P. Sorba, Nucl. Phys. B **145**, 119 (1978)
[4] Ya.I. Azimov *et al.*, Phys. Rev. C **68**, 045204 (2003)
[5] R.A. Arndt *et al.*, Phys. Rev. C **69**, 035208 (2004)
[6] R. Jaffe and F. Wilczek, Phys. Rev. D **69**, 114017 (2004)
[7] Y. Oh, H. Kim and S.H. Lee, Phys. Rev. D **69**, 094009 (2004)
[8] C. Garcia-Recio, M.F.M. Lutz and J. Nieves, Phys. Lett. B **582**, 49 (2004)
[9] COSY Proposal 136.1 (2004), http://www.fz-juelich.de/ikp/wasa/

[a]The Andrzej Sołtan Institute for Nuclear Studies,Świerk, Poland
[b]PNPI Gatchina, Russia
[c]IKP, Universität zu Köln, Germany

Deuteron Polarimetry at ANKE

D. Chiladze, A. Kacharava[a], F. Rathmann, and C. Wilkin[b] for the ANKE collaboration

The first measurement of the deuteron–induced charge–exchange reaction [1] was carried out at the ANKE spectrometer using a polarised deuteron beam at $p_d = 2400$ MeV/c. The polarised deuterons ($\approx 3\times10^9$) stored in the COSY ring impinge on a hydrogen cluster–jet target. Two fast protons, emitted in a narrow forward cone with momenta around half that of the deuteron beam, are detected by the Forward Detector (FD) system of the ANKE set–up. Figure 1 shows the ANKE experimental acceptance for singly particles for different reactions as functions of the laboratory production angle and magnetic rigidity, together with loci for the kinematics of different allowed reactions. The $dp \to dp$ reaction has a significant acceptance for $4^\circ < \theta^d_{\rm lab} < 10^\circ$. The observables A_y, A_{yy}, and A_{xx} of this reaction were studied previously at Argonne[2] and SATURNE[3] for $T_d = 1198$ MeV.

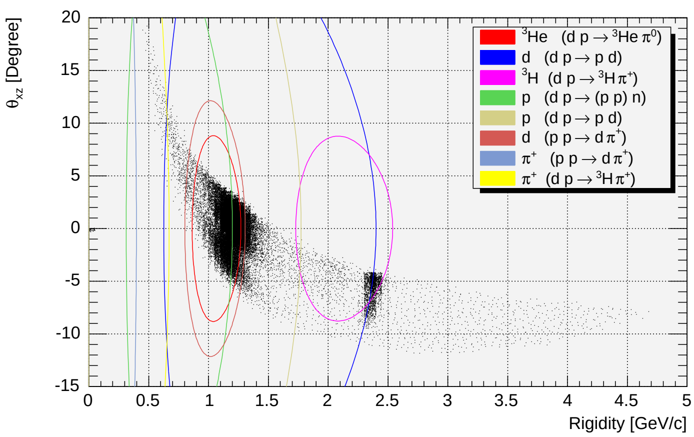

Fig. 1: ANKE experimental acceptance for different reactions in dp collisions at $T_d = 1170$ MeV.

The dp elastic peak region in the momentum spectrum of the single track events was fitted by the sum of a Gaussian and linear function, and events selected within 3σ of the mean. The $dp \to {}^3\mathrm{He}\,\pi^0$ reaction can be studied using just the ^{3}He information. The high momentum branch of ^{3}He particles was isolated well in off–line analysis, applying two–dimensional cuts in ΔE *versus* momentum and Δt *versus* momentum for individual layers of the forward hodoscope. The quasi–free $np \to d\pi^0$ can be clearly identified by detecting two final charged particles in the $dp \to p_{sp} d\pi^0$ reaction, where p_{sp} is a spectator proton which has essentially half the beam momentum. The differential cross section should be half of that for $pp \to d\pi^+$, whereas all the analysing powers should be equal. The charge–exchange process was identified from the missing–mass (see Fig. 2) with respect to the observed proton pairs and time difference information. The spectra for all spin modes reveal a well defined peak at M_{miss} equal to the neutron mass to within 1%; the mean value for the reconstructed neutron mass is $M_n = 940.4 \pm 0.2$ MeV/c^2. The background was less than 2% and stable, so that the charge–exchange process could be reliably identified.

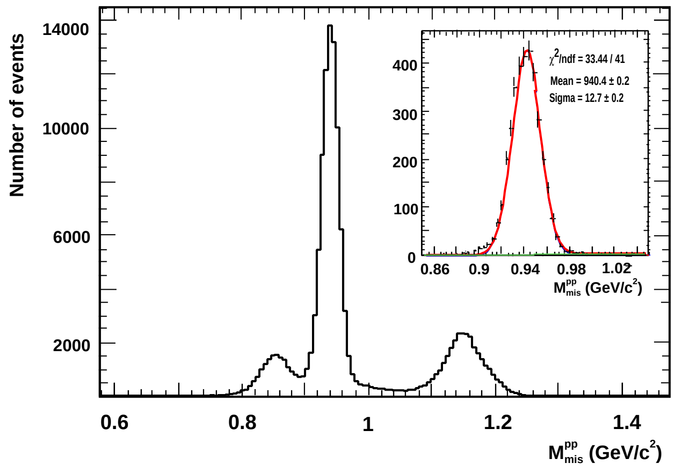

Fig. 2: Missing mass distribution of all observed proton pairs. The inset shows the distribution near the neutron mass for the pairs selected by the TOF.

Using the $\vec{d}p \to dp$, $\vec{d}p \to (2p)n$, $\vec{n}p \to d\pi^0$, and $\vec{d}p \to {}^3\mathrm{He}\,\pi^0$ reactions, which all have large and well known analysing powers, a simultaneous calibration of the vector and tensor components of the polarised deuteron beam at COSY becomes possible for the first time. The results are summarised in Table 1.

Reaction	Facility	α_z	α_{zz}
$\vec{d}p \to dp$	EDDA	0.74 ± 0.02	0.59 ± 0.05
$\vec{d}p \to dp$	ANKE	0.73 ± 0.02	0.49 ± 0.02
$\vec{n}p \to d\pi^0$	ANKE	0.70 ± 0.03	—
$\vec{d}p \to {}^3\mathrm{He}\,\pi^0$	ANKE	—	0.58 ± 0.05
$\vec{d}p \to (pp)n$	ANKE	—	0.48 ± 0.05

Table 1: Values of vector and tensor polarisation parameters. The given errors are only statistical.

The average of the ANKE measurements is $\alpha_z^{\rm ANKE} = 0.72\pm0.02$ and $\alpha_{zz}^{\rm ANKE} = 0.52\pm0.03$, which is compatible with EDDA results [4] measured prior to the ANKE run but at lower beam energy and intensity.

References:

[1] A. Kacharava et al., Proposal #125, (2003).
[2] M. Haji-Said et al., Phys. Rev. **C36**, 2010 (1987).
[3] J. Arvieux et al., NIM, **A273**, 48 (1988).
[4] B. Lorentz et al., proceedings of 9$^{\rm th}$ EPAC conference, July 5-9, 2004, Lucerne, Swiss.

[a] Universität Erlangen, Germany
[b] University College London, UK

Cell tests at ANKE

K. Grigoryev[1], R. Engels[2], A. Gussen[3], P. Jansen[3], H. Kleines[4], F. Klehr[3],
P. Kravtsov[1], B. Lorentz[2], F. Rathmann[2], J. Sarkadi[4], H. Seyfarth[2]
for the ANKE-Collaboration

The goal of the cell tests was to estimate the beam size at the ANKE target position. Prior to these tests, it was not known which size the COSY beam has at injection and after acceleration. These findings are needed to build the storage cells for the polarized target and, depending on the size of the cells, determine how much beam will be lost at injection.

For these tests, the frame with various apertures was constructed. The larger aperture had inner dimensions of the 50x25 mm (see Fig. 2). That is larger than the expected beam size. In order to move apertures into the beam position, the movable XY-table was mounted on the target chamber (as shown in Fig. 1). Initially, the frame is outside of the beam, to allow for other experiments operate. During the tests the frame can be moved in by using stepper motors with a step size of about 50 µm.

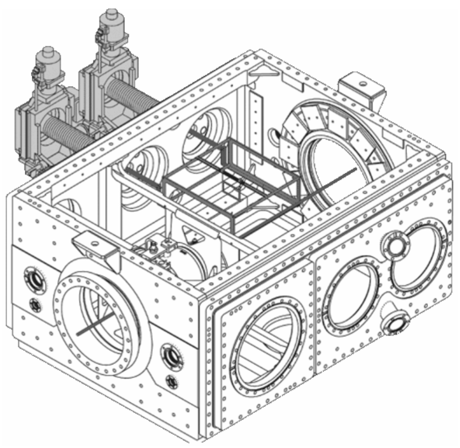

Fig. 1: Target chamber with XY-table and the frame supporting the apertures.

The COSY accelerator crew stabilized the beam center at one point and the first part of the tests was done at injection energy. The center of the large aperture was placed at the expected center of the COSY beam. By moving this aperture out beam starts to be destroyed and after a number of measurements the real beam center was calculated. These tests at injection give us the beam shape and the beam dimensions at injection (see figure 2).

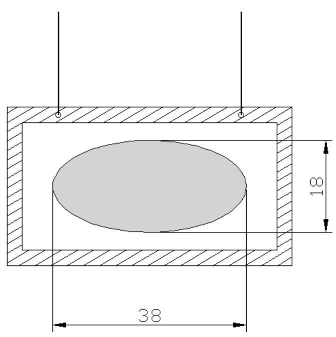

Fig. 2: COSY beam shape and dimensions at injection.

As it shown in figure 2, COSY beam is 18 x 38 mm in diameter. That means if beam and aperture are well-centered we did not destroy beam or hit aperture's walls at injection and about 100% of the injected protons are accelerated.

Tests with accelerated beam always start from the point of calculated COSY beam center. Only when acceleration is finished aperture was placed to measurement point. When aperture placed in the center of the beam after 10 minutes cycle beam intensity not changes. But when beam starts to hit one of the aperture walls intensity immediately drops. And at the time when beam was completely killed during the cycle its center is not to far away from the aperture wall. Result of these tests (shown in figure 3) gives an approximately dimensions of the accelerated beam. And what is very important – beam shape is close to circle.

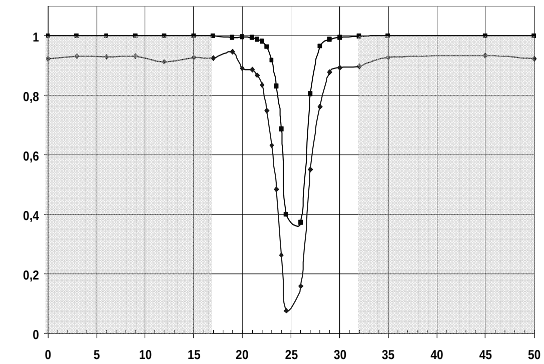

Fig. 3a: horizontal beam dimension scan.

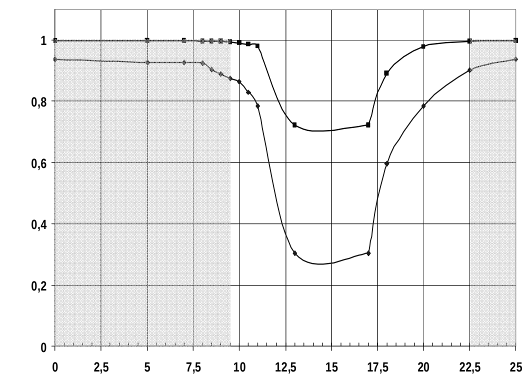

Fig. 3b: vertical beam dimension scan.

In booth case, horizontal and vertical scan of the COSY beam, measurements was carried out with no target (upper curve) and with switched on cluster target (lower curve). The cluster target density is about 10^{12} cm^2 that is 10 times higher then unpolarized gas target density. For the cell tests in 2005 results of these tests are very important.

[1] Petersburg Nuclear Physics Institute, Gatchina, Russia
[2] Institute for Nuclear Physics (IKP), FZ Juelich
[3] Zentralabteilung Technologie (ZAT), FZ Juelich
[4] Central Institute for Electronics (ZEL), FZ Juelich

A New Geant4 based Simulation Framework for ANKE

A. Mussgiller

The ROOT[1] based analysis framework RootSorter[2] provides an easy to use database interface that allows the storage and retrieval of any kind of parameter. A new Geant4[3] based Simulation has been developed that takes advantage of this parameter interface to construct the simulation geometry. The main aim of the development is to hide the internal structure of Geant4 as much as possible and only provide a simple interface to the Geant4 core. The control of the simulation is done in a similar way as in RootSorter which allows a quick start to the users who are already familiar with RootSorter.

Detector Components

The different ANKE detectors may be added to the simulation by calling a function with the name of the detector. Currently the following detectors are known to the simulation:

- Positive Side Detector - Pd (No MWPC)
- Negative Side Detector - Nd
- Forward Detector - Fd
- Spectator Detector - Vd
- D2 Vacuum Chamber
- New Target Chamber

A picture of the implemented detectors and passive geometries is shown in figure 1.

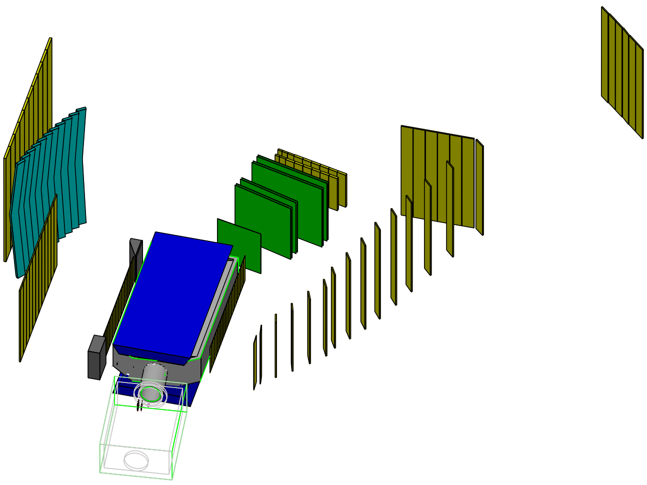

Fig. 1: Picture of the detectors and passive geometries implemented in the simulation

Particle Generator

At the moment the main source for primary particles is a ROOT file containing a Pluto++[4] generated event tree. Again, the type of the particle generator is selected by its name. The name of the used root file may be specified from within the user code, the Geant4 session or a Geant4 macro. The type of vertex at which the primary particles are generated may also be specified. It can be a point like or extended vertex with various shapes. The extended vertices give the opportunity to take the real target extension into account.

Physics Processes

The simulation framework offers the possibility to use any of the by Geant4 supplied physics processes lists. Since the available physics lists are mostly specialised on dealing with high energy particle physics it is possible to specify own physics processes that suit the users need. At the moment one additional physics list is implemented which is able to deal with all processes involved in the physics at ANKE.

Magnetic Field

Two different types of magnetic fields are implemented in the software, a ”box” field and a field map based on Mafia calculations. Both magnetic field classes are based on the fields available in RootSorter. The field strength is controlled via the parameter interface but may be overridden on the Geant4 command line or a macro.

Output

The output of the simulation is a ROOT file with a tree. Each in a simulation run used detector adds a branch to the tree which holds the detector specific results for each simulated event. For the Forward detection system for instance the branch will contain a list of hits in the hodoscope counters as well as the hits in the wire chambers. Each hit carries the information about the particle that produced the hit (type and momentum), its position and the time since the start of the event. In addition the list of generated particles and the position of each particles vertex is written to the tree. The output file does not contain any Geant4 related data which means that the analysis of the output file can be done without the use of Geant4.

Summary

The newly developed simulation framework provides an easy to use interface to the Geant4 core. All above listed key components are activated via the name of the component. The size of a full featured simulation of ANKE is as low as 20 lines of source code. The interface allows to extend the simulation by additional detectors, particle generators or field classes in a simple way. For developing extensions only a limited knowledge of Geant4 is required.
In the near future the implementation of all detectors will be finished. Up to this point the simulation framework has been used for several simulations involving the spectator detector.

References:

[1] Rene Brun and Fons Rademakers, ”ROOT - An Object Oriented Data Analysis Framework”, Proceedings AIHENP’96 Workshop, Lausanne, Sep. 1996, NIM A 389 (1997) 81-86.

[2] V. Hejny, M. Hartmann, A. Mussgiller, ”RootSorter: A New Analysis Framework for ANKE”, IKP Annual Report 2002

[3] S. Agostinelli et al, ”GEANT4: A Simulation Toolkit”, NIM A 506 (2003), 250-303

[4] Marios A. Kagarlis, ”Pluto++ - A Monte Carlo simulation tool for hadronic physics”, GSI Report 3, July 2000

Drift chamber with a c-shaped frame

J. Smyrski[1] for the COSY-11 collaboration

For tracking positively charged pions appearing in near-threshold reactions such as $pp \to pp\pi^+\pi^-$ with momenta by a factor of m_π/m_p smaller then the proton momenta the momentum acceptance of the COSY-11 experimental facility was extended towards smaller values. Another important advantage was the detection of positively charged kaons prior to their decay what is especially important for the measurement of the $pp \to ppK^+K^-$ close to threshold due to its small cross section on the level of a few nanobarns. For this, an additional drift chamber was built and installed in the free space along the COSY-11 dipole magnet.

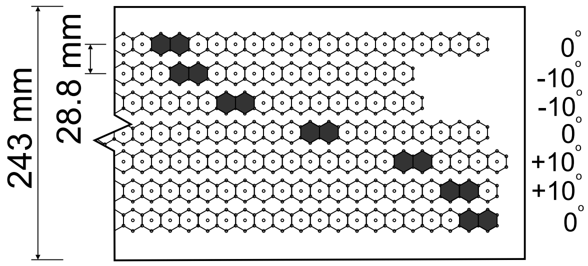

Fig. 1: Upper end-plate with indicated positions of openings for feedthrough used for mounting the wires. The shaded cells indicate the response of the chamber when one particle was registered

The sensitive chamber volume consists of hexagonal drift cells identical with the structure used in the central drift chamber of the SAPHIR detector [1]. The cells are arranged in seven detection planes as indicated in Fig. 1 showing one of two parallel aluminium endplates between which the wires are stretched. Three detection planes (1, 4 and 7) contain vertical wires, two planes (2, 3) have wires inclined at -10° and the remaining two planes (5, 6) contain wires inclined at $+10^\circ$. This arrangement makes it possible to reconstruct particle trajectories in three dimensions, also in cases of multi-track events. The two aluminium endplates for mounting the wires are 15 mm thick and are supported by two c-shaped frames made out of 20 mm thick aluminium (see a three-dimensional view in Fig. 2). The frames hold the total load of about 2.4 kN originating from the mechanical tension of the wires.

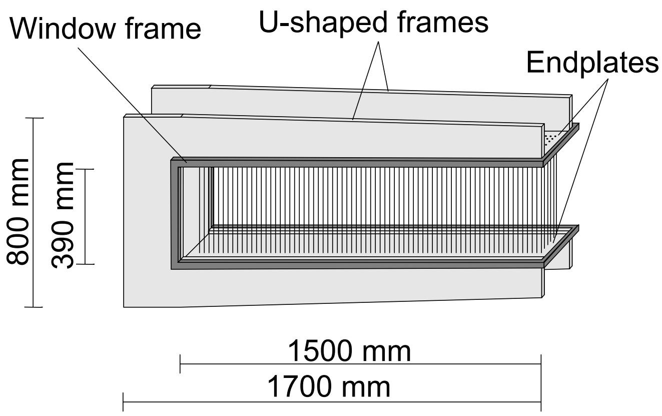

Fig. 2: Schematic three-dimensional view of the chamber frame for mounting the wires. The window for particles is 1500 mm wide and 390 mm high.

For the reconstruction of particle tracks a simple algorithm was developed and implemented as a computer code written in the C-language. The reconstruction proceeds in three stages: (i) finding track candidates in two dimensions, independent for each orientation of the wires, (ii) matching the two-dimensional solutions in three dimensions, (iii) three-dimensional fitting in order to obtain optimal track parameters. The chamber is calibrated using the experimental data. In a first step an approximate drift time to drift distance relation is determined by integration of the drift time spectra as provided by the uniform irradiation method. In the next step, corrections to this calibration are determined using an iterative procedure. For this, the average deviations between the measured and fitted distances of the tracks from the sense wires are calculated. Fig. 3 shows differences Δd of the measured and fitted distances calculated as a function of the drift time for three subsequent iterations. The mean value of Δd deviates from zero only after the first iteration (upper panel in Fig. 3) and the corresponding correction to the space-time relation is of the order of 0.3 mm. For higher iterations the corrections are negligible. The standard deviation of Δd is about 0.2 mm and is a measure of the single wire resolution. The chamber allows to determine the track position and inclination in the horizontal plane with an accuracy of about 0.3 mm and 1 mrad, respectively. In the vertical direction these accuracies decrease by about an order of magnitude, which is in accordance with the design values.For the tracking in the vertical magnetic field of the COSY-11 dipole magnet no higher precision was envisaged. For other applications the precision can be improved by choosing a larger inclination of the wires.

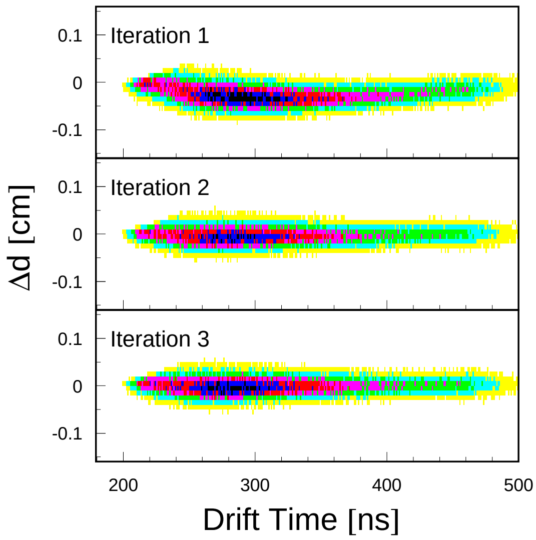

Fig. 3: Differences of the measured and fitted distances calculated as a function of the drift time for the first detection plane and the angular bin $\theta \in (50^\circ, 60^\circ)$ in three subsequent iterations of the calibration procedure.

References:

[1] W. J. Schwille et al., Nucl. Instr. and Meth. **A 344** (1994) 470.

[1] Institute of Physics, Jagellonian University, Poland

A method to disentangle single meson and multi-pion production rates in the missing mass spectra of the quasi-free $pn \to pnX$ reactions

P. Moskal for the COSY-11 collaboration

The measurements of the quasi-free $pn \to pn\eta$ and $pn \to pn\eta'$ reactions are being conducted at the COSY-11 facility by registering all outgoing nucleons from the $pd \to p_{sp}pnX$ reaction and using the missing mass technique for the identification of events with the creation of the meson under investigation [1]. Subscript $_{sp}$ denotes the spectator proton, which does not take part in the reaction, and X stands for the η, η' meson, or multi-pion system. In this report we will outline a technique [2] which permits to distinguish contributions of multi-pion and a single meson production in the missing mass spectrum of the quasi-free $pn \to pnX$ reaction when it is studied via the measurement of the $pd \to pnX\,p_{sp}$ process. The technique allows also to combine events corresponding to the multi-pion production at various excess energies in order to increase statistics for the determination of the shape of the multi-pion background at a fixed excess energy.

The known momentum of the proton beam and the indirect determination of the four-momentum vector of neutron inside the deuteron at the moment of the collision permit to determine the total energy available for the proton-neutron reaction for each registered event. Therefore, the collected data can be grouped according to the excess energy with respect to the $pn \to pn\eta$ process for instance. The production of the η meson can occur only if the excess energy $Q = \sqrt{s} - m_{proton} - m_{neutron} - m_{\eta}$ acquires positive value. According to the above definition Q is understood as an excess energy with respect to the $pn\eta$ system. Consequently such defined Q may also be negative, and in the case of the negative values of Q only pions may be created for example via the $pn \to pn\pi\pi$ reaction.

In order to establish the form of the background it would be sufficient to determine a missing mass spectrum ($\frac{dN^{\pi}}{dm}$) from an infinitesimal range of any of the negative values of Q, provided that the number of events written on tapes suffices to neglect any statistical fluctuations and that the shape of the reconstructed invariant mass of pions is independent of the excess energy Q. The latter assumptions allows to express the background distribution in a convenient way as a function of the difference between the kinematical limit ($m_{\eta} + Q$) and the given mass m: $B(m_{\eta} + Q - m)$.

Being not limited by statistics one could divide the range of positive values of Q into so narrow subranges that the resultant missing mass spectrum - in each subrange of Q - would be a simple sum of the form B and a signal from the η meson. The discussed situation is depicted schematically in figure 1. The lower panel of this figure shows the method of the construction of the background. If the two assumptions mentioned above were valid, then in order to derive a signal of the η meson from a missing mass spectrum it would be sufficient to subtract a missing mass spectrum determined for negative Q after the shift of the latter to the kinematical limit (dotted line) and normalization at the very low mass values where no events from the η meson production are expected (dashed-dotted line). In such a case the contribution of the $pn \to pn\eta$ reaction could be extracted without the necessity of any assumption of the unknown distribution of the background expressed as a function of the excess energy ($\frac{dN^{\pi}}{dQ}$).

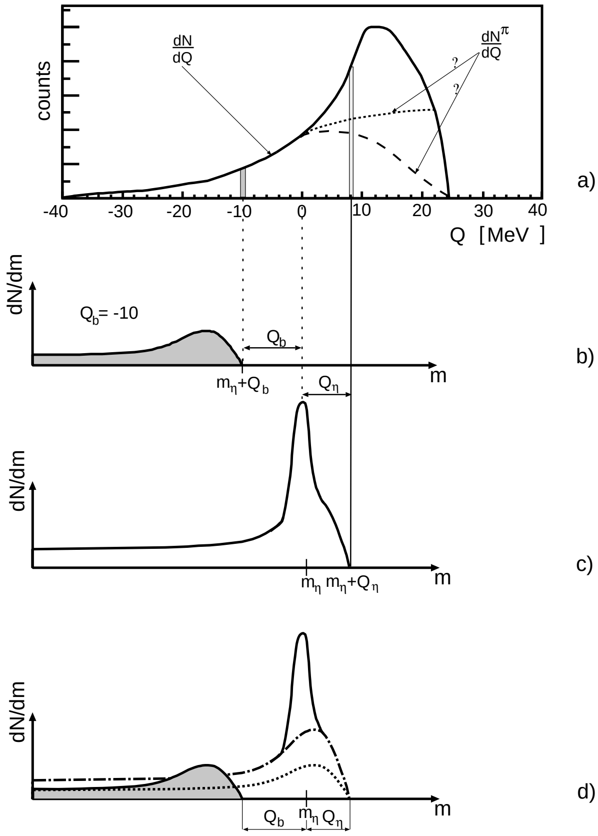

Fig. 1: a) Distribution of the excess energy with respect to the $pn \to pn\eta$ reaction plotted schematically for the beam momentum of $P_b = 2.075\ GeV/c$ [2]. b), c) Scheme of the missing mass spectra as derived for the negative (Q_b) and positive (Q_{η}) values of Q. d) The shape of the background in the mass spectrum for Q larger than zero can be constructed from the shape of the multi-pion mass distribution determined for Q less than zero.

However, by reviewing the experimental distribution of $\frac{dN}{dQ}$ [1] one recognizes that the obtained statistics is indeed insufficient for the derivation of the $\frac{dN^{\pi}}{dm}$ spectrum from the bin of Q with the width equal to the experimental resolution (FWHM = 5 MeV). Yet, the statistics can be improved significantly if all events registered with Q less than zero could be taken into account. This can be realized by adding to the missing mass calculated for a given event a value of $(Q_{\eta} - Q_b)$ which will shift the background events measured at Q_b to the kinematical limit defined by the Q_{η}. In this manner one constructs the background for the missing mass spectrum obtained for $Q = Q_{\eta}$. The resultant modified missing mass distribution obtained from the entire data sample of negative Q values can be identified with the function $B(m_{\eta} + Q_{\eta} - m)$ needed for the derivation of the background distribution within a finite excess energy bin. For more details the reader is referred to a more comprehensive report [2].

References:

[1] P. Moskal et al., AIP Conf. Proc. **717** (2004) 907.
[2] P. Moskal, Schriften des FZ-Jülich: Matter & Materials **21** (2004) 249.

Bremsstrahlung radiation in the deuteron–proton collision

J. Przerwa* for the COSY–11 collaboration

Bremsstrahlung radiation created in the collisions of nucleons is still the subject of interest since it is highly sensitive to the kind of the nucleon–nucleon potential, and hence may serve as a tool to discriminate between various existing potential models [1, 2]. At the COSY–11 experiment [3] a signal from γ–quanta was observed in the time–of–flight distribution for the neutral particles measured between the target and the neutral particle detector [4]. This encouraged us to analyse the data in view of the Bremsstrahlung radiation in a free $dp \rightarrow dp\gamma$ and a quasi–free $np \rightarrow np\gamma$ reactions. Data have been taken using a proton target and a deuteron beam with a momentum close to the threshold of the $dp \rightarrow dp\eta$ process. Events corresponding to the $dp \rightarrow dp\gamma$ and $dp \rightarrow ppn\gamma$ reaction have been identified by measuring the outgoing charged as well as neutral ejectiles. Details of the functioning of all detectors and the method of measurement can be found in references [3, 4, 5]. In order to identify the $dp \rightarrow dp\gamma$ reaction events with two tracks in the drift chambers and a simultaneous signal in the neutron detector have been selected. In figure 1 the squared mass of one particle is plotted versus the squared mass of the second registered particle.

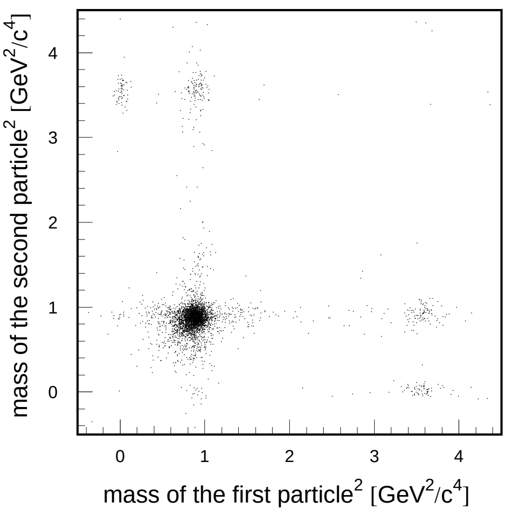

Fig. 1: Scatter plot of invariant masses determined for events with two charged particles measured in coincidence. The measurement was conducted using a hydrogen target and a deuteron beam with momentum of 3.204 GeV/c.

Based on this figure the measured reactions can be grouped according to the type of ejectiles. Thus reactions with two protons, proton and pion, proton and deuteron, and pion and deuteron can be clearly selected. Next for neutral particles the distribution of the time–of–flight between the target and the neutron detector was determined under the condition that one of the charged particles was identified as a proton and the other as a deuteron. In such case gamma quanta – due to the baryon number conservation – are the only one possible source of a signal in a neutron detector. Indeed a clear peak around the time corresponding to the time–of–light of the light was visible [5]. The gamma quanta may originate from Bremsstrahlung reaction or from the decay of produced mesons eg. via the $dp \rightarrow dp\pi^0 \rightarrow dp\gamma\gamma$ reaction sequence.

In order to distinguish between these hypotheses, one need to calculate the missing mass produced in the $dp \rightarrow dpX$ reaction. Figure 2 shows the distribution of the squared missing mass as obtained for the $dp \rightarrow dpX$ reaction. A significant peak around 0 MeV^2/c^4 — the squared mass of a gamma quanta — constitutes evidence for events associated to the deuteron–proton bremsstrahlung. In addition a broad structure at higher masses originating from two pions emitted from the $dp \rightarrow dp\pi^0\pi^0$ – or two gamma quanta from the $dp \rightarrow dp\gamma\gamma$ reaction is visible. However, to certify that the peak at zero MeV is indeed due to the gamma quanta from the bremsstrahlung process, one more issue needs to be clarified. At a value of 0.02 GeV^2/c^4 a peak originating from one pion production in the $dp \rightarrow dp\pi^0$ reaction is expected. The peak is not seen in the figure 2, however, since it is expected only about two standard deviations of the mass resolution from the center of the peak assigned to the γ production, we can not exclude a priori a systematical shift. Extensive Monte Carlo studies have to be performed.

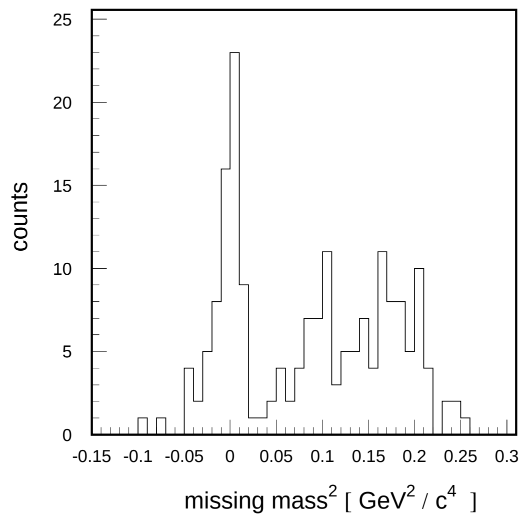

Fig. 2: Distribution of the squared missing mass for the $dp \rightarrow dpX$ reaction.

The analysis of the quasi–free $n\ p \rightarrow n\ p\ \gamma$ process via the $dp \rightarrow np\gamma p_{sp}$ reaction is more complicated, however in this case all three baryons, namely two protons and the neutron can be measured in the drift chambers and in the neutron detector, respectively, and the tentative identification of this reaction has been successfully performed [5].

References:

[1] N. A. Khokhlov *et al.*, *Phys. Rev.* **C 68**, 054002 (2003).
[2] M. D. Cozma *et al.*, *Phys. Rev.* **C 68**, 044003 (2003).
[3] S. Brauksiepe *et al.*, *Nucl. Instr.* & *Meth.* **A 376**, 397 (1996).
[4] P. Moskal *et al.*, e-Print Archive: nucl-ex/0311003.
[5] J. Przerwa, Diploma Thesis, Jagellonian University, Cracow (2004); e-Print Archive:hep-ex/0408016.

* Institute of Physics, Jagellonian University, Poland

Two-proton correlation function for the $pp \to pp\eta$ reaction.

P. Klaja[1], P. Moskal for the COSY-11 collaboration

A large enhancement in the excitation function of the $pp \to pp\eta$ reaction observed close to the kinematical threshold indicates a strong attractive interaction within the $pp\eta$ system [1]. The effect can be described assuming, that the proton-proton pair is produced from a large object of a 4 fm radius [2]. A study of the $pp\eta$ system is particularly interesting in the context of the search for the Borromean states. As Borromean we call a bound three-body system in which none of the two-body subsystems is bound. In nuclear physics the ^{11}Li and ^{6}He nuclei have been found to have such a property [3]. At present it is still not established whether the low energy $pp\eta$ system can form a Borromean or resonant state. Recently the COSY-11 collaboration published high statistics data for the $pp \to pp\eta$ reaction which will be used to elucidate this question [1]. These data are presently evaluated using the well known intensity interferometry method, commonly referred to as the HBT effect [4]. This technique permits to determine the size of the source from which the protons are emitted. It is based on the correlation function of the relative momenta between the two protons, which relates the space-time separation of the particles at the emission time to their momenta p_1 and p_2. This function can be expressed in terms of pair- and single-particle cross section [4]:

$$R(p_1, p_2) = C \cdot \frac{d^6\sigma/d^3p_1 d^3p_2}{(d^3\sigma/d^3p_1)(d^3\sigma/d^3p_2)} - 1, \qquad (1)$$

where C denotes the overall normalization constant. The shape of two-proton correlation function calculated including Coulomb interaction and Pauli exclusion principle depends on the spatial size of the source. In a present analysis we consider only the projection of the R function onto one dimension corresponding to the relative momentum of emitted protons $q = |\vec{p}_1 - \vec{p}_2|$. In the calculations we tentatively assumed a simultaneous emission of the two protons and approximated the effective spatial shape of the emission zone by the Gaussian distribution. In such case the standard deviation of this distribution - hereafter referred to as r_0 - constitutes the measure of the dimension of the source. For the simulations we adapted a computing procedure written by R. Lednicky [5]. Figure 1 displays proton-proton correlation functions calculated for the, $pp \to pp\eta$ reaction, assuming four different sizes of the emission source.

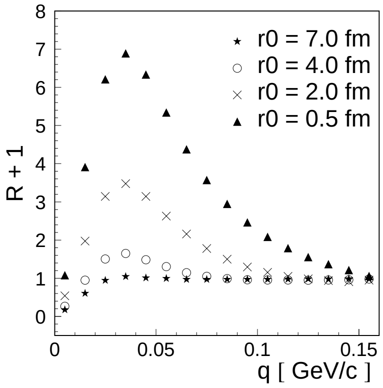

Fig. 1: Theoretical correlation functions of two protons for $r_0 = 0.5, 2.0, 4.0$ and $7.0 fm$.

One can see that the height of the peak at q ≈ 40 MeV/c depends significantly on the value of r_0 and therefore the magnitude of this maximum may serve as a measure of the volume of the reaction zone. Of course, generally the size of the reaction zone can be extracted by the comparison of the experimental and simulated correlation functions treating r_0 as a fitting parameter.

Since in the experiment the single particle yield has not been measured it is not possible to determine directly the denominator of equation 1. Therefore, in order to facilitate an extraction of the considered correlation function from the data, an alternative function $R(q)$ can be defined [4] as a ratio of the reaction yield $Y_{pp\eta}(q)$ to the uncorrelated yield $Y^*(q)$:

$$R(q) + 1 = C^* \frac{Y_{pp\eta}(q)}{Y^*(q)}, \qquad (2)$$

where C^* denotes an appropriate normalization constant. In practice, $Y^*(q)$ can be obtained via event mixing techniques, taking momentum of one proton from event m, and the momentum of the second proton from event m+k, where k is arbitrarily chosen. The correlation function derived from the data according to the formula 2 is presented in figure 2.

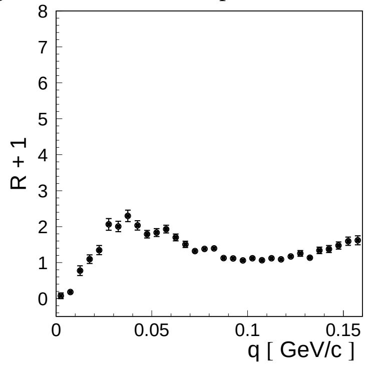

Fig. 2: The experimental two protons correlation function calculated from data [1] for the $pp \to ppX$ reaction.

A determined experimental spectrum shows a maximum at a value of q as predicted by simulations. A rough comparison between theoretical correlation functions shown in figure 1 and the experimental one indicates that the size of the reaction volume can be approximated by the Gaussian distribution with $r_0 \approx 3$ fm. However, in order to draw final conclusions we need to take into account an experimental spread in the theoretical calculations, and to distinguish between the multi-pion and η meson creation when evaluating the experimental data. At present, in order to calculate the coincidence ($Y_{pp\eta}(q)$) and uncorrelated ($Y^*(q)$) yields we took into account all events corresponding to the $pp \to ppX$ reaction for which the mass of the unobserved system X differs by no more than 1 MeV/c^2 from the mass of the η meson. In the near future, as a next step of the analysis, we will extract the correlation function for the $pp \to pp\eta$ reaction free of the multi-pion production background, and compare it to the calculations performed taking into account experimental resolution of the determination of q.

References:

[1] P. Moskal et al., Phys. Rev. **C 69** (2004) 025203.
[2] S. Wycech, Acta Phys. Pol. **B 27** (1996) 2981.
[3] M. V. Zhukov et al., Phys. Rep. **231** (1993) 151.
[4] D. H. Boal et al., Rev. Mod. Phys. **62** (1990) 553.
[5] R. Lednicky, private communication.

[1] Institute of Physics, Jagellonian University, Poland

The analysis' status of the $\vec{p}p \to pp\eta$ reaction at Q = 10 MeV

R. Czyżykiewicz and P. Moskal[1] for the COSY-11 collaboration

Studies on the production mechanism and structure of the η meson are part of the scientific program of the COSY-11 team. For this purpose the analysing power for the $\vec{p}p \to pp\eta$ reaction at different excess energies has been measured. For more detailed argumentation of this choice of the observable the reader is referred to [1, 2] or to the original theoretical papers [3, 4]. Feasibility studies from a first measurement of the analysing power of the $\vec{p}p \to pp\eta$ reaction were reported in [5]. Data gathered at the excess energy of Q = 40 MeV yielded rather small values of the analysing power, indicating pure *s*-wave production of the η meson, however they are afflicted with relatively large uncertainties. The origin of such large uncertainties lies mainly in the low polarisation level (about 50%) of the proton beam used at the time of the first measurement (January 2001). With the development of the quality of polarised beams at the COSY accelerator, the analysing power measurements have been continued at Q = 10 and 37 MeV. Partial results of the data analysis for a measurement at Q = 10 MeV are reported herein.

The method of the determination of the analysing power at COSY-11 has been introduced in reference [6]. The observables required to derive the analysing power are: i) the proton beam polarisation, ii) relative luminosity of the spin up and down cycles, and iii) the number of $\vec{p}p \to pp\eta$ events registered during spin up and spin down cycles (which correspond to the scattering to the left or the right side with respect to the polarisation plane).

The polarisation of the beam has been measured by two independent polarimeters. One installed close to the COSY-11 target [7], the other being the internal COSY polarimeter [9, 10] positioned about 10 meters further along the beam line. Data taken in parallel using both detection systems have been analysed. The results of both systems are in line and indicate the significant increase of the spin averaged polarisation up to P = 0.729± 0.002 (statistical uncertainty) compared to the above mentioned polarisation level available in January 2001.

Elastically scattered events, recorded in parallel, have also been used for the relative luminosity determination. The centre-of-mass region of proton angles that were registered by the COSY-11 acceptance has been divided into nine subranges of 2 degrees each for which the relative luminosity has been calculated according to the formula:

$$L_{rel}(\theta) = \frac{N_{up}(\theta)}{N_{down}(\theta)} \frac{1 + A_y^{el}(\theta)P}{1 - A_y^{el}(\theta)P}, \qquad (1)$$

where $N_{up}(\theta)$ and $N_{down}(\theta)$ are the numbers of elastically scattered events for spin up and down cycles into the solid angle around the direction given by the θ polar angle, P is the polarisation degree averaged over the spin up and down cycles and $A_y^{el}(\theta)$ are the analysing powers for the elastic scattering which were measured by the EDDA collaboration [11]. The averaged value of the relative luminosity was found to be $L_{rel} = 1.003 \pm 0.003$(stat) indicating good stability of the luminosity in the neighbouring cycles with different spin orientation.

Figure 1 depicts the missing mass distribution as obtained during the May 2003 run. The number of η mesons in the clear peak which is visible over the wide multipionic background was estimated to be around 3000, however for the more refined evaluation a precise estimation of the multipion background is required. Till now the data were corrected for effects caused by the relative position shifts between the beam and the target applying the method described in reference [8]. Using the momentum distribution of the elastically scattered protons we determined also the dimension of the proton beam and its momentum spread, a factors necessary to perform reliable simulations of the studied $\vec{p}p \to pp\eta$ and the background reactions.

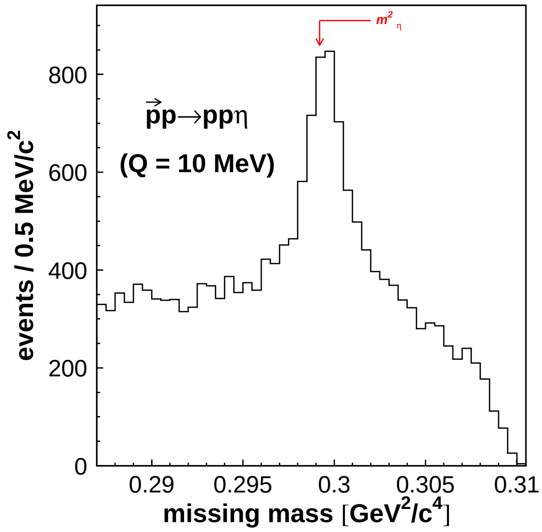

Fig. 1: Missing mass spectrum for the $\vec{p}p \to pp\eta$ reaction at the excess energy Q=10 MeV as measured by means of the COSY-11 setup.

At present the multi-dimensional acceptance corrections are being performed along with the simulations of the multipionic background events. The final results of the analysis should be available by summer 2005.

References:

[1] R. Czyżykiewicz et al., IKP, FZ-Jülich, Ann. Rep. 2003,
[2] R. Czyżykiewicz et al., AIP Conf. Proc. **717** (2004) 858; nucl-ex/0312006.
[3] G. Fäldt and C. Wilkin, Phys. Scripta **64** (2001) 427.
[4] K. Nakayama et al., Phys. Rev. **C 65** (2002) 045210.
[5] P. Winter et al., Phys. Lett. **B 544** (2002) 251, erratum-ibid.**B553** (2003) 339.
[6] P. Winter, diploma thesis, Jül-3943 (2002).
[7] R. Czyżykiewicz, Schriften des Forschungszentrum Jülich, Matter and Materials **21** (2004) 122.
[8] P. Moskal, e-Print Archive: hep-ph/0408162.
[9] B. Lorentz, FZ-Jülich, private communication (2003).
[10] F. Bauer and K. Büsser, Nucl. Instr. and Meth. **A 431** (1999) 385.
[11] M. Altmeier et al., Phys. Rev. Lett. **85** (2000) 1819.

[1] Institute of Physics, Jagellonian University, Poland

Status of the analysis of the $pn \to pn\eta$ reaction

M. Janusz[1] and P. Moskal for the COSY–11 collaboration

The total cross section for the reaction $pp \to pp\eta$ was determined by the WASA/PROMICE collaboration to be about 6.5 times smaller than for the $pn \to pn\eta$ reaction in the excess energy range between 16 MeV and 109 MeV [1]. Here we report on preliminary results of a measurement by the COSY-11 collaboration investigating the $pd \to pn\eta p_{sp}$ reaction, where p_{sp} denotes the spectator proton. This experiment was conducted as a test of feasibility to measure the meson production via quasi-free $pn \to pnX$ reactions at the COSY-11 facility equipped with the neutron – and the spectator detectors. The beam momentum was taken such that the maximum rate of the registered $pn \to pn\eta$ events occurs at the excess energy range between 0 and 20 MeV allowing to establish the energy dependence of the total cross section of the $pn \to pn\eta$ reaction in the unknown energy region close to the kinematical threshold.

For a preliminary estimation of the total integrated luminosity we used the coincidence rate between the S1 – and S4 detectors [2] and assumed that the fraction of this trigger rate due to the elastically scattered protons was constant during the entire run. Thus only tentative values of the cross sections are quoted in this report. The total integrated luminosity was estimated to be $\approx 103\ nb^{-1}$.

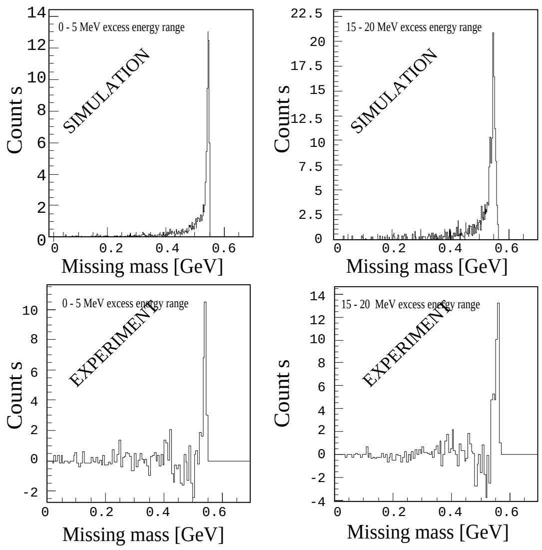

Fig. 1: The comparison of the missing mass spectra from simulation and experiment for two energy subranges as indicated inside figures.

The η and multi-pion production cannot be distinguished from each other on the event-by-event basis by means of the missing mass technique. However, we can distinguish the number of registered $pn \to pn\eta$ reactions from the multi-pion background comparing the missing mass distributions for Q values larger and smaller than zero, where Q is understood as an excess energy with respect to the $pn\eta$ system. Knowing that negative values of Q can only be assigned to the multi-pion events we can derive the shape of the missing mass distribution corresponding to these events [3]. Taking into account that the resolution of the excess energy determination amounts approximately to 5 MeV (FWHM) [4], we have divided the whole range of the excess energy into four subranges with widths corresponding to 5 MeV. For each partition the missing mass spectrum was determined. In parallel a missing mass distribution was established also for the negative values of Q and after a shift to the kinematical limit and normalization at mass values lower than 0.3 GeV it was subtracted from the histograms for the positive Q values. The normalization was performed separately for each of the considered subranges of Q. Figure 1 shows exemplary missing mass spectra from the simulation and the experiment. They are in qualitative agreement, though the modulations below the η peak in the experimental spectra indicates that the background subtraction needs to be improved [3].

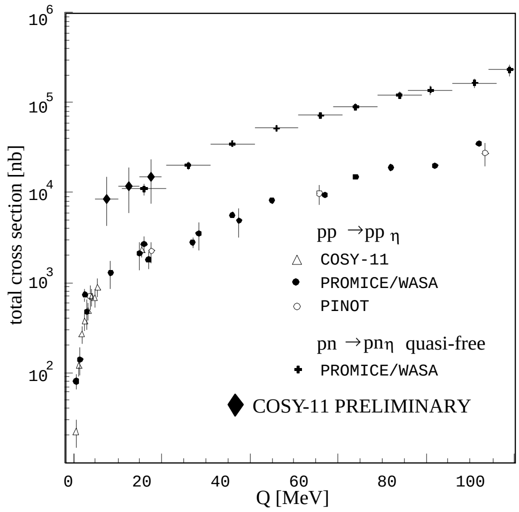

Fig. 2: Preliminary results of the total cross section for the η meson production in the quasi-free $p-n$ scattering. Diamonds indicate COSY-11 preliminary results, and the other points show the data from [1, 5].

Figure 2 shows the comparison between the total cross sections for the $pn \to pn\eta$ reaction determined by the WASA/PROMICE collaboration and the preliminary results obtained by the simplified analysis of the COSY-11 data. The error bars for the COSY-11 points are very conservative and certainly will be reduced subsequently with the advance of the analysis.

References:

[1] H. Calén et al., Phys. Rev. **C 58** (1998) 2667
[2] M. Janusz, P. Moskal, Schriften FZ-Jülich **21** (2004) 238.
[3] P. Moskal, Schriften FZ-Jülich **21** (2004) 249.
[4] R. Czyżykiewicz, Berichte des FZ-Jülich, Jül-4017 (2002).
[5] J. Smyrski et al., Phys. Lett. **B 474** (2000) 182; F. Hibou et al., Phys. Lett. **B 438** 41 (1998) 41; F. Calén et al., Phys. Lett. **B 366**(1996) 39; E. Chivassa et al., Phys. Lett. **B 322** (1994) 270.

[1] Institute of Physics, Jagellonian University, Poland

Determination of the COSY beam polarisation by means of the COSY-11 setup

R. Czyżykiewicz and P. Moskal[a] for the COSY-11 collaboration

Measurements of the polarisation observables require the accurate monitoring of the polarisation degree. In the recent measurements of the analysing power at COSY-11 (reported in [1, 2, 3]) beam polarisation determination have been performed using the COSY-11 polarimeter. For this purpose the elastically scattered events have been registered in two mutually perpendicular planes: In the plane perpendicular to the polarization vector and in the plane comprising polarisation vector but perpendicular to the beam. COSY-11 is only an one-arm detection setup. In order to measure the asymmetry in the subsequent cycles of the COSY operation the proton spin has been flipped. Thus the asymmetry for the elastically scattered protons under a given polar angle Θ can be expressed as:

$$\varepsilon = \frac{N_L - N_R}{N_L + N_R}, \qquad (1)$$

where N_L and N_R refer to the number of elastically scattered protons which were registered at the angle Θ in the plane perpendicular to the polarisation vector, during the spin down and up cycles, respectively. The duration of a single cycle was 300 s, being significantly less than the time scale (10 hours) for a substantial changes of the density of the target. Anyhow, the small luminosity variation between the spin up and down cycles was taken into account by normalizing N_L and N_R from equation 1 to the number of elastic triggers in the vertical plane - N_0^{dn}(for spin down) and N_0^{up}(for spin up) - which were registered by an independent sub-detector system operating in parallel presented in figure 1 [5, 6, 7].

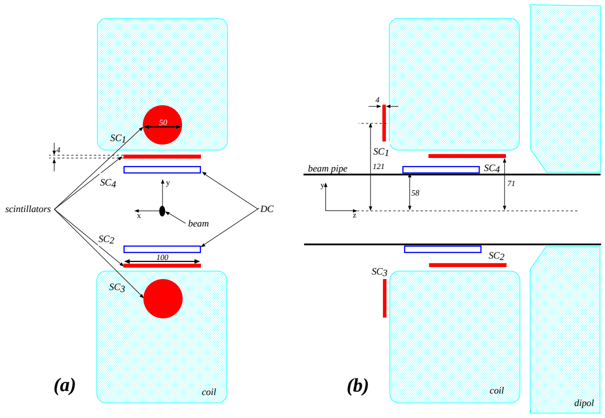

Fig. 1: Schematic view of the detection subsystem for registration of the elastically scattered events in the polarisation plane. (a) Front view. (b) Side view.

For N_0^{dn} and N_0^{up} determination the coincidences of the following scintillators was chosen[1]: $(SC_1 \wedge SC_2) \vee (SC_3 \wedge SC_4)$. The final formula[1] for the polarisation degree as a function of the proton scattering angle in the centre-of-mass system (θ) reads:

$$P(\theta) = \frac{1}{A_y^{el}(\theta)} \frac{N_R(\theta)/N_0^{up} - N_L(\theta)/N_0^{dn}}{N_R(\theta)/N_0^{up} + N_L(\theta)/N_0^{dn}}. \qquad (2)$$

For the calculations the three ranges of the centre-of-mass angle has been chosen, spanned from $\theta_{min} = 37^\circ$ to $\theta_{max} = 49^\circ$. Analysing powers for the proton-proton elastic scattering (A_y^{el}) were taken from reference [8]. The results of the polarisation determination are presented by full black circles in figure 2.

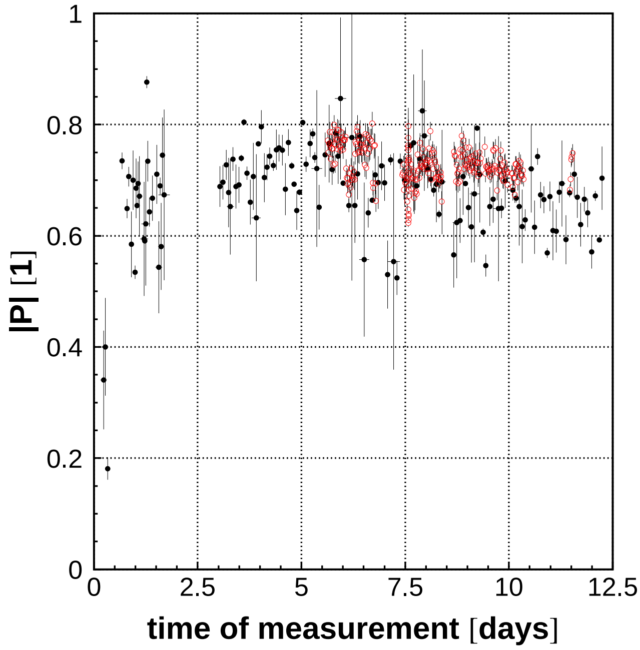

Fig. 2: Polarisation degree versus the time of the measurement as obtained during the COSY-11 April 2003 run.

Since in the former experiments we have also used the alternative methods for monitoring of the polarisation level which were based on the measurements with the EDDA polarimeter [9] or with the Hamburger polarimeter [10, 11], the comparison of the COSY-11 data with the polarisation values obtained by means of the latter method was possible and is presented in figure 2. In that figure, data of [11] are presented as open red circles. Both COSY-11 – and the Hamburger polarimeter results are in good agreement. The average polarisation value was extracted to be P = 0.729± 0.002 (statistical uncertainty).

More details of the determination of the absolute value of polarisation has been presented in [7]. The important feature is that one is able to monitor the absolute values of polarisation for both spin ”up” and ”down” orientations, which is desirable for decreasing the systematical error in the analysing power calculation.

References:

[1] R. Czyżykiewicz et al., contribution to the Annual Report (2003).
[2] R. Czyżykiewicz et al., AIP Conf. Proc. **717** (2004) 858; nucl-ex/0312006.
[3] R. Czyżykiewicz et al., contribution to this reports.
[4] P. Winter et al., Phys. Lett. **B544** (2002) 251.
[5] I.-A. Pellmann, Diploma Thesis (1999), Berichte des Forschungszentrum Jülich, Jül-3686.
[6] P. Kowina et al., contribution to the Annual Report (2001) 14.
[7] R. Czyżykiewicz et al., Schriften des Forschungszentrum Jülich, Matter and Materials **21** (2004) 122.
[8] M. Altmeier et al., Phys. Rev. Lett. **85** (2000) 1819.
[9] K. Ulbrich, Bonn University, private communication (2003).
[10] F. Bauer, K. Büsser, Nucl. Instr. & Meth. **A 431** (1999) 385.
[11] B. Lorentz, FZ-Jülich, private communication (2003).

[a] Institute of Physics, Jagellonian University, Poland

[1]For a detailed discussion reader is referred to [7].

Development of the COSY-11 simulation program for the study of the $dp \to dp\eta$ reaction

C. Piskor-Ignatowicz*, P. Moskal, J. Smyrski* for the COSY–11 collaboration

The deuteron-η interaction is of the special interest due to the possible existence of the η-nucleus bound or quasi-bound states predicted by Ueda [1]. The η meson production near threshold in the three nucleon system is much less explored as compared to the two nucleon system [2]. For the $dp \to dp\eta$ reaction near threshold only total cross section data exist for two excess energies Q = 1.5 $\pm$ 0.6 and 3.8 $\pm$ 0.6 MeV measured with the spectrometer SPESIII at the SATURNE accelerator [3]. The energy dependence of the total cross section for this reaction is expected to be very sensitive to the $d-\eta$ interaction since even much weaker $p-\eta$ interaction significantly modifies the shape of the excitation function as observed in the $pp \to pp\eta$ reaction [4]. The aim of the experiment performed by the COSY-11 collaboration is the determination of the $d-\eta$ interaction and study of the η production mechanism in the $dp \to dp\eta$ reaction. The experiment was carried out with the internal deuteron beam of the COSY accelerator scattered on the proton target of the cluster jet type. In the case of the $dp \to dp\eta$ reaction at the threshold the outgoing deuterons have about two times larger momentum than the outgoing protons and, consequently, their deflection in the magnetic field of the COSY-11 dipole magnet is two times smaller. They leave the COSY-11 vacuum chamber through 10 cm wide and 5.6 cm high forward window as shown in figure 1.

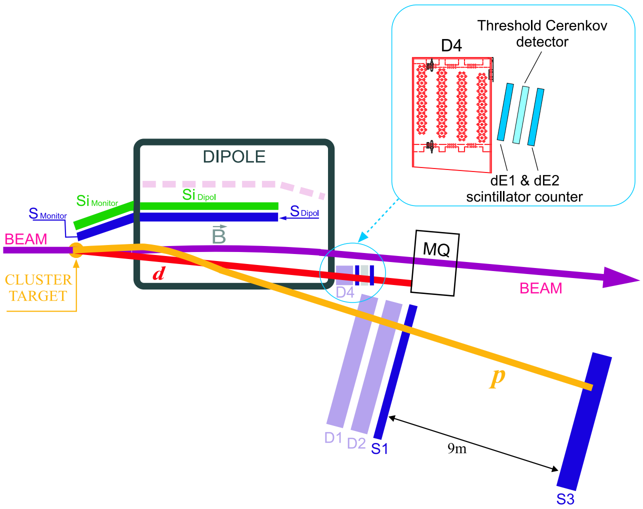

Fig. 1: Detection setup of the COSY-11 experiment [5]. Protons are measured in the drift chambers D1, D2, as well as in the scintillator hodoscopes S1, and S3. For the deuterons, small drift chamber D4, two scintillators dE1, dE2 and Cerenkov threshold counter were installed.

Protons are registered in the standard COSY-11 drift chambers D1, D2, as well as in the scintillator hodoscopes S1 and S3. In the previous year we conducted a measurement of the $pd \to pd\eta$ reaction at four values of excess energies [6] and also performed the first step of the data analysis showing a clear separations of protons, deuterons and ^3He nuclei registered. We also reported a clear signals for the quasi-free $pp \to pp$ and $pp \to d\pi^+$ reactions used for the determination of the luminosity. At present we are at the last stage of accomplishing the programme for the analysis of the $dp \to dp\eta$ events. A corresponding computing procedure necessary for the track reconstruction, and the geometry of the hexagonal drift chamber, are being implemented into the complex computer programme enabling the simulation and analysis of the reactions measured. For the registration of deuterons from the $pd \to pd\eta$ reaction a small drift chamber D4 with two scintillators dE1, dE2 and Cerenkov threshold counter were installed in the space between the dipole exit window and the quadrupole magnet MQ. The chamber D4 has a box shape with dimensions of 13 cm x 18 cm x 18 cm. It consists of seven detection planes: four planes with 10.4 cm vertical wires separated by three planes with 12.70 cm horizontal wires. Each detection plane contains hexagonal cells with the width of 1.1 cm. The distance between adjacent planes is 1.65 cm. Two projections of the drift chamber D4 are shown in figure 2.

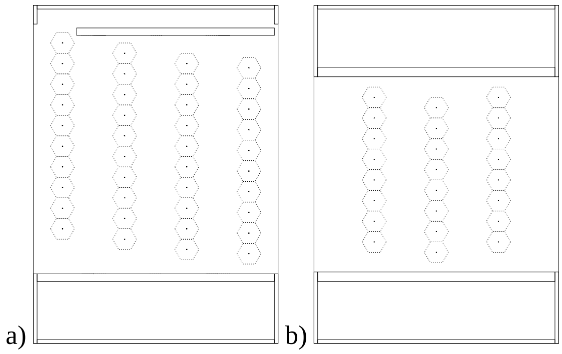

Fig. 2: (a) Top view of the D4 drift chamber showing four identical detection planes, containing 10 cells with vertical wires. (b) Side view presenting three planes containing 8 cells of horizontal wires, each.

The chamber allows for the three dimensional particle tracks reconstruction. The particles momenta are determined by tracing their trajectories in the magnetic field of the dipole magnet back to the target position. Behind the drift chamber D4 two 5 mm thick scintillators dE1 and dE2 are placed. Their signals (if in coincidence) are used as a trigger for the D4 detector readout and as a stop signal for the time–of–flight measurement on the 2 m path from the target. The time of the reaction at the target is derived from measurement of the velocity of the associated particle registered in the scintillator hodoscopes S1 and S3 and from the time measured by the S1 detector. Such a solution enables the particles identification. In order to reduce the proton background a 2 cm plexi glass threshold Cerenkov detector is used. Further improvement of the particle identification is done by taking into account the energy losses in the scintillators. Data analysis is in progress.

References:

[1] T. Ueda, Phys. Rev. Lett. **66** (1991) 297.
[2] J. Smyrski et al., COSY Proposal No. **99** (2001).
[3] F. Hibou et al., Eur. Phys. J. **A7** (2000) 537.
[4] P. Moskal, e-Print Archive: hep-ph/0408162.
[5] S. Brauksiepe et al., Nucl. Instr. & Meth. **A 376** (1996) 397.
[6] C. Piskor-Ignatowicz et al., Schriften FZ-Jülich: Matter & Materials **21** (2004) 272.

* Institute of Physics, Jagellonian University, Poland

Investigations on the pd → ^{3}He η′ production at COSY-11

H.-H. Adam[1], A. Täschner[1], A. Khoukaz[1], N. Lang[1], T. Mersmann[1] and R. Santo[1]
for the COSY-11-Collaboration

Measurements on the near-threshold production of neutral mesons in the reaction channel pd→^{3}He X^0 (X^0 = η, ω, η′, ϕ) are of general interest for many reasons. In combination with an efficient ^{3}He identification and four-momentum determination this reaction channel might be well suited for rare decay studies of neutral mesons. Furthermore, in case of e.g. the η-meson production recent measurements resulted in data which are remarkable for both their strength and energy dependence. The observed rapid decrease of the production amplitude squared $|f|^2$ with increasing excess energy at threshold was found to be dominated by a strong ^{3}He-η final state interaction and the presence of N*(1535) resonance [1, 2]. In contrast to this, only little is known for the corresponding case of the η′ meson production. In the near threshold region only one data point exists at a very low excess energy. Therefore, new data close to threshold enable to study the corresponding production amplitude with respect to the absolute scale and a possible deviation from phase-space expectations, similar to the η case. The determination of the excitation function in the near-threshold region will also be valuable for studies on the dominant production mechanism and the confirmation of theoretical predictions.
Investigations on the pd → ^{3}He η′ reaction close to threshold at excess energies of 5, 10, 15 and 40 MeV have been performed using the COSY-11 installation and signals of this reaction channel have been detected successfully (see figure 3).
The identification of the outgoing ^{3}He nuclei and the determination of their four momentum vectors is possible by using a set of drift chambers allowing for a momentum determination and scintillator hodoscopes providing energy loss information (see figure 1).

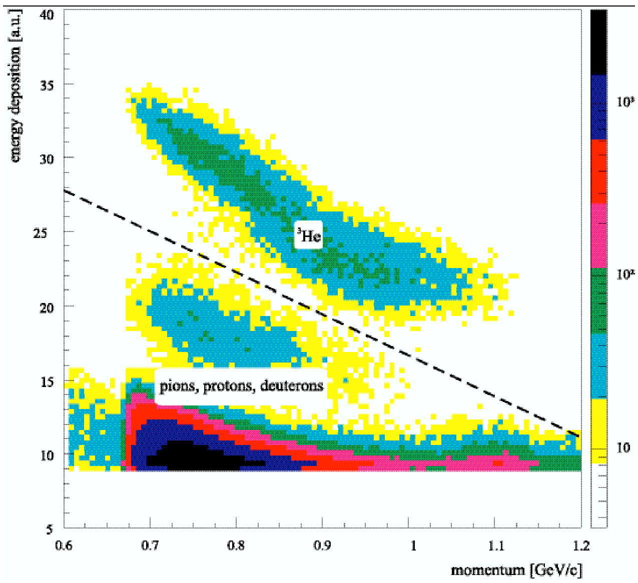

Fig. 1: Identification of ^{3}He nuclei using both the reconstructed momentum and the energy loss in a scintillator hodoscope. The possibility for a clean separation from other particles is indicated by the dashes line.

With this information available, the mass of an unobserved particle X of the two-body reaction pd → ^{3}He X can be reconstructed, which leads to a full event reconstruction for the two particle final state of interest (figures 2,3). The further analysis of the data will allow to extract total cross sections.

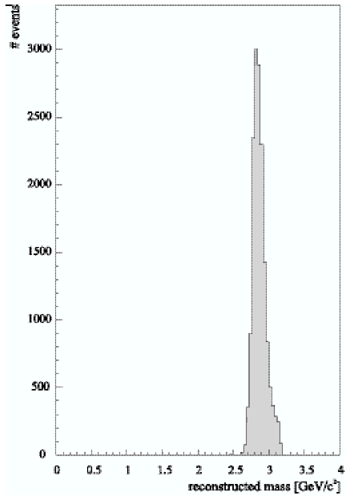

Fig. 2: Reconstructed mass of the detected ^{3}He nuclei. The picture presents the selected events at Q = 10 MeV.

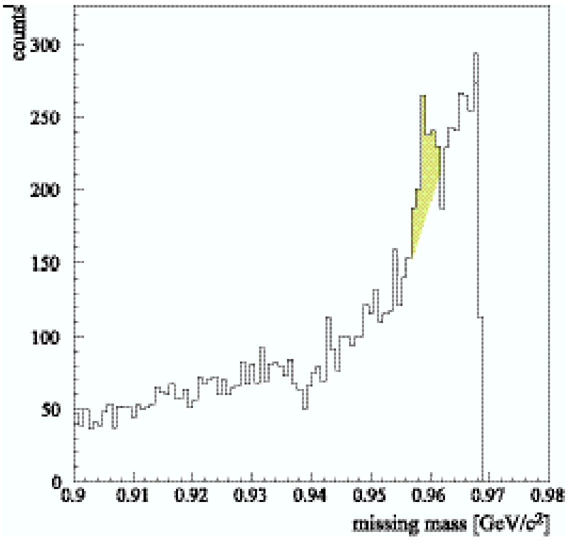

Fig. 3: Missing mass spectrum of the reaction pd→^{3}He X, obtained at an excess energy of Q = 10 MeV and integrated over a range of cms scattering angles of -0.6 ≤ cosΘ* ≤ 0.6.

This work ist supported by the Forschungszentrum Jülich.

References:

[1] G. Fäldt and C. Wilkin, Nucl. Phys. A 587 (1995) 769.
[2] H.-H. Adam et al.; Proceedings of the second symposium on threshold meson production in pp and pd interaction; 1-3 June 2004; Matter and Material, Vol. 21, ISBN 3-89336-366-1

[1] Institut für Kernphysik, Universität Münster

Energy and momentum resolution of the COSY–11 neutron detector.

T. Rożek, D. Grzonka for the COSY-11 collaboration

The detection of neutral particles is one of the most challenging tasks in experimental physics. Neutrons must be detected via nuclear reactions resulting in charged particles or electromagnetic radiation which produce a detector signal. Usually the neutron conversion happens in a calorimeter which has to be sufficiently large to get high conversion efficiencies [1]. The measured neutron energy in such a calorimeter results from the total deposited energy. However, as long as the detector is in a significant distance from the target the energy determination of the neutral particles is easier achievable via a time of flight measurement. Therefore, the total energy of a neutron doesn't have to be deposited in the calorimeter and only the first generated timing signal in the scintillator is needed allowing the detector to be much smaller and the analysis less complicated. The COSY – 11 neutron detector [2] is an array of 24 modules read out on both sides, with the first row of it being positioned at a distance of 7.36 m from the target. Additionally, it is equiped with VETO scintillators to discriminate against charged particles. Each module is built of eleven lead plates interlayed by eleven scintillator plates (with dimensions of 270 x 90 x 4 mm^3) [2] (see Fig. 1). The energy of the neutron is determined from time of flight - assuming a hit in the detector being due to the neutron. The global timing for the neutron detector is taken as the difference between the time of the reaction in the target and the shortest time in the neutron detector (given by the first module which fired).

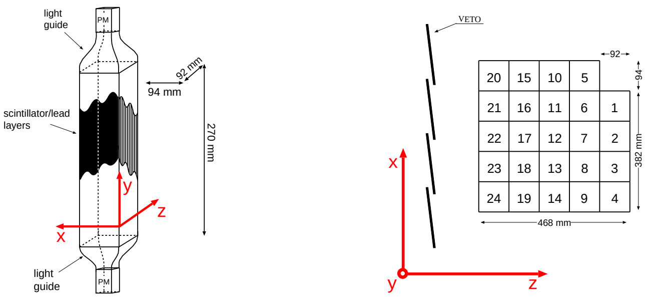

Fig. 1: In the left part a single module of the neutron detector and in the right the COSY – 11 neutron detector arrangement with VETO scintillators are depicted. Direction of the 'z' axis is the direction of the beam.

In the studies of meson or/and hyperon production near threshold with a neutron in the exit channel, the accurate neutron energy calculation has fundamental influence on the missing mass resolution of the investigated particle. E.g. in the $pp \to nK^+\Sigma^+$ reaction the four momenta of the K^+ and the neutron have to be determined in order to calculate the missing mass for the identification of Σ^+ events. Extending the analysis of [3] to the $pp \to nK^+\Sigma^+$ channel, the energy and momentum resolution of the COSY – 11 neutron detector was determined. The neutron energy resolution depends on the time of flight accuracy and the precise measurement of the flight path:

$$E = m_n\sqrt{1+\beta^2\cdot\gamma^2} \quad ; \quad \gamma = \frac{1}{\sqrt{1-\beta^2}} \quad \text{and} \quad \beta = \frac{l_n}{T_n},$$

with the neutron mass m_n and the distance l_n between target and the conversion point. The neutron time of flight (T_n) is obtained relative to the reconstructed time in the target by backtracking positively charged particles (e.g. K^+) through the magnetic field to the target. The inaccuracy of T_n stems from the neutron detector time resolution which was found to be 0.4 ns [4] and the accuracy of time determination in the target of about 0.22 ns [5]. An additional uncertainty in the neutron energy calculation is caused by the distance measurement. The neutron path is defined as a difference between the position of the target and the location of the first module which gave a signal.

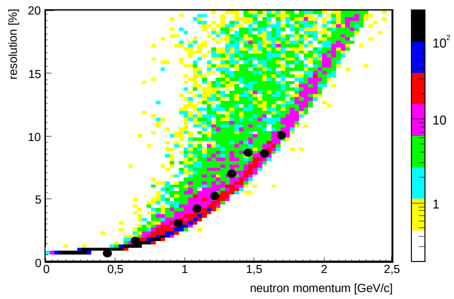

Fig. 2: Momentum resolution for the COSY – 11 neutron detector. The black filled circles are from MC studies and entries of the coloured distribution are the expected errors of the individual neutron detector signals interpreted as a neutron.

In the "energy hermetic" calorimeters the relative energy/momentum resolution improves with an increased neutron energy see e.g. [6]. Using the time of flight method the resolution decreases with an increased neutron energy [7].
In the LAND neutron detector with a neutron flight path of about 15 m the neutron energy resolution for $E_{kin} \leq 1GeV$ is in the order of 5 % [7]. For the COSY – 11 neutron detector the energy resolution for neutrons within this range is less than 8 % which is a rather good result. In the figure 2 the neutron momentum resolution (σ) at COSY – 11 is shown. In Monte Carlo studies neutrons with known momenta were generated (P_{gen}), and by the usual analysis procedure their momenta were reconstructed (P_{recon}). The width (σ) of the $P_{gen} - P_{recon}$ distribution is given by the black circles. Furthermore for each signal in the neutron detector (not necessarily a neutron) of an event sample from the $2.74GeV/c$ data the expected relative momentum error from the known uncertainties given above is determined and plotted in figure 2. The resulting distribution is in very good agreement with the MC results that confirms the realistic MC event generation. A direct experimental determination of the momentum resolution was not possible because reaction channels like $pp \to pn\pi^+$ which would allow this were not detected with a reasonable statistics.

References:

[1] Glenn F. Knoll Radiation detection and measurement, 3rd edition New York: John Wiely & Sons, Inc., 1999.
[2] P. Moskal, Ann. Rep. 1996, IKP FZ-Jülich, **Jül-3365** 35.
[3] J. Przerwa MSc thesis, Berichte des FZ-Jülich, **Jül-4141**.
[4] T. Rożek and P. Moskal, Ann. Rep. 2002, IKP FZ-Jülich, **Jül-4052**.
[5] M. Wolke, PhD. thesis, , IKP FZ-Jülich, **Jül-3532**.
[6] R. Wigmans, Nucl. Instr. & Meth. **A 259** 389 - 429 1987.
[7] T. Blaich, Nucl. Instr. & Meth. **A 314**136 - 154 1992.

Excitation function of the $pp \to ppK^+K^-$ reaction near threshold

P. Winter for the COSY-11 collaboration

The COSY-11 collaboration extended the rather small existing database [1–3] on the $pp \to ppK^+K^-$ reaction near the production threshold by two measurements at excess energies of $Q = 10$ and $28\,\mathrm{MeV}$, both lying below the ϕ-meson threshold. The total cross section at $Q = 17\,\mathrm{MeV}$ [1] significantly exceeds the expectations for a pure non-relativistic phase space. Besides the known strong proton-proton final state interaction, such an effect could be caused by additional interactions in the proton-kaon systems. The K^+K^- system is linked with the nature of the scalar resonances a_0/f_0. These resonances are described as $q\bar{q}$ states [4], $qq\bar{q}\bar{q}$ states [5], $K\bar{K}$ molecules [6,7], hybrid $q\bar{q}$/meson-meson systems [8] or even quarkless gluonic hadrons [9]. The strength of the K^+K^- interaction plays an important role [7] in the understanding of these resonances, which can be studied in the elementary $K\bar{K}$ production in pp collisions.

For both energies, the calibration was improved and the final analysis was performed. The explicit details of the analysis can be found elsewhere, e. g. [3, 10, 11].

After the identification of two protons and a K^+, a clear signal in the missing mass spectrum at the kaon mass is observed for both energies (as an example see figure 1 at $Q = 28\,\mathrm{MeV}$). Before final cross sections will

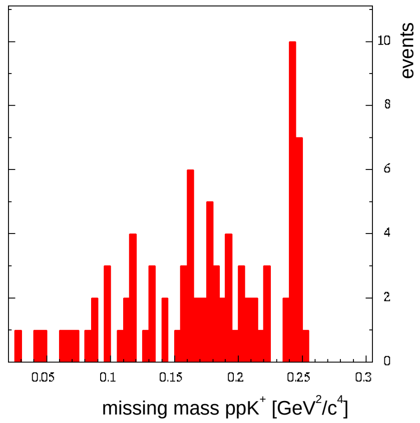

Fig. 1: Squared missing mass of the ppK^+-system with an additional demand for a hit in the dipole scintillator for $Q = 28\,\mathrm{MeV}$.

be presented, last detailed studies of different experimental parameters like the beam width and the beam momentum spread have to be performed. They can be reconstructed by looking at different experimental observables (see for example [12]), e.g. invariant and missing masses, in order to optimize the agreement between the data and the Monte-Carlo studies which are needed for studying the detection efficiency.

The luminosity has been extracted via a simultaneous measurement of the elastic pp scattering. Together with the detection efficiency, first preliminary cross sections for both excess energies were calculated. The excitation function is shown in figure 2 together with some theoretical predictions. It is obvious, that the cross section exceeds all lines towards lower energies. It remains an open question if the discrepancy will be solved by accounting for the pp and pK interaction simultaneously. Furthermore, the four-body final state has to be incorporated correctly whereas the dash-dotted line as a first attempt just includes the pp-FSI deduced for the three body final state. To further study the degree of this

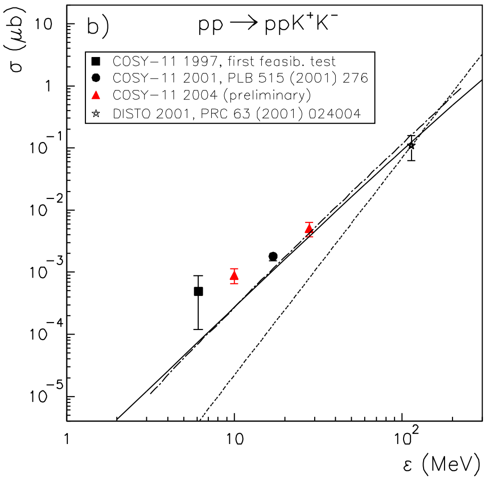

Fig. 2: Excitation of the reaction $pp \to ppK^+K^-$ with the new preliminary data at $Q = 10$ and $28\,\mathrm{MeV}$. The dashed line is the pure non-relativistic phase space ($\propto Q^{\frac{7}{2}}$), the solid line is a calculation without the pp-FSI but an energy dependent matrix element [13] and the dash-dotted line results from a parametrization of the pp-FSI.

strong rise, a new measurement at $6\,\mathrm{MeV}$ [14] will be performed soon in order to increase the existing statistics at this energy of only two counts.

References:

[1] C. Quentmeier *et al.*, Phys. Lett. **B 515**, 276 (2001), [nucl-ex/0103001].
[2] F. Balestra *et al.*, Phys. Rev. **C 63**, 024004 (2001), [nucl-ex/0011009].
[3] M. Wolke, Dissertation, Westfälische Wilhelms-Universität Münster, 1997, IKP Jül-3532.
[4] D. Morgan and M. R. Pennington, Phys. Rev. **D 48**, 1185 (1993).
[5] R. L. Jaffe, Phys. Rev. **D 15**, 267 (1977).
[6] J. D. Weinstein and N. Isgur, Phys. Rev. **D 41**, 2236 (1990).
[7] D. Lohse, J. W. Durso, K. Holinde and J. Speth, Nucl. Phys. **A 516**, 513 (1990).
[8] E. Van Beveren *et al.*, Z. Phys. **C 30**, 615 (1986).
[9] R. L. Jaffe and K. Johnson, Phys. Lett. **B 60**, 201 (1976).
[10] C. Quentmeier, Dissertation, Westfälische Wilhelms-Universität Münster, 2001.
[11] P. Winter, Dissertation in preperation, University of Bonn.
[12] P. Moskal *et al.*, Nucl. Instr. & Meth. **A 466**, 448 (2001), [nucl-ex/0010010].
[13] A. Sibirtsev, W. Cassing and C. M. Ko, Z. Phys. **A 358**, 101 (1997), [nucl-th/9612040].
[14] P. Winter and M. Siemaszko, IKP-KFA (2004), COSY Proposal No. 61.4.

Study of the Reaction np $\rightarrow$ ppπ^- for Excess Energies $<$ 100 MeV above Threshold

E. Kuhlmann* for the COSY-TOF Collaboration

Our studies of π-producing reactions in the NN-system have recently been extended to the np-entrance channel by use of a deuterium beam which was focussed onto our standard LH_2 target. Employing the spectator tagging method, the np $\rightarrow$ ppπ^- reaction could be scanned for the range of excess energies ΔQ = 10-100 MeV at just one beam momentum p_d=1.85 GeV/c. Three charged ejectiles show up in the exit channel where only the pions will emerge at polar angles larger than 30°. Crucial to the experiment is the simultaneous detection of the spectator proton which is expected to be found with roughly half the beam momentum within a narrow cone around the beam axis. For a detailed investigation of this reaction we used the COSY-TOF spectrometer with its huge solid angle coverage of $> 1\pi$ which allows to measure β, ϑ and ϕ of each charged particle; their momentum 4-vectors are then obtained via suitable mass hypotheses and a test of various kinematical constraints. Even if the pions will escape detection, the information gathered from the three protons alone is sufficient to completely reconstruct each event including the Fermi momentum of the "beam neutron" bound within the deuteron. In addition to extracting from the measurements angular and momentum distributions as well as Dalitz plots for the range of excess energies mentioned above, we aim at a test of the spectator model which is based on two assumptions: (1) the proton in the deuteron is a spectator, which influences the reaction only in terms of the associated Fermi motion of the bound neutron, and (2) the matrix element for quasifree pion production from a bound and hence off-shell neutron is identical to that for free pion production from an unbound neutron at the same two-body energy and momentum transfer.

In the following, results obtained from a sample of less than 10% of all data will be presented. Pions with β-values <0.5 are stopped within the various start detector modules and those escaping with $\vartheta > 57°$ can also not be detected in the endcap or the barrel. Hence, we had set up two main trigger conditions for the experiment, one where 4 hits were required and a second one with 3 hits; events of the latter kind were recorded with a reduction factor of 10. The first step in the analysis of the 4-hit events was to identify the pion by starting from four possible hypotheses, i.e. the pion being particle 1, 2, 3 or 4. For each case the sums of longitudinal and transverse momentum components p_l and p_t were calculated. We chose as the correct assignment the one where these sums were closest to the ones given from kinematics, namely p_l=p_d and p_t=0. In case of 3-hit events, the pion was assumed to be the missing particle and its 4-momentum components were deduced via missing mass analysis as well as energy and momentum conservation. The spectator proton was then identified as the one proton which was detected closest to the beam axis with momentum near p_d/2. By transformation of the spectator 4-momentum into the deuteron-CM-system, the 4-momentum vector of the neutron could be obtained with the deduced neutron mass always being smaller than its free mass, sometimes by more than 10%. After transforming back into the LAB-system, all relevant parameters for the "beam-neutrons" are fixed. It should be noted that these parameters as e.g., mass, actual beam momentum and beam direction differ from event to event. As an example, the range of excess energies is shown in the left half of fig. 1, the reconstructed Fermi momentum is given on the right. The shift towards larger momenta as observed for the experimental data is due to the strong rise in cross section of the np $\rightarrow$ ppπ^- reaction, which leads to an enhancement of the larger momenta.

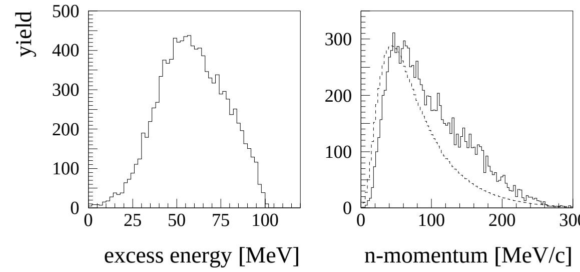

Fig. 1: *left: range of excess energies extracted event-by-event from the data; right: Fermi momentum distribution of the bound neutron (histogram) in comparison with the one derived from an analytic parametrization of the deuteron wave function (Hulthen function).*

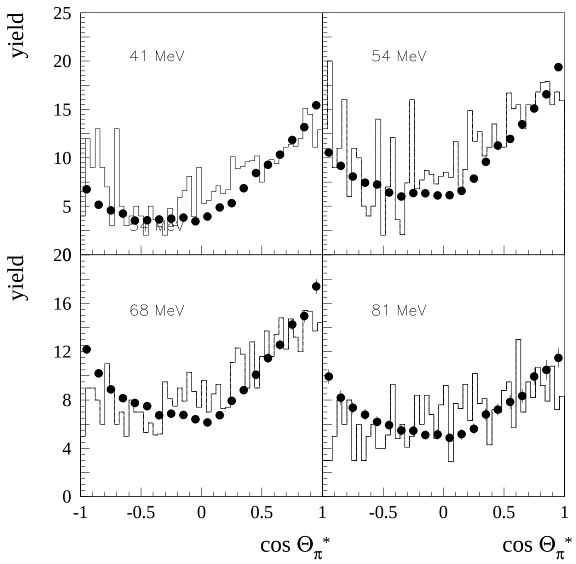

Fig. 2: π^- *angular distributions of the reaction np $\rightarrow$ ppπ^- in comparison with data taken from [1].*

As a final example, π^- angular distributions in the ppπ^- CM system obtained for four excess energy bins are shown in fig. 2 and compared to previously published data [1] where a neutron beam was employed. So far, no acceptance corrections have been applied, nevertheless the agreement is very good, which we take as yet another proof of the homogeneous detector performance.

References:

[1] M. Daum et al., Eur. Phys. J. C23 (2002) 43

* IKTP, Technische Universität Dresden
supported by the BMBF

Simulation of the detection efficiency of $pK^0\Sigma^+$ with a polarized target at COSY-TOF

E. Roderburg
for the COSY-TOF Collaboration

1.) Motivation

In 2003 and 2004 experimental hints for a five quark state ("Pentaquark") were published. At COSY some evidence for this particle was found in the invariant mass spectrum of K^0p at 1530 MeV/c^2 [1]. It was noticed that COSY offers a unique possibility to determine the parity of this hypothetical particle. The parity can be detected by determining the spin of both protons in the initial state by using polarized beam and target. [2] [3]. In the following the detection efficiency of a measurement with a polarized target combined with a modified COSY-TOF setup is examined.

2.) Input for the Simulation

For the simulation the program package mcTOF, which is based on GEANT 3.2 [4], is used. The experimental setup is based on the Frozen Spin Target from Bonn/Bochum as used in the PS185 experiment [5] and a modified COSY-TOF detector. The front part of the TOF detector is removed, all detectors are operated at normal pressure. The active target is inside a cylinder with a diameter of 40 mm and a length of 80 mm filled with liquid helium. It consists of liquid butanol with thickness of ±4mm in beam direction. The target cryostat provides 2 windows of 20 μm titanium for the beam and the scattered particles with an opening angle of $\pm 32^0$. A scintillation start counter, which is used for the multiplicity trigger (2 charged particles $\rightarrow$ 4 charged particles), is situated as close as possible to the target (24 mm from the target center). It is followed by a silicon microstrip detector 6mm farther downstream. In 30 cm distance from the center a stack of straw drift chambers will be used with a sensitive square area of 1 m^2. The TOF tank with the barrel, ring and quirl counters is simulated with the endcap at 3300 mm distance from the target center.
The proton beam with a momentum of 2.95 GeV/c is simulated with a width, which has a gaussian distribution of σ=0.7mm at the target. Multiple scattering, energy loss, and hadronic interaction of the particles are included in the calculations.

3.) Results of the Simulation

The principle of the measurement of the reaction pp$\rightarrow$ p$K^0\Sigma^+$ is the detection of the secondary vertex of the K^0 decaying into 2π with the coincident detection of the kink in the Σ^+ track due to its decay into pπ^0 or nπ^+. The trigger condition of multiplicity change requires the decay of the K^0 to be behind the start counter, by this effect 60% of the events are lost (s. Fig. 1).
The Σ^+ track has to be measured with the silicon microstrip detector, therefore events with the Σ^+ decaying in front of the microstrip detector are lost (72%). The condition that the decay pions of the K^0 decay have to be detected with the straw drift chamber introduces a loss of 39%. The loss due to the detection of the Σ^+ decay pion with the straw detector is less due to the larger forward boost of the Σ^+ and amounts to 10%. At a beam momentum of 2.95 GeV/c the particle of the primary vertex are submitted to a large forward boost, therefore the losses due to the limited opening angle of the target

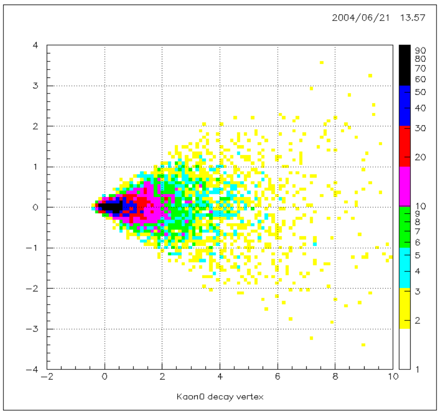

Fig. 1: Spatial distribution of the K^0 decay vertex (longitudinal versus transversal component) [cm]

window can be neglected (s. Fig. 2 for the K^0, which has the largest opening angle). The detection of the four charged particles with the stop detector (barrel, ring quirl) adds an inefficiency of 25 %.

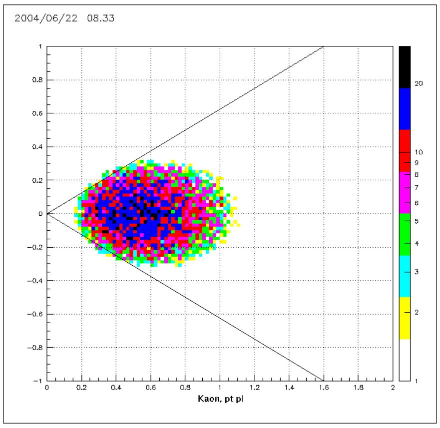

Fig. 2: K^0 longitudinal versus transversal momentum in GeV/c. The black lines indicate the limits due to the target window

Combining these effects one gets a detection efficiency of 7.5%. Including the decay probability of K^0 into two charged pions (68.8%) and the fact, that only K^0*Short* can be detected, the overall detection efficiency is **2.5%**.

References:

[1] The COSY-TOF Collaboration, Phys. Lett. **B595** (2004) 127
[2] A.W. Thomas, K. Hicks, A. Hosaka, Prog.Theor.Phys. 111 (2004) 291-293
[3] C. Hanhart, J. Haidenbauer, K. Nakayama, U.-G. Meißner, hep-ph/0407107
[4] http://wwwasdoc.web.cern.ch/wwwasdoc/geant_html3
[5] B. Bassalleck et al, Phys.Rev.Lett.**89** (2002) 212302

Detection of the η signal in the missing mass spectrum of pp → ppx

E. Roderburg and P. Zupranski
for the COSY-TOF Collaboration

1.) Measurement

The data were taken during one week in October 2002 with the long COSY-TOF setup. The beam momentum was 2.15 GeV/c, which corresponds to an excess energy of 58.8 MeV for the η production. The beam polarization was determined from the elastic $\vec{p}p$ scattering to be 75% ± 5%. 100 two track events per second were recorded. The goal of the measurement was to examine the onset of higher partial waves of the η production and to measure the analyzing power of this process [1].

2.) Experimental Method

The reaction pp → ppη is measured by detecting both protons of the final state. Their momentum is determined by a time of flight measurement. The neutral η particle is reconstructed with the missing mass method. The maximum opening angle of the protons connected with an η production is ± 18.85^0, which corresponds to the acceptance of the end-cap of the TOF detector. The event selection is to have exactly two track events hitting the TOF-endcap. The missing mass distribution contains events from ppπ^0, pp$\pi^0\pi^0$,..., pp4π^0. Events from pp$\pi^+\pi^-$, pp2($\pi^+\pi^-$) are only accepted, if the pions don't hit the end cap of the detector, thus these events are strongly suppressed.

3.) Results

The neutral multi-pion reactions are simulated and submitted to the acceptance and the trigger conditions of the experiment. In Fig. 1 the Monte Carlo results are compared with the measurement.

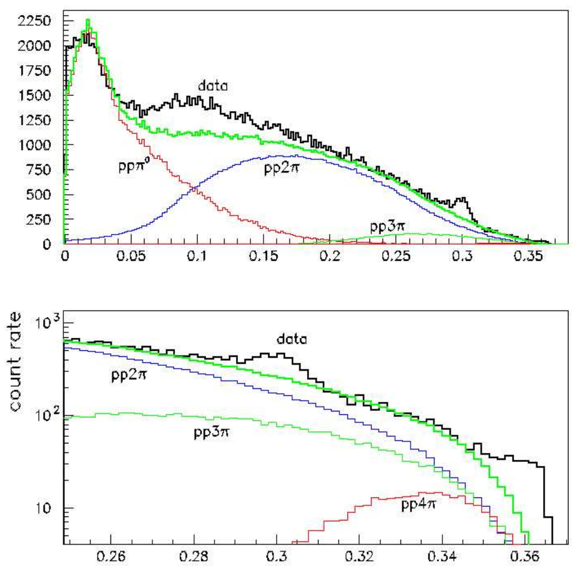

Fig. 1: Squared missing mass distribution [GeV^2/c^4]. The upper figure shows the full range, in the lower figure the distribution in the missing mass range around the η is plotted in a logarithmic scale.

The cross sections of the multi-pion reactions are chosen to fit the measured data apart from the region around the η. The data are compared with a simulation of the η signal by assuming a cross section of 10 μb for ppη at the excess energy of 58.8 MeV. These values of cross section for the multi-pion production, which fit best the background distribution, are listed in the following table:

ppπ^0	2.45 mb
pp2π^0	580 μb
pp3π^0	25 μb
pp4π^0	1 μb

The simulation of the background is in good agreement with the measured data, only at the region of m_x^2 = 0.1 GeV^2/c^4 the simulation differs from the measurement. This may be due to the effect, that the simulations assume s-wave production, but in the lower region of m_x^2 the excess energy of ppπ^0 and pp2π^0 is high enough to produce p and d waves.
In order to determine the number of η events in the missing mass distribution the measured data are compared with the sum of the simulated pion background (as shown in Fig. 1) and simulated η events. The number of simulated η events is adapted to fit best the data in the range of the η mass. This is shown in Fig. 2 .

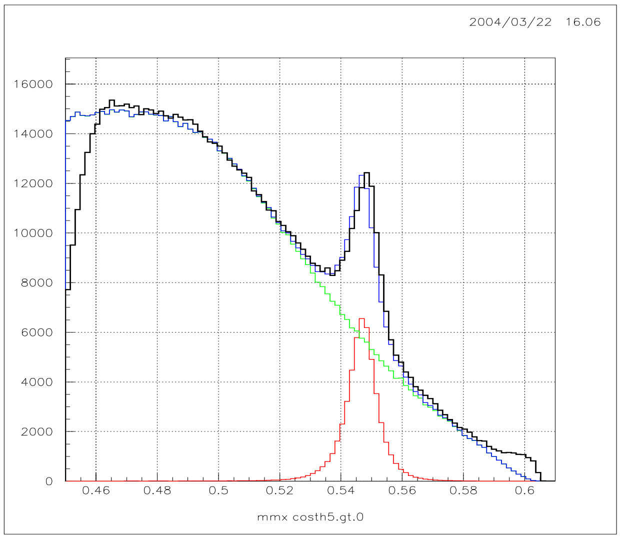

Fig. 2: Missing mass distribution [GeV/c^2]. Only events of the forward cm angles of the η are shown. The black curve shows the measured data, the green curve the simulated pion background, the red curve the simulated η events, to fit the measured curve. The blue curve is the sum of the simulated pion and η events. The deviation below m_x =0.46 GeV/c^2 is due to a cut in the data to enrich the η events.

References:

[1] E. Roderburg and P. Zupranski, Proposal 41.4 http://www.fz-juelich.de/ikp/COSY-TOF/experiment/physik_programm.html

The Analysis Framework TofRoot for Online and Offline Analysis[&]

M.Schulte-Wissermann*, K.-Th.Brinkmann*, S.Dschemuchadse*, R.Jäkel*, L.Karsch*, W.Ullrich*, G.Y.Sun*
for the COSY-TOF-Collaboration

General Concepts of TofRoot

Data analysis in modern nuclear physics is all but a simple task. For example, during each beamtime the TOF-spectrometer typically produces 100 GB-500 GB of raw data, originating from over 2000 channels (QDC/TDC). Prior to any physics analysis, all of these channels have to be calibrated for geometry and time-of-flight, and the data have to be converted into physical information (tracks). In order to perform this calibration/conversion *efficiently*, a strategy had been defined which can be summarized briefly in a set of concepts: *use of teamwork*, *standardization*, *automatization*, *reuse of existing implementations*, *control*, *book-keeping*, and *documentation*.

Following these concepts, an analysis framework based on the popular ROOT-package [1] was implemented during the last five years ([2]-[6]). The resulting framework - consisting of ≈ 60 classes, ≈ 40 programs, and many aiding functions/macros - is called **TofRoot**.

The TofRoot scheme of the data conversion and calibration is shown in Fig. 1. Starting from tape, the data are converted into four successive data-formats, where each proximate format reflects a higher level of calibration. The necessary calibration values are evaluated automatically by routines taking the different formats as input. The calibration data is stored in a data-base (`TofCal`), and then applied by conversion programs. In the final format (CAL) the user can directly access track-information, i.e. starting-point, track-fit-quality, direction, time-of-flight, and TDC/QDC conversions.

Due to this modus operandi the calibration/conversion separates into disjunct parts. This leads to some considerable advantages:

1. Programs can be implemented, debugged, and improved with minimum influence on the framework as a whole.
2. Single tasks can be assigned to single co-workers. This strongly improves the team-work capability.
3. The whole framework can easily be administrated at one, central location.
4. Since the calibration/conversion is carried out only once (and made persistent in the final format, "CAL"), the actual analysis of the data is very fast[1].

Current Developments - Online and Offline Analysis

Strong effort has been put into further improvements of the **D**resden **O**nline **M**onitor (DOM). However, this did not hamper progress in offline analysis. Due to the concepts of standardization and reuse-of-code, the development of online and offline routines is strongly connected: The DOM uses the first data format (RAW) to process and store the online data. In this way, all routines, functions, classes and programs reading this format can directly access the online data. In return, all new functionality implemented for the DOM can directly be used to improve the offline performance.

[1]Depending on the task, 3000-100000 event/s (2GHz CPU).

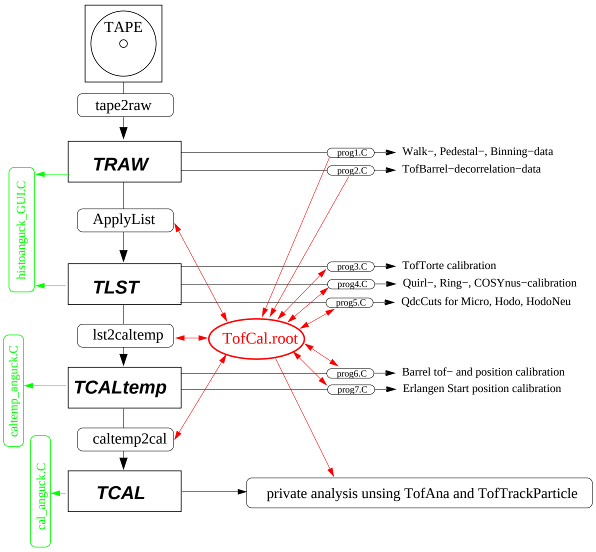

Fig. 1: *Schematic view of the TofRoot data-flow. Four successive data formats are used from which standardized routines (automatically) evaluate calibration parameters.*

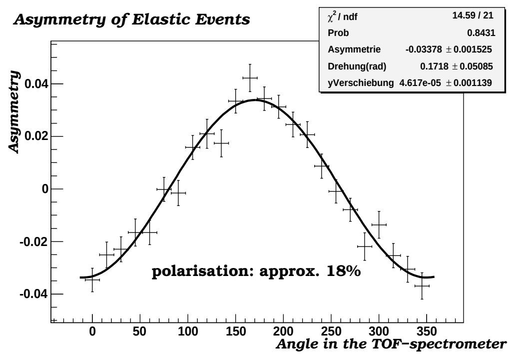

Fig. 2: *The asymmetry of elastically scattered events (⇒ polarization) is evaluated with the same function, online as well as offline.*

This constructive interaction between offline and online analysis will be sketched using two examples:

1.) In April 2004, a beamtime was performed asking for a polarized beam with very ambitious parameters ($p_{beam} > 3\,GeV/c$, electron cooling, extraction to the TOF). While the beam polarization *within* the COSY ring can be measured rather easily, COSY-TOF lacks an *external* polarimeter in the TOF hall. Therefore the amount of polarization must be deduced from the TOF spectrometer data, and since this information is needed during beam-tuning, the polarization must be evaluated 'truly online'. Using older data, a routine to preselect elastic events and to calculate the polarization was developed before the beamtime. During the beamtime, the code was optimized and allowed a true online determination of the polarization (i.e. by 'clicking' the online GUI). The very same code is used in offline analysis, today; a sketch of an asymmetry distribution is shown in Fig. 2.

Resolution and Efficiency of the Straw Tracker for COSY-TOF

W.Erven[1], K.Kilian[2], V.Kozlov[3], I.Mohos[2], R.Nellen[2], S.Orfanitski[3], T.Sefzick[2], A.Ucar[2], P.Wüstner[1], K.Zwoll[1], and P.Wintz[2]
For the COSY-TOF Collaboration
[1]Zentralinstitut für Elektronik, [2]Institut für Kernphysik, [3]Moscow State University

The straw tracker for COSY-TOF will consist of a stack of 15 vertical frames, each frame containing a planar double-layer of 208 straw tubes. Three different, alternating azimuthal alignments (φ-angles 0°, 120°, 240°) of the frames allow a 3-dimensional track reconstruction. The straw tubes are glued together in close-packed double-layers which are self-supporting and maintain the required wire and tube tension by the gas over-pressure inside the single straws. By that, the overall weight of the detector is reduced to an absolute minimum, important for a clean, background-free tracking close to the target in the COSY-TOF spectrometer [1].

The spatial position and intrinsic resolution of single tubes inside a vertical double-layer frame have been checked using cosmic ray tracks. Two long scintillator strips are placed in parallel above and below a straw frame with a distance of *2400mm* to each other. The strips' length of *900mm* and width of *35mm* cover almost the full straw length of *1050mm* and the full double-layer thickness of *18.75mm*. Cosmic ray tracks with a coincident crossing of both strips are recorded and reconstructed in two dimensions using the information from at least four hit straws. For the analysis a set of *16* neighbouring straws is selected, small enough to resolve individual contributions. The long data-taking time of seven days also allows to check time-dependent variations related to the gas mixture (Ar/CO_2, 82/18% at 2.25bar absolute pressure) or electronic threshold drifts.
Assuming a constant[1] cosmic incidence density $\Delta N/\Delta R$ of the tracks the isochrones[2] radius - drift time relation $R(t)$ is derived from the entries N_i in the measured drift time spectrum of a single straw according to the following formula:

$$R(t_i) = \frac{\sum_{i=0}^{i=i_t} N_i}{N} \times \left(R_{tube} - R_{wire}\right) + R_{wire}.$$

R_{tube} and R_{wire} being the radius of tube and wire, N the sum of all bin entries N_i. After time conversion and offset correction all drift time spectra of the selected straws show a clean range, sharply ending at the same maximum drift time corresponding to the inner tube radius R_{tube}. A polynomial of fifth order is sufficient to fit the $R(t)$ relation for all straws together (Fig.1).
The six calibration parameters $P_{i=1...6}$ together with the time offset are used for the track reconstruction. A minimum number of four hit straws are required to start a linear fit of the track parameters (α, P) minimising the normalised χ^2:

$$\chi^2 = \frac{1}{N-2} \sum_{i=1}^{N} \left(\frac{\Delta r_i(\alpha, P)}{\sigma_{r_i}} \right)^2 .$$

[1] Including a left-right reflection of all tracks.
[2] The isochrone contains all space points belonging to the same electron drift time. For straws with concentric wire and tube this object is a cylinder.

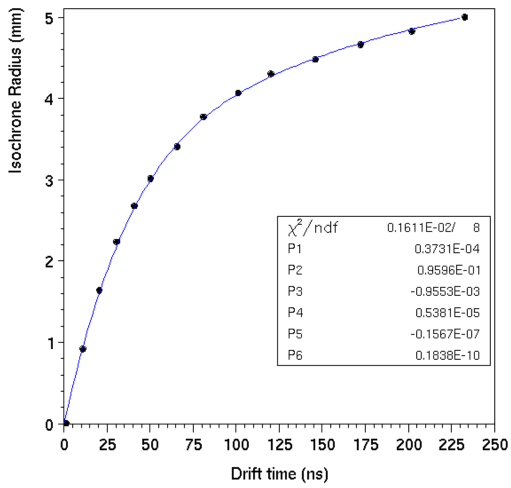

Fig. 1: Isochrones radius - drift time relation, parameterised using a polynomial of fifth order (parameters P_1-P_6).

With Δr_i being the shortest distance between track and isochrones r_i in straw i, σ_r the spatial resolution at r_i, and N the number of hit straws. The mean of the Gaussian-like Δr_i-distribution of each single straw is used to check and redefine the tubes' position, accordingly. Then, all tracks are reconstructed again. The observed maximum position shifts of $\pm 80\mu m$ confirm the mechanical tolerance of the tubes' alignment at both ends by the pickup straps, allowing a maximum position spread[3] of $\pm 100\mu m$. In addition, an expected wire displacement in the tube during assembly[4] and wire bending by gravitational sag[5] and electric field contributes to a small smearing of the $R(t)$ calibration.
Fig.2 shows the final χ^2-distribution[6] of the *1054* reconstructed tracks and the isochrones residuals Δr_i of the *5645* straw hits. The residuals' spread is highly symmetric around a small mean of $4\mu m$, indicating no systematic error. The deviation (σ) of about 85μm is a measure of the mean spatial resolution of a single straw.
The resolution inside a tube strongly depends on the isochrones radius or track-wire distance as can be seen in Fig.3. For a constant gas mixture and density and a given electric field the spatial information is smeared by the statistical spread of the primary ionization clusters along the track, the diffusion of the electron cloud drifting to the anode wire and the gas amplification process. Finally, the electronic readout resolution of the amplified and shaped charge signal is limited by the pulse rise time and noise smearing at the discriminator threshold level. All effects

[3] A free elongation of the single tubes must be provided.
[4] Estimated to be ~ $50\ \mu m$ (σ).
[5] Calculated to be below $20\ \mu m$ (maximum).
[6] The χ^2-peak position (< *1)* still indicates a small overestimation of the spatial resolution error σ_r in the fits.

The p-n-reaction studied via *fsi*

GEM collaboration

There is a very extensive literature on the $pp \to \pi^+ d$ reaction and many detailed analyses have been made [1], but much less is known about the production of the continuum in the $pp \to \pi^+ pn$ case. Data covering low excitation energies generally show the strong S-wave final-state-interaction (*fsi*) peak corresponding to the pn spin-triplet which has, as a characteristic energy scale, the binding energy of the deuteron ($B_t = 2.22\,\mathrm{MeV}$). However, the energy resolution is generally insufficient to identify the analogous spin-singlet *fsi* peak, for which the corresponding energy scale is only $B_s = 0.07\,\mathrm{MeV}$ [2].

We have performed a high resolution study employing the magnetic spectrograph Big Karl to measure positively charged pions from $p + p$-interactions. The optical properties of the spectrograph were extensively studied with direct beam and the $pp \to d\pi^+$ reaction at lower beam momenta around 800 MeV/c. Excellent beam properties were achieved by using a beam which was cooled by electrons at injection energy and stochastically extracted. A rather thin liquid hydrogen target of only 2 mm thickness made straggling in the target a negligible quantity. Thin target walls of only 1 μm thickness yielded a very small background (30 counts per 0.2 MeV bin).

The reactions of interest, i. e.

$$p + p \quad \to \quad \pi^+ + d, \tag{1}$$

$$p + p \quad \to \quad \pi^+ + \{pn\} \tag{2}$$

were measured at a beam momentum at 1640 MeV/c. The calculation underestimates the cross section by a factor of two. The standard way out has been so far to add the contribution of the virtual state in the $S = 0$, $T = 1$ system. At low excitation energies one expects that

$$\begin{aligned} &\frac{d^2\sigma}{d\Omega\, dx}(pp \to \pi^+ \{pn\}_s) \\ &= \xi \left(\frac{\varepsilon + B_t}{\varepsilon + B_s}\right) \frac{d^2\sigma}{d\Omega\, dx}(pp \to \pi^+ \{pn\}_t)\,, \end{aligned} \tag{3}$$

where we use the factor ξ to quantify the ratio of spin-singlet to spin-triplet production. We found it impossible to reproduce the data with this *ansatz*. However, if we use the predicted forms of the two states to fit the data, a very small fraction for the singlet state is found which is campatible with zero. This is shown in Fig. 1. The only possibility to account for the missing yield seems to be the $T = 0$, $J = 1$ state with $l = 2$: the D-state. As has been stressed elsewhere [3], the extrapolation theorem linking the bound and scattering wave functions is only valid if one can neglect completely D-state effects [4]. Though the D-state wave functions are suppressed at short distances by the centrifugal barrier, the S-wave is also reduced in this region by the repulsive core. Thus the D-state might be significant for pion production despite the relatively small probability in the deuteron, especially if S-D interference terms are important. However, a calculation with a full three body final state is missing so far and will be out of range of the present study.

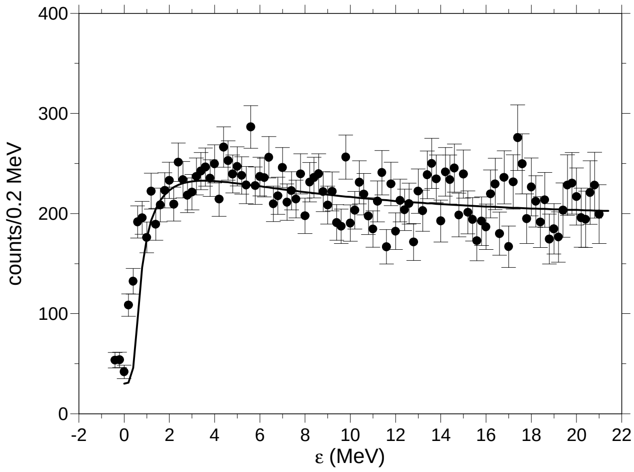

Fig. 1: Comparison of the data (histogram) with the fitted triplet plus singlet state.

However, a calculation of the excitation function of reaction 1 indicates the importance of the D-state, esp. the interference between the S-state and the D-state.

References:

[1] R.A. Arndt et al., Phys. Rev. C 48 (1993) 1926, http://gwdac.phys.gwu.edu/

[2] R. Machleidt, Phys. Rev. C 63 (2001) 024001.

[3] A. Boudard, G. Fäldt and C. Wilkin: Phys. Lett. B 389, 440 (1996).

[4] G. Fäldt and C. Wilkin, Phys. Scripta 56 (1997) 566.

Evaporation of composite particles from the spallation of Au by energetic protons

PISA collaboration

We report analysis of the data obtained from the recent PISA collaboration experiment performed for the 2.5 GeV p+Au collisions. The experimental spectra were absolutely normalized by comparison of our ^{4}He data measured at 35 deg. with ^{4}He results of NESSI collaboration [1] obtained at 30 deg. at the same proton beam energy. Whereas NESSI investigation was concentrated on measurements of very light reaction products (^{1,2,3}H, ^{3,4}He and ^{6,7}Li) we studied also channels with emission of heavier particles ^{7,9,10}Be,^{10,11,12}B, C, N, O and less abundant lighter particle channels ^{6}He and ^{8}Li.

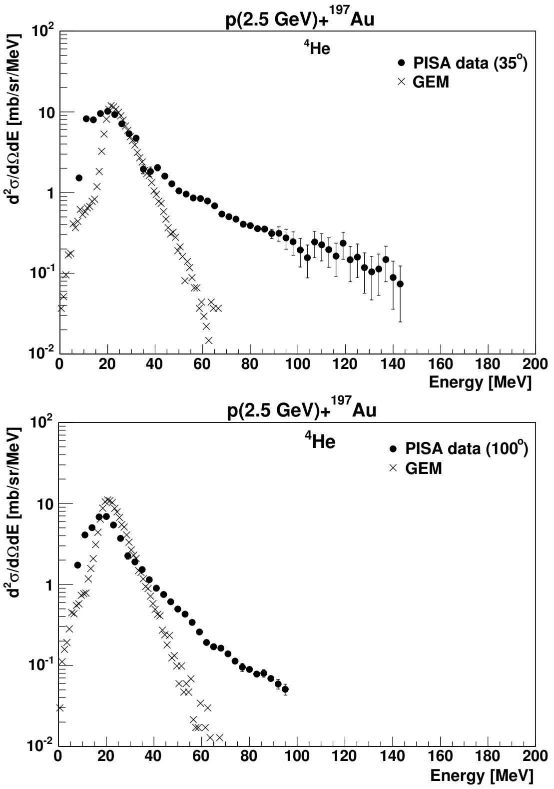

Fig. 1: Comparison between energy spectra of ^{4}He measured at 35^{o} and 100^{o} by PISA (full dots) and INCL4.2+GEM model calculations (crosses).

The widely accepted mechanism of collisions of high energy protons with nuclei consists in the following two stage picture of the reaction: (i) the projectile induces intranuclear cascade of nucleon-nucleon collisions which leads to excitation of the nucleus, and (ii) the excited nucleus emits nucleons and various composite particles. Different theoretical approaches can be used in order to describe the reaction mechanism responsible for the excitation of the nucleus and for the emission of spallation products following the excitation of nuclear matter. We have used the Liege intranuclear cascade model INCL4.2 [2] for description of the first stage of the reaction, and the Generalized Evaporation Model (GEM) of S. Furihata [3] for the second stage. The same values of parameters of the models were applied as those exploited by Letourneau et al. [1] for reproduction of the evaporative cross section for light ejectiles. As can be seen in the fig. 1 the low energy component of the emitted ^{4}He can be well reproduced by the evaporation process, however, a significant contribution corresponding to the non-evaporative mechanism being present in the high energy part of the experimental spectra cannot be accounted for in the model.

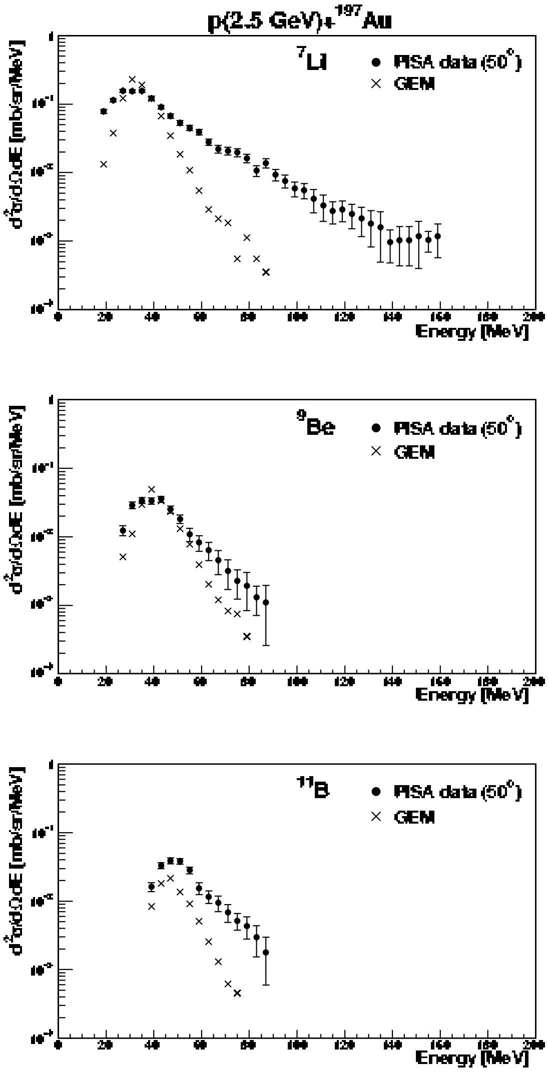

Fig. 2: Comparison between energy spectra of ^{7}Li,^{9}Be and ^{11}B measured at 50^{o} by PISA collaboration (full dots) and INCL4.2+GEM model calculations (crosses).

The same effect is observed for heavier ejectiles as shown in the fig. 2. The evaporation of ejectiles from the equilibrium phase should be approximately isotropic in the laboratory system since only small velocity of the compound nucleus (of the order of $\beta \approx 0.0036$ along the beam direction) is predicted by calculation within INCL4.2. Thus, the high energy tail of the spectra, which is evidently anisotropic in the laboratory system (cf. the fig. 1), must correspond to some preequilibrium process. The analysis of this contribution to the spectra is discussed in the next report.

References:

[1] A. Letourneau et al., Nucl. Phys A 712 (2002) 133
[2] J. Cugnon et al., Nucl. Phys. A 620 (1997) 475
[3] S. Furihata, Nucl. Inst. Meth. in Phys. Res. B 171 (2000) 251

Preequilibrium mechanism of the spallation of Au by energetic protons

PISA collaboration

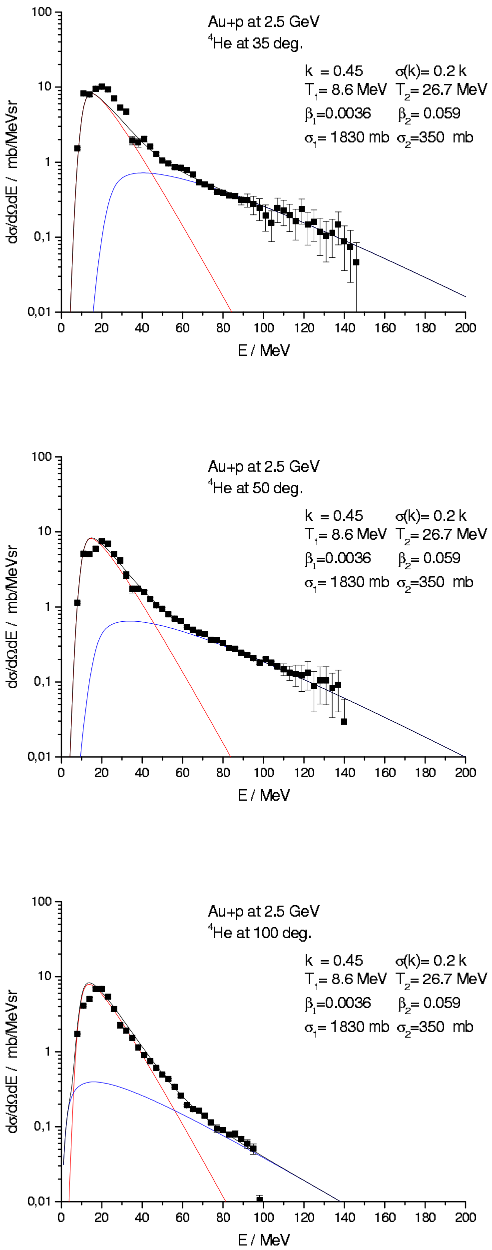

Fig. 1: Energy spectra of ^{4}He fitted with the sum of two Maxwell functions. The red and blue curves represent the contributions of these two moving sources, and black solid line is their sum.

It was shown in another contribution to the present Annual Report that the two-step model of the reaction, i.e. intranuclear cascade of nucleon-nucleon collisions leading to creation of the equilibrated compound nucleus and the subsequent evaporation of the composite particles is not able to describe the high energy part of the experimental spectra obtained by PISA collaboration from Au+p collisions at 2.5 GeV proton beam energy. In the present report we discuss a phenomenological analysis which has been performed to study properties of these spectra.

The phenomenological "moving source" model [1–3] applied for this purpose uses the Maxwell-Boltzmann distribution to describe energy dependence of the cross section whereas it assumes the isotropic emission of the particles in the frame corresponding to the emitting source. As shown by Westfall et al. [1], the single Maxwell-Boltzmann distribution cannot describe the full energy spectra because generally two components are observed: a low velocity, low temperature component and a high velocity, high temperature component. The slower source represents the equilibrium process, i.e. it should reproduce results of INCL4.2+GEM calculations whereas the fast source corresponds to pre-equilibrium emission. Thus the velocity of the slower source was fixed at value predicted by INCL4.2 model for the resulting compound nucleus – β=0.0036. Other parameters of the slow source, i.e. the temperature parameter and the total (angle integrated) cross section were fitted together with respective parameters of the fast source to reproduce the shape of the spectra and their angular dependence. Very good description of the spectra was obtained as can be seen in the fig. 1 for ^{4}He ejectiles. The reproduction of spectra for other ejectiles is of the same quality. Values of the parameters obtained from the fits enabled us to derive interesting conclusions on the mechanism of the reactions responsible for the high energy part of the spectra: (i) Velocity of the fast emitting source is in most cases larger than that which can be obtained by the target nucleus after complete momentum transfer from the proton projectile, i.e. the emitting source must be significantly lighter than the target. (ii) The recoil of emitting source, which can be estimated from the dependence of the temperature parameter on the mass of the ejectile [3], allows to state that mass of the fast source is approximately equal to 20, (iii) The total (angle integrated) cross section parameters enables us to determine contribution of the preequilibrium process to the reaction under consideration. The fig. 2 shows that ^{4,6}He and ^{6,7,8}Li are mainly (more than $\sim$ 80%) emitted from the slow source, i.e. from the compound nucleus. On the contrary, the heavier ejectiles ^{7,9,10}Be, ^{10,11}B, and ^{3}He appear predominantly as result of preequillibrium processes.

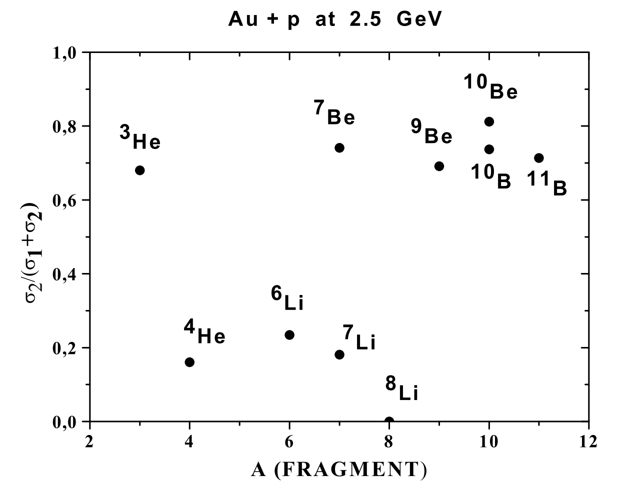

Fig. 2: Contribution of the preequilibrium mechanism to the emission of composite fragments from Au+p collisions at 2.5 GeV proton beam energy.

References:

[1] G. D. Westfall et al., Phys. Rev. C 17 (1978) 1368
[2] E. K. Hyde et al., Phys. Rev. C 4 (1971) 1759
[3] J. A. Gaidos et al., Phys. Rev. Lett. 42 (1979) 82

Isotope identification with hybrid BCD-Si telescope

PISA Collaboration

The PISA experiment is devoted to measure double differential cross section for spallation products coming from various targets (C, N, O, Si, Fe, Ni, Ag, Au, U) bombarded by protons of energies up to 2.5 GeV. In order to obtain undistorted information about the mechanism of the primary reactions, the use of thin targets is indispensable. In order to compensate for the low reaction rate due to the use of very thin targets the experiment is performed at internal site of COSY accelerator in Jülich, Germany. The purpose of the PISA detection system is to register charged reaction products over the broadest possible range of energies with emphasis on detection of low energy particles [1]. As the device which permits the registration of very low energy threshold gas-filled ionization chamber was chosen. Directly behind the chamber a telescope of three silicon detectors is installed. Such formed detection arms are ended with phoswitch detector.

Analysis of the data collected in runs of PISA experiment shows that ionisation chamber with Frisch grid (called also Bragg Curve Detector, BCD) used typically to identify the atom number and to measure the energy of particles stopped in BCD can be effectively used also to identify their masses [2, 3, 4]. It was achieved by very careful design and construc-

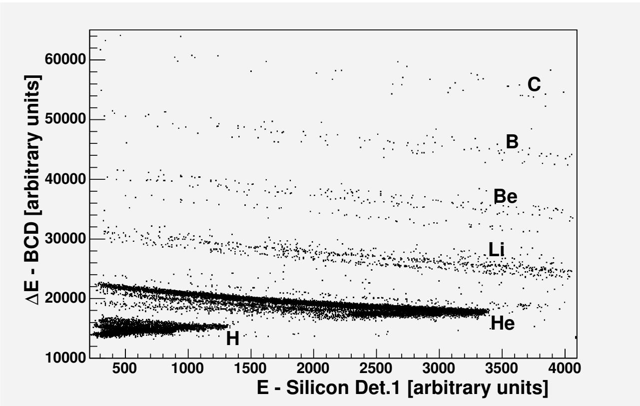

Fig. 1: ΔE-E distributions where ΔE is the energy deposited in the volume of Bragg Curve Detector while E is deposit of energy in the silicon detector placed behind.

tion of BCD used in PISA experiment and by special processing of signal performed by high-fidelity current amplifier combined with 40-MHz sampling ADC. The main problem that had to be overcome is the small amount of charge produced by the particles passing in gas volume since no charge multiplication process occurs in the detector. For the detected fast heavy ions the number of secondary electrons released by ionization is of order 10^4 per MeV of energy loss, with several to tens of MeV being lost in the active BCD volume. These electrons must drift over the substantial detector length ($\sim$200mm) with as little as possible recombination. In order to achieve this goal, not only the detector geometry but as well the gas used, its pressure and the applied voltages have to be carefully selected [2]. It was even decided to use isobutane instead of P10 gas mixture (90% argon, 10% methane) because isobutane is characterized by a 12% lower mean energy needed for electron-pair production. A crucial aspect of proper performance as reliable gas flow system. When the gas is not refreshed continuously its detection eficiency drops significantly. This is caused by the admixture of electronegative gases in isobutane (as oxygen and vapor of water). It is not enough to use isobutane of high purity as substantial amount of the electronegative admixtures attach initially to the vessel walls and are hidden in the pores of various parts of the detector. Only constant flow of uncontaminated isobutane washes the admixtures out. The pressure in the BCD volume is kept constant (with an accuracy better than 1%) by an electronic unit, which according to the readout of a pressure sensor controls the opening fraction of the electromagnetic dosage valve.

Large amount of data collected in the 2004 experimental run of PISA allows to draw conclusion concerning identification of particles by means of hybrid BCD - silicon telescope. In Fig1. two-dimensional histogram of deposits of energies are shown for particles that penetrated through BCD and were stopped in silicon detector placed behind BCD. On abscissa deposits in silicon detector while on ordinate deposits in BCD are shown. Clear identification of elements up to carbon

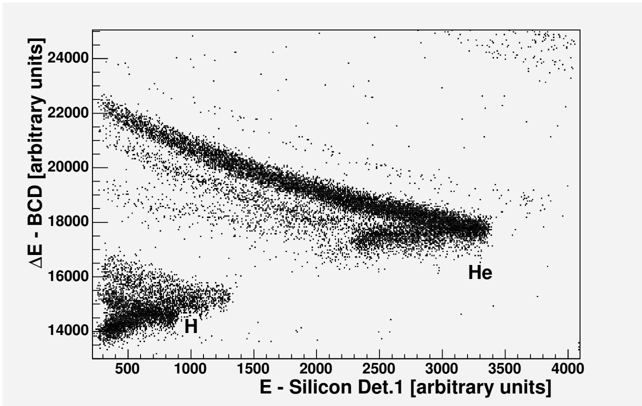

Fig. 2: Zoomed part of Fig.1

is evidently observed. Moreover, some limited mass identification is possible for light elements like hydrogen, helium, lithium. ^{7}Be isotope is also well separated from other isotopes of this element. This method certainly improves identification of particles, making possible identification for particles which passed through BCD and were stopped in next detector. This experimentally confirmed ability of BCD to serve as ΔE detector broadens its apliccability. On Fig.2 part of zoomed Fig.1 is plotted in order to show how well different isotopes of hydrogen and helium are separated from each other.

References:

[1] The PISA Coll., **IKP/COSY Annual Report 1999**, Jül-3744, ISSN0944-2952, p.175ff (1999)

[2] R. Barna, et al., Nucl. Instr. and Meth., **A519**, 610 (2004)

[3] R. Barna et al.: **ESS 03-167-T** ISSN 1433-559X, (2003)

[4] A. Bubak, **PhD-Thesis**, Univ.Katowicze (2004)

Detailed Studies on a Cryogenic Methane-Hydrate Moderator

V. Bollini, A. Bubak, D. Filges, F. Goldenbaum, B. Lensing, K. Nünighoff, N. Paul, Ch. Pohl, D. Prasuhn,
K.Pysz, H. Schaal, M. Wohlmuther (IKP); H. Conrad (IFF); N. Bayer,T. Matzerath, H. Soltner, H. Stelzer (ZAT);
H. Tietze-Jaensch (ESS-CPT); W. Ninaus (TU-Graz); S. Kulikov, A. Smirnov (JINR-Dubna);
P.D. Ferguson, F.X. Gallmeier, E.B. Iverson (SNS-ORNL)

Whereas neutron scattering experiments –using only small samples– identified, that methane-hydrate shows the expected behaviour, the next step was the investigation of the feasibility of a cryogenic moderator based on methane-hydrate. In Fig.1 the measured energy spectra of methane and ice are compared with the spectrum of methane-hydrate at T=20 K. It can be seen that methane-hydrate does not show a superposition of the ice and methane spectra. In the energy range below 10 meV the spectrum of methane-

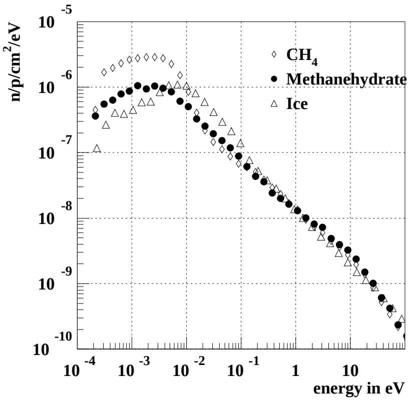

Fig. 1: *Measured energy spectra for ice, methane, and methane-hydrate.*

hydrate shows the same shape like solid methane, but the intensity is reduced by a factor two. For higher energies -between 4 meV and 300 meV- the methane-hydrate moderator shows a slightly higher neutron flux than the methane moderator. However, the flux of the ice moderator is superior to the methane-hydrate moderator as well as the methane moderator in the energy range between 5 meV and 100 meV. Based on the assumption that both materials –CH_4 and H_2O– will show their own spectral characteristics, Monte-Carlo-Simulations applying the MCNPX code werde performed. Instead of the real mixture of CH_4+5.75·H_2O a simplified

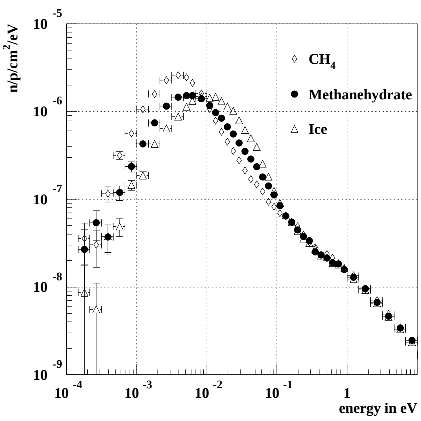

Fig. 2: *MCNPX simulations of the energy spectra for ice, methane, and methane-hydrate.*

mixture of CH_4+6·H_2O was used. From the comparison with solid methane and ice a similar result as observed in the experimentally measured data could be observed, as can be seen in Fig. 2. For energies below 6 meV methane-hydrate shows a higher intensity than ice, but a lower intensity than solid methane. In the energy region between 10 meV and 100 meV the intensity of a methane-hydrate moderator is higher as compared to methane, but lower than ice. This effect could be explained by the hydrogen density. In case of ice at T=20 K the hydrogen density is $7.873 \cdot 10^{22}$ atoms/cm^3 and for solid methane it is $7.950 \cdot 10^{22}$ atoms/cm^3. The according hydrogen density of methane in methane-hydrate is only $1.496 \cdot 10^{22}$ and $4.488 \cdot 10^{22}$ for ice in methane-hydrate respectively. From these values we can determine the ratios a and b and calculate a methane-hydrate spectrum from the measured CH_4 and ice spectra as given in Eq. 1.

$$\Phi(E)_{hydrate} = a \cdot \Phi(E)_{methane} + b \cdot \Phi(E)_{ice} \qquad (1)$$

Fig. 3 shows a comparison auf the measured, simulated, and calculated spectrum derived with Eq. 1. Below 3 meV the spectra of measured and calculated methane-hydrate are identical. In the energy range between 3 meV and 100 meV the calculated spectrum shows a higher intensity than the

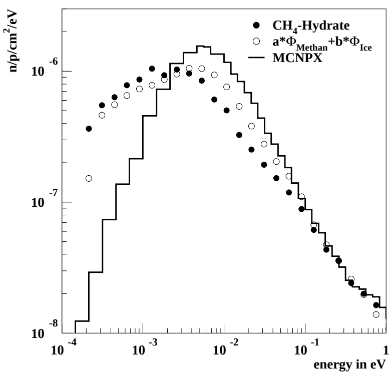

Fig. 3: *Comparison of simulated and measured spectra of methane-hydrate. Additionally a synthetical methane-hydrate spectrum based on Eq. 1.*

measured one and the spectrum is more similar to the MCNPX simulation. From this result it can be concluded, that the moderation of neutrons at the hydrogen atoms of the ice cages in methane-hydrate is less efficient than compared with normal ice Ih. However, the moderation properties of the methane molecule inside methane-hydrate is comparable with normal solid methane, but the intensity is reduced due to the lower hydrogen density. Furthermore it can be seen, that the experimental spectra differs from the MCNPX simulation in the energy range below 1 meV. This effect is due to reflected neutrons in the stainless steel beam tube, an effect which cannot be described with available Monte-Carlo transport codes like e.g. MCNPX or HERMERS.

Discrepancies between Simulation and Experiment due to Total Reflected Neutrons

V. Bollini, A. Bubak, D. Filges, F. Goldenbaum, B. Lensing, K. Nünighoff, N. Paul, Ch. Pohl, D. Prasuhn, K.Pysz, H. Schaal, M. Wohlmuther (IKP); H. Conrad (IFF); N. Bayer,T. Matzerath, H. Soltner, H. Stelzer (ZAT); H. Tietze-Jaensch (ESS-CPT); W. Ninaus (TU-Graz); S. Kulikov, A. Smirnov (JINR-Dubna); P.D. Ferguson, F.X. Gallmeier, E.B. Iverson (SNS-ORNL)

It has been observed, that especially in the cold energy range the measured spectra differs from the predicted shape. In the energy range below approximately 1 meV the experimental data show higher intensities than the simulated values. This discrepancy was not understood and in a specific experiment the reason for this effect was investigated. It was found out, that the higher intensity of cold neutrons in the experiment is due to cold neutrons reflected at the walls of the neutron flight path made of stainless steel. Stainless steel include ≈16 % Ni, which is also used as a coating material for neutron guides, because of its property to reflect thermal and cold neutrons. In the first step an ice moderator experiment at T=20 K was performed. The difference between the experimental spectrum and a MCNPX simulation in the energy range below 1 meV was found again, as can be seen in Fig. 1. In the next step, two additionally Cd-appertures with a thickness of 1 mm and a hole with a diameter of d=30 mm were placed in the region of the scattering crystal in order to absorb neutrons reflected at the beam tube walls. Fig. 2 shows the comparison between the experimental spectrum and the according MCNPX simulation. In this case, the agreement between experiment and simulation –especially in the energy range below 1 meV– is very good. It can be concluded, that the stainless steel beam tube is abel to reflect cold neutrons and thus works as a neutron guide. In order to verify this results, a simple Monte-Carlo simulation of a cylindrical Ni-guide with McStas, a Monte-Carlo Code for designing neutron scattering instruments, was performed. The simulated energy spectrum in Fig 3 shows a drastic increase of the neutron flux below 1 meV. However, the McStas simulation used an ideal neutron guide made of pure Ni, but the increase of the flux due to total reflected neutrons can easily be seen.

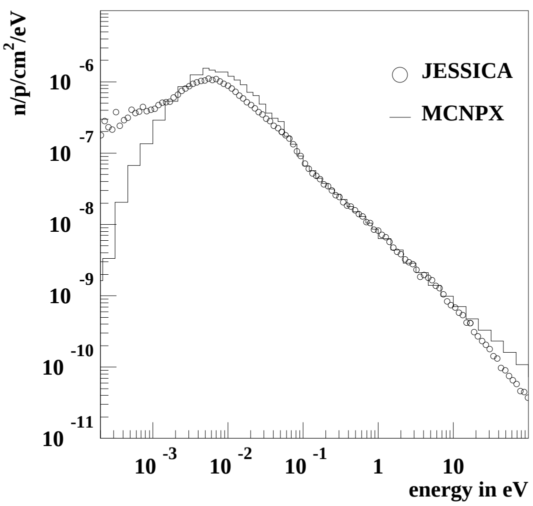

Fig. 1: Energy spectrum of an ice moderator at T=20 K measured without Pb-collimator and without additionally Cd-appertures in the neutron flight path.

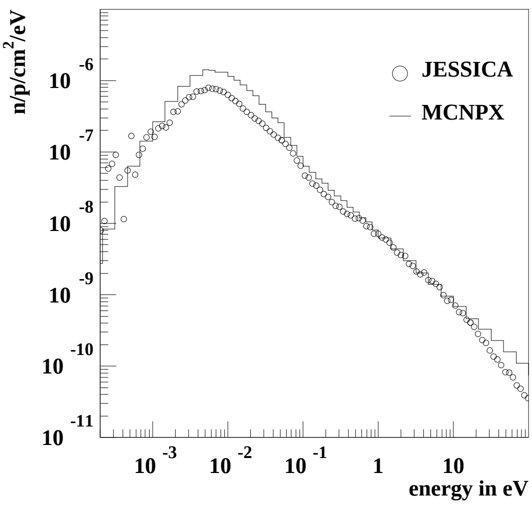

Fig. 2: Energy spectrum of an ice moderator at T=20 K measured without Pb-collimator, but with two additionally Cd-appertures in the neutron flight path.

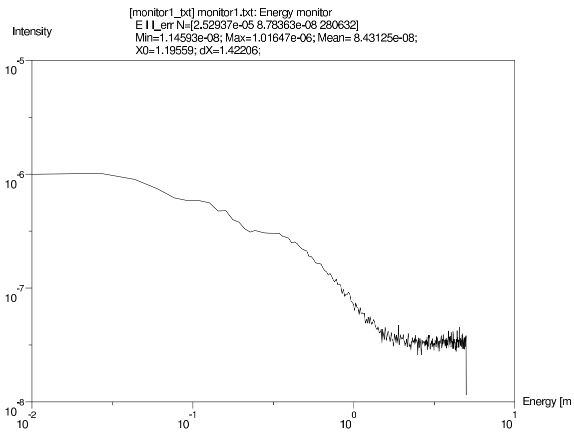

Fig. 3: Energy spectrum transported .

These results demonstrated, that with the available transport codes the transport of cold neutrons through a complex geometry cannot be simulated correctly, because neutron optic properties, like reflection of neutrons at the side walls of an evacuated beam tube, are not included. Considering design studies of advanced neutron sources or simulation of ultra cold neutron sources, it is important to include such properties in existing Monte-Carlo systems. A first step could be a coupling to existing Monte-Carlo programms like McStas or Vitess, which are used for designing neutron scattering experiments. Unfortunately theses programs are not able to deal with real material mixtures and assume ideal materials.

Comparison of the wavelength dependent time-of-flight spectra of methane, methane-hydrate and ice at T=20K

V. Bollini, A. Bubak, D. Filges, F. Goldenbaum, B. Lensing, K. Nünighoff, N. Paul, Ch. Pohl, D. Prasuhn, K.Pysz, H. Schaal, M. Wohlmuther (IKP); H. Conrad (IFF); N. Bayer,T. Matzerath, H. Soltner, H. Stelzer (ZAT); H. Tietze-Jaensch (ESS-CPT); W. Ninaus (TU-Graz); S. Kulikov, A. Smirnov (JINR-Dubna); P.D. Ferguson, F.X. Gallmeier, E.B. Iverson (SNS-ORNL)

One major question concering the performance of a moderator at a pulsed spallation source is the time structure of the neutron pulse. A small pulse width and a fast decay time of the pulse is desired. With a pyrolitic graphite crystal neutrons with a wavelength fulfilling the Bragg condition

$$n \cdot \lambda = 2 \cdot d \cdot sin\,\Theta \qquad (1)$$

are selected. Here λ is the wavelength in Å, d is the lattice spacing, Θ is the Bragg angle, and n is the order of the reflection. The measured time-of-flight spectra for ice, methane, and methane-hydrate at T=20 K are shown in Fig. 1. The neutron flux is not normalized but the background is already subtracted. These spectra represents the time structure inside the moderator for a specific wavelength. From the re-

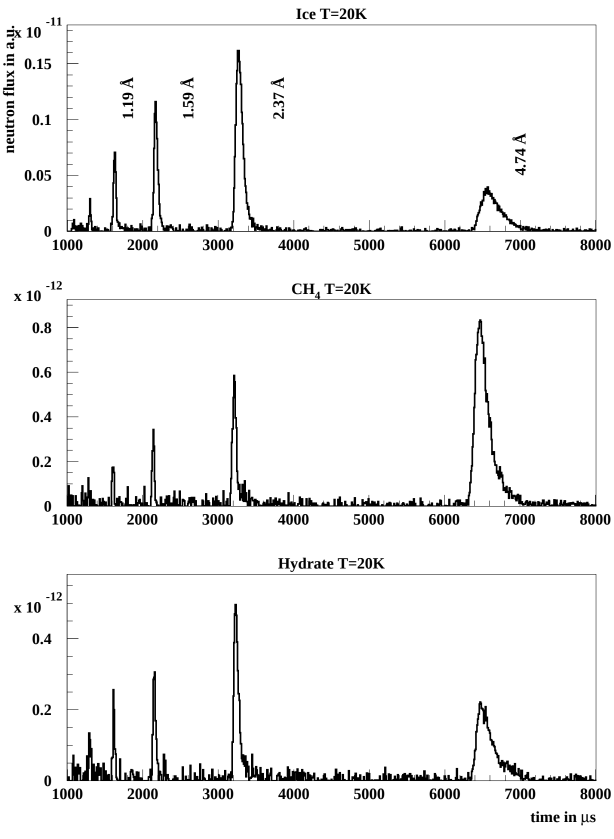

Fig. 1: Comparison of wavelength dependent TOF-spectra of ice, methane, and methane-hydrate at a temperatur of T=20 K.

lations of the peak heights the increase of the intensity in the lower energy range in methane-hydrate can be observed. In the next step the pulse widths were determined as FWHM. The comparison of the three materials is shown in Fig. 2. Whereas ice shows the broadest pulses, the peaks are narrower in case of methane and methane-hydrate. The decay time of the neutron pulse was determined with an exponential fit. The derived decay times are plotted in Fig. 3. It

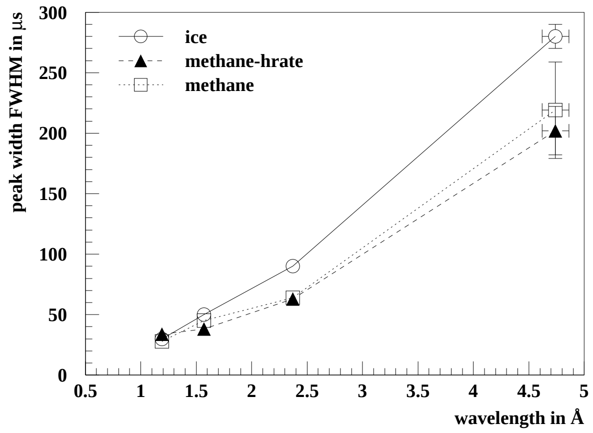

Fig. 2: Comparison of the peakwidth in FWHM for methane, ice, and methane-hydrate.

can be concluded that, solid methane is a very fast moderator material compared to normal ice. Methane-hydrate lies in between for longer wavelenghts and is compareable with methane at shorter wavelengths. From these results it can be

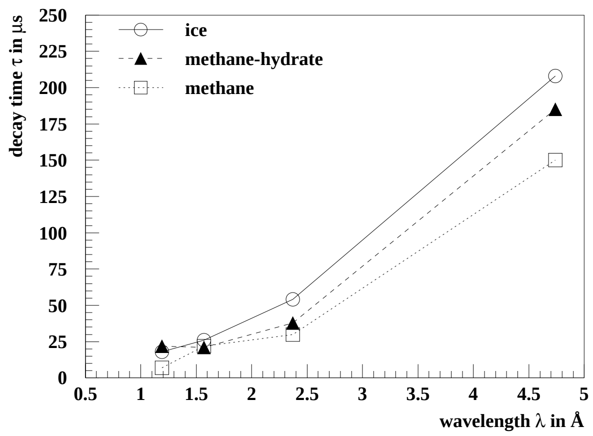

Fig. 3: Comparison of the decay time in μs for methane, ice, and methane-hydrate.

concluded, that methane-hydrate benefits from the encaged methane molecules as compared with normal ice. The intensity in the lower energy range as well as the time behaviour is dominated by the methane molecules.

Simulations for production of mesons via quasi-free proton-neutron scattering at the WASA 4π-detector.

M. Janusz[1], J. Złomańczuk[2], P. Klaja[1], P. Moskal, W. Oelert, J. Przerwa[1] for COSY-11 and WASA@COSY collaborations

Part of the physics program of the COSY-11 collaboration concerns the study of the production of η and η' mesons in collisions of nucleons. Measurement of the excitation functions of the $pp \to pp\eta$ and $pp \to pp\eta'$ reactions were completed and at present we extend our investigations to one-dimensional differential distributions [1, 2]. In parallel we also explore the spin and isospin degrees of freedom in the creation of the mentioned mesons. To perform such a study we extended the COSY-11 detection set-up by a neutron – [3] and a spectator detector [4]. First successful measurements of the $pn \to pn\eta$ and $\vec{p}p \to pp\eta$ reactions have proven the feasibility to study the quasi-free $pn \to pnX$ reactions as well as polarisation observables using the newly accomplished experimental set-up [5, 6]. Though COSY-11 possesses unprecedented precision for the determination of the momentum of the charged ejectiles its rather modest acceptance led us to consider whether the discussed studies could be continued more efficiently with the WASA detector when it will be installed at the cooler synchrotron COSY [7]. As a first step in January 2004 the COSY-11 collaboration presented two Letters of Intent [8, 9] describing the general physics motivations and advantages of continuing the studies by means of the 4π detector. However, detailed estimations of possible advantages and/or disadvantages require quantitative simulations of the response of the WASA detector to the investigated reactions. For this purpose we began to perform simulations of the $pp \to pp\eta'$ reaction, and also of the quasi-free processes like $pn \to pn\eta'$ and $pn \to pn\eta$. Results of the very first studies are presented in two separated reports [10, 11]. For the calculations we have applied one of the two simulation packages used by the WASA collaboration, assuming temporarily the arrangement of the WASA detector components as presently in operation at CELSIUS [12]. The computation package chosen is based on the GEANT simulations program and the dedicated software package ODIN (Onlie/Offline Data INspection) for the analysis of data and the WASA-experiment control [13]. It is written in the languages Fortran and C and the whole project is maintained using the Microsoft Developer Studio. This program was previously optimized for the analysis of the $pp \to pp\pi^0$ [14], $pd \to ^3He\eta$ [15] and $pd \to pd\eta$ [16] reactions. Thus, as a very first exercise we have extended it to enable the simulations and analysis of the quasi-free processes like $pd \to pn\eta p_{sp}$, where p_{sp} denotes the spectator proton and implemented procedures for the calculations of the excess energy of the $pn \to pn\eta$ process according to the method described in references [17, 18]. As a first task we checked to what extent the accuracy obtained in the measurements of the quasi-free $pn \to pn\eta$ reaction performed by the PROMICE/WASA collaboration is due to the approximation used in the calculation of the excess energy and to what extent it is due to the experimental resolution of the detection set-up. For calculating the excess energy it is assumed that the transverse components of the Fermi momentum of the target nucleon are zero. Figure 1 demonstrates the spectrum obtained for the difference between the real excess energy and the one determined under this supposition. The distribution indicates that using this approximation one overestimates the real excess energy - on the average - by a few MeV. This is, however, less than the experimental resolution which amounts to about 8 MeV [17].

Further studies, aiming at the precise comparison between the COSY-11 and WASA facilities in view of the experimental resolution for the invariant mass determination, excess energy and acceptance are in progress.

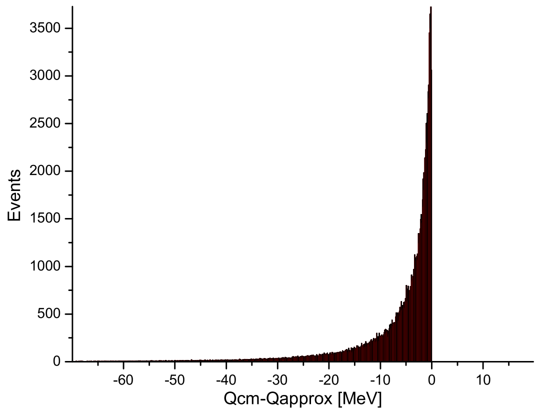

Fig. 1: Distribution of the difference between the real and approximated excess energy of the quasi-free $pn \to pn\eta$ reaction simulated for the $pd \to pn\eta p_{sp}$ process at the proton beam momentum of 2.075 GeV/c. For details see text.

References:

[1] A. Khoukaz et al., Eur. Phys. J. **A 20** (2004) 345.
[2] P. Moskal et al., Phys. Rev. **C 69** (2004) 025203.
[3] J. Przerwa, e-Print Archive: hep-ex/0408016.
[4] R. Bilger et al., Nucl. Instr. & Meth. **A 457**, 64 (2001).
[5] R. Czyzykiewicz et al., AIP Conf. Proc. **717** (2004) 858.
[6] P. Moskal et al., AIP Conf. Proc. **717** (2004) 907.
[7] B. Höistad et al., Proposal for the Wide Angle Shower Apparatus (WASA) at COSY-Jülich, e-Print Archive: nucl-ex/0411038
[8] P. Moskal et al., Letter of Intent **No. 14** for an experiment with a 4π electro-magnetic calorimeter at COSY (2004). http://ankecvs.ikp.kfa-juelich.de/femc04/en/talks.shtml
[9] P. Winter et al., Letter of Intent **No. 17** for an experiment with a 4π electromagnetic calorimeter at COSY (2004). e-Print Archive: nucl-ex/0406034
[10] J. Przerwa et al., contribution in this annual report.
[11] P. Klaja et al., contribution in this annual report.
[12] J. Zabierwoski et al., Nucl. Instr. and Meth. **A 379** (1996) 57.
[13] J. Złomańczuk, Internal WASA report, Uppsala, (2003)
[14] J. Złomańczuk et al., Phys. Lett. **B 436** (1998) 251.
[15] R. Bilger et al., Phys. Rev. **C 65** (2002) 044608.
[16] R. Bilger et al., Phys. Rev. **C 69** (2004) 014003.
[17] H. Calén et al., Phys. Rev. Lett. **79** (1997) 2642.
[18] J. Stepaniak, H. Calén, Schriften FZ-Jülich Matter & Materials **21** (2004) 224.

[1] Institute of Physics, Jagellonian University, Poland.
[2] Dep. of Radiation Sciences, Uppsala University, Sweden.

The work has been supported by *RII3/CT/2004/506078 – HadronPhysics-Activity -N4:EtaMesonNet*

Investigation of the η'-proton interaction at the COSY-11 and WASA@COSY facilities

P. Klaja[1], J. Złomańczuk[2], M. Janusz[1], P. Moskal, W. Oelert, J. Przerwa[1] for COSY-11 and WASA@COSY collaborations

During 2004 the COSY-11 collaboration has published results on the $pp \to pp\eta$ reaction at the excess energy of $Q = 15.5\ MeV$ [1]. Especially interesting is the structure determined for the proton-proton invariant mass distributions which reveals a statistically significant enhancement at large proton-proton momenta. The structure could be due to the η-proton interaction, but a firm explanation remains at present a challenge for the theory since it requires a rigorous three-body approach to the system with complex potentials.

On the experimental side it is natural to ask whether the enhancement will also appear in the case of the production of other mesons. Specifically interesting in that context are the π^0 and η' mesons, the SU(3) flavour neutral partners of the η meson. We have chosen for the comparison the η' meson mainly because its interaction with nucleons is still quantitatively not established, and thus the observation of a signal originating from the proton-η' interaction would be already exciting in itself. Secondly, because the η' meson is much heavier than the pion and the relevant angular momenta in the $pp\eta'$ system are expected to be zero at Q = 15.5 MeV, at this energy the $pp\pi^0$ system has significant contribution from higher partial waves [2].

At a beam momentum of 3.257 GeV/c, corresponding to an excess energy of Q = 15.5 MeV, the $pp \to pp\eta'$ reaction was measured with rather high statistics by the COSY-11 collaboration. The investigations were performed at exactly the same excess energy as those for the $pp \to pp\eta$ reaction in order to permit a direct comparison between the results for η and η' mesons and hence to facilitate drawing less model dependent conclusions. The data are presently analyzed and the overall number of registered $pp \to pp\eta'$ events amounts to about 13000 [3]. Due to the missing mass technique used, it is impossible to identify univocally the studied reaction on the event-by-event basis. The experimentally determined ratio of the signal to the unavoidable multi-pion background amounts to about $\approx$0.25 [3]. Nevertheless, the achieved statistics will allow for the reduction of the multi-pion background in one-dimensional differential spectra and we will see whether these spectra will reveal some remarkable signals. Yet, the full information of the mutual interaction between ejectiles is excessible from the two-dimensional Dalitz plot. Unfortunately, the present COSY-11 data do not permit for its background-free determination without the loss of the required accuracy. A qualitative improvement of the data basis can only be made if additionally to the registration of outgoing baryons the gamma quanta from the decay of the meson will be detected. This would allow to obtain multi-dimensional differential distributions free of (or at least with drastically reduced) multi-pion background. Needless to say that the more particles are registered in coincidence the more crucial becomes the detection acceptance. Therefore, a scan of the phase space of the reactions characterized by 1 μb cross section is feasible only at a detector facility possessing an acceptance close to 4π. For such studies the WASA detector will be well suited after it is installed at COSY [4]. We intend to use this detector for the determination of a background free Dalitz plot and to begin we have performed simulation studies in order to estimate the acceptance of the WASA detector for the $pp \to pp\eta'$ reaction. Figure 1(left) shows a two protons invariant mass spectrum for all simulated events and in figure 1(right) the corresponding spectrum is extracted only for those events for which two protons were reconstructed. The acceptance given in figure 2 is a ratio of the spectra from figure 1(right) and figure 1(left) for every bin of invariant mass. Here only the decay channel $\eta' \to \gamma\gamma$ was taken into account at the present condition of the WASA detector. However, for the η' meson identifications, one can use further decay sequences as e.g. $\eta' \to \pi^0\pi^0 \to 6\gamma$ [5]. The spectra indicate that with the present forward detector and reconstruction algorithms the effciency of the protons reconstruction from the $pp \to pp\eta'$ reaction is not high and both the modifications of forward detector (FD), which will improve track coordinate measurements, energy measurements and particle identification for the higher energies, as well as the development of the reconstruction procedures suitable for protons with kinetic energy up to at least 500 MeV, are needed.

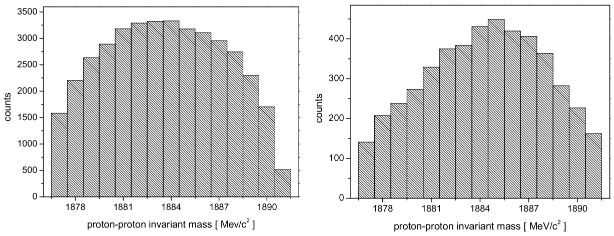

Fig. 1: Proton-proton invariant mass spectra. (left) generated, (right) reconstructed from signals in the detector. For the reconstruction noly events with the invarian mass of the $\gamma\gamma$ system larger than 800 MeV were taken into account.

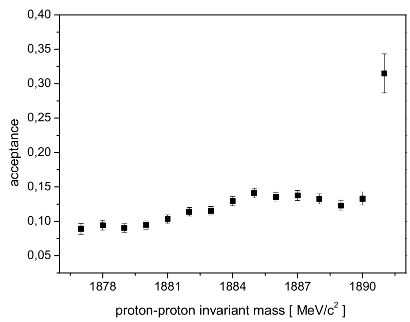

Fig. 2: Ratio of the spectra from figure 1. (see text)

References:

[1] P. Moskal et al., Phys. Rev. **C 69** (2004) 025203.
[2] J. Złomańczuk et al., Phys. Lett. **B 436** (1998) 251.
[3] J. Przerwa et al., Ann. Rep. 2003 IKP, FZ-Jülich, **Jül-4107** (2004).
[4] B. Höistad et al., Propsal for the WASA@COSY, (2004), e-Print Archive: nucl-ex/0411038
[5] P. Moskal et al., Letter of Intent **No. 14** for an experiment with a 4π electro-magnetic calorimeter at COSY (2004). http://ankecvs.ikp.kfa-juelich.de/femc04/en/talks.shtml

[1] Institute of Physics, Jagellonian University, Poland
[2] Dep. of Radiation Sciences, Uppsala University, Sweden

The work has been supported by *RII3/CT/2004/506078 – HadronPhysics-Activity -N4:EtaMesonNet*

Detection possibilities of the quasi–free $p\,n \to p\,n\,\eta'$ reaction at the WASA detector

J. Przerwa[1], J. Złomańczuk[2], M. Janusz[1], P. Klaja[1], P. Moskal, W. Oelert for the COSY-11 and WASA@COSY collaborations

In August 2004, for the first time the η' meson production in the proton–neutron collision [1] has been studied close to the kinematical threshold at the COSY–11 facility, an internal magnetic spectrometer installed at the cooler synchrotron COSY. The measurement of the quasi–free $p\,n \to p\,n\,\eta'$ reaction was conducted with a proton beam ($p_{beam} = 3.35 GeV/c$) and with a deuteron cluster target. The expriment was based on the measurement of the four-momenta of the outgoing nucleons. Events corresponding to the creation of the η' meson will be identified off-line via the missing mass technique, and the total energy available for the quasi-free proton-neutron reaction can be calculated for each event from the vector of the momentum of the spectator proton. The spectator protons are measured by the dedicated silicon-pad detector [2]. At present the analysis aiming for establishing the excitation function for the $p\,n \to p\,n\,\eta'$ reaction is in progress and will deliver values for the total cross section in the excess energy range between 0 and 20 MeV. A tentative elaboration of the quasi-free elastic proton-proton scattering showed that the luminosity averaged over the three weeks of measurement amounted to about $4 \cdot 10^{30}$ cm^{-2} s^{-1}. With such luminosity – depending on the anticipated reaction mechanism – we expect between 40 and 260 measured and reconstructed events per day [1].

Such investigation could be extended to excess energies (up to $\approx$ 150 MeV) using the WASA facility at COSY [5, 6]. In this case the method of the measurement will be different from the one used at COSY-11, since with the present WASA set-up one cannot detect spectator protons. Yet, as it is shown for the studies of the $pd \to pn\eta p_{sp}$ reaction at CELSIUS [4], the measurement of the gamma quanta originating from the decays of the η' and the registration of the fast outgoing proton suffice to distinguish the quasi-free $pn \to pn\eta'$ process from other recations and to reconstruct the excess energy for each event [3]. If the spectator proton and outgoing neutron are not measured than one can calculate the excess energy only approximately since in this case we deal with six unknown variables (two unknown momentum vectors) and only four equations for energy and momentum conservation. Assuming that the transverse component of the momentum of the target nucleon is equal to zero one can calculate the approximate value of the excess energy [4, 3]. Figure 1 demonstrates the excess energy distribution simulated for the $pd \to pn\eta' p_{sp}$ reaction (dashed line) and the result obtained when applying the above approximation (solid line). On the average the reconstructed values of Q are a few MeV larger then generated (see also Figure 2). Such a shift, however, is much smaller than the smearing caused by the experimental resolution of the measurement of the four-momentum vectors of the gamma quanta and the proton. For example, the experimental smearing in the case of the $pn \to pn\eta$ reaction is about 8 MeV [4]. In order to estimate this for the $pn \to pn\eta'$ reaction we have performed simulation studies of the response of the WASA detector assuming the detection arrangement as it is used at present at CELSIUS [7]. As a first step we have chosen only one decay channel of the η' meson with a branching ratio 0.02, viz $p\,n \to p\,n\,\eta' \to p\,n\,\gamma\gamma$ process. Figure 3 depicts result obtained for the distribution of the difference between the generated and reconstructed excess energies. The resolution is unacceptable to perform the study of the $pn \to pn\eta'$ reaction using the present WASA detection system and the temporary reconstruction algorithm, which was optimized for the less energetic protons. For the discussed investigations the present configuration of the forward detector must be improved in order to allow a better determination of the energy of the forward scattered protons. This resolution could be improved also when taking into account signals from neutrons which may react in the forward detector with 36% probability [5]. A quantitative answer requires further investgations.

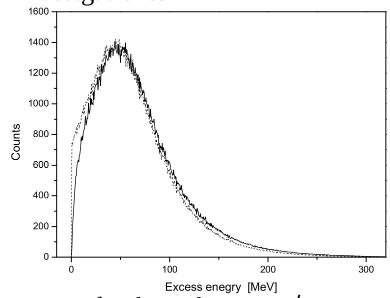

Fig. 1: Excess energy for the $p\,d \to p\,n\,\eta' p_{sp}$ reaction simulated at a proton beam momentum of 3.35 GeV/c. For details see text.

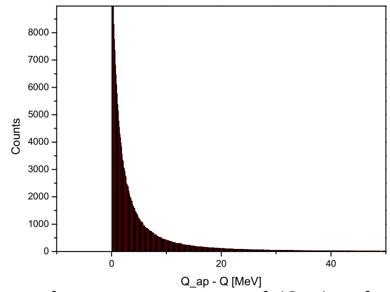

Fig. 2: Difference between approximated (Q_{ap}) and real (Q) excess energy for the $p\,n \to p\,n\,\eta'$ reaction.

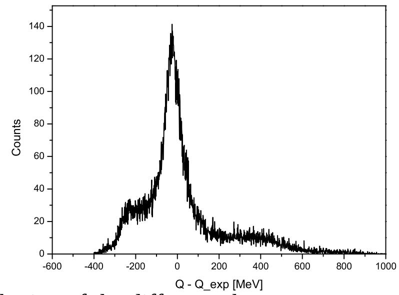

Fig. 3: Distribution of the difference between generated and reconstructed excess energy.

References:

[1] P .Moskal et al., COSY Proposal **No. 133** (2003).
[2] R. Bilger et al., Nucl. Instr. & Meth. **A 457**, 64 (2001).
[3] J. Stepaniak, H. Calén, Schriften FZ-Jülich Matter & Materials **21** (2004) 224.
[4] H. Calén et al., Phys. Rev. Lett. **79** (1997) 2642.
[5] B. Höistad et al., Propsal for the WASA@COSY, (2004), e-Print Archive: nucl-ex/0411038
[6] P. Moskal et al., Letter of Intent No. 14 (2004).
[7] J. Zabierowski et al., Phys. Scripta **T99** (2002) 159.

[1] Institute of Physics, Jagellonian University, Poland
[2] Dep. of Radiation Sciences, Uppsala University, Sweden

The work has been supported by *RII3/CT/2004/506078 – HadronPhysics-Activity -N4:EtaMesonNet*

Simulation of the reaction $pp \to d\pi^+\eta$ for WASA*

P. Fedorets[a], M. Büscher, V.P. Chernyshev[a], V.Yu. Grishina[b], V. Hejny, V. Kleber[c], L.A. Kondratyuk[a], A.E. Kudryavtsev[a]

The reaction $pp \to da_0^+ \to d\pi^+\eta$ followed by $\eta \to \gamma\gamma$ can be measured at COSY with the WASA facility by detecting deuterons in the forward detector (FD) and pions and photons in the central detector (CD). The reaction can be identified by reconstruction of the masses $m(\eta)$=inv($\gamma\gamma$) and $m(d)$=m.m.($\pi^+\gamma\gamma$). The study of the reaction $pp \to da_0^+$ is preferable to $pp \to pna_0^+$, since the ratio of cross sections for the resonant/nonresonant reactions is about one order larger for the deuteron in final state [1].

Two main background reactions are expected: non-resonant production $pp \to d\pi^+\eta$ and $pp \to pn\pi^+\eta$ with misidentification of a proton as a deuteron.

In order to investigate the background suppression, simulations were performed for the $a_0^+(980)$ production and both background reactions. In the simulations the following initial distributions have been used: for $a_0^+(980)$ production according to the Quark-Gluon Strings Model (QGSM) [2], for direct $d\pi^+\eta$ production via N^*- and Δ-resonance excitation [3, 4, 5] and for $pn\pi^+\eta$ a phase space distribution. Figure 1 shows the invariant masses ($\pi^+\eta$) for these reactions. The cross sections have been estimated according to Refs. [3, 6, 7] as $\sigma(a_0^+)$:$\sigma(d\pi^+\eta)$:$\sigma(pn\pi^+\eta) = 1.1$:3.5:96. Thus, the expected background from the reaction $pp \to pn\pi^+\eta$ is about two orders higher than the a_0^+ signal.

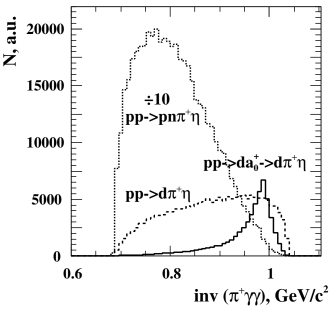

Fig. 1: Invariant mass ($\pi^+\eta$) for $a_0^+(980)$ production in $pp \to da_0^+ \to d\pi^+\eta$ and two background processes: direct production $pp \to d\pi^+\eta$ and $pp \to pn\pi^+\eta$ (divided by a factor 10).

Due to the high kinetic energies of protons and deuterons for a COSY beam energy $T = 2.65$ GeV they cannot be stopped in the FD and their initial kinetic energy cannot be reconstructed. Moreover, their energy losses become close to minimal ionizing and the standard WASA@CELSIUS $\Delta E/E$ method cannot be used for *p/d* separation.

In order to suppress the proton background a set of cuts has been used. The first cut was applied to the reconstructed m.m.($\pi^+\gamma\gamma$) (Fig. 2(a)). The cut at 1.95 GeV suppresses protons by a factor $\sim$1.6. A 2-dimensional distribution energy losses *vs.* kinetic energy of the deuteron calculated from pion and two photons is correlated for a_0^+ events (Fig. 2(b)). Applying a gate $\pm$20 MeV protons can be suppressed by a factor $\sim$3.9.

The next cuts have been applied to the difference between measured azimuthal and polar angles of forward particles and expected deuteron angles calculated from the measured pion and two photons. If one assumes that all forward particles are deuterons, then the real deuterons are seen as lines and the

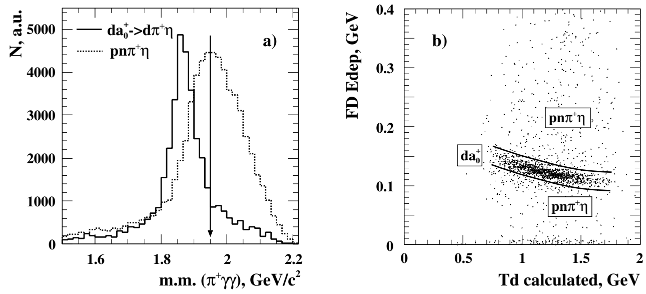

Fig. 2: (a) Reconstructed missing mass ($\pi^+\gamma\gamma$) for $pp \to da_0^+ \to d\pi^+\eta$ and $pp \to pn\pi^+\eta$. The cut is indicated by the arrow. (b) Energy losses in FD *vs.* kinetic energy of deuterons calculated from the measured pion and two photons. The cuts are indicated by curves.

protons are smeared (Fig. 3(a,b)). With an azimuthal angle cut of $\pm 20°$ and a polar angle $\pm 2°$, protons can be suppressed by a factor $\sim$21.

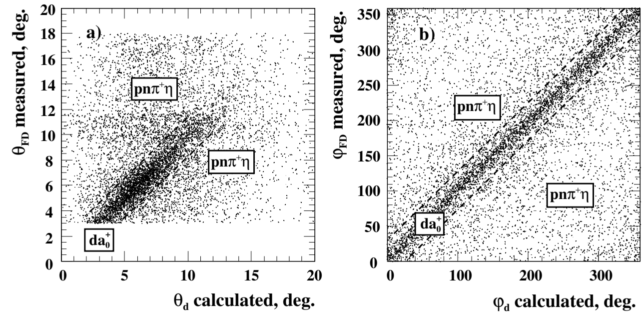

Fig. 3: (a,b) Measured forward angles *vs.* angles calculated for deuterons. The cuts are shown by lines.

Additional proton suppression comes from the different acceptances for a_0^+ and $pn\pi^+\eta$ events by a factor $\sim$1.3

Taking into account all mentioned cuts and the difference in acceptance the total proton suppression factor is: $1.3 \times 1.6 \times 3.9 \times 21 \approx 170$. Thus, it is expected that the a_0^+ resonance production in the reaction $pp \to da_0^+ \to d\pi^+\eta$ can be measured with WASA.

References:

[1] Proposal "WASA at COSY", nucl-ex/0411038.
[2] V.Y. Grishina *et al.*, Eur. Phys. J. A **21**, 507 (2004).
[3] V. Grishina *et al.*, Annual Report 2000 of the IKP, FZ Jülich, p.30;
[4] L.A. Kondratyuk *et al.*, Phys. of Atom. Nucl. **66**, No. 1, 152 (2003).
[5] A.E. Kudryavtsev *et al.*, Phys. of Atom. Nucl. **66**, No. 10, 1946 (2003).
[6] V. Grishina *et al.*, Eur. Phys. J. A **9**, 277 (2000).
[7] V. Grishina, private communication.

[a]ITEP, Moscow, Russia
[b]INR, Moscow, Russia
[c]IKP, Universität zu Köln, Germany
*Supported by grants COSY-FFE-41520733, ISTC-1966, DFG-436RUS-113/733,787, RFBR02-02-16349, DFG-RFBR03-02-04013, 02-02-04001

2.2 Experiments at External Facilities

Usability of permanent magnets as Ioffe trap at ATRAP

U. Bechstedt, F. Esser[1], H. Glückler[1],F. Goldenbaum, D. Grzonka, G. Hansen[1], S. Martin, W. Oelert, T. Sagefka, T. Sefzick, H. Soltner[1], Z. Zhang
for the ATRAP-Collaboration

The ATRAP experiment studies the production of cold antihydrogen atoms via the antiproton-positron interaction in a nested Penning trap configuration aiming for a CPT test by comparing the 1s-2s transition energy of hydrogen and antihydrogen. To achieve ultimate precision trapping of neutral antihydrogen atoms is essential. One way to trap neutral antihydrogen atoms is a magnetic trap with field gradients introducing a force onto the magnetic moment of the atom.
An alternative to super-conducting magnets which have to be used for maximum field strengths are permanent magnets by which reasonable field gradients can be achieved. The advantage of permanent magnets compared to super-conducting magnets is the very easy operating effort, no need for power supply and cooling, and the low cost. A disadvantage is the reduced flexibility since the magnetic field cannot be changed or switched off at least apart from very complicated geometric constructions.
Permanent magnets are widely used for beam line elements but the operability within a strong external magnetic field at low temperatures – as it is requested by the ATRAP experiment – has to be demonstrated.
To check the behaviour of a permanent magnet under the required conditions test measurements have been performed at a super-conducting solenoid of the University of Leipzig.
Small blocks (1 x ½ x ¾ inch^3) of Co_2Sm_{17}, magnetized at TRiDUS [1], with field strength of about 0.5 T at the surface were exposed to various external fields. The direction of the external field was always perpendicular to the field directions of the magnetized probes. The exposure to the external field results in a reduction of the magnetization. In fig. 1 the decrease of the magnetization for several probes and different ramp speeds is shown as a function of the maximum field strength of the solenoid.

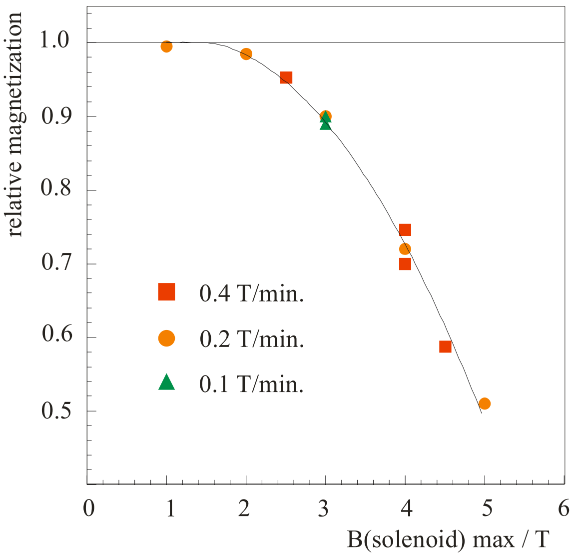

Fig. 1: Reduction of the magnetization in the permanent magnet normalized to the initial value for various field strengths of the outer solenoid field.

The measurements were performed by ramping up the solenoid to a chosen field strength followed by a ramp down to zero fields. The measured field at the permanent magnet probes after this cycle is normalized to the measurement before the external field was applied.
Independent of the ramp speed all data points follow one line. Measurements have been performed for ramp speeds of 0.1, 0.2 and 0.4 T/min which was the maximum possible ramp speed.
The various tests show that the loss of magnetization depends essentially on the maximum outer field strength to which the probe is exposed which then stays constant as long as the applied field is below this maximum value.
In fig. 2 the decrease of magnetization after exposure to a 3 T external field is shown as a function of the exposure time.

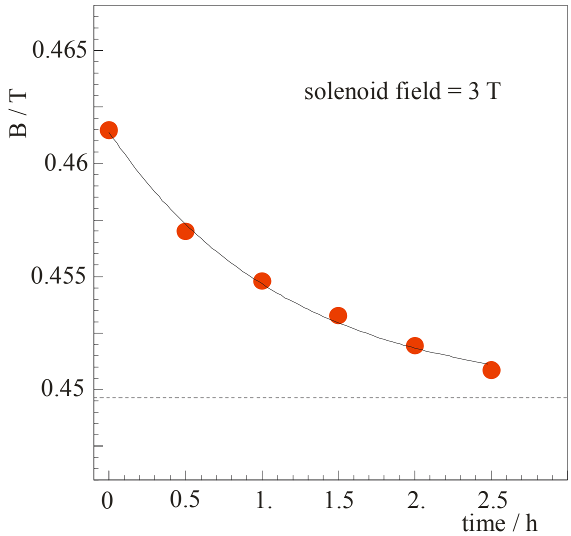

Fig. 2: Time dependence of the de-magnetisation of a test piece exposed to a solenoid field of 3T.

The de-magnetisation follows an exponential decrease given by the solid line with a time constant of about 1.2 hours. It saturates at about 0.45 T which is a reduction of 2.5 %. One of the probes was kept for 10 hours in the solenoid at 2.5 T without any further change of the measured permanent field strength within the error bars.
These basic tests have shown that a stable operation of a permanent quadrupole magnet within a strong solenoid field is possible. Apart from the initial de-magnetization no slow reduction or damage of the quadrupole field is expected. Also the low temperature is no problem. In a separate test a permanent magnet probe was repeatedly dipped into liquid Helium and warmed up to room temperature without any damage or visible cracks.

We would like to thank Prof. P. Esquinazi and Dr. M. Ziese for the excellent assistance during the measurements in Leipzig.

References:
[1] TRiDUS Magnetics and Assemblies, www.tridus.com

[1] ZAT FZ-Jülich

Charged particle cloud in a combined Penning/Ioffe trap

U. Bechstedt, F. Esser[1], H. Glückler[1], F. Goldenbaum, D. Grzonka, G. Hansen[1], S. Martin, W. Oelert, T. Sagefka, T. Sefzick, H. Soltner[1], Z. Zhang
for the ATRAP-Collaboration

The trapping of neutral antihydrogen atoms $\overline{H}_0$ which is required for high precision spectroscopy at the ATRAP experiment needs a magnetic quadrupole field for the radial confinement in the trap. The easiest way would be to superpose such a magnetic field gradient to the Penning trap for the charged ingredients of $\overline{H}_0$: the antiprotons and positrons.

According to a theorem valid for charged plasma [1], confined radially by the rotation in a constant magnetic field, any inhomogeneous magnetic field distribution results in instability for the trapping of charged particles. On the other hand calculations of single particle movements in a Penning trap within a magnetic quadrupole field showed that stable orbits are possible [2].

At the ATRAP experiment first tests have been performed to trap charged particles in a Penning trap surrounded by a permanent quadrupole magnet. In fig.1 the set-up is shown.

Due to space limitations the BGO detector surrounding the Penning trap was replaced by a permanent magnet tube. It consists of 6 rings with 16 elements, respectively, magnetized in the direction indicated by the arrows which results in a quadrupole field in radial direction.

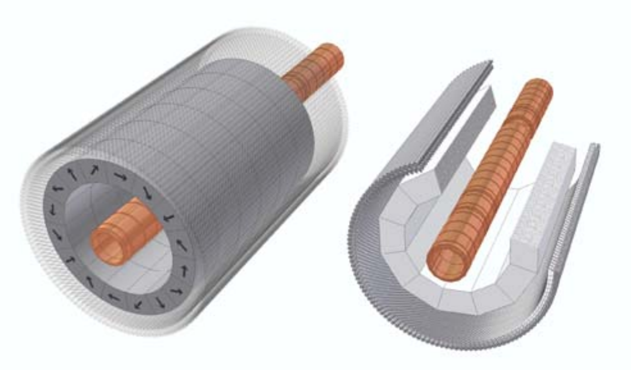

Fig. 1: Assembly of the magnetic quadrupole (left side) surrounding the Penning trap. On the right side the normal set-up with BGO detector is shown which was replaced by a permanent magnet with an inner diameter of 58 mm.

The magnetic gradient was about 18 T/m before installation and was reduced to 15 T/m after exposure to a field of 3 T in the ATRAP solenoid as expected from tests with permanent magnet probes [3]. For details of the ATRAP setup see [3] and references therein.

The loading and trapping of charged particles was tested with electrons in a solenoid field of up to 3 T. Various number of electrons were loaded which correspond to particle clouds typically used for the antihydrogen production, and the number of electrons as a function of trapping time was recorded.

Fig. 2 displays the electrode structure in the lower part of the trap with the surrounding quadrupole is. The electron clouds were trapped for about 70 minutes at the electrode T6 which exceeds clearly the typically time needed for antihydrogen experiments. The quadrupole field at this position is still at its maximum value. Every 8 minutes the number of electrons in the clouds was measured using a non-destructive radio frequency method [4] by moving the electron cloud to the position “e trap” where a RF circuit is attached. At a 1 T solenoid field within the studied trapping time of 70 minutes the number of electrons was reduced by about 25% at the end but at 2 T and 3 T it could be achieved that within the error bars no losses occur.

It seems that a stable trapping of electrons is possible.

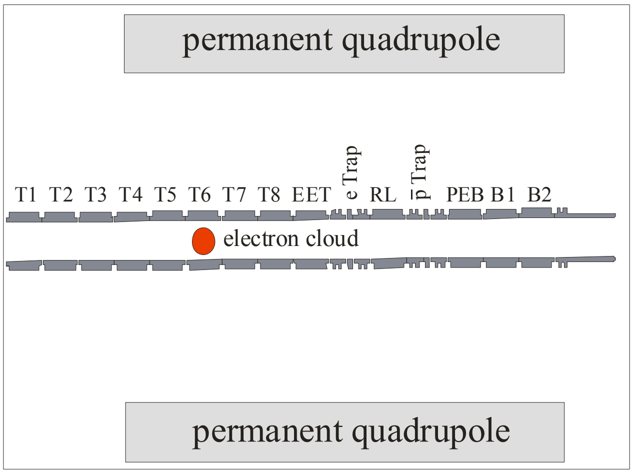

Fig. 2: Electrode structure of the lower trap part with the surrounding quadrupole and the electron cloud trapped at T6.

These first results of stable electron clouds in a Penning trap within an inhomogeneous solenoid field increases the confidence that a combined Penning / Ioffe trap may work for the production and trapping of antihydrogen. The applied magnetic gradient was rather small compared to technically possible solutions with gradients in the order of 100 T/m. In the present set-up it was limited by the geometry which could be filled with permanent magnets. In the final set-up for antihydrogen trapping studies much more space will be available at ATRAP-II and with an increased volume of permanent magnet material gradients of about 100 T/m are possible. Further tests combined with calculations have to be performed to check if trapping with higher magnetic gradients will work.

References:

[1] T. M. O'Neil, Phys. Fluids, 23:2216 - 2218, 1980.
[2] T. M. Squires, P. Yesley, and G. Gabrielse, Phys. Rev. Lett., 86:5266-5269, 2001.
[3] ATRAP contributions to this report.
[4] G. Gabrielse et al., Phys. Rev. Lett. **82**, 3198 (1999).

[1] ZAT FZ-Jülich

High resolution spectroscopy of the Kβ transition in muonic hydrogen

D. F. Anagnostopoulos[a], D. Covita[b], H. Fuhrmann[c], D. Gotta, A. Hirtl[c], A. Gruber[c], P. Indelicato[d], T. Ishiwatari[c], E.-O. Le Bigot[d], M. Nekhipelov, J. M. F. dos Santos[b], P. Schmid[c] L. M. Simons[e], M. Trassinelli[d], J. F. C. A. Veloso[b], J. Zmeskal[c]

A high resolution X-ray spectroscopy of the Kβ transition in muonic hydrogen has been performed with a set-up similar to the measurement of the strong interaction width of the ground state in pionic hydrogen [1].

The main motivation for the muonic hydrogen measurement was a deeper understanding of processes governing the de–excitation in exotic hydrogen atoms which influence the extraction of a strong interaction width from pionic hydrogen.

The strong interaction width itself is extracted by comparing a measured line shape with a well determined resolution function. Unfortunately there exist acceleration effects like the so–called Coulomb de-excitation which leave the pionic hydrogen atom with kinetic energies resulting in a Doppler broadening similar to the Strong interaction broadening. The Coulomb de–excitation may result in quite substantial kinetic energies [2]. As reliable cross sections are not yet available for this process, it was decided to check the calculations in muonic hydrogen which may be considered to be a twin system of the pionic hydrogen atom with the advantage of not experiencing strong interaction. The final goal is to constrain cascade parameters for the evaluation of the strong interaction width of the ground state in pionic hydrogen.

In addition the formation of molecular states in excited states similar to the well known muon catalyzed fusion mechanism in the ground state may lead to a deformation of the line shape falsifying the result for pionic hydrogen [4].

The measurement took place end of 2004 at the πE5 channel of the ring cyclotron of PSI. In a set-up similar to the pionic hydrogen experiment a Si 111 crystal was used. The determination of the response function of this crystal with X-rays from a dedicated ECRIT source is described in a parallel article in this annual report [3].

The particle density of the cryogenic hydrogen target was choosen to be equivalent to 12 bar at room temperature. The count rate was at about 6 per 1 Coulomb accumulated proton charge of the accelerator and a total of about 10000 X-ray events has been collected in a 4 weeks measurement.

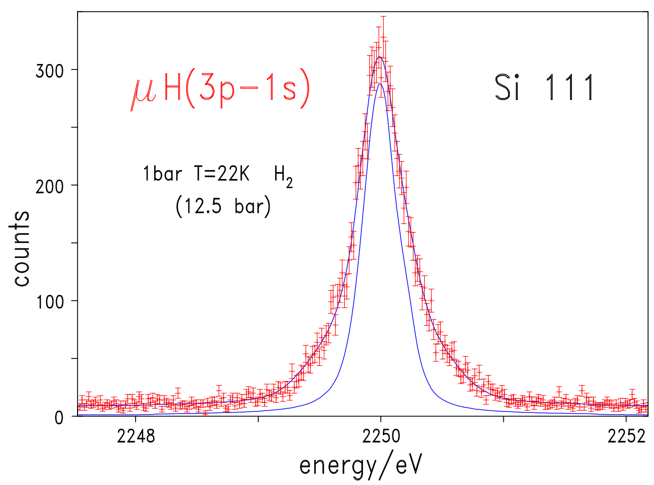

Fig. 1: The spectrum of Kβ transition in muonic hydrogen measured with a Si111 crystal is shown together with a best fit and the corresponding resolution function.

In Figure 1 a spectrum of the Kβ transition of muonic hydrogen is shown together with a fit to the data. In addition the response function as obtained from the ECRIT measurements is depicted. It contains the theoretical hyperfine splitting of the triplet and singlet ground state together with their statistical weights. The broadening of the measured line is attributed to Doppler broadening which is caused by acceleration effects during the cascade finally feeding the 3p level.

The fit relied on the assumption that the feeding transitions may convert their transition energy by Coulomb de–excitation into kinetic energy which in the case of the Kβ transition may reach values of about 60 eV. This energy was subdivided into 5 regions and their relative weights had been used as fit parameters. At the present state of evaluation a low energy component of 0–2 eV could be identified to exist with a probability of about 60%. The components with higher energies are at present subject of investigation.

The spectrometer was installed in a way that a range of 10 eV to lower energies was accessible to measurement. In this region the background was found to be flat and no distortion of the line itself could be observed. As a result X–ray transitions from molecular levels can be excluded at the percent level. This corroborates earlier findings from pionic hydrogen measurements where no pressure dependent shift of the energy of the Kβ transition could be identified.

Moreover in one step of the evaluation the number of regions for the kinetic energy distribution was reduced to two. This measure allowed the fitting of the hyperfine intensity distribution. The fitted singlet to triplet ratio was in this case still depending on assumptions on the width of the two kinetic energy distributions. A central value for this ratio could be obtained, however, to be 2.8 with an error 0.2. This is not too much different from the statistical occupation of 3:1 and constitutes the first measurement of the hyperfine population of the ground state in muonic hydrogen.

References:

[1] http://pihydrogen.web.psi.ch.
[2] T. S. Jensen, Eur. Phys. J. **D31**, 11 (2004).
[3] S. Boucard et al., this annual report.
[4] E. Lindroth, J. Wallenius, S. Jonsell, Phys. Rev. **A68** 032502(2003).
S. Kilic, J. P. Karr, L. Hilico, Phys. Rev. **A70**, 042506 (2004).

[a] Dept. Mat. Sc., Univ. Ioannina, Greece
[b] Dept. of Phys., Univ. Coimbra, Portugal
[c] SMI, Österr. Akademie d. Wiss., Vienna
[d] Lab. Kastler–Brossel, Univ. P. et M. Curie, Paris
[e] PSI, Switzerland

The resolution function of a Bragg spectrometer at pionic hydrogen energies

S. Boucard[a] D. Covita[b], H. Fuhrmann[c], A. Hirtl[c] D. Gotta, A. Gruber[c], P. Indelicato[a], E.-O. Le Bigot[a], J. M. F. dos Santos[b], P. Schmid[c] L. M. Simons[d], L. Stingelin[d], M. Trassinelli[a] J. F. C. A. Veloso[b], A. Wasser[d], J. Zmeskal[c]

The final goal of the new pionic hydrogen experiment is the determination of the strong interaction width of the ground state in pionic hydrogen with an accuracy of about 10 meV [1]. Such an accuracy can be achieved by measuring the energy of radiative transitions feeding the ground state with a high resolution Bragg spectrometer. Up to now a spectroscopy of the 2p–1s (2.436 keV), 3p–1s (2.886 keV) and the 4p–1s (3.043 keV) transitions has been performed at different pressures. Spherically bent Si or quartz crystals had been used with a curvature radius of about 3 m, a diameter of 100 mm and a thickness of smaller than 0.3mm. For these parameters bent crystal theory predicts a negligible influence of the bending process on the resolution function [2]. Imperfections in the crystal material itself and defects produced during the fabrication, however, could distort the resolution function. An experimental determination of it for all crystals used in the pionic hydrogen experiment is therefore indispensable.

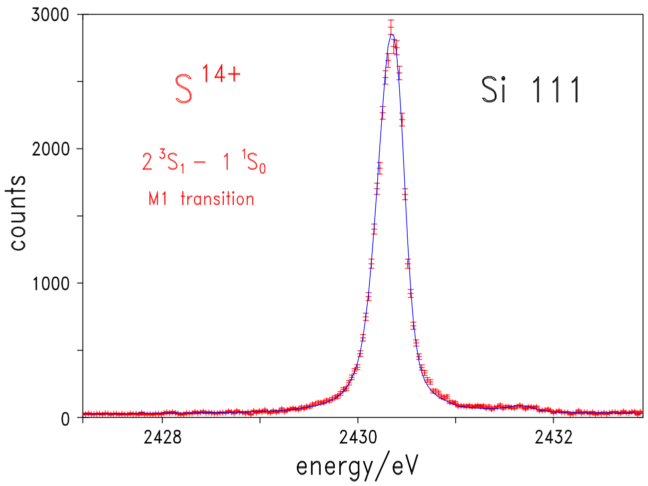

Fig. 1: The spectrum of the M1 transition from helium-like sulfur measured with a Si 111 crystal is shown together with a best fit.

Monte Carlo simulations of X-ray spectra had been performed in order to study the impact of uncertainties in the resolution function on the error in the strong interaction width. It turned out that at an intensity on the level of some 10000 is required in the measured response function. In addition a ratio for peak to background of 100:1 should be reached. In order to reach this goal the PSI-ECRIT device [3] has been tuned to produce X-rays from highly charged sulfur, clorine and argon ions. Helium–like atoms formed with these elements emit narrow Xray lines with energies of 2.430, 2.757 and 3.104 keV, respectively, which overlaps well with the pionic hydrogen X–rays in question. The intensity of highly charged ions was optimized by producing a better vacuum inside the ECR source using a cryopump and reducing the number of insertions inside the vacuuum chamber. The intensity gain permitted to insert a narrow collimator near the ECR plasma, which resulted in a much improved peak/background ratio. A total of about 10 hours was needed to determine the response function for one crystal in sufficient detail including a search for the correct focal position and a change of apertures in front of the crystals.

In Figure 1 a spectrum of the M1 transition of helium-like sulfur taken with a Si 111 crystal is shown together with a best fit to the data. A crystal aperture with a horizontal opening of 60mm was used. In the fit a small known contribution of lithium-like sulfur was included. The fit function is produced from the theoretical response function of the crystal spectrometer by folding it with a Gaussian the width of which being one of the fitting parameters. As a result a Gaussian with a width of about 60 μrad was sufficient to explain the data. The corresponding values for the energies of argon and clorine as well as values for a quartz 10-1 crystals are shown in Table 1. The values for the additional Gaussians decrease linearly with energy in the case of Si and remain constant for quartz. Obviously in the case of Si a surface contribution exists in addition to an overall bulk contribution similar in value for both crystals.The resulting energy resolution for the Si 111 crystals is about 10- 20% better than the corresponding values for quartz because of more favorable Bragg angles. This led to the choice of the Si crystals for a measurement of the Doppler broadening in muonic hydrogen described in this annual report [4].

Table 1: The value for the addditional Gaussian part needed to interprete the measured data is shown for the different M1 transitions for two crystals. The resulting resolution in terms of the FWHM value is shown as well.

crystal/energy [eV]	Gaussian [μrad]	FWHM [meV]
Si 111 /2430	58.3 ± 2.3	319 ± 15
Si 111 /2757	42.5 ± 1.5	405 ± 30
Si 111 /3104	27.7 ± 2.1	425 ± 32
qu 10-1/2430	26.9 ± 3.8	356 ± 30
qu 10-1/3104	28.2 ± 2.2	501 ± 40

References:

[1] http://pihydrogen.web.psi.ch.
[2] G. Hölzer, O. Werhahn, E. Förster, Cryst. Res. Technol. **69**, 185, (1998).
[3] S. Biri, L. M. Simons, D. Hitz, Rev. Sci. Instr. **71**, 1116 (2000).
[4] D. F Anagnostopoulos et al., this annual report.

[a] Lab. Kastler–Brossel, Univ. P. et M. Curie, Paris
[b] Dept. of Phys., Univ. Coimbra, Portugal
[c] SMI, Österr. Akademie d. Wiss., Vienna
[d] PSI, Switzerland

Study of the breathing mode of the nucleon in high energy proton-proton scattering

H.P. Morsch and P. Zupranski[1]
[1]Soltan Institute for Nuclear Studies,
Pl-00681 Warsaw, Poland

To complement N* experiments at COSY energies we have analysed baryon resonances in p-p scattering at energies of 5-30 GeV from Brookhaven and CERN experiments in the 60's. In all these data several structures have been observed, the $\Delta(1232)$ and resonances at about 1400 MeV, 1520 MeV, 1680 MeV and 2190 MeV, see e.g. [1,2]. Spectra at different beam momenta together with our resonance fits are shown in Fig.1. Interestingly, the strongest resonance is observed

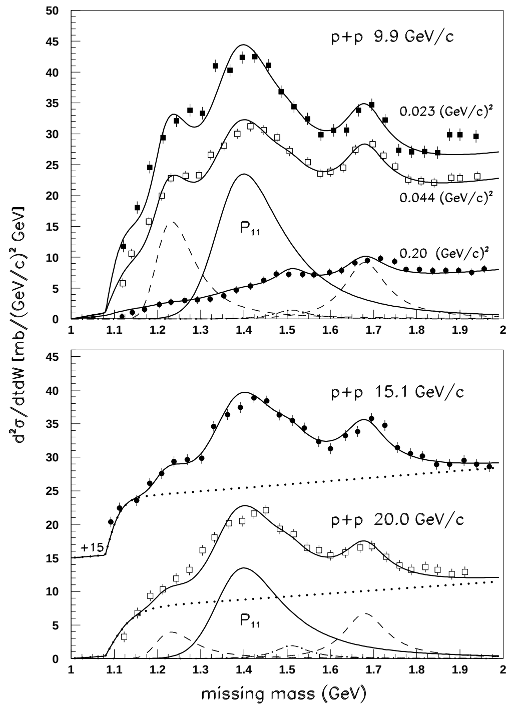

Fig. 1: Missing mass spectra of $p+p \to p\,x$ at different beam momenta in comparison with our resonance fits. The resonance at 1400 MeV is the strongest N* observed.

with a centroid mass m_o of $1400 \pm 10 MeV$ and a width of $200 \pm 20 MeV$, in excellent agreement with the scalar P_{11} observed in α-p scattering (see [3]). The P_{11} assigment for this resonance is confirmed by the t-dependence of the (p,p') differential cross section, which shows a much steeper slope than for the other resonances, indicating clearly L=0 excitation. The absolute cross sections are consistent with the full energy weighted sum rule [4], again supporting the results from α-p.

Information on the decay of the strong P_{11} resonance can be deduced also from high energy experiments. A study of 4 prong events of the reaction $pp \to pp\pi^+\pi^-$ has been made [5] at a beam momentum of 6.6 GeV/c. In the invariant $\pi^+\pi^-$ mass spectrum, see Fig. 2, a strong rise of the yield has been observed above the 2πN threshold. We calculated the $\pi^+\pi^-$ mass spectrum corresponding to the resonances observed in Fig. 1. We found, that the resonance at 1400 MeV gives rise to a strong peak in the $\pi^+\pi^-$ spectrum, whereas the resonances at higher mass are smeared out. By taking into account correctly the multi-pion background, we obtain a good description of the spectrum with a 2π-N decay branch $B_{2\pi}$ of the scalar P_{11} at 1400 MeV of 75$\pm$20%. This is also consistent with the picture of a double resonance structure of the Roper resonance (see [3]).

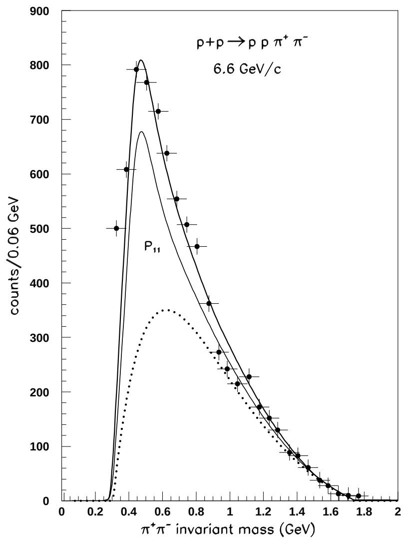

Fig. 2: Invariant $\pi^+\pi^-$ mass spectrum from ref. [5] in comparison with a resonance fit consistent with Fig. 1. The multi-pion background is given by the dotted line.

1. E.W. Anderson, et al., Phys. Rev. Lett. 16, 855 (1966)
2. R.M. Edelstein, et al., Phys. Rev. D 5, 1073 (1972)
3. H.P. Morsch and P. Zupranski, Phys. Rev. C 61 (1999) 024002
4. H.P. Morsch, Z. Phys. A 350, 61 (1994)
5. E. Colton, P.E. Schlein, E. Gellert, and G.A. Smith, Phys. Rev. D 3, 1063 (1971)

3 Theoretical Physics

H. Polinder, J. Haidenbauer and Ulf-G Meißner

Recently the nucleon-nucleon (NN) interactions has been described successfully using chiral effective field theory [1] . The power counting is applied to the NN potential in this work and the potential consists of pion-exchanges and a series of contact interactions with an increasing number of derivatives to parameterize the shorter ranged part of the NN force. The main advantage of this scheme is that calculations can be improved systematically by going to higher order in the power counting.

In this work we want to extend this scheme to the hyperon-nucleon (YN) interaction. For this purpose we first have to investigate the $SU(3)$ structure of the four baryon contact interactions in lowest order. The lowest order contact term for the NN interactions is given by [2]

$$\begin{aligned}\mathcal{L} &= C_i\left(\bar{N}\Gamma_i N\right)\left(\bar{N}\Gamma_i N\right) \ , \\ &= -\frac{1}{2}C_S\left(\varphi_N^\dagger\varphi_N\right)\left(\varphi_N^\dagger\varphi_N\right) \\ &\quad -\frac{1}{2}C_T\left(\varphi_N^\dagger\sigma\varphi_N\right)\left(\varphi_N^\dagger\sigma\varphi_N\right) \ , \end{aligned} \tag{1}$$

where only the large components of the nucleon spinors are considered in lowest order. Here $-C_S/2 = C_1 + C_2$, $-C_T/2 = 2C_3 + C_4$ and Γ_i are the usual elements of the Clifford algebra [3]: $\Gamma_1 = 1, \Gamma_2 = \gamma^\mu, \Gamma_3 = \sigma^{\mu\nu}, \Gamma_4 = \gamma^\mu\gamma_5, \Gamma_5 = \gamma_5$. The two contact term constants C_S and C_T are determined by fitting to the experimental NN data.

In the case of the YN interactions we will consider a similar $SU(3)$ invariant coupling. The leading order contact terms for the octet baryon-baryon interactions, invariant under Lorentz transformations and Hermitian, are given by the $SU(3)$ invariants

$$\begin{aligned}\mathcal{L}^1 &= \tilde{C}_i^1\left\langle\bar{B}_a\bar{B}_b\left(\Gamma_i B\right)_a\left(\Gamma_i B\right)_b\right\rangle \ , \\ \mathcal{L}^2 &= \tilde{C}_i^2\left\langle\bar{B}_a\bar{B}_b\left(\Gamma_i B\right)_b\left(\Gamma_i B\right)_a\right\rangle \ , \\ \mathcal{L}^3 &= \tilde{C}_i^3\left\langle\bar{B}_a\left(\Gamma_i B\right)_a\left(\Gamma_i B\right)_b\bar{B}_b\right\rangle \ , \\ \mathcal{L}^4 &= \tilde{C}_i^4\left\langle\bar{B}_a\left(\Gamma_i B\right)_a\bar{B}_b\left(\Gamma_i B\right)_b\right\rangle \ , \\ \mathcal{L}^5 &= \tilde{C}_i^5\left\langle\bar{B}_a\left(\Gamma_i B\right)_b\bar{B}_b\left(\Gamma_i B\right)_a\right\rangle \ , \\ \mathcal{L}^6 &= \tilde{C}_i^6\left\langle\bar{B}_a\left(\Gamma_i B\right)_b\left(\Gamma_i B\right)_a\bar{B}_b\right\rangle \ , \\ \mathcal{L}^7 &= \tilde{C}_i^7\left\langle\bar{B}_a\left(\Gamma_i B\right)_a\right\rangle\left\langle\bar{B}_b\left(\Gamma_i B\right)_b\right\rangle \ , \\ \mathcal{L}^8 &= \tilde{C}_i^8\left\langle\bar{B}_a\left(\Gamma_i B\right)_b\right\rangle\left\langle\bar{B}_b\left(\Gamma_i B\right)_a\right\rangle \ , \\ \mathcal{L}^9 &= \tilde{C}_i^9\left\langle\bar{B}_a\bar{B}_b\right\rangle\left\langle\left(\Gamma_i B\right)_a\left(\Gamma_i B\right)_b\right\rangle \ . \end{aligned} \tag{2}$$

Here a and b denote the Dirac indices of the particles, B is the usual irreducible octet representation of $SU(3)$ for the $J^P = \frac{1}{2}^+$ baryons given by

$$B = \begin{pmatrix} \frac{\Sigma^0}{\sqrt{2}} + \frac{\Lambda}{\sqrt{6}} & \Sigma^+ & p \\ \Sigma^- & \frac{-\Sigma^0}{\sqrt{2}} + \frac{\Lambda}{\sqrt{6}} & n \\ -\Xi^- & \Xi^0 & -\frac{2\Lambda}{\sqrt{6}} \end{pmatrix} , \tag{3}$$

and the brackets $\langle\ldots\rangle$ denote taking the trace in the three dimensional flavor space. The Clifford algebra elements are here actually diagonal 3×3-matrices in flavor space.

Making use of the trace property $\langle AB\rangle = \langle BA\rangle$, we see that the terms 3 and 6 in Eq. (2) are equal to the terms 2 and 1 respectively. Also making use of the Fierz theorem [4] one can

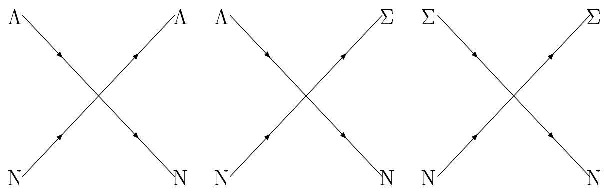

Fig. 1: Lowest order contact hyperon-nucleon interactions

show that the terms 1, 4 and 8 are equivalent to the terms 2, 5 and 7 respectively. We do not need to consider term 9, since it does not contain NN and YN interactions. Writing the terms 2,5 and 7 plus their Fierz rearranged equivalents 1,4 and 8 explicitly in the isospin basis and performing a Fierz rearranged to remove terms like $\left(\bar{\Lambda}\Gamma_i N\right)\left(\bar{N}\Gamma_i\Lambda\right)$, etc., we find for the NN and YN contact interactions

$$\begin{aligned}\mathcal{L}^2 &= C_i^2\left\{\frac{1}{3}\left(\bar{\Lambda}\Gamma_i\Lambda\right)\left(\bar{N}\Gamma_i N\right)\right. \\ &\quad +\left[\left(\bar{\Sigma}\cdot\Gamma_i\Sigma\right)\left(\bar{N}\Gamma_i N\right) + i\left(\bar{\Sigma}\times\Gamma_i\Sigma\right)\cdot\left(\bar{N}\tau\Gamma_i N\right)\right] \\ &\quad \left.-\frac{1}{\sqrt{3}}\left[\left(\bar{N}\tau\Gamma_i N\right)\cdot\left(\bar{\Lambda}\Gamma_i\Sigma\right) + H.c.\right]\right\} \ , \\ \mathcal{L}^5 &= C_i^5\left\{\frac{5}{3}\left(\bar{\Lambda}\Gamma_i\Lambda\right)\left(\bar{N}\Gamma_i N\right) + \left(\bar{N}\Gamma_i N\right)\left(\bar{N}\Gamma_i N\right)\right. \\ &\quad +\left[\left(\bar{\Sigma}\cdot\Gamma_i\Sigma\right)\left(\bar{N}\Gamma_i N\right) - i\left(\bar{\Sigma}\times\Gamma_i\Sigma\right)\cdot\left(\bar{N}\tau\Gamma_i N\right)\right] \\ &\quad \left.+\frac{1}{\sqrt{3}}\left[\left(\bar{N}\tau\Gamma_i N\right)\cdot\left(\bar{\Lambda}\Gamma_i\Sigma\right) + H.c.\right]\right\} \ , \\ \mathcal{L}^7 &= C_i^7\left\{2\left(\bar{\Lambda}\Gamma_i\Lambda\right)\left(\bar{N}\Lambda N\right) + 2\left(\bar{\Sigma}\cdot\Gamma_i\Sigma\right)\left(\bar{N}\Gamma_i N\right)\right. \\ &\quad \left.+\left(\bar{N}\Gamma_i N\right)\left(\bar{N}\Gamma_i N\right)\right\} \ . \end{aligned} \tag{4}$$

The YN contact interactions in Eq. (4) lead to the contributions given in Fig.1. If we consider, similar to Eq. (1), only the large components of the Dirac spinors in Eq. (4) then we need to determine six contact constants for the NN and YN interactions in lowest order: C_S^2, C_T^2, C_S^5, C_T^5, C_S^7 and C_T^7. So in addition to the two contact constants fixed by the NN data, we have to determine four more contact constants. We will fit the existing YN data to determine these constants.

References:

[1] E. Epelbaum, W. Glöckle, and U.-G. Meißner, arXiv:nucl-th/0405048 ,
E. Epelbaum, W. Glöckle, and U.-G. Meißner, Nucl. Phys. **A671**, 295 (2000).

[2] E. Epelbaoum, W. Glöckle, and U.-G. Meißner, Nucl. Phys. **A637**, 107 (1998),
E. Epelbaum, *The Nucleon-Nucleon Interaction in a Chiral Effective Field Theory*, PhD thesis, Ruhr-Universität Bochum, 2000, unpublished.

[3] J. D. Bjorken and S. D. Drell, *Relativistic Quantum Fields*, McGraw-Hill Inc., New York, 1965.
We follow the conventions of this reference.

[4] T.-P. Cheng and L.-F. Li, *Gauge theory of elementary particle physics*, Oxford University Press, Oxford, 1984.

Accuracy test of FSI approaches for extracting scattering lengths

A.M. Garsparyan*, J. Haidenbauer, C. Hanhart

Recently we proposed a method that allows extraction of the YN scattering lengths from data on hyperon production reactions directly [1]. In particular, we derived an integral representation for the ΛN scattering lengths in terms of a differential cross section of reactions with large momentum transfer such as $pp \to K^+ p\Lambda$ or $\gamma d \to K^+ n\Lambda$. It reads

$$a_S = \lim_{m^2 \to m_0^2} \frac{1}{2\pi} \left(\frac{m_\Lambda + m_N}{\sqrt{m_\Lambda m_N}} \right) \mathbf{P} \int_{m_0^2}^{m_{max}^2} dm'^2 \sqrt{\frac{m_{max}^2 - m^2}{m_{max}^2 - m'^2}}$$
$$\times \frac{1}{\sqrt{m'^2 - m_0^2}\,(m'^2 - m^2)} \ln |A_S(m'^2)|^2 \,, \qquad (1)$$

where $A_S(m'^2)$ is the production amplitude of a Λ–nucleon pair with invariant mass m'^2 and total spin S. Furthermore, $m_0^2 = (m_\Lambda + m_N)^2$, where m_Λ (m_N) denotes the mass of the Lambda hyperon (nucleon), and m_{max} is some suitably chosen cutoff in the mass integration. **P** denotes that the principal value of the integral is to be used and the limit has to be taken from above. This formula enables determination of the scattering lengths to a theoretical uncertainty of at most 0.3 fm, subject to possible but controlable influences of the final-state interactions in the KN and $K\Lambda$ systems [1].

The method is applicable to all large momentum transfer reactions, as long as the final ΛN system is dominated by a single partial wave. Thus, the number of contributing partial waves has to be reduced by appropriate kinematical requirements. For S waves it is sufficient to limit the relative energies of the final ΛN system to values below 40 MeV in the range of the mass integration to get accurate results.

The derivation of Eq. (1) is based on dispersion relations which provide a connection between the reaction amplitude of the production process with the phase shifts of the interaction in the final state in terms of dispersion integrals,

$$A(m^2) \propto \exp\left[\frac{1}{\pi} \int_{m_0^2}^{\infty} \frac{\delta(m'^2)}{m'^2 - m^2 - i0} dm'^2 \right] , \qquad (2)$$

cf. Ref. [1] for details. Let us investigate the case when the phase shifts are given by the first two terms in the effective range expansion,

$$p' \,\mathrm{ctg}(\delta(m'^2)) = -1/a + (1/2) r p'^2 \,, \qquad (3)$$

over the whole energy range. Here p' is the relative momentum of the final state particles under consideration in their center of mass system, corresponding to the invariant mass m'^2. In this case the relevant integrals can be evaluated in closed form as [2]

$$A(m'^2) \propto \frac{(p'^2 + \alpha^2) r/2}{-1/a + (r/2) p'^2 - ip'} \,, \qquad (4)$$

where $\alpha = 1/r(1 + \sqrt{1 - 2r/a})$. Eq. (4) is the so-called Jost-function approach to the treatment of the final state interaction (FSI) and is commonly used for extracting scattering lengths from production reactions [3].

A further simplification can be made if one assumes that $a \gg r$. This situation is practically realized in the $^1S_0$ partial wave of the pp or pn systems. Then the energy dependence of the quantity in Eq. (4) is given by

$$A(m'^2) \propto \frac{1}{1 + iap'} \,, \qquad (5)$$

as long as $p' \ll 1/r$. Is coincides then with the energy dependence of pp elastic scattering (if we disregard the effect of the Coulomb interaction). Therefore one expects that, at least for small kinetic energies, pp elastic scattering and meson production in NN collisions with a pp final state exhibit the same energy dependence [2, 4], which indeed was experimentally confirmed. This treatment of FSI effects is offen referred to as Migdal-Watson approach.

In the following we present a comparison of the reliability of the three methods described above. For that purpose we take different YN models from the literature and calculate the amplitude $A(m^2)$ for them via Eq. (2). Then this amplitude is used for extracting the scattering length by means of the dispersion integral Eq. (1) or from the approximative prescriptions given by Eqs. (4) and (5). For comparision we consider also the $^1S_0$ partial wave of the np system.

The results are summarized in Table 1. The second column contains the correct scattering length evaluated directly from the potential model. One can see that the extraction of the scattering length via the dispersion integral (1) yields results pretty close to the original values for all considered potentials. In fact, in most cases the deviation is significantly smaller than the uncertainty of the method, estimated in Ref. [1] to be 0.3 fm. The results of the Jost-function approach exhibit a systematic offset in the order of 0.3 fm. The situation is much worse for the Migdal-Watson approach where a similar offset is found though now in the order of 0.6 fm. As a consequence, the extracted values differ by 50 % or more from the correct scattering lenghts. Only for the $^1S_0$ np partial wave the disagreement is only in the order of 5 %. Here the reliability of the Jost-function and Migdal-Watson approaches are comparable. This is in agreement with the expectations mentioned above.

model	$a[fm]$	disp.int.	Jost	Watson
Jülich 01 singlet	-1.02	-1.03	-1.28	-1.67
Nijmegen 97a singlet	-0.73	-0.75	-0.98	-1.33
Nijmegen 97f singlet	-2.59	-2.57	-2.96	-3.35
Jülich 01 triplet	-1.89	-1.66	-2.05	-2.42
Nijmegen 97a triplet	-2.13	-1.98	-2.37	-2.75
Nijmegen 97f triplet	-1.69	-1.61	-2.00	-2.37
Argonne v14 singlet	-23.71	-23.54	-24.56	-24.79

References:

[1] A.M. Gasparyan, J. Haidenbauer, C. Hanhart, J. Speth, Phys. Rev. C **69**, 034006 (2004).

[2] M. Goldberger and K. Watson, *Collision Theory* (Wiley, New York 1964).

[3] F. Hinterberger and A. Sibirtsev, Eur. Phys. J. A **21**, 313 (2004).

[4] K. Watson, Phys. Rev. **88**, 1163 (1952); A.B. Migdal, Sov. Phys. JETP **1**, 2 (1955).

* ITEP, 117259, B. Cheremushkinskaya 25, Moscow, Russia

New results on the limit for the with of the exotic $\Theta^+(1540)$ resonance

A. Sibirtsev, J. Haidenbauer, S. Krewald, and Ulf-G. Meißner*

Evidence for a narrow baryon resonance with positive strangeness, the Θ^+, has been found by more than ten experimental collaborations with masses ranging from 1521 to 1555 MeV and widths from 9 and 24 MeV (these widths are usually upper limits given by the respective detector resolution) [1]. The width of the Θ^+ is of particular importance to understand the nature of this state. Constraints for the width of the Θ^+ resonance can be deduced from K^+N and K^+d data which are available in the relevant momentum range, $417 < k_0 < 476$ MeV/c, of the incident kaons, cf. Ref. [2] for further information.

In a recent paper our group [3] has reexaminated the existing data on total K^+N cross sections in the I=0 and I=1 isospin channels based on a KN model calculation utilizing the meson-exchange model of the Jülich group [4]. It was concluded that the rather strong enhancement of the cross section caused by the presence of a Θ^+ with a width of 20 MeV is not compatible with the existing information on KN scattering. Only a much narrower Θ^+ state, with a width in the order of 5 MeV or less, could be reconciled with the existing data base, cf. Ref. [3] – or, alternatively, the Θ^+ state must lie at an energy much closer to the KN threshold.

In the present paper we want to extend the work of Ref. [3]. We perform a direct comparison of a calculation of the reaction $K^+d \to K^0pp$ with the corresponding experimental information. One has to keep in mind that the information on the K^+N interaction in the isospin $I = 0$ channel has been inferred from data on the K^+d reaction. In the extraction procedure it is implicitly assumed that the K^+N amplitude shows no sharp structure. Therefore, it is more conclusive to calculate explicitly observables for the reactions $K^+d \to K^+np$ and $K^+d \to K^0pp$ based on K^+N interaction models that include a $\Theta^+(1540)$ resonance so that a direct comparison with experimental data is possible. Then "medium" effects such as the broadening of the resonance by the Fermi motion of the nucleons in the deuteron and the interaction of the nucleons in the final state can be dealt with rigorously.

For the calculation of the reaction $K^+d \to K^0pp$ we follow, in general, the theoretical procedure which was originally developed by Stenger et al. [5]. The amplitude T_d for the deuteron breakup reaction is

$$T_d = \sqrt{16\pi^3 m_d}\,[T_N(q)u(p) + T_N(p)u(q)], \qquad (1)$$

where m_d is the deuteron mass, p and q are the momenta of the two final nucleons, u is the (S-wave) deuteron wave function and T_N is elementary KN amplitude. Further details can be found in Ref. [2].

In Fig. 1a we present results for the integrated $K^+d \to K^0pp$ cross section as a function of the kaon momentum in comparison to the available experimental information. Evidently there are data in the region where the Θ^+ is supposed to be located (the largest and smallest resonance masses reported so far are indicated by bars in Fig. 1) and those provide rather restrictive constraints for the Θ^+ width. Fortunately, there are two independent measurements in the critical energy range. One can see from Fig. 1a that none of the model calculations with a Θ^+ width larger than 1 MeV is compatible with the data. Widths of 1 MeV or less can be certainly accommodated though we should say here that we did not explore the effect of such narrow widths in an actual model calculation.

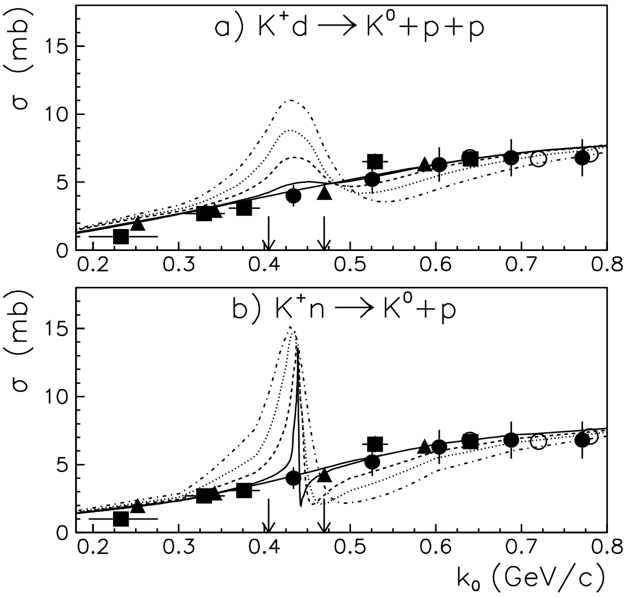

Fig. 1: Total $K^+d \to K^0pp$ cross section as a function of the kaon momentum. The curves in a) show our full results for the original Jülich KN model without the Θ^+ resonance (solid line) and the variants with a Θ^+ and with different widths (Γ_Θ=1 MeV - solid with bump; 5 MeV - dashed; 10 MeV - dotted; and 20 MeV - dash-dotted). The curves in b) correspond to a calculation for the reaction $K^+n \to K^0p$ assuming that the neutron target is at rest. The vertical arrows indicate the range of kaon momenta corresponding to the smallest and the largest values found experimentally for the mass of the Θ^+ resonance.

If we disregard the two data points that lie within the Θ^+ region then there is a gap that allows to fit in such a resonance with a width of $\Gamma_\Theta \approx 5$ MeV without increasing the χ^2/data by more than 10% [2].

In order to illustrate the impact of the stationary neutron approximation we show here also calculations for the two-body reaction $K^+n \to K^0p$, cf. Fig. 1b. Comparing the two panels of the figure one can see to which extend the resonance is broadened by the Fermi motion of the nucleons in the deuteron and by the integration over the three-body phase space.

References:

[1] For a recent review see e.g. E.Klempt, hep-ph/0404270.
[2] A. Sibirtsev, J. Haidenbauer, S. Krewald, and U.-G. Meißner, Phys. Lett. **B 599** (2004) 230.
[3] J. Haidenbauer and G. Krein, Phys. Rev. **C68** (2003) 052201(R).
[4] M. Hoffmann *et al*, Nucl. Phys. **A593** (1995) 341.
[5] V.J. Stenger et al., Phys. Rev. **134** (1964) B1111.

* also at: Universität Bonn, Helmholtz-Institut für Strahlen und Kernphysik, D-53115 Bonn, Germany

Analysis of Θ^+ production in $\mathrm{K}^+ - \mathrm{Xe}$ collisions

A. Sibirtsev, J. Haidenbauer, S. Krewald, and Ulf-G. Meißner*

Recently, evidence for a narrow strangeness $S=+1$ baryon resonance, now called $\Theta^+(1540)$, has been reported in Ref. [1] based on a measurement of Kaon photoproduction on ^{12}C and subsequently such a structure was also observed in the invariant mass spectrum of the kaon-nucleon (KN) system in other reactions. One of those reactions is the collision of K^+ mesons with Xe nuclei where a Θ^+ signal was observed by the DIANA collaboration [2].

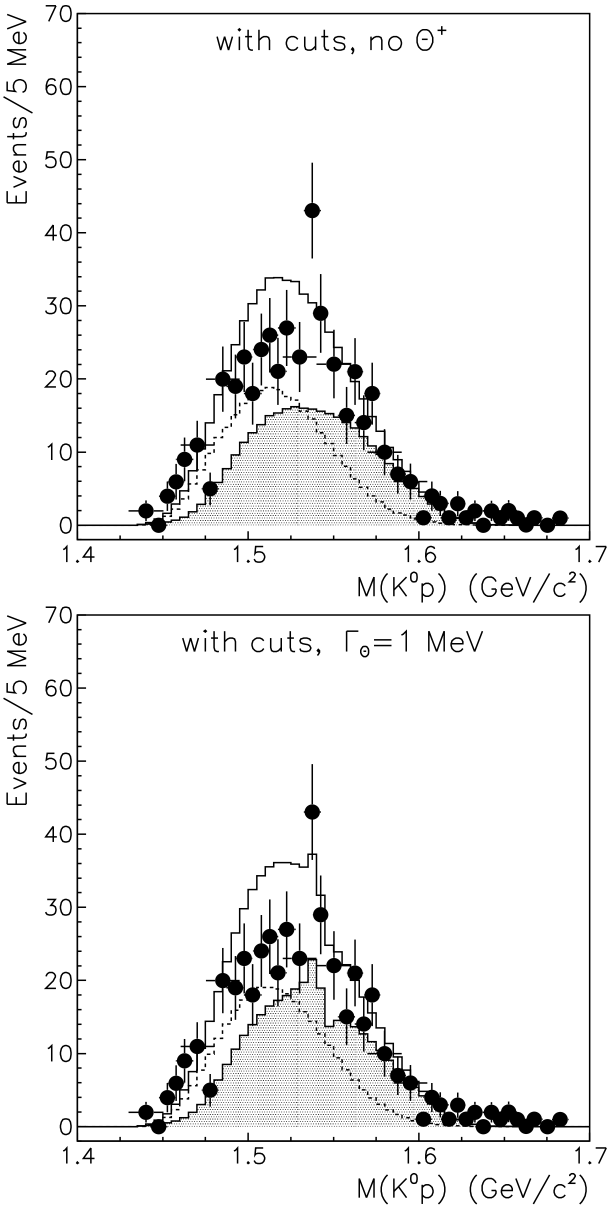

Fig. 1: The K^0p invariant mass spectrum from the K^+Xe reaction. The circles are the data (with cuts) from Ref. [2]. The hatched histograms show our results for the spectrum from direct $K^+n \to K^0p$ production on a bound target neutron, while for the dashed curve an additional single rescattering of the proton was taken into account. The solid curve is their sum.

We have performed a detailed and microscopic calculation of the K^0p effective mass spectrum for the charge-exchange reaction $K^+Xe \to K^0pX$ [3]. We aim at a quantitative analysis of the mass spectrum that was published by the DIANA collaboration [2]. The main ingredient of our calculation is an elementary KN scattering amplitude that is taken from the meson-exchange model developed by the Jülich group [4]. The role and significance of the $\Theta^+(1540)$ for a quantitative description of the DIANA data is investigated by employing variants of the Jülich KN model where a Θ^+ resonance with different widths was included consistently [5, 6] assuming that this exotic resonance has spin 1/2.

Details of our model calculation for the reaction $K^+Xe \to K^0pX$ can be found in Ref. [3]. Here we only want to mention that we take into account the direct charge exchange reaction, $K^+n \to K^0p$, on a neutron bound in the Xe nucleus but also nuclear rescattering effects of the final proton in the nucleus. Rescattering of the final K^+ is not considered. Those effects should be small because of the large mean free path of the Kaon.

Results of our model calculation are presented and compared to the experimental K^0p invariant mass spectrum provided by the DIANA collaboration in Fig. 1. Note that we consider here the data sample where kinematical cuts were applied to enhance the signal of the Θ^+. (Results for the case without cuts can be found in Ref. [3].) The upper figure shows result without a Θ^+ whereas in the lower figure a Θ^+ with positive parity a mass of 1540 MeV, and a width of Γ_Θ = 1 MeV was included. We present separately the contributions of direct $K^+n \to K^0p$ production (hatched histograms) and of proton rescattering (dashed lines), and also the full results (solid curve). The description of the data for the full calculation is of comparable quality for both scenarios, cf. Fig. 1, and leads to similar results for the χ^2/dof [3]. Larger values for Γ_Θ, however, produce a strongly increased χ^2/dof and are therefore ruled out by the DIANA data. The same conclusions were reached for a $\Theta^+(1540)$ with negative parity cf. Ref. [3].

References:

[1] T. Nakano et al., Phys. Rev. Lett. **91**, 012002 (2003).
[2] V.V. Barmin et al., Phys. Atom. Nucl. **66**, 1715 (2003) [hep-ex/0304040].
[3] A. Sibirtsev, J. Haidenbauer, S. Krewald, and U.-G. Meißner, nucl-th/0407011, Eur. Phys. J. **A**, in press.
[4] M. Hoffmann *et al*, Nucl. Phys. **A593** (1995) 341.
[5] J. Haidenbauer and G. Krein, Phys. Rev. **C68** (2003) 052201(R).
[6] A. Sibirtsev, J. Haidenbauer, S. Krewald and Ulf-G. Meißner, Phys. Lett. B **599**, 230 (2004).

* also at: Universität Bonn, Helmholtz-Institut für Strahlen und Kernphysik, D-53115 Bonn, Germany

Some aspects of Θ^+ parity determination in the reaction $\gamma N \to \Theta^+ \bar{K} \to N K \bar{K}$

A. I. Titov,[ab] H. Ejiri,[cd] H. Haberzettl,[e] and K. Nakayama[f]

The first evidence for the Θ^+ pentaquark discovered by the LEPS collaboration at SPring-8 [1] was subsequently confirmed in other experiments [2, 3, 4, 5, 6, 7]. None of these experiments could determine the spin and the parity of the Θ^+. Some proposals to do this in photoproduction processes using single and double polarization observables were discussed. The difficulty in determining the spin and parity of Θ^+ in the reaction $\gamma N \to \Theta^+ K^-$ is due to the way the pentaquark state is produced. Models of the Θ^+ photoproduction from the nucleon based on the effective Lagrangian approach have been developed. As has been pointed out, there are great ambiguities in calculating the (spin) unpolarized and polarized observables. A possible solution to these problems is to use more complicated "model-independent" (triple) spin observables [8, 9, 10]. These spin observables involve the linear polarization of the incoming photon, and the polarizations of the target nucleon and the outgoing Θ^+. Using basic principles, such as the invariance of the transition amplitude under rotation, parity inversion and, in particular, the reflection symmetry with respect to the scattering plane, one can arrive at unambiguous predictions which depend only on the Θ^+ parity in the reaction $\gamma N \to \Theta^+ \bar{K}$. The key aspect of the model-independent predictions is that in the final state the total internal parity of outgoing particles are different for positive and negative Θ^+ parity. We skip the discussions of the practical implementation of using the triple spin observables since experimental observations of the spin orientation of the strongly decaying Θ^+ is extremely difficult. Instead, we focus on the basic aspects of this idea. For simplicity, in the following we limit our discussion for determining the Θ^+ parity to isoscalar spin-1/2 Θ^+. In fact, most theories predict the J^P of Θ^+ to be $1/2^+$ or $1/2^-$.

There are two difficulties in applying the "model-independent" formalism for the parity determination. First, the final state in the photoproduction experiment is the three-body state $NK\bar{K}$ (and not the two body $\Theta^+\bar{K}$)-state. The spin observables in the initial and final channels are deduced by their parities irrespective of the intermediate Θ^+ parity. It is difficult, therefore, to find the pertinent "model-independent" observables for this case. Second, the contribution of the non-resonant background of the reaction $\gamma N \to NK\bar{K}$ cannot be neglected. The observed ratio of the resonance peak to the non-resonant continuum reported in the photoproduction experiments is about $1.5-2$. This means that the difference between the resonant and non-resonant amplitudes is a factor of two and therefore the non-resonant background may modify the spin-observables considerably.

In this work we analyze the problem of how to determine the parity of the Θ^+ pentaquark in the reaction $\gamma N \to K\Theta \to NK\bar{K}$, where $N = n, p$ within a effective Lagrangian approach.. Our model calculations indicate that the contribution of the non-resonant background of the reaction $\gamma N \to NK\bar{K}$ cannot be neglected, and that suggestions to determine the parity based solely on the initial-stage process $\gamma N \to K\Theta$ cannot be implemented cleanly. We discuss the various mechanisms that contribute to the background, and we identify some spin observables which are sensitive mostly to the Θ^+ parity rather than to the details of the production mechanism. found in Ref.[11].

References:

[1] T. Nakano *et al.* [LEPS Collaboration], Phys. Rev. Lett. **91**, 012002 (2003).

[2] V. V. Barmin *et al.* [DIANA Collaboration], Phys. Atom. Nucl. **66**, 1715 (2003).

[3] S. Stepanyan *et al.* [CLAS Collaboration], Phys. Rev. Lett. **91**, 252001 (2003).

[4] V. Kubarovsky, S. Stepanyan *et al.* [CLAS Collaboration], Phys. Rev. Lett. **92**, 032001 (2004).

[5] J. Barth *et al.* [SAPHIR Collaboration], Phys. Lett. **B572**, 127 (2003).

[6] A. E. Asratyan, A. G. Dolgolenko, and M. A. Kubantsev, Phys. Atom. Nucl. **67**, 682 (2004), Yad. Fiz. **67**, 704 (2004).

[7] L. Camiller *et al.* [SAPHIR Collaboration], Phys. Lett. **B 572**, 127 (2003).

[8] H. Ejiri, http://www.spring8.or.jp/e/conference/appeal/proceedings/Theta+Spin.pdf.

[9] M. P. Rekalo and E. Tomasi-Gustafsson, arXiv:hep-ph/0401050.

[10] K. Nakayama and W. G. Love, Phys. Rev. C **70**, 012201 (2004).

[11] A. I. Titov, H. Ejiri, H. Haberzettl, and K. Nakayama, nucl-th/0410098.

[a]Advanced Photon Research Center, Japan Atomic Energy Research Institute, Kizu, Kyoto, 619-0215, Japan
[b]Bogoliubov Laboratory of Theoretical Physics, JINR, Dubna 141980, Russia
[c]Natural Science, International Christian University, Osawa, Mitaka, Tokyo, 181-8585, Japan
[d]Research Center for Nuclear Physics, Osaka University, Ibaraki, Osaka 567-0047, Japan
[e]Center for Nuclear Studies, Department of Physics, The George Washington University, Washington, DC 20052, USA
[f]Department of Physics and Astronomy, University of Georgia, Athens, GA 30602, USA

Consistent analysis of the reactions $\gamma p \to p\eta'$ and $pp \to pp\eta'$

K. Nakayama* and H. Haberzettl**

The production of η' mesons in the reactions $\gamma p \to p\eta'$ and $pp \to pp\eta'$ is described consistently within a relativistic meson exchange model of hadronic interactions. The photoproduction can be described quite well over the entire energy range of available data [1] by considering an S_{11} and a P_{11} resonance, in addition to the t-channel mesonic current. The observed angular distribution is due to the interference between the t-channel and the nucleon resonance s- and u-channel contributions. Our analysis yields positions close to 1650 MeV and 1870 MeV for the S_{11} and P_{11} resonances, respectively. We argue that, at present, identifying these states with the known $S_{11}(1650)$ resonance and the missing P_{11} resonance predicted at 1880 MeV, respectively, would be premature. It is found that the nucleonic current is relatively small and that the $NN\eta'$ coupling constant cannot be much larger than $g_{NN\eta'} = 3$. Currently, we are incorporating the new (preliminary) data from the CLAS collaboration [2] into our analysis.

As for the $pp \to pp\eta'$ reaction, different current contributions are constrained by a combined analysis of this and the photoproduction reaction. We found that it is difficut to describe simultaneously the 47-MeV and 144-MeV angular distributions measured by the COSY-11 [3] and DISTO [4] collaborations, respectively.

Details of our model as well as of the calculations can be found in Ref.[5].

References:

[1] R. Plötzke *et al.*, Phys. Lett. **B444**, 555 (1998); J. Barth *et al.*, Nucl. Phys. **A691**, 374c (2001).
[2] M. Dugger and B. R. Ritchie, private communication.
[3] A. Khoukaz *et al.*, Eur.Phys.J.**A20**, 345 (2004).
[4] F. Balestra *et al.*, Phys. Lett. **B491**, 29 (2000).
[5] K. Nakayama and H. Haberzettl, Phys. Rev. **C69**, 065212 (2004).

* Department of Physics and Astronomy, University of Georgia, Athens,GA 30602, USA
** Center for Nuclear Studies, Department of Physics, The George Washington University, Washington DC 20052, USA

Bounds on bound η^3He system

A. Sibirtsev, J. Haidenbauer, Ulf-G. Meißner*, J. Niskanen+

Recently our knowledge on the η^3He scattering length was revisited [1] via a systematic analysis of presently available data on the reaction $pd\to\eta^3$He. Since this quantity is closely related to the existence of bound states, it is natural to extend this study and to investigate in how far the limits deduced for the scattering length in Ref. [1] provide also constraints on the binding energy for the η^3He system. In particular, a phenomenological understanding of the relation between the scattering length and the depth of the binding and the width of the state would be valuable in planning possible experiments aimed for the direct observation of bound states. In this paper we present a calculation where both the depths and widths of the bound states together with the corresponding scattering length are interconnected in terms of complex potentials [2].

The η-nucleus optical potential is taken to be proportional to the density of the ^{3}He nucleus,

$$V=-\frac{4\pi}{2\mu_{\eta\mathrm{He}}}(V_R+iV_I)\rho(r), \tag{1}$$

for which the Gaussian form

$$\rho(r)=\frac{1}{(\sqrt{\pi}\alpha)^3}\,e^{-r^2/\alpha^2} \quad \text{with } \alpha=\sqrt{\frac{2}{3}}\,\langle r^2\rangle^{1/2} \tag{2}$$

corresponding to an rms radius 1.9 fm is adopted. Within the standard optical model calculations the strength parameters V_R and V_I were taken as thrice the elementary ηN scattering length adjusted with the ratio of the reduced masses of the η-nucleus system and the ηN system as

$$V_R+iV_I=3a_{\eta N}\,\frac{\mu_{\eta\mathrm{He}}}{\mu_{\eta N}}\,. \tag{3}$$

Here the sign definition of the scattering length is given by the standard effective range convention in meson physics

$$q\cot\delta=\frac{1}{a}+\frac{1}{2}r_0q^2+O(q^4)\,. \tag{4}$$

We should emphasize, however, that the present study is not an optical model calculation in the above narrow sense. Instead, here the strength parameters V_R and V_I are freely varied to study for which scattering lengths one might expect bound states to exist and with which energies. As a numerical check, the values of V_R=2.235 fm and V_I=1.219 fm yield the η^3He scattering length $a_{\eta\mathrm{He}}=-2.31+i2.57$ fm in agreement with the result of Ref. [3].

Fig. 1 shows our results for the η^3He binding energy B and width Γ as functions of the imaginary and real parts of the η^3He scattering length. The different symbols indicate our results for B and Γ of 1, 2, 4, 5, 10 and 20 MeV. The solid and dashed contours show our χ^2+1 solutions for the η^3He scattering length [1].

Presently there are no data or any solid arguments to prove that the real part of the η^3He scattering length actually is negative which is a necessary condition to have a bound η^3He system. But, to estimate the possible binding energy B and width Γ we select our solution for $a_{\eta\mathrm{He}}$ with a negative real part.

It may be noted that the result of our analysis [1] while taking $\Re a_{\eta\mathrm{He}}<0$ would be within the binding region as shown by

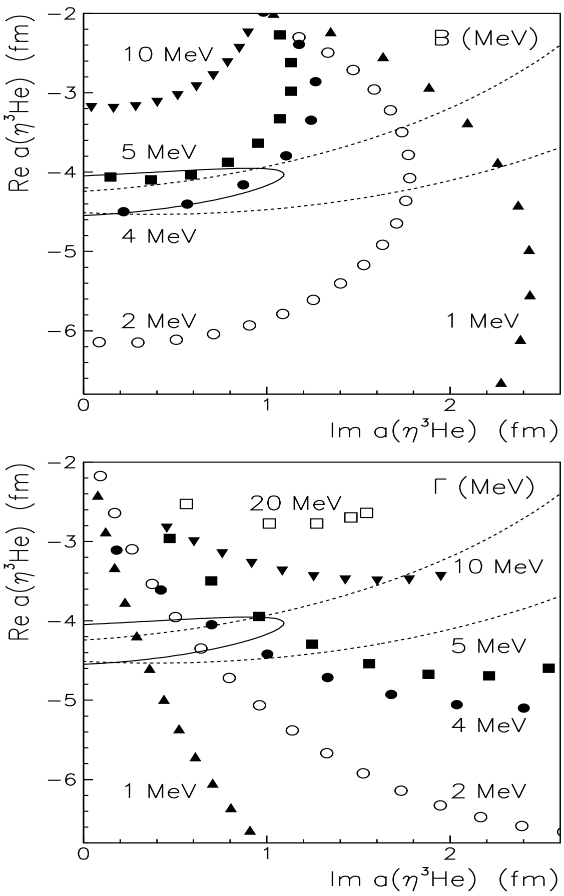

Fig. 1: The η^3He binding energy B (upper panel) and width Γ (lower panel) as functions of the imaginary and real parts of the η^3He scattering length. Results are presented for B and Γ of 1 MeV (triangles), 2 MeV (open circles), 4 MeV (close circles), 5 MeV (close squares), 10 MeV (inverse triangles) and 20 MeV (open squares). The solid and dashed contours show our χ^2+1 solutions for the η^3He scattering length [1].

the contour lines in Fig.1. In fact, the standard rectangular error limits [1] $a_{\eta^3\mathrm{He}}=(-4.3\pm0.3)+i(0.5\pm0.5)$ fm would suggest a bound state with the binding energy B=4.3±1.2 and width Γ=2.8±2.8 MeV. Taking our solution shown by the dashed lines in Fig.1 we deduce the limits for η^3He binding energy $B\leq5$ MeV and the width $\Gamma\leq10$ MeV.

References:

[1] A. Sibirtsev, J. Haidenbauer, C. Hanhart, and J. A. Niskanen, Eur. Phys. J. A **22**, 495 (2004).
[2] A. Sibirtsev et al., Phys. Rev. C **70**, 1 (2004).
[3] C. Wilkin, Phys. Rev. C. **47**, R938 (1993).

* also at: Universität Bonn, Helmholtz-Institut für Strahlen und Kernphysik, D-53115 Bonn, Germany
+ Department of Physical Sciences, PO Box 64, FIN-00014 University of Helsinki, Finland

Flatté-like distributions and the $a_0(980)/f_0(980)$ mesons

V. Baru*, J. Haidenbauer, C. Hanhart, A. Kudryavtsev*, Ulf-G. Meißner+

Usually to get information about the properties of the light scalar mesons $f_0(980)$ and $a_0(980)$ the so-called Flatté parametrization [1] for the differential mass distributions is used. This parametrization is a slightly modified relativistic version of the Breit-Wigner distribution. It reads, e.g., for the a_0 channel

$$\frac{d\sigma_i}{dm} \propto \left| \frac{m_R\sqrt{\Gamma_{\pi\eta}\Gamma_i}}{m_R^2 - m^2 - im_R(\Gamma_{\pi\eta} + \Gamma_{K\bar{K}})} \right|^2, \tag{1}$$

with the partial widths $\Gamma_{\pi\eta} = \bar{g}_\eta q_\eta$ and $\Gamma_{K\bar{K}} = \bar{g}_K\sqrt{m^2/4 - m_K^2}$ above threshold and $\Gamma_{K\bar{K}} = i\bar{g}_K\sqrt{m_K^2 - m^2/4}$ below threshold, respectively. The subscript i in Eq. (1) labels the $\pi\eta$ and/or $K\bar{K}$ channels. Furthermore, m_R is the nominal mass of the resonance, m is the invariant mass ($m^2 = s$) and q_η is the corresponding center-of-mass momentum in the $\pi\eta$ system. $\bar{g}_\eta$ and $\bar{g}_K$ are dimensionless coupling constants [2].

Despite of the wealth of available experimental data concerning the $f_0(980)$ and $a_0(980)$ resonances there are still large uncertainties in the parameters extracted for both resonances. The compilation of results for the a_0 meson, presented in Ref. [2], clearly demonstrates that the resulting absolute values of $\bar{g}_\eta$ ($\Gamma_{\pi\eta}$) and $\bar{g}_K$ differ significantly for different analyses. At the same time it also reveals that the ratios of the coupling constants, $R = \bar{g}_K/\bar{g}_\eta$, are more or less consistent with each other for practically all the parameter sets extracted from the experimental data. For the $f_0(980)$ meson the situation is very similar for most of the results compiled in Ref. [2].

In the present paper we investigate the features of Flatté or Flatté-like parametrizations. Specifically, we demonstrate that the relative stability for the ratio R and the large variations in the absolute values of the coupling constants and masses, evidenced by the different analyses in the literature, can be understood. It is simply a consequence of a specific scaling behaviour of the Flatté amplitude for energies near the $K\bar{K}$ threshold.

For energies near the $K\bar{K}$ threshold the resonance part of the elastic scattering amplitude for the channel with the light particles ($\pi\eta$ for the $a_0(980)$ case or $\pi\pi$ for the $f_0(980)$ meson) can be written in a nonrelativistic form by

$$f_{el} = -\frac{1}{2q}\frac{\Gamma_P}{E - E_{BW} + i\frac{\Gamma_P}{2} + i\bar{g}_K\frac{k}{2}} . \tag{2}$$

This nonrelativistic expression can be derived starting out both from the relativistic Flatté formula (see Ref. [2]) and from the Flatté-like distributions like the one introduced by Achasov (see Ref. [2] for more details). Here we use the notation $\Gamma_P = q\bar{g}_P$ for the inelastic width, where P stands for the $\pi\eta$ or $\pi\pi$ channels and q is the corresponding center-of-mass momentum. The energies are defined with respect to the $K\bar{K}$ threshold, i.e.

$$E = \sqrt{s} - 2m_K, \quad m_R = 2m_K + E_R, \tag{3}$$

where $m_K = (m_{K^+} + m_{K_0})/2$ and m_R is the nominal mass of the resonance. The parameter E_{BW}, which would correspond to the peak position of the standard nonrelativistic Breit-Wigner (BW) resonance, i.e. in the limit $\bar{g}_K \to 0$, is defined as $E_{BW} = E_R$ for the Flatté distribution. In addition the relative $K\bar{K}$ momentum, k, that also appears in Eq. (2), is given by $k = \sqrt{m_K E}$. Note that k is imaginary for $E < 0$, i.e. for $\sqrt{s} < 2m_K$.

We consider here the case of elastic scattering in the resonance approximation corresponding to Eq. (2), i.e. without any background contributions. Then, for $E > 0$ the elastic cross section is given by

$$\sigma_{el} = 4\pi|f_{el}|^2 = \frac{\pi\bar{g}_P^2}{(E - E_{BW})^2 + (\Gamma_P + \bar{g}_K k)^2/4} . \tag{4}$$

For $E < 0$ we get

$$\sigma_{el} = \frac{\pi\bar{g}_P^2}{(E - E_{BW} - \kappa\bar{g}_K/2)^2 + \Gamma_P^2/4} , \tag{5}$$

where $\kappa = \sqrt{m_K|E|}$ is the modulus of the imaginary $K\bar{K}$ momentum k. In the vicinity of the $K\bar{K}$ threshold we may omit E in Eqs. (4) and (5) which leads us to the following approximate expressions for the cross section valid near the $K\bar{K}$ threshold

$$\begin{aligned} \sigma_{el} &= \frac{4\pi}{q^2}\frac{1}{\alpha^2 + (1 + Rk/q)^2}, \ E > 0 , \\ \sigma_{el} &= \frac{4\pi}{q^2}\frac{1}{(\alpha + R\kappa/q)^2 + 1}, \ E < 0 , \end{aligned} \tag{6}$$

where $\alpha = 2E_{BW}/\Gamma_P$ and $R = \bar{g}_K/\bar{g}_P$.

We see that in the approximation (6) the cross section does not depend on all three Flatté parameters, E_{BW} and the coupling constants $\bar{g}_P$ and $\bar{g}_K$, but only on the ratios R and α. Neglecting terms which are of higher order than k (κ) we get from Eqs. (6)

$$\sigma_{el} = \frac{4\pi}{q^2}\frac{1}{1 + \alpha^2}X, \tag{7}$$

where

$$X = 1 - \frac{2R}{1 + \alpha^2}\frac{k}{q} \ \text{ for } \mathrm{E} > 0,$$

and

$$X = 1 - \frac{2R\alpha}{1 + \alpha^2}\frac{\kappa}{q} \ \text{ for } \mathrm{E} < 0.$$

Obviously the right and the left slopes (with respect to k (κ)) of the elastic cross section at the $K\bar{K}$ threshold are given only in terms of the ratios R and α. Note that the sign of the slope $d\sigma/d\kappa$ for $E < 0$ depends on the sign of E_{BW} (α), whereas the slope $d\sigma/dk$ for $E > 0$ is always negative. Thus, the near-threshold momentum dependence of the invariant mass spectrum allows to determine both parameters R and α unambiguously from data – but clearly not all three parameters of the Flatté parametrization (1).

References:

[1] S. Flatté, Phys. Lett. **63B**, 224 (1976).
[2] V.Baru et al., nucl-th/0410099, Eur. Phys J. A, in press.

* ITEP, 117259, B. Cheremushkinskaya 25, Moscow, Russia
+ also at: Universität Bonn, Helmholtz-Institut für Strahlen und Kernphysik, D-53115 Bonn, Germany

Spectrum and decays of kaonic hydrogen

Ulf-G. Meißner*, Udit Raha (Bonn), Akaki Rusetsky (Bonn)

The ongoing DEAR experiment at the DAΦNE facility (LNF-INFN) aims at an accurate measurement of the ground-state strong energy shift and width of kaonic hydrogen, and the strong shift of kaonic deuterium. Preliminary results of the measurements for the kaonic hydrogen have been reported in Ref. [1], $\Delta E_1^s = 202 \pm 45$ eV, $\Gamma_1 = 250 \pm 138$ eV. Here, ΔE_1^s stands for the strong-energy-level shift of the ground state of the kaonic hydrogen (total energy shift minus certain electromagnetic contributions), and Γ_1 denotes the width of the ground-state. It should be pointed out that these results are in contradiction with the earlier measurements, see the figure. The final goal of the DEAR experiment is to extract precise values of the KN S-wave scattering lengths from the data by using some counterpart of Deser-type relations. Neglecting isospin-breaking corrections altogether, in the case of kaonic hydrogen these relations are given by

$$\Delta E_1^s - i\,\Gamma_1/2 = -2\alpha^3\mu_c^2\,a_{K^-p}\,, \tag{1}$$

with $a_{K^-p} = (a_0 + a_1)/2$, where μ_c denotes the reduced mass of the K^-p system, and a_0, a_1 stand for the $I = 0, 1$ S-wave KN scattering lengths in QCD in the isospin limit ($\alpha = 0$, $m_d = m_u$). In addition, our definition of the isospin limit implies that the particle masses in the multiplets are taken equal to the charged particle masses in the real world (proton, π^+, $K^+, \cdots$). Further, in the experimental proposal it has been stated that the precise knowledge of the KN scattering lengths could allow one to deduce more accurate values for the KN σ-terms and the strangeness content of the nucleon. In practice, however, the implementation of the above program might pose a rather big challenge to theory. For this reason, in this paper we restrict ourselves to the moderate goal of relating the KN scattering lengths to the measurable characteristics of kaonic hydrogen at the accuracy that matches the experimental precision. Using these scattering lengths for determining the parameters of the low-energy kaon-nucleon interactions is thus out of the scope of the present paper. In [2] we derived the formal expression for the strong shifts of the energy levels in kaonic hydrogen in QCD, up-to-and-including $O(\delta^4)$ in the isospin breaking parameter $\delta \sim \alpha, m_d - m_u$. The use of the non-relativistic effective Lagrangian approach allows one to treat that otherwise extremely complicated problem with a surprising ease. We discover that large isospin-breaking corrections arise, in particular, due to the following sources: (a) s-channel rescattering with the $\bar K^0 n$ intermediate state (cusp effect), and (b) Coulomb corrections that are non-analytic in α. We further prove that the remaining corrections are analytic in δ at $O(\delta)$. Examining some of these corrections, on the other hand, we do not find a big effect – the obtained values are at the percent level, which one expects to be a typical size of isospin breaking in QCD. The present status of corrections in kaonic hydrogen can be summarized by the modified Deser-formula

$$\begin{aligned}\Delta E_n^s - \frac{i}{2}\,\Gamma_n &= -\frac{\alpha^3\mu_c^3}{2\pi M_{K^+}n^3}\,(\mathcal{T}_{KN}^{(0)} + \delta\mathcal{T}_{KN})\,\times \\ &\times\;\left\{1 - \frac{\alpha\mu_c^2 s_n(\alpha)}{4\pi M_{K^+}}\,\mathcal{T}_{KN}^{(0)} + \delta_n^{\rm vac}\right\}\end{aligned} \tag{2}$$

where $\mathcal{T}_{KN}^{(0)}$, $\delta\mathcal{T}_{KN}$ are given by

$$\begin{aligned}\mathcal{T}_{KN} &= \mathcal{T}_{KN}^{(0)} + \frac{i\alpha\mu_c^2}{2M_{K^+}}\,(\mathcal{T}_{KN}^{(0)})^2 + \delta\mathcal{T}_{KN} + O(\delta)\,, \\ \mathcal{T}_{KN}^{(0)} &= 4\pi\left(1 + \frac{M_{K^+}}{m_p}\right)\frac{\frac{1}{2}\,(a_0 + a_1) + q_0 a_0 a_1}{1 + \frac{q_0}{2}\,(a_0 + a_1)}\end{aligned} \tag{3}$$

and $\delta\mathcal{T}_{KN} = O(\delta)$. This is the final formula, which is best suited for the analysis of the experimental data. Instead of the combination $\frac{1}{2}\,(a_0 + a_1)$ which enters in the original Deser formula, we propose to focus on the extraction of the quantity $\mathcal{T}_{KN}^{(0)}$ from the experimental data. The reason for this is that $\mathcal{T}_{KN}^{(0)}$ already includes the dominant non-analytic corrections in a parameter-free form. The remaining analytic corrections at $O(\delta)$ are contained in the quantities $\delta\mathcal{T}_{KN}$ and $\delta_n^{\rm vac}$. The evaluation of $\delta\mathcal{T}_{KN}$ within ChPT could be interesting, but possibly complicated due to the expansion in the strange quark mass. At the present stage, in the absence of such calculations, the best is to include $\delta\mathcal{T}_{KN}$ in the estimate of the systematic error. From the above discussion one may hope that the effect from $\delta\mathcal{T}_{KN}$ should not exceed a few percent, which is a natural size of electromagnetic corrections. For a comparison of the DEAR data with predictions derived from the analysis of KN scattering data see the figure.

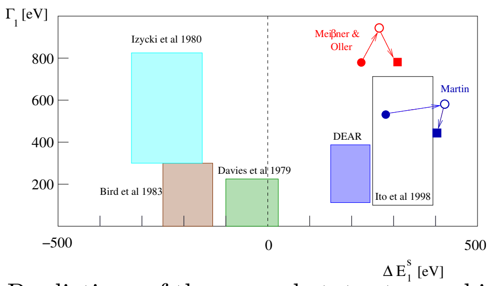

Fig. 1: Predictions of the ground-state strong shift ΔE_1^s and width Γ_1. Filled circles correspond to using the Deser formula (1), empty circles to using $\mathcal{T}_{KN}^{(0)}$ instead of $(a_0 + a_1)/2$ in this formula, and filled boxes to our final formula (2) with $\delta\mathcal{T}_{KN} = \delta_n^{\rm vac} = 0$

References:

[1] M. Cargnelli *et al.* (DEAR Collaboration), in Proceedings of "HadAtom03" Workshop, 13-17 October 2003, ECT* (Trento, Italy), [hep-ph/0401204].

[2] U.-G. Meißner, U. Raha and A. Rusetsky, Eur. Phys. J. C **35** (2004) 349 [hep-ph/0402261].

*Also at HISKP, Universität Bonn

Partial-wave analysis for $\vec{p}\vec{p} \to pp\pi^\circ$

P. N. Deepak, J. Haidenbauer, and C. Hanhart

We present here a first step towards a full partial-wave decomposition of the reaction $pp \to pp\pi 0$, using as input only the data from the recent IUCF measurement [1]. We compare the extracted amplitudes to those from a meson exchange model [2].

Ignoring the participation of any D-waves in the final state, as in [1], a set of 12 partial-wave amplitudes participate in the reaction, given explicitly, in table IV of Meyer et al. [1]. Thus there are a priori 24 real unknowns (12 complex amplitudes). However, as overall phases are unobservable and the final-NN-state channel-spins do not mix with each other in any of the spin-observables measured in [1], we choose the first two amplitudes in table IV of [1] to be real. This leaves 22 real numbers to be determined. Using Eqs. (2) and (17) of [3], explicit partial-wave expansions for all the observables defined in [1], including the unpolarized differential cross section, were obtained, which immediately leads to the partial-wave decomposition of the coefficients E, F_k, G_k^{ij} and H_k^{ij}, defined in [1], which are bilinear in the partial-wave amplitudes. We need to mention here that the partial-wave amplitudes defined by us are obtained by multiplying the ones given in [3] by a factor, $(4\pi)^3(\mathrm{i})^{l-l_q-l_p}$. Note, however, that all the values given in table IV of [1] for the various coefficients are integrated with respect to the outgoing two nucleon (relative) kinetic energy, ϵ. The coefficients E, F_k, G_k^{ij} and H_k^{ij} are thus expressed in terms of numerous I_{mn} given by (using non-relativistic kinematics)

$$I_{mn}(E_{\rm cm}) = \int_0^{\epsilon_{\rm max}} T_m(E_{\rm cm},\epsilon)\, T_n^*(E_{\rm cm},\epsilon)\, q\, p\, \mathrm{d}\epsilon,$$

with $m,n = 2,\ldots,12$, T_κ, $\kappa = 1,\ldots,12$ corresponding to the κth partial-wave amplitude in table IV of [1], in that order and $E_{\rm cm}$, q, p denote respectively the total energy, the magnitudes of the momenta of the pion and the final-NN-system, in c. m. We now need to make an assumption regarding the ϵ-dependence of the T_κ, to proceed further. In principle one could use dispersion integrals to relate the phase motion and energy dependence of the T_κ to the energy dependence of elastic-pp-scattering phase shifts. However, in this first analysis we use a simplified ansatz, namely $T_\kappa(E_{\rm cm},\epsilon) \propto q^{l_q(\kappa)} p^{l_p(\kappa)}$, which should hold as long as the outgoing momenta are small compared to the inverse of the production radius. This assumption was also used in the fitting procedure of [1] in order to determine some of the coefficients E, F_k, G_k^{ij} and H_k^{ij} from the data, for the statistical accuracy of the data did not allow for a separate fit of these coefficients at each energy. From the above ansatz, one easily derives $I_{mn}(E_{\rm cm}) = z_m\, z_n^*\, \eta^x$, with x respectively equal to 6,7 and 8 for $PsPs$, $PsPp$ and $PpPp$ interfering terms. Here $\eta = q_{\rm max}/m_\pi$, with $q_{\rm max}$ being the largest possible value of pion momentum for a given incident energy, m_π is the pion mass and z_m, z_n are complex quantities (energy-independent by assumption) to be determined from the data. Since T_1 does not interfere with any of the other partial-waves and since its final-state-interaction does not show a power-law behaviour, we parametrize it as $I_{11}(E) = \int_0^{\epsilon_{\rm max}} |T_1(E_{\rm cm},\epsilon)|^2\, q\, p\, \mathrm{d}\epsilon = |z_1|^2$ and extract it at each of the four bombarding energies individually. These assumptions lead us to 117 equations with 21 real unknowns (since z_2 is assumed to be real). Since we know the explicit dependence of E on z_1, with z_1 being real, it is directly determined (up to a sign). The errors in the z_i, $i = 2,\ldots,12$ were determined using the method outlined in [4]. The uncertainty in z_1, is determined by that in E. The solutions were obtained by $\chi 2$-minimization and the $\chi 2$ per degree of freedom obtained was 1.7. A comparison of the obtained values for $|z_i|$, made with the model predictions [2], is shown in Fig. 1. We see that a majority of the partial-wave amplitudes are reproduced even quantitatively (if one takes into account the error bars of the partial-wave analysis). But a serious discrepancy occurs in the amplitude z_9 and to a lesser extent also in z_{12}. This discrepancy and its connection with the dynamical ingredients of the model need to be explored in the future. Considerable deviations also in the amplitudes z_{13} and especially in z_{14}, which correspond to D-waves in the final state, indicate that these amplitudes might not be negligible, as assumed in [1] and need to be taken into account in any future analysis of the reaction $pp \to pp\pi 0$. Further, the figure suggests also that Δ degrees of freedom have to be taken into account explicitly in any model that aims at a quantitative description of the reaction $pp \to pp\pi 0$.

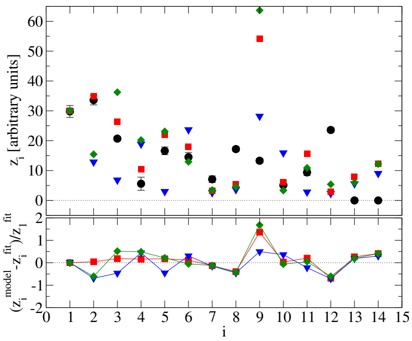

Fig. 1: Comparison of the extracted $|z_i|$ (black circles) with corresponding predictions of the Jülich model [2]; the squares (inverted triangles) refer to model-results with inclusion (omission) of the Δ isobar. For the diamonds only Δ excitations before the pion emission are included. The upper panel shows the results for the various amplitudes, normalized to the s-wave and the lower panel shows the relative deviations from the extracted values.

References:

[1] H. O. Meyer et al., Phys. Rev. C **65**, 027601 (2001).
[2] C. Hanhart, J. Haidenbauer, O. Krehl and J. Speth, Phys. Lett. B **444**, 25 (1998).
[3] G. Ramachandran, P. N. Deepak and M. S. Vidya, Phys. Rev. C **62**, 011001(R) (2000).
[4] K. H. Burrell, Am. J. Phys. **58** (2), 160 (1990).

ω Production in pp Collisions

P.N. Deepak, G. Ramachandran,* M.S. Vidya,† J. Balasubramanyam,‡ Venkataraya§

The experimental study of meson production in NN collisions has attracted considerable interest during the last decade and a half. At c.m. energies close to threshold, the relative kinetic energies between the particles in the final state are small and an analysis involves, therefore, only a few partial waves. On the other hand, a large momentum transfer is involved when an additional particle is produced in the final state in the NN collision, thus making the reaction sensitive to the features of the NN interaction at short distances, where the nucleons start to overlap. Unlike the pion which is spinless, production of a heavy meson like ω which has spin 1 permits us to make observations with regard to its spin state also apart from measuring the angular distributions in polarized beam and polarized target experiments. Experimental data on total [1] and differential [2] cross-sections for $pp \to pp\omega$ have already been published and proposals are underway [3] to study heavy meson production in NN collisions using polarized beams and targets at COSY.

The purpose of the present paper is to extend the earlier work [4] on the model independent approach based on irreducible tensor techniques to include final states containing mesons with non-zero spin (like ω) and also to study the spin state of the meson in $pp \to pp\vec{\omega}$.

Let $\boldsymbol{p}_i$ denote the initial c.m. momentum, $\boldsymbol{q}$ the momentum of the meson produced with spin parity s^π and $\boldsymbol{p}_f$, the relative momentum, $(1/2)(\boldsymbol{p}_1 - \boldsymbol{p}_2)$ between the two nucleons with c.m. momenta $\boldsymbol{p}_1$ and $\boldsymbol{p}_2$ in the final state. The double differential cross section for meson production in c.m. may be written as $(\mathrm{d}^2\sigma)/(\mathrm{d}^3p_f\mathrm{d}\Omega) = (2\pi D v^{-1})\mathrm{Tr}(\boldsymbol{T}\rho^i\boldsymbol{T}^\dagger)$, where D denotes the final three particle density of states, $\boldsymbol{T}$ denotes the on-energy-shell transition matrix and $\boldsymbol{T}^\dagger$ its hermitian conjugate, $v = 4|\boldsymbol{p}_i|/E$ at c.m energy E and ρ^i denotes the initial spin density matrix, $\rho^i = \frac{1}{4}(1 + \boldsymbol{\sigma}_1 \cdot \boldsymbol{P})(1 + \boldsymbol{\sigma}_2 \cdot \boldsymbol{Q})$, if $\boldsymbol{P}$ and $\boldsymbol{Q}$ denote respectively the beam and target polarizations. If s_i and s_f denote the initial and final spin states of the NN system, the initial and final channel spins for the reaction are s_i and S respectively, where S can assume values $S = |s_f - s|, \ldots (s_f + s)$. Making use of the irreducible tensor operator techniques introduced in [5], we may express $\boldsymbol{T}$ in the operator form

$$\boldsymbol{T} = \sum_\alpha \sum_{\lambda=|s_f-s_i|}^{(s_f+s_i)} \sum_{\Lambda=|S-s_i|}^{(S+s_i)} (S^s(s,0) \otimes S^\lambda(s_f,s_i))^\Lambda \cdot \mathcal{T}^\Lambda(\alpha,\lambda)), \qquad (1)$$

where $\alpha = (S, s_f, s_i)$ denotes collectively the spin variables. The irreducible tensor amplitudes $\mathcal{T}^\Lambda_\nu(\alpha,\lambda)$ of rank Λ, which characterize the reaction, are given by

$$\mathcal{T}^\Lambda_\nu(\alpha,\lambda) = W(ss_f\Lambda s_i; S\lambda)[\lambda] \sum_\beta \sum_j W(s_i l_i SL; j\Lambda) \times T^j_{\alpha,\beta}((Y_l(\hat{\boldsymbol{q}}) \otimes Y_{l_f}(\hat{\boldsymbol{p}}_f))^L \otimes Y_{l_i}(\hat{\boldsymbol{p}}_i))^\Lambda_\nu, \qquad (2)$$

in terms of the partial wave amplitudes $T^j_{\alpha,\beta}$ which depend on c.m. energy E, the invariant mass W of the final NN system, total angular momentum j, apart from α and $\beta = (l, l_f, L, l_i)$ which denotes collectively the orbital angular momentum l of the emitted meson, the initial and final relative orbital angular momenta l_i and l_f of the NN system and the total orbital angular momentum L in the final state, which takes values $L = |l_f - l|, \ldots, (l_f + l)$. The notation $[\lambda] = \sqrt{2\lambda+1}$ is used apart from standard notations [6]. If I_i and I_f denote respectively the initial and final isospin quantum numbers of the NN system, Pauli exclusion principle and parity conservation restrict the summations to terms satisfying $(-1)^{l_i+s_i+I_i} = -1 = (-1)^{l_f+s_f+I_f}$ and $(-1)^{l_i} = \pi\,(-1)^{l_f+l}$, where π denotes the intrinsic parity of the meson.

We may characterize the state of polarization of the ω meson in $pp \to pp\vec{\omega}$ by the density matrix ρ^s, in the standard form $\rho^s = (2s+1)^{-1}\sum_{k=0}^{2s}(\tau^k \cdot t^k)$, noting that $\tau^k_\nu \equiv S^k_\nu(s,s)$. It can be shown, using standard spin-algebra, that the Fano statistical tensors t^k_ν are given by

$$t^k_\nu = \frac{2\pi D}{v}\frac{1}{4} \sum_{\alpha,\alpha',\lambda,\Lambda,\Lambda'} (-1)^{\lambda-s}\delta_{s_is_i'}\delta_{s_fs_f'}[s_f]^2[s]^3[\Lambda][\Lambda'] \times W(s\Lambda s\Lambda';\lambda k)(\mathcal{T}^\Lambda(\alpha,\lambda) \otimes \mathcal{T}^{\dagger\Lambda'}(\alpha',\lambda))^k_\nu, \qquad (3)$$

at the double differential level. The vector and tensor polarizations of ω (with $s = 1$) are readily obtained by setting $k = 1, 2$ respectively in (3). Further details, including those for the determination of the channel-spin cross sections, which are not given here due to lack of space, can be found in our preprint [7].

References:

[1] F. Hibou *et al.*, Phys. Rev. Lett. **83**, 492 (1999).

[2] S. Abd El-Samad *et al.*, Phys. Lett. **B 522**, 16 (2001).

[3] P. Moskal *et al.*, Prog. Part. Nucl. Phys. **49**, 1 (2002); C. Hanhart, Phys. Rep. **397**, 155 (2004); F. Rathmann *et al.*, Study of Heavy Meson production in NN collisions with polarized Beam and Target, Letter of Intent to COSY-PAC No. 81 (Jülich 1999); F. Rathmann *et al.*, Czech. J. Phys. **52**, Suppl. A (2002)

[4] G. Ramachandran, P.N. Deepak and M.S. Vidya, Phys. Rev. C **62**, 011001(R) (2000); G. Ramachandran and P.N. Deepak, Phys. Rev. C **63**, 051001(R) (2001).

[5] G. Ramachandran and M.S. Vidya , Phys. Rev. C **56**, R12 (1997).

[6] M.E. Rose, *Elementary theory of angular momentum* (Wiley, New York, 1957).

[7] G. Ramachandran *et al.*, *nucl-th/0501001.*

*Indian Institute of Astrophysics, Koramangala, Bangalore, 560034, India

†School of Physical Sciences, JNU, New Delhi, 110067, India

‡K. S. Institute of Technology, Bangalore, 560062, India

§Vijaya College, Bangalore, 560011, India

Infrared regularization for spin-1 fields

P.C. Bruns (Bonn), Ulf-G. Meißner*

Chiral perturbation theory (CHPT) is the effective field theory of the Standard Model at low energy. It is based on the spontaneously broken approximate chiral symmetry of QCD. The pions, kaons and the eta can be identified with the Goldstone bosons of chiral symmetry breaking. Their interactions are weak and vanish in the chiral limit of zero quark masses when the energy goes to zero. This is a consequence of Goldstone's theorem and allows for a consistent power counting. It is, however, known since long that vector and axial-vector mesons also play an important role in low energy hadron physics, as one example we mention the fairly successful description of the pion charge form factor in terms of the (extended) vector dominance approach (for more details, see e.g. the review [1]). These heavy degrees of freedom decouple in the chiral limit and at low energy from the Goldstone bosons. Nevertheless, they leave their imprint in the low-energy effective field theory of QCD by saturating the low-energy constants, which has been termed resonance saturation [2]. In [3] we are interested in an extension of CHPT where these spin-1 fields (vector and axial-vector mesons) are accounted for explicitly. We have presented an extension of the infrared regularization scheme originally developed for baryon chiral perturbation theory. The pertinent results of this investigation can be summarized as follows:

1) The most economic way to deal with vector mesons in chiral perturbation theory is to utilize the antisymmetric tensor field formulation as stressed in [2]. When vector mesons appear in tree graphs only, calculations are straightforward. Of course, other formulations like the vector field approach can also be used, the equivalence between the various schemes can be proven utilizing different methods.

2) When vector mesons appear in loops, the appearance of the large mass scale complicates the power counting, as it is also known from the inclusion of baryons in CHPT. In essence, loop diagrams pick up large contributions when the loop momentum is close to the vector meson mass. To the contrary, the contribution from the soft poles (momenta of the order of the pion mass) that leads to the interesting chiral terms of the low-energy EFT (chiral logs and alike) obeys power counting.

3) The standard case of infrared regularization [4] applies to graphs were the heavy particle line runs through the Feynman graph under consideration. For these cases a very elegant splitting of a Feynman parameter integral allows to unambigouosly separate the infrared singular from the regular part.

4) In the case of spin-1 fields, new classes of self-energy graphs appear. The case for lines with small external momenta but a vector meson line appearing inside the diagram in analyzed in [3] and the singularity structure of the corresponding integrals is discussed. The infrared singular part for such types of integrals is explicitly constructed. As examples, the Goldstone boson self-energy and the triangle diagram are worked out.

5) A different type of one-loop graphs appears in the vector meson self-energy, where only light particles (Goldstone bosons) run in the loop. Also for this case, the the corresponding infrared singular part is extracted, see [3], and the contribution to the vector meson mass is worked out. We briefly discuss the problems related to the imaginary part of such type of diagrams.

6) As an application, the pion mass dependence of the ρ-meson mass is considered. it is shown that there are many contributions with unknown low-energy constants, still one is able to derive a compact formula for $M_\rho(M_\pi)$. We analyze existing lattice data and conclude that the ρ-meson mass in the chiral limit is bounded between 650 and 800 MeV. We have also discussed the $\pi\rho$ sigma term.

The methods outlined here can be applied to many interesting problems, for example one could systematically analyze vector meson effects on Goldstone properties like form factors or polarizabilities or extend these considerations to systems including baryons (for a first step see e.g. [5]).

References:

[1] U.-G. Meißner, Phys. Rept. **161** (1988) 213.
[2] G. Ecker, J. Gasser, A. Pich and E. de Rafael, Nucl. Phys. B **321** (1989) 311.
[3] P. C. Bruns and U.-G. Meißner, `[hep-ph/0411223]`.
[4] T. Becher and H. Leutwyler, Eur. Phys. J. C **9** (1999) 643 `[hep-ph/9901384]`.
[5] B. Borasoy and U.-G. Meißner, Int. J. Mod. Phys. A **11**, 5183 (1996) `[hep-ph/9511320]`.

*Also at HISKP, Universität Bonn

Orthonormalization procedure for chiral effective nuclear field theory

V. Bernard (ULP Strasbourg), H. Krebs (Bonn), Ulf-G. Meißner*

Effective field theory methods applied to few-nucleon systems have become a powerful tool to establish a systematic and precise formulation of nuclear physics consistent with the symmetries of QCD, in particular its spontaneously and explicitly broken chiral symmetry. The field was initiated by a series of papers of Weinberg [1, 2, 3] and has matured considerably. Recently, two-nucleon dynamics based on effective field theory (EFT) with explicit pions (we do not consider the so-called pionless EFT in this work.) has been worked out at next-to-next-to-next-to-leading order (NNNLO), see [4, 5] (note, however, that only in [5] a detailed analysis of the theoretical uncertainties at this order is given as it is required for any sensible EFT analysis.). Due to the appearance of shallow bound states a purely perturbative treatment like in chiral perturbation theory for systems with pions or with one nucleon is inappropriate. However, as stressed already by Weinberg, one can apply the power counting in the construction of the so-called effective potential. Through iteration of this effective potential one obtains the full physical scattering amplitude. In the case of nucleon-nucleon scattering, it was shown in [1] that the power counting is violated if one considers diagrams containing two-nucleon intermediate states. From that, the simplest definition of the effective potential can be given as follows: the effective potential is the sum of all time-ordered diagrams which contain in each intermediate state at least one pion. No violation of the power counting appears on the level of the effective potential, thus it can be constructed perturbatively in terms of the usual small parameters q/Λ_χ and M_π/Λ_χ, with q a generic external momentum, M_π the pion mass and $\Lambda_\chi \simeq 1\,\text{GeV}$ the scale of chiral symmetry breaking. The extension of these arguments to pion production or the inclusion of the $\Delta(1232)$ is straightforward if one takes into account the new scales appearing in these cases (see e.g. [6]). We will not consider such extensions here specifically, although our formalism is general enough to include these. Once the effective potential is constructed to a given order in the chiral expansion, the full T-matrix generating the bound and scattering states can be calculated by solving the Lippmann-Schwinger equation, $T = V_{\text{eff}} + V_{\text{eff}} G_0 T$, with G_0 the two-nucleon propagator. Even though this definition of the effective potential is very simple, one encounters some disadvantages. The potential is energy-dependent and not hermitean. This makes it difficult to apply it to scattering processes involving more than two nucleons. A solution to this problem was given by Epelbaum and collaborators [7], who showed that the method of unitary transformations developed by Fukuda, Sawada and Taketani [8] and by Okubo [9] can be applied to generate an energy-independent and hermitean potential consistent with the power counting of chiral perturbation theory (the effective potential). While this method is quite powerful, it suffers from the disadvantage that for different processes one has to define different model spaces and each time to construct the operator A, which parameterizes the corresponding unitary transformation, and to deduce the resulting hermitean effective Hamiltonian. We propose here another scheme based on the $\hat{Q}$-box expansion of Kuo and collaborators [10, 11]. The main results of this study [13] are:

i) We have shown that the $\hat{Q}$-box expansion respects the chiral expansion: only a finite number of $\hat{Q}$-boxes contribute to the effective potential at a given chiral order.

ii) We have constructed an explicit algorithm that allows one to construct the effective potential for any process involving nucleons, pions and photons (or other external sources) to a given order in the chiral expansion.

iii) We have shown for various examples that when one requires the on-shell condition to the asymptotic states, one recovers the expressions based on time-ordered perturbation theory, as it should be.

iv) An explicit application of the method developed here is the calculation of the fourth-order corrections to the three-body contributions in neutral pion electroproduction off the deuteron, see [12].

References:

[1] S. Weinberg, Phys. Lett. B **251** (1990) 288.
[2] S. Weinberg, Nucl. Phys. B **363** (1991) 3.
[3] S. Weinberg, Phys. Lett. B **295** (1992) 114 [hep-ph/9209257].
[4] D. R. Entem and R. Machleidt, Phys. Rev. C **68** (2003) 041001 [nucl-th/0304018].
[5] E. Epelbaum, W. Glöckle and U.-G. Meißner, [nucl-th/0405048], accepted for publication in Nucl. Phys. A.
[6] C. Hanhart, Phys. Rept. **397** (2004) 155 [hep-ph/0311341].
[7] E. Epelbaoum, W. Glöckle, Ulf-G. Meißner, Nucl. Phys. A **637** (1998) 107 [nucl-th/9801064].
[8] N. Fukuda, K. Sawada, M. Taketani, Prog. Theor. Phys. **12** (1954) 79
[9] S. Okubo, Prog. Theor. Phys. **12** (1954) 603
[10] T.T.S Kuo, S. Y. Lee, K. F. Ratcliff, Nucl. Phys. A **176** (1971) 65
[11] G. Li, K. K. Ng, T. T. S. Kuo, Phys. Rev. C **25** (1982) 2877
[12] H. Krebs, V. Bernard and U.-G. Meißner, Eur. Phys. J. A **22** (2004) 503 [nucl-th/0405006].
[13] H. Krebs, V. Bernard and U.-G. Meißner, [nucl-th/0407078], accepted for publication in Annals Phys. .

*Also at HISKP, Universität Bonn

Baryon masses in cut-off regularized chiral perturbation theory and application to lattice results

Matthias Frink, Ulf-G. Meißner*, Ilka Scheller (Bonn)

The nucleon mass as a function of the pion mass in comparison to lattice data from CP-PACS and UKQCD was studied in [1]. In that paper, a detailed discussion of cut-off regularization (CR) and dimensional regularization (DR) was also given. In the work [2], we have extended such studies to the three-flavor case. The baryon masses have been worked out to fourth order in the chiral expansion using CR, extending and complementing earlier work [3, 4]. We work in the isospin limit $m_u = m_d$ and thus consider four different states, the nucleon (N), the lambda (Λ), the sigma (Σ) and the cascade (Ξ) particle. As in the SU(2) case, the leading one-loop representation that leads to the time-honoured non-analytic mass shift $\sim M_P^3$ ($P \in \{\pi, K, \eta\}$) can only be used to consider Goldstone boson masses below 300 MeV, compare the dashed line in Fig. 1. This can also be seen when one plots the nucleon mass as a function of the cut-off Λ, only for such small pion masses one develops a stable plateau below the chiral symmetry breaking scale (that means independence of the cut-off as remanded by renormalization group arguments). To achieve a better accuracy, one can add an improvement term which is formally of fourth order and use its low-energy constant to cancel the leading cut-off dependence $\sim M_P^4/\Lambda$. In the two-flavor case, this procedure is straightforward. In the three flavor case, it is more subtle since for a given baryon B this operator consists of three terms $\alpha_1 M_\pi^4 + \alpha_2 M_\pi^2 M_K^2 + \alpha_3 M_K^4$ (using the GMO relation to eliminate terms $\sim M_\eta$), and the α_i are combinations of the dimension four LECs d_i from the effective meson-baryon Lagrangian. We have determined the d_i in the following manner: We have demanded that for physical values of M_π (M_K), the pion (kaon) mass expansion of the nucleon mass passes through its physical value. Furthermore, we restrict the d_i to not vary by more than $\pm 0.1\,\mathrm{GeV}^{-3}$ from the values found in [3]. Under these conditions, we have tried to fit the (partially quenched) SU(3) lattice data from MILC [5] for pion masses below $\sim$ 550 MeV. This is shown by the solid line in Fig. 1. In fact, the trend of the data is reproduced but one can not fit them exactly. This set of values for the d_i is called the "optimal set". Of course, at fourth order there are additional contributions from loop graphs. Utilizing the optimal set in the complete fourth order calculation leads to a good description of the MILC data for pion masses up to 700 MeV as displayed by the dot-dashed line in Fig. 1. Also shown in this figure is the fourth order calculation based on the calculation from 1997 [3] in which the LECs were determined to some extent by resonance saturation. We see that the curve based on these values of the LECs gives a less satisfactory description of the MILC data. We have also studied the kaon mass dependence of m_N and conclude that the nucleon mass in the chiral SU(3) limit can not be determined very precisely from the existing lattice data. To address the issue of the theoretical uncertainty of such an approach, we have varied the d_i by $\pm 0.2\,\mathrm{GeV}^{-3}$, which is larger than existing phenomenological uncertainties. We find that for pion masses below 500 MeV the theoretical error is fairly small, in agreement with the findings in [1]. For the first time, we have also compared such extrapolation functions for the Λ and the Ξ with the data from MILC. While the Λ behaves similar to the nucleon, the pion mass dependence of m_Ξ is appreciably weaker, which can be understood from the fact that this particle contains only one valence light quark. These investigations clearly demonstrate that SU(3) baryon chiral perturbation theory, despite the slower convergence than observed for its two-flavor cousin, is a useful tool to connect lattice results for unphysical quark masses with the physical world. More lattice data at lower pion masses are clearly needed to sharpen these conclusions.

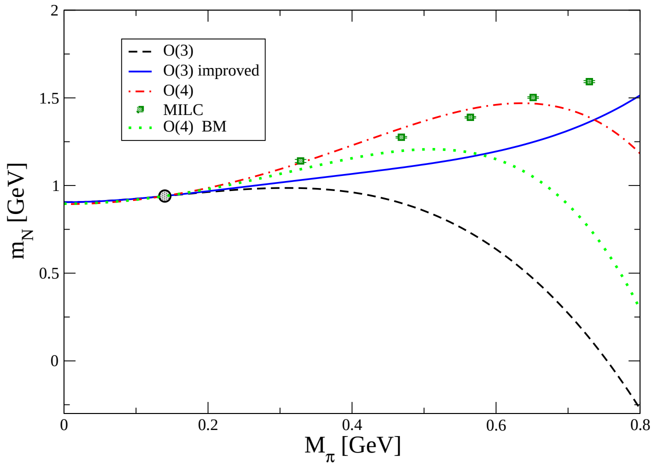

Fig. 1: Pion mass dependence of the nucleon mass. The dashed line gives the parameter-free third order result, the solid line the one with the improvement term as discussed in the text. Complete fourth order results are displayed by the dot-dashed and dotted lines for the optimal set of the LECs d_i and the values from [3], respectively. The filled circle shows the physical nucleon mass for the physical value of M_π. The data are from MILC [5].

References:

[1] V. Bernard, T. R. Hemmert and U.-G. Meißner, Nucl. Phys. A **732** (2004) 149 [hep-ph/0307115].

[2] M. Frink, U.-G. Meißner, and I. Scheller, *in preparation.*

[3] B. Borasoy and U.-G. Meißner, Annals Phys. **254** (1997) 192 [hep-ph/9607432].

[4] M. Frink and U.-G. Meißner, JHEP **0407** (2004) 028 [hep-lat/0404018].

[5] C. W. Bernard *et al.*, Phys. Rev. D **64** (2001) 054506 [arXiv:hep-lat/0104002].

*Also at HISKP, Universität Bonn

Chiral extrapolations of baryon masses for unquenched three-flavor lattice simulations

Matthias Frink, Ulf-G. Meißner*

Lattice QCD supplied with chiral perturbation theory is a powerful non-perturbative tool to analyze the structure of QCD in the confinement regime. It has been realized that lattice simulations performed at unphysically large quark masses can be extrapolated systematically to the physical limit based on functions derived in chiral perturbation theory or extensions thereof. Many observables like the pion mass, nucleon form factors and so on have been discussed in the literature, we focus here [1] on the simplest baryonic two-point functions, namely the masses of the ground state octet. While there is still on-going debate about the precise implementation of such schemes in terms of regulator prescriptions and the corresponding resummation of classes of higher order terms, there is little controversy about the inherent usefulness of such studies. This is documented by the excellent fits one obtains for the quark mass expansion of the nucleon mass applied to two-flavor simulations, which typically have pion masses larger than 400 MeV, see e.g. [2]. It should also be pointed out that such two-flavor studies can be constrained by chiral perturbation theory analyses of pion-nucleon scattering, since these allow one to pin down some combinations of the low-energy constants (LECs) appearing in the quark mass expansion of the nucleon mass. Still, simulations at lower quark masses are needed to further sharpen these analyses The situation is entirely different in the three–flavor sector. Only recently a large lattice effort was initiated to study tree–flavor dynamical QCD, and it will take some time before detailed results are available. In the meson sector, one has little doubt that chiral perturbation theory can be applied, although there are speculations of a strong flavor dependence of certain order parameters. In the baryon sector, the issue of the convergence of the chiral expansion is not settled, but it is fair to say that more higher order calculations are needed for a final clarification. Calculations of the nucleon (baryon) mass(es) to third and fourth order in various variants of chiral perturbation theory have been performed. It is obvious that for reliable extrapolation functions for the baryon masses one has to go beyond the leading non-analytic terms $\sim m_{\rm quark}^{3/2}$, because these do not even provide a reliable extrapolation function for two flavors. It is thus mandatory to consider at least the terms quadratic in the quark masses. This will be the topic of the present paper. In contrast to the earlier work [4], we perform the calculation in a Lorentz-invariant framework based on the so-called infrared regularization (IR). Furthermore, we also include all strong isospin breaking effects $\sim m_u - m_d$ up-to-and-including fourth order in the chiral expansion. Concerning the inclusion of the spin-3/2 decuplet, we follow exactly the lines of [2], were it is discussed how such effects can be absorbed in the values of certain LECs. We are well aware that present day lattice studies are far from reaching the required accuracy to resolve these fine effects, but we hope that the representations given here will become useful in the future. We summarize the main results of this work:

1) We have calculated the octet baryon masses to fourth order in the chiral expansion within a Lorentz-invariant formulation of baryon chiral perturbation theory. In contrast to earlier works (with the exception of Ref. [3] which utilizes an UV cutoff) we have systematically included strong isospin breaking, $m_u \neq m_d$. This amounts to considering all terms quadratic in the quark masses.

2) To disentangle the dependence of the baryon masses on the three light quark masses, one has to consider the dimension two and four chiral meson-baryon Lagrangians. At dimension two, one has three symmetry breaking LECs (b_0, b_D, b_F) and nine dynamical LECs, that enter at fourth order in the tadpole diagrams. The effect of five of these can be effectively absorbed in the dimension four LECs d_i. At dimension four, we have seven LECs, which appear in various combinations in the masses.

3) We have derived chiral extrapolation functions for the octet ground state baryons, including all isospin breaking terms linear in the mixing angle ε, given by $\tan 2\varepsilon = \sqrt{3}(m_d - m_u)/(2m_s - m_u - m_d)$. These constitute the main result of this work and might be used to analyze unquenched three-flavor simulations at varying quark masses above their physical values. The equations collected in this section can be obtained as a Mathematica notebook from the authors upon request. The corresponding meson mass representations of the baryon masses that are not truncated at order ε are also given.

4) We have performed the matching to the two-flavor case to obtain constraints on various combinations of dimension two and four SU(3) low-energy constants. We have also reviewed the determination of LECs in SU(2) and the symmetry breaking dimension two SU(3) LECs and also given resonance saturation estimates for the SU(3) LECs, based on the earlier work in [4].

5) The various sigma terms $(\sigma_{\pi N}, \sigma_{KN}^{(0,1)})$ can be obtained by differentiation of the mass formulas with respect to the quark masses. The corresponding extrapolation functions can be obtained from the authors upon request.

References:

[1] M. Frink and U.-G. Meißner, JHEP **0407** (2004) 028 `[hep-lat/0404018]`.

[2] V. Bernard, T. R. Hemmert and U.-G. Meißner, Nucl. Phys. A **732** (2004)(149) `[hep-ph/0307115]`.

[3] J. Gasser, Annals. Phys. **136** (1981) 62.

[4] B. Borasoy and U.-G. Meißner, Annals Phys. **254** (1997) 192 `[hep-ph/9607432]`.

*Also at HISKP, Universität Bonn

High precision calculation of the two-nucleon system in chiral effective field theory

E. Epelbaum (JLab), W. Glöckle (Bochum), Ulf-G. Meißner*

In this work [1], we have considered the interactions between two nucleons at next-to-next-to-next-to-leading order (N^3LO) in chiral effective field theory. The pertinent results of this study can be summarized as follows:

i) The two–nucleon potential at N^3LO consists of one-, two- and three-pion exchanges and a set of contact interactions with zero, two and four derivatives, respectively. We have applied spectral function regularization [2] to the multi-pion exchange contributions. This allows for a better separation of the low and high momentum components in the pion loop diagrams than dimensional regularization. Within this framework, we have shown that three-pion exchange can safely be neglected. The corresponding cut–off is varied from 500 to 700 MeV. The LECs related to the dimension two and three $\bar{N}N\pi\pi$ vertices are taken consistently from studies of pion-nucleon scattering in chiral perturbation theory. In the isospin limit, there are 24 LECs related to four–nucleon interactions which feed into the S–, P– and D–waves and various mixing parameters.

ii) We have reviewed the various isospin breaking mechanisms and proposed a novel ordering scheme, based on one small parameter that collects strong as well as electromagnetic isospin violation, accompanied by a particular counting rule for photon loops. In the actual calculations, we have included the leading charge-independence and charge-symmetry breaking four–nucleon operators, the pion mass difference in the 1PE, the kinematical effects due to the nucleon mass difference and the same electromagnetic corrections as done by the Nijmegen group (the static Coulomb potential and various corrections to it, magnetic moment interactions and vacuum polarization). This is done because we fit to the Nijmegen partial waves. In the future, it would be important to also include isospin violation in the 2PE, $\pi\gamma$-exchange and the isospin breaking corrections to the pion-nucleon scattering amplitude.

iii) We have discussed in some detail the form of the scattering equation that is used to iterate the potential and similar for the bound state. We use the Lippmann-Schwinger equation with the relativistic form of the kinetic energy. Such an approach can easily be extended to external probes or few–nucleon systems. We have also discussed the reduction to a nonrelativistic form which be might of easier use in some applications. The LS equation is regulated in the standard way, with the cut-off varied from 450 to 600 MeV.

iv) The total of 26 four–nucleon LECs has been determined by a combined fit to some np and pp phase shifts from the Nijmegen analysis together with the nn scattering length value $a_{nn} = -18.9\,\text{fm}$. The resulting LECs are of natural size.

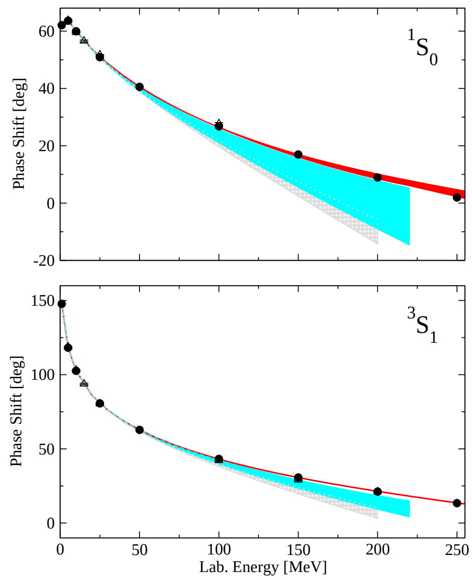

Fig. 1: S-waves at NLO (grey bands), at NNLO (blue bands) and at N^3LO (red bands). Circles (triangles): Nijmegen (VPI) PWA.

v) The description of the low phase shifts (S, P, D) is excellent, see Fig. 1. In all cases, the N^3LO result is better than the NNLO one with a sizeably reduced theoretical uncertainty. This holds in particular for the problematic $^3P_0$ wave which was not well reproduced at NNLO. The peripheral waves (F, G, H, ...), that are free of parameters, are also well described with the expected theoretical uncertainty related to the cut–off variations. We stress that the description of the phases in general improves when going from LO to NLO to NNLO to N^3LO, as it is expected in a converging EFT.

vi) The resulting S-wave scattering lengths and range parameters in the np and pp systems are in good agreement with the ones obtained in the Nijmegen PWA. In addition, we can give theoretical uncertainties for all these quantities, which are mostly in the one percent range.

vii) The deuteron properties are further predictions. In particular, we have not included the binding energy in the fits, the deviation from the experimental value is in the range from 0.4 to 0.07%. The asymptotic S-wave normalization and the asymptotic D/S are also well described. The remaining discrepancies in the quadrupole moment and the rms matter radius are related to the short-ranged two-nucleon current not considered here.

References:

[1] E. Epelbaum, W. Glöckle, U.-G. Meißner, `[nucl-th/0405048]`, Nucl. Phys. A (2005) in print.

[2] E. Epelbaum, W. Glöckle and U.-G. Meißner, Eur. Phys. J. A **19** (2004) 125 `[nucl-th/0304037]`.

*Also at HISKP, Universität Bonn

Isospin dependence of the three-nucleon force

E. Epelbaum (JLab), Ulf-G. Meißner*, J.E. Palomar (Valencia)

Three–nucleon forces (3NFs) are well established in nuclear physics. Although small compared to the dominant two–nucleon force (2NF), they are nevertheless needed to gain a quantitative understanding of nuclei and nuclear physics. A recent example in this context is the discussion of the 3NF effects in proton–deuteron scattering, see e.g. [1, 2]. Other examples are the binding energy difference between ^{3}H and ^{3}He or the saturation properties of nuclear matter. Only in the last decade a theoretical tool has become available to systematically analyze few–nucleon forces and consider such fine but important aspects as isospin–violation in such forces and in systems made of a few nucleons. This tool is the extension and application of chiral perturbation theory to systems with more than one nucleon which require an additional non–perturbative resummation to deal with the shallow nuclear bound states and large S-wave scattering lengths. While 3NFs in the isospin limit have been analyzed in some detail, see e.g. [3, 4, 5, 6], the question of isospin–violation in the 3NF has not yet been addressed in this framework. The work reported in [8] is intended to fill this gap. Here, we summarize the pertinent results of this investigation.

i) We have given a classification scheme for A–nucleon forces according to their isospin dependence. In the 3N system, one finds three different classes of forces, according to their transformation properties under isospin and charge–symmetry transformations. These are: *Class I* forces are isospin scalars; *Class II* forces satisfy: $[V_{II},\ \mathbf{T}] \neq 0$ and $[V_{II},\ P_{cs}] = 0$, where the charge symmetry operator P_{cs} transforms proton and neutron states into each other, $P_{cs} = e^{i\pi T_2} = \prod_{a=1}^{A} e^{i\pi t_2(a)} = \prod_{a=1}^{A} (i\tau_2(a))$. Also, the total isospin operator $\mathbf{T}$ is given by the sum of the isospin operators $\mathbf{t}$ of the individual nucleons: $\mathbf{T} = \sum_{a=1}^{A} \mathbf{t}(a)$. *Class III* forces break charge symmetry but do not lead to isospin mixing in the two–nucleon system: $[V_{III}^{2\mathrm{N}},\ \mathbf{T}] \neq 0$, $[V_{III}^{2\mathrm{N}},\ P_{cs}] \neq 0$, and $[V_{III}^{2\mathrm{N}},\ \mathbf{T}^2] = 0$. This extends the scheme of Henley and Miller [9] for the two-nucleon system.

(ii) We have worked out the leading and subleading isospin–violating 3NFs. The leading contributions are generated by one– and two–pion exchange diagrams with their strength given by the strong neutron–proton mass difference. The subleading corrections are again given by one– and two–pion exchange diagrams, driven largely by the charged–to–neutral pion mass difference and also by the electromagnetic neutron–proton mass difference and the dimension two electromagnetic LEC f_1, that plays an important role in the pion–nucleon system [10].

(iii) It is interesting to compare these findings with what is known about isospin violation in 2N systems. First of all, we notice a (formally) larger relative size of the isospin–breaking corrections compared to the two–nucleon sector. Indeed, isospin–breaking 3NFs are suppressed by q/Λ compared to the isospin–conserving 3NFs, while the suppression factor in case of the 2NF is $(q/\Lambda)^2$. Here, q denotes a genuine small parameter and Λ the pertinent hard scale. Secondly, the leading isospin–breaking corrections to the 2N and 3N forces arise from different sources. In particular, the dominant contribution to the 3NF is governed by the proton–to–neutron mass difference, which only gives a sub–subleading isospin–breaking correction to the 2N force. Further, charge dependence of the pion–nucleon coupling constant does not show up in the 3NF at the considered order. Similarly, the leading isospin–breaking 3N contact interaction is of the order $\epsilon M_\pi^2 (q/\Lambda)^3 \sim (q/\Lambda)^6$ and therefore does not need to be included. Last but not least, we notice that the hierarchy of isospin–violating forces observed in the two–nucleon system (i.e. charge–independence–breaking forces are stronger than charge–symmetry–breaking forces [7]) is not valid for three–nucleon forces.

(iii) We have estimated the relative strength of the leading and subleading corrections compared to the isospin–conserving 3NF at the same order. Isospin–violating 3NFs are expected to provide a small but non–negligible contribution to the ^{3}He–^{3}H binding–energy difference.

In the future, these isospin–breaking forces should be used to analyze three- and four–nucleon systems based on chiral EFT, extending e.g. the work presented in [6].

References:

[1] R.V. Cadman et al., Phys. Rev. Lett. **86** (2001) 967 `[nucl-ex/0010006]`.

[2] K. Ermisch et al., Phys. Rev. C **68** (2003) 051001 `[nucl-ex/0308012]`.

[3] S. Weinberg, Nucl. Phys. B **363** (1991) 3.

[4] U. van Kolck, Phys. Rev. C **49** (1994) 2932.

[5] J. L. Friar, D. Hüber and U. van Kolck, Phys. Rev. C **59** (1999) 53 `[nucl-th/9809065]`.

[6] E. Epelbaum et al., Phys. Rev. C **66** (2002) 064001 `[nucl-th/0208023]`.

[7] U. van Kolck, Ph.D. Thesis, University of Texas at Austin, 1993, UMI-94-01021-mc.

[8] E. Epelbaum, U.-G. Meißner and J. E. Palomar, "Isospin dependence of the three-nucleon force," `[nucl-th/0407037]`.

[9] E.M. Henley and G.A. Miller, in *Mesons and Nuclei*, M. Rho and G.E. Brown, eds. (North–Holland, Amsterdam 1979), Vol. I p. 405.

[10] U.-G. Meißner and S. Steininger, Phys. Lett. B **419** (1998) 403 `[hep-ph/9709453]`.

*Also at HISKP, Universität Bonn

Universal Properties of the Four-Nucleon System

L. Platter, H.-W. Hammer (Seattle), Ulf-G. Meißner*

It has been known for a long time that realistic nucleon-nucleon potentials which predict the triton binding energy B_3 correctly also give the right binding energy B_4 for the α-particle. In fact, potentials making different predictions for the triton binding energy will give results for the α-particle energy which will lie on a straight line in the B_3-B_4-plane. This linear correlation is known as the Tjon line.

Effective theories exploit a separation of scales in physical systems and are thus ideally suited to extract their universal properties. Recently, an effective field theory with contact interactions has been applied to the three-body system [1] with large two-body scattering length. This effective theory is (with the corresponding power counting) an expansion in ℓ/a, where ℓ is the typical energy scale of the underlying interaction and a is the scattering length of the two-body system. It turns out that a further three-body datum is needed to renormalize observables in the three-body system. This fact is represented by a three-body force at leading order in all three-body calculations. The value of the corresponding coupling constant is fixed by using for example the triton binding energy.

We have extended this work to the four-nucleon system and computed the binding energy of the α-particle within this framework [2]. However, instead of a field theoretical approach, we have chosen a quantum mechanical approach. We generated the leading order potentials for the singlet- and the triplet-channel and employed the Yakubovsky equations to compute the binding energies. The triton binding energy was used to fix the three-body force. This approach has also been applied to the four-boson system [3], in this case predictions were made for the binding energies of the ^{4}He tetramer. For the α-particle we find a binding energy of $B_\alpha = 29.5$ MeV. If the deuteron binding energy B_d is used instead of the triplet scattering length a_t, we obtain $B_\alpha = 26.9$ MeV. Our framework allows us now to analyze the universal properties of the four-nucleon system. By varying the three-body binding energy, the linear correlation between three- and four-body binding energies shows up naturally. The result is shown in Fig.1 for the two different choices of two-body input parameters. The deviation from the empirical values is a result of finite range contributions which were not taken into account. The resulting band in Fig.1 gives thus an estimate of higher order contributions. Thus, the Tjon line can be understood as a result of the large scattering length in the two-body system. In the near future finite range contributions should be included. The analysis of scattering processes within this framework also represents an interesting avenue.

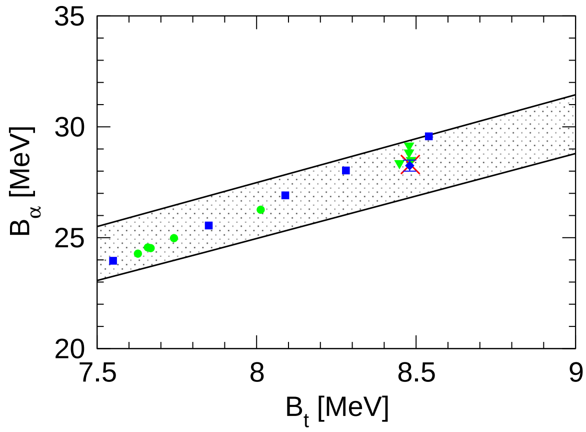

Fig. 1: The correlation between the binding energies of the triton and the α-particle (the Tjon line). The lower (upper) line shows our leading order result using a_s and B_d (a_s and a_t) as two-body input. The grey dots and triangles show various calculations using phenomenological potentials without or including three-nucleon forces, respectively. The squares show the results of chiral EFT at NLO for different cutoffs while the diamond shows the N^{2}LO result. The cross shows the experimental point.

References:

[1] P.F. Bedaque, U. van Kolck, and H.-W. Hammer, Nucl. Phys. A **646**, 444 (1999).

[2] L. Platter, H. W. Hammer and U.-G. Meißner, arXiv:nucl-th/0409040, Phys. Lett. B, in print.

[3] L. Platter, H. W. Hammer and U.-G. Meißner, Phys. Rev. A **70**, 250 (2004).

* also at HISKP, Univ. Bonn

Universal Properties of the Four-Boson System with Short-Range Interactions

L. Platter, H.-W. Hammer (Seattle), Ulf-G. Meißner*

Effective theories are a convenient tool to extract universal properties of physical systems at low energies. An effective field theory with contact interactions has recently been applied to the three-body system and been used to explain a correlation between the dimer-particle scattering length and the three-body binding energy called the Philips line as a consequence of a large scattering length in the two-body system [1]. A particular characteristic of this approach is that a three-body force at leading order is needed to renormalize observables. In order to fix the value of this three-body force one three-body datum is needed as for example the three-body binding energy. Once, the three-body coupling is fixed from this observable, predictions for other observables can be made.
Whether higher many-body forces are needed in systems with more than three particles is not known yet. A first step which promises further insight into the power counting of many-body forces is of course the analysis of the four-body system. We have used the same framework to compute binding energies of the four-boson system and to analyze its renormalization properties [2]. However, instead of a field-theoretic we used a quantum mechanical approach. We derived the effective potential at leading order and used it along with the well-known Yakubovsky equations to compute the binding energies of the four-body system. We analyzed the renormalization properties of results and found evidence that no four-body force is needed at leading order. A further goal was to make a prediction for the ^{4}He tetramer binding energies. As mentioned above, to do this one needs a three-body input to fix the value of the three-body coulping constant. Although the existence of these weakly bound few-body states has been proven experimentally, the binding energies have not been measured yet. However, there exist various calculations with realistic potentials which make different predictions for the trimer binding energy. Thus, instead of choosing a particular value for the trimer binding energy, we computed four-body binding energies for various three-body binding energies. We found a linear correlation between three- and four-body binding energies shown in Fig.1. This linear correlation is well-known and is called Tjon line in nuclear physics. We have fitted the scaling functions shown in Fig. 1 with linear expressions and obtained:

$$\begin{aligned}
\frac{B_4^{(0)}}{B_2} &= -24.752 + 4.075\frac{B_3^{(0)}}{B_2}\,, && 69 \leq \frac{B_3^{(0)}}{B_2} \leq 142\,,\\
\frac{B_4^{(0)}}{B_2} &= -742.0 + 645.1\frac{B_3^{(1)}}{B_2}\,, && 1.54 \leq \frac{B_3^{(1)}}{B_2} \leq 2.00\,,\\
\frac{B_4^{(1)}}{B_2} &= -0.662 + 1.034\frac{B_3^{(0)}}{B_2}\,, && 65 \leq \frac{B_3^{(0)}}{B_2} \leq 125\,,\\
\frac{B_4^{(1)}}{B_2} &= -178.0 + 159.4\frac{B_3^{(1)}}{B_2}\,, && 1.52 \leq \frac{B_3^{(1)}}{B_2} \leq 1.92\,.
\end{aligned}$$

These relations can be used to predict the tetramer ground and excited state energies to leading order for any potential for which one of the trimer energies and the dimer binding energy are known.

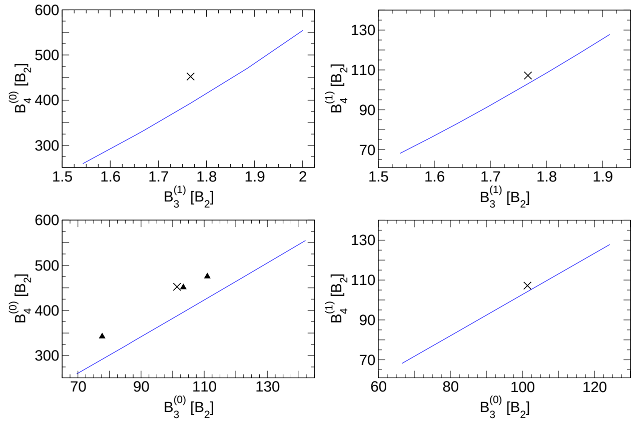

Fig. 1: The correlations between the ground and excited state energies of the ^{4}He trimer and tetramer. Upper row: the four-body excited state energy $B_4^{(1)}$ (left panel) and ground state energy $B_4^{(0)}$ (right panel) as a function of the three-body excited state energy $B_3^{(1)}$. Lower row: the same quantities as a function of three-body ground state energy $B_3^{(0)}$. The solid line shows the leading order effective theory result and the cross denotes the calculation for the LM2M2 potential by Blume and Greene [3]. The triangles show the results for the TTY, HFD-B, and HFDHE2 potentials [4, 5].

References:

[1] P.F. Bedaque, U. van Kolck, and H.-W. Hammer, Nucl. Phys. A **646**, 444 (1999).
[2] L. Platter, H.-W. Hammer, and U.-G. Meiß-ner, Phys. Rev. A **70**, 052101 (2004).
[3] D. Blume and C.H. Greene, J. Chem. Phys. **112**, 8053 (2000).
[4] M. Lewerenz, J. Chem. Phys. **106**, 4596 (1997).
[5] S. Nakaichi-Maeda and T.K. Lim, Phys. Rev. A **28**, 692 (1983).

* also at HISKP, Univ. Bonn

The Four-Boson System with Short-Range Interactions in two Dimensions

L. Platter, H.-W. Hammer (Seattle), Ulf-G. Meißner*

The progress in condensed matter physics has made it possible to create low-dimensional atomic systems. A two-dimensional boson system has been realized experimentally with hydrogen adsorbed on a helium surface [1]. Recently, it was shown that N weakly interacting bosons in two dimensions have interesting universal properties [2]. In particular the size of the binding energies increases exponentially

$$\frac{B_N}{B_{N-1}} \approx 8.567 \quad , \quad N \gg 1 \; . \tag{1}$$

Corrections are expected to start at order $1/N^2$ and are thus expected to be small for large N. For realistic interactions with finite range r_0, the equations are valid for N large but below a critical value,

$$1 \ll N < N_{crit} \approx 0.931 \ln \frac{R_2}{r_0} + \mathcal{O}(1), \tag{2}$$

where R_2 is the size of the two-boson droplet. The same work included a high precision calculation of the the trimer binding energies. It was found that ground state has a binding energy of $B_3^{(0)} = 16.522688(1)B_2$ and the excited state has binding energy of $B_3^{(1)} = 1.2704091(1)B_2$. The trimer binding energy disagrees by a factor of two from the predicted value, however, for larger N this prediction is supposed to get better. In this light, we have calculated the binding energies of the two-dimensional four-boson system with short-range interactions [3]. We generated the leading order potential within the effective theory with contact interactions and employed the Yakubovsky equations to compute the binding energies. For a sufficiently shallow two-body bound state our results are universal, in the sense that any realistic finite-range potential will give the same results for the four-body binding energies. This method has also been applied to the four-boson system in three spatial dimensions. It exploits a separation of scales in physical systems and is ideally suited to compute their universal properties. In principle, finite range corrections can be calculated systematically within this approach. Similar to the three-body system we find to bound states: one ground state with binding energy $B_4^{(0)} = 197.3(1)B_2$ and one excited state with $B_4^{(1)} = 25.5(1)B_2$. A comparison of this result with the large-N prediction from Ref.[2] is shown in Fig.1. It would be interesting to test this prediction at even larger N. Further, it would be valuable to create bosonic N-body clusters in experiments and measure their binding energies.

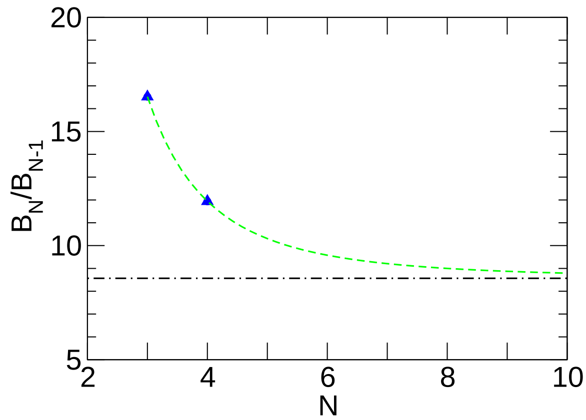

.

Fig. 1: B_N/B_{N-1} as a function of N. The dot-dashed line shows the asymptotic value of 8.567. The dashed line is an estimate of how the large-N value is approached.

References:

[1] A.I. Safonov, S.A. Vasilyev, I.S. Yasnikov, I.I. Lukashevich, and S. Jaakkola, Phys. Rev. Lett. **81**, 4545 (1998).

[2] H. W. Hammer and D. T. Son, arXiv:cond-mat/0405206.

[3] L. Platter, H. W. Hammer and U.-G. Meißner, Few Body Syst. **35**, 169 (2004).

[4] L. Platter, H. W. Hammer and U.-G. Meißner, Phys. Rev. A **70**, 250 (2004).

* also at HISKP, Univ. Bonn

Nucleon-Nucleon Potential in Finite Nuclei

U.T. Yakhshiev[1,2], Ulf-G. Meißner[3], A. Wirzba, A.M. Rakhimov[4] and M.M. Musakhanov[2]

We consider the spin-isospin–independent central part of the residual nucleon-nucleon (NN) potential in finite spherical nuclei taking into account the deformation effects of the nucleons within the surrounding nuclear environment. It is shown that inside the nucleus the short-range repulsive contribution of the potential is increased and the intermediate attraction is decreased. We identify the growth of the radial component of the spin-isospin independent short-range part of the in-medium nucleon-nucleon interaction as the responsible agent that prevents the radial collapse of the nucleus [1].

The Skyrme model and its variants are the only type of models that are formulated in terms of hadronic degrees of freedom *and* that allow for a simultaneous description of both single-baryon and multi-baryon properties. In fact, as shown by us in Ref. [2], Skyrme-type models even allow for a simple inclusion of the background of a finite nucleus. Thus, it is only natural to investigate in this framework the nucleon–nucleon (NN) interactions in the nuclear medium because of their role in the formation of nuclear matter.
In order to generate a central attraction at intermediate distances, we have generalized the model of Ref. [2] on the basis of scale invariance and conformal anomaly in such a way that, in addition to the chiral fields, a scalar dilaton field is included as well.

The results of the calculations for a single skyrmion confirm that the published results of Ref. [2] also hold in the presence of the scalar dilaton degree of freedom; especially, the increase of the radial size parameters of the chiral fields *and* and the dilaton field with increasing density is in qualitative agreement with the overall picture of the swelling of the nucleon inside the nucleus.
The new results for the residual NN interaction, calculated in the framework of the generalized Skyrme model, are summarized in Fig. 1, where the spin-isospin-independent central part V^c_{NN} of the residual NN potential in ^{40}Ca is shown as an example. Let us emphasize that this model has not been fine-tuned to reproduce the free space results quantitatively. But the qualitative changes are evident: the short-range repulsive contribution of the potential is increased and the intermediate attraction is decreased in the nuclear medium.
This can be interpreted as follows: It is known that the residual NN potential becomes repulsive when neighboring nucleons overlap. It is furthermore known that the sizes of the nucleons increase in the medium, as it is indeed the case for our model. Therefore the overlap-regions increase with density. This leads to a build-up of the repulsive part of the potential at high densities, when the two-nucleon system is near the center of the nucleus.
From our previous studies [2] we know that the nucleon mass is the smallest near the center of nucleus and increases when the nucleon is moved to the surface. Due to this phenomenon, nucleons should actually collapse to the center of the nucleus. In other words, due to the attractive mean-field potential, nucleons should move to the center. On the other hand, the nucleon concentration near the center of the nucleus does, as shown in Fig. 1, increase the repulsive residual potentials between nucleons such that nucleons are expelled from the center. Consequently, an equilibrium state arises and therefore saturation of the nuclear matter density results. In this case nucleons stop their radial motion towards the center of the nucleus, but their motion in a shell with given radius continues. A further inclusion of the Pauli mechanism in this picture could finally provide for the shell description of finite nuclei.

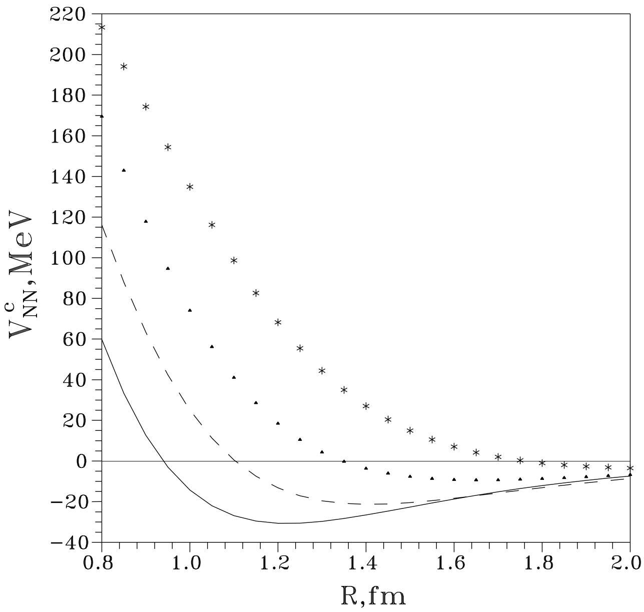

Fig. 1: Spin-isospin-independent central part of the residual NN potential in ^{40}Ca. The solid line corresponds to the free NN potential, whereas the dashed line, dotted line and stars refer to a radially aligned NN-system that is located at a distance $D = 4$ fm, 3 fm and 0 fm, respectively, from the center of the nucleus.

In summary, in the interior region of the heavy nucleus the residual NN potential is strongly repulsive and compensates the mean-field attractive potential in a such way that the nuclear density saturates. These results are consistent with other studies applying different models. However, one should remember that the Skyrme-type models are the only models that are formulated in terms of hadronic (non-quarkish) degrees of freedom *and* that can simultaneously describe both single-baryon as well as multi-baryon properties in free space *and* in the medium. In the framework of such a class of models our results are indeed new.

References:

[1] U.T. Yakhshiev, U.-G. Meißner, A. Wirzba, A.M. Rakhimov, M.M. Musakhanov, arXiv:nucl-th/0409002.

[2] U.T. Yakhshiev, M.M. Musakhanov, A.M. Rakhimov, U.-G. Meißner, A. Wirzba, Nucl. Phys. A **700**, 403 (2002).

[1] NuRI, Pusan National University, Korea
[2] ThPhysDep, National University of Uzbekistan, Tashkent
[3] HISKP (Theorie), Universität Bonn and IKP, FZ Jülich
[4] Inst. of Nucl. Phys., Academy of Sciences, Usbekistan

Ultraperipheral Collisions at Relativistic Heavy Ion Collisiders and Production of QED Pairs at RHIC

G. Baur, K. Hencken*, U.Dreyer*, D. Trautmann*

Ultraperipheral relativistic heavy ion collisions ("UPC") are accompanied by very strong electromagnetic fields of very short duration. This electromagnetic pulse can be viewed as a spectrum of equivalent photons which extends to very high energies. The parameter which characterizes the strength of the interaction is the Coulomb parameter η:

$$\eta = \frac{Z_1 Z_2 e^2}{\hbar v} \approx Z_1 Z_2 \alpha \tag{1}$$

where Z_1 and Z_2 are the charges of the nuclei and $v \approx c$ is the relative velocity of the ions. For heavy nuclei like Au-Au (RHIC) or Pb-Pb (LHC) we have $\eta \gg 1$.

This strong field also leads to important higher order effects of the electromagnetic interaction[8]. These multiphoton exchange processes are studied using perturbation theory and the sudden or Glauber approximation. In many important cases, the multi-photon amplitudes factorize into independent single-photon amplitudes. These amplitudes have a common impact parameter vector, which induces correlations between the amplitudes. Impact-parameter dependent equivalent-photon spectra for simultaneous excitation are calculated, as well as, impact-parameter dependent $\gamma\gamma$-luminosities. Excitations, like the multiphonon giant dipole resonances, vector meson production and multiple e^+e^- pair production can be treated analytically in a bosonic model, analogous to the emission of soft photons in QED.

Probabilities for the excitation of the giant dipole resonance (GDR) and e^+e^--pair production are very large, of the order of one for small impact parameters [1]. This means that these processes will also occur simultaneously with other interesting processes, where the probabilities are generally much smaller than one. There is also mutual excitation, where each ion is excited to the (one phonon) GDR state. This process has been studied experimentally at RHIC [2]; it is important for the luminosity determination and for triggering on UPCs[3, 4].

The probability $P(b)$ of other inelastic processes is in general much smaller than one. An important process is diffractive vector meson production (especially ρ^0-production). Probabilities for ρ^0-production in close (grazing) collisions are about 0.01 or 0.03 for RHIC and the LHC, respectively[7]. One example of simultaneous processes is giant dipole resonance excitation (followed by neutron decay) accompanied by ρ^0-production. This process was studied experimentally at STAR[4].

Another example of simultaneous processes is giant dipole resonance excitation and e^+e^- pair production. This was recently observed at STAR/RHIC[10]. Due to the requirement of giant resonance excitation events with small impact parameters(but still larger than twice the nuclear radius) are selected. In these collisions higher order effects should be enhanced. The experimental results of [10] are in good agreement with lowest order QED calculations [11] using the methods of [8] and [6, 12]. A typical graf is shown in Fig.1. We refer to [11] for further details.

At CERN a Yellow Report to document the physics potential of UPC is currently being prepared. The field is also reviewed in [13].

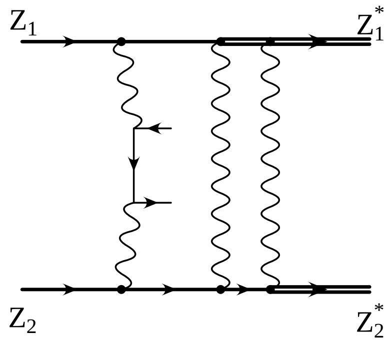

Fig. 1: One of the diagrams which describes mutual giant dipole resonance excitation and electron pair production

References:

[1] G. Baur, K. Hencken, D. Trautmann, S. Sadovsky, Y. Kharlov, Phys. Reports 364 (2002) 359.
[2] M. Chiu et al., Phys. Rev. Lett. 89 (2002) 012302.
[3] A. Baltz, C. Chasman, and S. N. White, Nucl. Instrum & Meth. 417 (1998) 1.
[4] C. Adler et al., Phys. Rev. Lett.89 (2002) 272302.
[5] K. Hencken, D. Trautmann and G. Baur, Phys. Rev. A51 (1995) 998.
[6] K. Hencken, D. Trautmann and G. Baur, Phys. Rev. A51 (1995) 1874.
[7] S. Klein and J. Nystrand, Phys. Rev. C60 (1999) 014903.
[8] Gerhard Baur, Kai Hencken, Andreas Aste, Dirk Trautmann and Spencer R. Klein Nucl. Phys. A729(2003)787
[9] G. Baur in *Proceedings of the workshop on "Electromagnetic Probes of Fundamental Physics", Erice, Italy, Oct. 16–21, 2001*, edited by W. Marciano and S. White, p. 183, Singapore, 2003, World Scientific, available as hep-ph/0112239.
[10] J.Adams et al. Phys.Rev.C70(2004)031902(R)
[11] K.Hencken, G.Baur and D.Trautmann Phys.Rev.C 69(2004)054902
[12] A.Alscher, K.Hencken, D.Trautmann and G.Baur Phys. Rev.A 55(1997)396
[13] K.Hencken, invited talk at the conference "Physics at LHC" 13-17 July 2004, Vienna, Austria, Kai Hencken, Gerhard Baur, Ute Dreyer and Dirk Trautmann: Ultraperipheral Collisions Proceedings of Physics at LHC to be published in Czechoslovak Journal of Physics Vol.54(2004) Suppl. A

* Institut für Theoretische Physik, Universität Basel, CH-4056 Basel, Switzerland

Recent Developments in Electromagnetic Dissociation with Fast Heavy Ions

G. Baur, K. Hencken*, D. Trautmann*and S. Typel†

The theory of intermediate energy Coulomb dissociation and its applications is discussed in [1, 2, 3]. Intermediate energy Coulomb excitation and dissociation is also of great interest for the radioactive beam facilities (existing, being built or planned)all over the world.

We describe the basic theory and new results concerning especially higher order effects in the dissociation of neutron halo nuclei. Some new applications of Coulomb dissociation for nuclear astrophysics [4] and nuclear structure physics are discussed. For a general discussion of indirect methods in nuclear astrophysics we refer to [5].

Such investigations are well suited for secondary (radioactive) beams. Due to the time-dependent electromagnetic field the projectile is excited to a bound or continuum state, which can subsequently decay. If 1^{st} order electromagnetic excitation is the dominant effect, experiments can directly be interpreted in terms of electromagnetic matrixelements, which also enter, e.g., in radiative capture cross-sections, like (n,γ) or (p,γ) reactions. The question of higher order effects is therefore very important. A good way to treat higher order effects in a general way is to solve the time-dependent Schrödinger equation numerically. Analytic methods are also useful to study the dependence of higher order effects on the relevant parameters. This has been done for a simple and realistic model for Coulomb dissociation of neutron halo nuclei [6], where it was shown that at high beam energies the effects are reassuringly small. The present level of precision can be judged from a recent determination of the $p_{1/2}$ and $p_{3/2}$ scattering lengths of the n+^{10}Be system[7]. In this determination the GSI data on ^{11}Be electromagnetic dissociation[8] were used as an input.

We also discuss new possibilities, like the experimental study of two-particle capture and applications to r- and rp-process nuclei, see also [9, 10], where some of the opportunities are described. Low-lying dipole strength has been observed in weakly bound neutron rich nuclei (see [6] for further references). Low lying dipole strength is a systematic effect in proton-neutron asymmetric nuclei. This could affect significantly the r-process abundances [11], due to the change in the r-process path. Coulomb dissociation studies will be very useful in this context.

A cluster version of the GGT(Gellmann-Goldberger-Thirrring) sum rule is discussed in [12]. We refer to this paper for further details. Sum rules for stable nuclei, like the GGT and the TRK (Thomas-Reiche-Kuhn) sum rule, have played an important role in the understanding of global properties of well bound system and their excitation spectrum. One of their major features are their universality.

The TRK sum rule has been extended into the domain of very proton and very neutron rich nuclei or other systems with a pronounced clustering structure. For these systems a so-called "cluster sum rule" was derived and is has lead to some insight in the low-lying dipole strength (sometimes called the "pigmy resonance") in such systems. We want to show here that this cluster sum rule can also be derived from the Gellmann-Goldberger-Thirring (GGT) sum rule. Whereas this approach leads ultimatively to the same mathematical expression as the TRK sum rule (as it does already for stable nuclei), the approximations and assumptions are quite different in this case and therefore some further insight into the nature of the cluster sum rule can be gained. One advantage of this "new" sum rule is, that it is not based on the long-wavelength limit and Siegert's theorem and that it is not restricted to the dipole excitation spectrum alone. We review the foundations of the TRK cluster sum-rule and the approximations used before deriving the GGT version. We discuss its application to system with more than two clusters and also discuss that deviations from the sum rule results are expected to be smaller in the case of clustered systems. We apply the result to some systems with either a halo-structure or a cluster structure.

References:

[1] G.Baur invited talk, ECT* Trento Workshop on Spectroscopic factors 2-12 March 2004 Direct Reactions with Exotic Nuclei transparencies see http://www.df.unipi.it/ angela/trentotalks/baur.pdf

[2] G.Baur, K.Hencken, D.Trautmann and S.Typel Proceedings of the International Workshop on Gross Properties of Nuclei and Nuclear Excitations, Hirschegg , Austria, January 11-17,2004

[3] G. Baur, K. Hencken and D.Trautmann, "Coulomb Dissociation in Hadron- and Astrophysics", Prog. in Part. and Nucl. Phys., 51(2003) 487

[4] G.Baur, C.A. Bertulani and H.Rebel, Nucl Phys. A**458** (1986) 188.

[5] S.Austin "High Energy Approaches to Low Energy Phenomena in Astrophysics", to appear in Proceedings of *EMI-2001*, Osaka, December 2001, available as e-print nucl-th/0201010

[6] S.Typel and G.Baur, Phys.Rev C **64**(2001) 024601, available as e-print nucl-th/0101033.

[7] S.Typel and G.Baur Phys. Rev. Lett. 93(2004) 142502

[8] R.Palit et al. Phys. Rev. C68(2003)034318

[9] "An International Accelerator Facility for Beams of Ions and Antiprotons", Conceptual Design Report. GSI November 2001.

[10] RIA WEB page, `http://www.phy.anl.gov/ria/`

[11] S. Goriely Phys. Lett. B**436** (1998) 10.

[12] Kai Hencken, Gerhard Baur and Dirk Trautmann Nuclear Physics A 733(2004)200

* Institut für Theoretische Physik, Universität Basel,
Klingelbergstraße 82, CH-4056 Basel, Switzerland
† GSI, Darmstadt

Effective-Range Approach and Scaling Laws for Electromagnetic Strength in Neutron Halo Nuclei

S. Typel*, G. Baur

Electromagnetic strength functions of halo nuclei exhibit universal features that can be described in terms of characteristic scale parameters. For a nucleus with nucleon+core structure the reduced transition probability, as determined, e.g., by Coulomb dissociation experiments, shows a typical shape that depends on the nucleon separation energy and the orbital angular momenta in the initial and final states. The sensitivity to the final-state interaction (FSI) between the nucleon and the core can be studied systematically by varying the strength of the interaction in the continuum. In the case of neutron+core nuclei analytical results for the reduced transition probabilities are obtained by introducing an effective-range expansion. The scaling with the relevant parameters is found explicitly. General trends are observed by studying several examples of neutron+core and proton+core nuclei in a single-particle model assuming Woods-Saxon potentials. Many important features of the neutron halo case can be obtained from a square well model. Rather simple analytical formulae are found. The nucleon-core interaction in the continuum affects the determination of astrophysical S factors at zero energy in the method of asymptotic normalisation coefficients (ANC). It is also relevant for the extrapolation of radiative capture cross sections to low energies. We expect that our model with its rather simple analytical results can serve as a good testing ground to investigate the validity of low energy expansions. The present work is published in [1]. A very detailed account, also with applications to proton halo nuclei is given in [2].

The most important parameter for halo nuclei is $\gamma = qR$, where q is related to the binding energy E_b by $E_b = \hbar^2 q^2/(2\mu)$ where μ is the reduced mass of the (A+n) system and R is the range of the (A+n) interaction. This parameter γ is small for halo nuclei with their large size $1/q$ and serves as a convenient expansion parameter. For low neutron energies we can use the effective range expansion for the phase shift. We restrict ourselves to the lowest order term, i.e.

$$tan(\delta_l) = -(x c_l \gamma)^{2l+1}$$

where $x = k/q$. The neutron wave number is k and c_l is a reduced scattering length which is treated as a free parameter and fitted to the experiment. We assume that the scattering length has a natural value with c_l being of $O(1)$. The reduced dipole transition probability $\frac{dB}{dE}$ is given in terms of the shape function $S_{l_i}^{l_f}$ as

$$\frac{dB}{dE} = (Z_{eff}e)^2 \frac{2\mu}{\pi\hbar^2} \frac{3}{4\pi} (l_i 010|l_f 0)^2 \frac{|C_{l_i}|^2}{q^5} S_{l_i}^{l_f}$$

where Z_{eff} is the effective charge, C_{l_i} the asymptotic normalization coefficient, l_i and l_f denote the nuceon angular momenta in the initial and final states respectively. We obtain analytical expressions for the shape functions assuming that the main contribution to the radial integral arises from radii larger than R. This assumption is well fulfilled for halo nuclei [1, 2]. In Fig.1 we compare our approach to the Coulomb breakup data of ^{11}Be from GSI [3]. This nucleus shows a very pronounced halo structure with an $s_{1/2}$ -neutron bound by 504 keV. There is also a bound excited $p_{1/2}$-state at 320 keV excitation energy. Its presence is felt in the reduced scattering parameter $c_1^{1/2}$ which we extract [1] from the experimental results[3].

The universal shape function $S_{l_i}^{l_f}$ which determines the reduced excitation probability can be expanded in the halo parameter γ and is given for a $s \rightarrow p$ transition by (see [1, 2] where also other cases are given)

$$S_0^1 = \frac{4x^3}{(1+x^2)^4}(1 - c_1^3(1+3x^2)\gamma^3 + \ldots)$$

The present approach is also applied to the electromagnetic strength in the neutron rich isotope ^{23}O, which was recently studied at GSI [4]. Due to the increasing Coulomb barrier, proton halo nuclei will tend to become less important for heavier nuclei. The halo effect for neutrons, on the other hand, is expected to be present for heavier nuclei also, where the present approach will find further applications.

We finally note that low lying E1 strength is also an important issue of s- and r-processes in nuclear astrophysics [5, 6]. The methods developed in this work are potentially very useful in this context also.

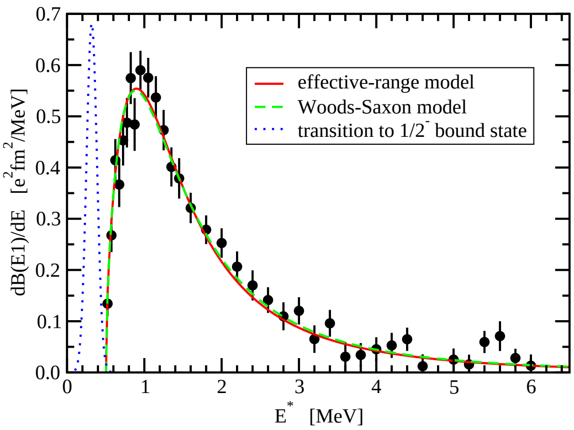

Fig. 1: Reduced transition probability as a function of the excitation energy E^* compared to experimental data extracted from the Coulomb breakup of ^{11}Be. For further explanation see [1]

References:

[1] S.Typel and G.Baur, Phys. Rev. Lett 93(2004)142502
[2] S. Typel and G. Baur, nucl-th/0411069, submitted to Annals of Physics
[3] R.Palit et al. Phys.Rev.C68(2003)034318
[4] C.Nociforo et al. Phys. Lett. B , in press
[5] T.Rauscher et al. Phys.Rev.C66(2002)028802
[6] S.Goriely Phys. Lett. B 436(1998)10

* GSI, Darmstadt.

The Trojan-Horse Method: Investigation of the Threshold Region

S. Typel*, G. Baur

The Trojan-Horse method is an indirect approach to determine the energy dependence of astrophysical S factors at low energies. The idea is to extract the cross section of a two-body reaction $A+x \rightarrow C+c$ from a suitably chosen three-body reaction $A+a \rightarrow C+c+b$ (where $a=b+x$ is the Trojan horse) with the help of nuclear reaction theory (like, e.g. DWBA) [1]. In a certain part of the three-body phase space the momentum transfer to the spectator b is small and the quasi-free scattering process dominates the reaction. For general discussions see e.g. [2]. In Ref. [3] a general theoretical framework of the Trojan-Horse method is presented, see also [4].

A striking parallelism of (d,p) spectra in the continuum region and the elastic neutron scattering cross section (where σ_l denotes the cross section in partial wave l) on the same target nucleus was observed already a long time ago in [5]. This was explained in a modified plane wave approach in Ref. [6]. The cross section of the transfer reaction is modified as compared to the direct two-body cross section by "stripping enhancement factors" that depend on the angular momentum l of the transferred neutron. The relation is given by (see eq. 6 of Ref. [6] or eq. 79 of [3])

$$\frac{d^2\sigma}{d\Omega_p dE_p} = \sum_l \sigma_l F_l(x,y) \tag{1}$$

where $d^2\sigma/(d\Omega_p dE_p)$ denotes the (d,p) double differential cross section. The "stripping enhancement factor" or "Trojan-Horse factor" (THF) is denoted by $F_l(x,y)$, where x and y are reduced kinematical variables [3, 6].

It is of special interest to study the limit of stripping to bound and unbound states (continuum). We treat two cases, in the first there is only the channel $A+x$ at $E_{Ax}=0$, in the second there is also absorption due to the presence of other open channels $C+c$.

To study the first case we imagine that the strength of the single particle potential V_{Ax} is decreased, so that the bound state close to threshold (a halo state), disappears and shows up as a resonance in the continuum. For $l>0$ this bound state turns into a resonance, and the cross section to this resonance (defined as an integral over an energy region which is several times larger than the width) joins smoothly to the stripping to the bound states, see [6]. Due to the absence of the angular momentum barrier for $l=0$ there are some peculiarites which we study now. Stripping to bound states is determined by the asymptotic normalization constant B (see eqs. A54-56 of [7]) of the bound state wave function and the behavior of the Hankel function $h_l(iqr)$ where q is related to the binding energy. Since

$$B \sim q^{3/2} \quad \text{for} \quad l=0 \tag{2}$$

and

$$B \sim q^{l+1}R^{l-1/2} \quad \text{for} \quad l>0 \tag{3}$$

the stripping cross section (see e.g. eq. 17 of [6]) to a (halo) state with $l=0$ tends to zero for q going to zero, while it stays finite for $l>0$. We note that the presence of a bound state close to zero energy leads to a large scattering length in the $A+x$-system which leads to an enhancement of the elastic breakup cross section. When the strength of the potential is decreased, the bound state becomes a virtual state, which again leads to a very large scattering length, see also [8]. In this context it seems interesting to note that about 30 years ago a new type of threshold effects was predicted in [9] (what is now called a halo state was referred to as a puffy state in those days).

Let us now treat the case with absorption. Such an absorption is in principle always present in the radiative capture channel $C+c=B+\gamma$, where $B=(A+x)$. Another example is the ^{6}Li(p,α)^{3}He reaction studied via the $d+{}^6$Li reaction in [10]. In this case a finite value of the differential cross section for $E_{Ax}=0$ is obtained, see e.g. eq. 79 of [3]. When the transferred particle x is a neutron, the penetration factor P_l goes as k^{2-2l} (see eqs. 77 and A19 of [3]). The cross section for $A+x \rightarrow C+c$ behaves as k^{2l-1}(for $l=0$ this is Fermi's $1/v$-law). Together with the phase space factor in eq. 79 of [3] a finite nonzero cross section is obtained at the $E_{Ax}=0$ threshold. Generalizing the formalism of IAV [11] and KI [12] to $E_{Ax}<0$ one can show that there is a continous transition of the double differential cross section $d^2\sigma/(d\Omega_b dE_b)$ to states with $E_{Ax}<0$.

One may also envisage applications of the Trojan-Horse method with exotic nuclear beams. An unstable (exotic) projectile hits a Trojan-Horse target allowing to study specific reactions on exotic nuclei that are not accessible in direct experiments. We mention the d(^{56}Ni,p)^{57}Ni reaction studied in inverse kinematics in [13]. In this paper stripping to bound states was studied; an extension to stripping into the continuum would be of interest for this and other reactions of this type.

References:

[1] G. Baur, Phys. Lett. B **178**, 135 (1986).

[2] Frank Strieder and Claus Rolfs. Key reactions in stellar burning: LUNA and other new approaches, NUPECC News, Vol. 11, No. 3, p. 5 (2001).

[3] S. Typel and G. Baur, Ann. Phys. **305**, 228 (2003), see also nucl-th/0208069.

[4] G. Baur and S. Typel, Proceedings of the International Conference Fusion03: From a Tunneling Nuclear Microscope to Nuclear Processes in Matter, Matsushima; Miyagi, Japan November 12-15, 2003, Progress of Theoretical Physics Supplement Number 154, 333 (2004).

[5] H. Fuchs et al., Phys. Lett. **37B**, 285 (1971).

[6] G. Baur and D. Trautmann, Z. Physik **267**, 103 (1974).

[7] S. Typel and G. Baur, nucl-th/0411069, submitted to Ann. Phys.

[8] G. Blanchon, A. Bonaccorso, and N. Vinh Mau, Nucl. Phys. A **739**, 259 (2004).

[9] P. v. Brentano, B. Gyarmati, and J. Zimanyi Phys. Lett. **46B**, 177 (1973).

[10] A. Tumino et al., Phys. Rev. C **67**, 065803 (2003).

[11] M. Ichimura, N. Austern, and C.M. Vincent, Phys. Rev. C **32**, 431 (1985).

[12] A. Kasano, M. Ichimura, Phys. Lett. **115B**, 81 (1982).

[13] K. E. Rehm et al., Phys. Rev. Lett. **80**, 676 (1998).

* GSI, Darmstadt.

Near threshold enhancement of the $p\bar{p}$ mass spectrum in J/Ψ decay

A. Sibirtsev, J. Haidenbauer, S. Krewald, Ulf-G. Meißner*, A.W. Thomas+

Recently the BES Collaboration [1] reported a near-threshold enhancement in the proton-antiproton ($p\bar{p}$) invariant mass spectrum, observed in the $J/\Psi{\to}\gamma p\bar{p}$ decay. Fitting this $p\bar{p}$ invariant mass spectrum below 1.95 GeV by a Breit-Wigner resonance function by assuming that the $p\bar{p}$ system is in an S-wave resulted in a resonance mass of $M{=}1859^{+3+5}_{-10-25}$ MeV and a total width of $\Gamma{<}30$ MeV. A comparable fit to the data could be achieved with a P-wave Breit-Wigner function with $M{=}1876{\pm}0.9$ MeV and $\Gamma{=}4.6{\pm}1.8$ MeV [1].

The proximity of these resonance masses to the $p\bar{p}$ reaction threshold (which is at 1876.54 MeV) nourished speculations that the observed strong enhancement could be a signal of an $N\bar{N}$ bound state. An alternative explanation put forward by the BES collaboration invokes similarities of the observed enhancement in the $p\bar{p}$ mass spectrum near threshold with the strong energy dependence of the electromagnetic form factor of the proton around $\sqrt{s}{\approx}2m_p$, in the timelike region, as determined in the reaction $p\bar{p}{\to}e^+e^-$. In the latter case it was argued that the sharp structure seen in the experiment could be caused by a narrow, near-threshold vector-meson ($J^{PC}{=}1^{--}$) resonance with $M{=}1870{\pm}10$ MeV and $\Gamma{=}10{\pm}5$ MeV.

An entirely different and much more conventional interpretation of the observed enhancement was suggested in Refs. [2, 3]. The authors of these papers argue that the enhancement is primarily due to the final state interaction (FSI) between the produced proton and antiproton. Note, however, that the scattering length approximation was used in those studies and it remains unclear to which extent this approximation is valid for the large energy range covered by the BES data. Therefore, in the present paper we re-analyse the near threshold enhancement in the $p\bar{p}$ invariant mass spectrum reported by the BES Collaboration, but utilizing now a realistic model of the $N\bar{N}$ interaction [4] directly.

The $J/\Psi{\to}\gamma p\bar{p}$ decay rate is given as

$$d\Gamma = \frac{|A|^2}{2^9\pi^5 m^2_{J/\Psi}}\,\lambda^{1/2}(m^2_{J/\Psi},M^2,m^2_\gamma) \times\lambda^{1/2}(M^2,m^2_p,m^2_p)\,dM d\Omega_p\,d\Omega_\gamma, \tag{1}$$

where the function λ is defined by

$$\lambda(x,y,z) = \frac{(x-y-z)^2-4yz}{4x}, \tag{2}$$

M is the invariant mass of the $p\bar{p}$ system, Ω_p is the proton angle in that system, while Ω_γ is the photon angle in the J/Ψ rest frame. After averaging over the spin states and integrating over the angles, the differential decay rate is

$$\frac{d\Gamma}{dM} = \frac{(m^2_{J/\Psi}-M^2)\sqrt{M^2-4m^2_p}}{2^7\pi^3 m^3_{J/\Psi}}\,|A|^2\,, \tag{3}$$

where A is the total $J/\Psi{\to}\gamma p\bar{p}$ reaction amplitude. Note that A is dimensionless.

A very simple treatment of FSI effects is due to Watson and Migdal. These authors suggested that the reaction amplitude for a production and/or decay reaction which is of short-ranged nature can be factorized in terms of an elementary production amplitude A_0 and the $p\bar{p}$ scattering amplitude T of the particles in the final state,

$$A_{prod} \approx NA_0\cdot T, \tag{4}$$

where N is a normalization factor.

Results based on the Watson/Migdal prescription for the $p\bar{p}$ invariant scattering amplitudes squared are shown in Fig. 1 for the $^1S_0$ partial wave in the $I{=}0$ (solid line) and $I{=}1$ (dashed line) channels. We consider the isospin channels separately because the actual isospin mixture in the final $p\bar{p}$ system depends on the reaction mechanism and is not known, cf. the comments in Ref. [5]. Note that the squared $p\bar{p}$ scattering amplitudes $|T|^2$ were all normalized to the BES data at the invariant mass $M(p\bar{p}){-}2m_p$=50 MeV by multiplying them with a suitable constant. Evidently, the mass dependence of the BES data can indeed be described with FSI effects induced by the $^1S_0$ scattering amplitude in the $I{=}1$ isospin channel. The $I{=}0$ channel leads to a stronger energy dependence which is not in agreement with the BES data.

Further results, specifically for the $J/\Psi{\to}\pi^0 p\bar{p}$ invariant mass spectrum, and some critical comments can be found in Ref. [5].

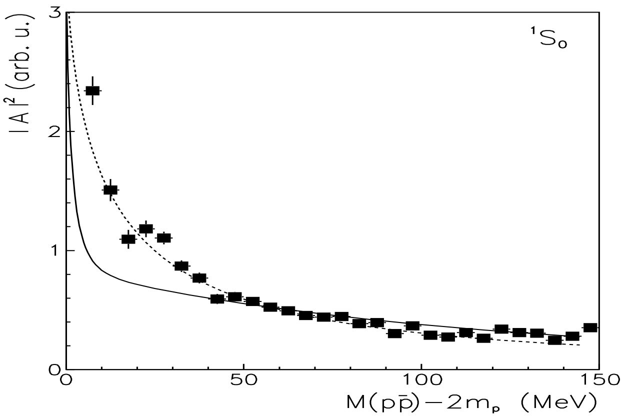

Fig. 1: Invariant $J/\Psi{\to}\gamma p\bar{p}$ amplitude $|A|^2$ as a function of the $p\bar{p}$ mass. The squares represent the experimental values of $|A|^2$ extracted from the BES data[1] via Eq.(3). The curves are the scattering amplitude squared ($|T|^2$) predicted by the $N\bar{N}$ model A(OBE) [4] for the $^1S_0$ partial waves and the $I{=}0$ (solid) and $I{=}1$ (dashed) channels, respectively.

References:

[1] J.Z. Bai et al., Phys. Rev. Lett. **91**, 022001 (2003).

[2] B. Kerbikov, A. Stavinsky, and V. Fedotov, Phys. Rev. C **69**, 055205 (2004).

[3] D.V. Bugg, Phys. Lett. B **598**, 8 (2004).

[4] T. Hippchen, J. Haidenbauer, K. Holinde, V. Mull, Phys. Rev. C **44**, 1323 (1991); V. Mull, J. Haidenbauer, T. Hippchen, K. Holinde, Phys. Rev. C **44**, 1337 (1991).

[5] A. Sibirtsev et al., hep-ph/0411386.

* also at: Universität Bonn, Helmholtz-Institut für Strahlen und Kernphysik, D-53115 Bonn, Germany

+ Jefferson Lab, 12000 Jefferson Ave., Newport News, VA 23606, US

Radiative tritium β–decay and the neutrino mass

V. Bernard (ULP Strasbourg), S. Gardner (Kentucky), Ulf-G. Meißner*

Empirical evidence of neutrino oscillations in atmospheric, solar, and reactor neutrino data compels the existence of non-zero neutrino masses, yet such experiments are insensitive to the absolute scale of a neutrino mass, for the oscillation experiments determine $\Delta m_{ij}^2 \equiv m_i^2 - m_j^2$, where m_i is the mass of neutrino i. To determine the absolute value of the neutrino mass requires different methods. Cosmological constraints on the neutrino mass do exist, though our focus shall be on the study of the electron energy spectrum in tritium β-decay near its endpoint, as this represents the most sensitive terrestrial measurement. The spectrum shape constrains the mass of the neutrino, be it of Dirac or Majorana character, and the inferred mass is insensitive to phases in the neutrino mixing matrix — in contradistinction to the constraint on the neutrino mass from neutrinoless double β-decay. An accurate theoretical description of the expected electron energy spectrum is crucial to the determination of the neutrino mass; this demand grows as the sensitivity of the experiments increase. Indeed, future studies expect to probe the neutrino mass at the sub-eV level [1]. It is our purpose to realize a theoretical form of the requisite accuracy, though we shall begin by describing the form used in earlier tritium experiments. With an anti-electron neutrino of mass m_ν, neglecting neutrino mixing for simplicity, the Fermi form of the electron energy spectrum for tritium β-decay is

$$\begin{aligned}\frac{d\Gamma_F}{dE_e} &= \frac{G_F^2}{2\pi^3}|\mathcal{M}|^2 F(Z,R_{\rm e},E_e)p_e E_e(E_e^{\max}-E_e)\\ &\times \sqrt{(E_e^{\max}-E_e)^2-m_\nu^2}\,,\end{aligned}$$

where G_F is the Fermi constant, p_e, E_e, and $E_e^{\max}$ are the momentum, energy, and maximum endpoint energy, respectively, of the electron, and $|\mathcal{M}|^2$ is the absolute square of the nuclear matrix element, with $|\mathcal{M}|^2 \sim 5.3$. A form of this ilk has been used to bound m_ν in previous experimental analyses of molecular tritium β-decay. Following the usual practice, we include a non-zero neutrino mass in the phase space contribution only. The Fermi function, $F(Z,R_{\rm e},E_e)$, captures the correction due to the Coulomb interactions of the electron with the charge Ze of the daughter nucleus. We adopt the usual expression, derived from the solutions of the Dirac equation for the point-nucleus potential $-Z\alpha/r$ evaluated at the nuclear radius $R_{\rm e}$; it differs from unity by a contribution of $\mathcal{O}(\alpha)$. The Fermi function includes the dominant electromagnetic effect, though an accurate extraction, or bound, of the neutrino mass does demand the inclusion of the remaining $\mathcal{O}(\alpha)$ correction. We shall demonstrate this point explicitly. This last effect, termed the radiative correction, is conventionally separated into an "inner" piece Δ_R, which is absorbed in $|\mathcal{M}|^2$, as it is energy independent and thus of no consequence to our current study, and an "outer" piece δ_R that is due to Sirlin [2]. Since the absolute neutrino mass scale is inferred through the shape of the electron energy spectrum in the endpoint region, it is crucial to predict the shape of the theoretical spectrum with high accuracy. To this end, we update the calculation of Ref. [2] to take the energy resolution of the electron detector into account [3]. To understand the significance of this, we recall that Sirlin's function contains not only virtual photon corrections to the β-decay process but also bremsstrahlung contributions, to yield an additional real photon in the final state. Only their sum is infrared finite; the infrared divergence in each contribution is regulated by giving the photon a small mass λ, with the $\lambda \to 0$ limit to be taken after the sum has been computed and the infrared divergent pieces cancelled. The finite portion of the bremsstrahlung contribution is sensitive to the precise manner in which the experiment is effected. In Sirlin's function the energy resolution of the electron detector is implicitly assumed to be zero; that is, the e^- and γ are always distinguishable. A consequence of this is that Sirlin's function contains a logarithmic divergence as $E_e \to E_e^{\max}$. This singularity can be removed by including soft photon contributions to all orders in perturbation theory [4]; however, it can also be removed by taking the energy resolution of the detector into account, as we consider here. As a consequence the $\mathcal{O}(\alpha)$ correction we compute to the shape of the electron energy spectrum is *finite* as $E_e \to E_e^{\max}$. However, as necessary, it has no impact on the radiative correction to the total decay rate. We have shown that the shape correction associated with this $\sim 2\%$ shift mimicks a negative value of m_ν^2. We believe it is necessary to update earlier experimental analyses to take this theoretical correction into account more precisely, to realize an accurate determination of the neutrino mass. A highly accurate theoretical spectrum can be found by modifying the form used in earlier experimental analyses of ^{3}H β-decay, through the substitution $F \to F^* + (\alpha/2\pi)g(\Delta E, E_e, E_e^{\max}) + \mathcal{R}$, using $g(\Delta E, E_e, E_e^{\max})$ derived in [3] and $\mathcal{R}$ subsumes the recoil corrections. Our focus has been on $g(\Delta E, E_e, E_e^{\max})$ and $\mathcal{R}$; theoretical corrections to these terms accrue from i) $\mathcal{O}(Z\alpha^2)$ corrections, which are known, and ii) $\mathcal{O}(1\%)$ corrections to the recoil-order term, but such corrections would appear beyond the scope of current and planned experiments. The corrected Fermi function F^*, which includes corrections such as those due to the finite nuclear size and to charge screening of the nuclear charge by atomic electrons. From the viewpoint of the theoretical radiative and recoil corrections, a sub-eV determination of the neutrino mass should be possible.

References:

[1] A. Osipowicz *et al.* [KATRIN Collaboration], `[hep-ex/0109033]`.

[2] A. Sirlin, Phys. Rev. **164** (1967) 1767.

[3] S. Gardner, V. Bernard and U.-G. Meißner, Phys. Lett. B **598** (2004) 188 `[hep-ph/0407077]`.

[4] W. W. Repko and C. Wu, Phys. Rev. C **28** (1983) 2433.

*Also at HISKP, Universität Bonn

Radiative neutron β–decay in effective field theory

V. Bernard (ULP Strasbourg), S. Gardner (Kentucky), Ulf-G. Meißner*, C. Zhang (Kentucky)

Experimental studies of β–decay at low energies have played a crucial role in the rise of the Standard Model (SM). In recent years, continuing, precision studies of neutron β–decay have been performed, to better both the determination of the neutron lifetime and of the correlation coefficients. Taken in concert, these measurements yield the weak coupling constants g_V and g_A; g_V, in turn, yields the Cabibbo-Kobayashi-Maskawa (CKM) matrix element V_{ud} and, with the empirical values of V_{us} and V_{ub}, the most precise test of the unitarity of the CKM matrix. As the neutron measurements improve, further SM tests become possible, such as a precision test of the CVC hypothesis, as well as of the absence of second-class currents, yielding, generally, improved constraints on the appearance of non-$V-A$ currents. To realize a SM test to a precision of $\sim 1\%$ or better requires the application of radiative corrections. One component of these corrections, the "outer" radiative correction, is captured by electromagnetic interactions with the charged, final-state particles, in the limit in which their structure is neglected. In this, neutron radiative β–decay enters, and we consider it explicitly [1]. We find neutron radiative β–decay interesting in its own right, though the process has yet to be observed — only an upper bound exists. Anticipating its measurement, however, and as the precision of such improves, we can (i) hope to effect an alternative determination of the weak couplings g_V and g_A. (ii) We can study the hadron matrix elements in subleading order, $\mathcal{O}(1/M)$, with M the neutron mass. Here, we note the connection to radiative muon capture on the proton, which permits the determination of the induced pseudoscalar coupling constant g_P. (iii) We can use neutron radiative β–decay to test the Dirac structure of the weak current, through the determination of the circular polarization of the associated photon. As recognized shortly after the discovery of parity violation in β–decay, the photon emitted in associated radiative processes should be circularly polarized. In integrating over the phase space, it becomes apparent that the photon becomes $\sim$100% polarized only when its energy grows large; in our explicit calculations we confirm that the predictions for internal bremsstrahlung, i.e., for radiative orbital electron capture of S-state electrons, are germane to radiative β–decay as well. This prediction follows from a perfectly right-handed antineutrino and from the absence of scalar, tensor, and pseudoscalar interactions in leading order.

In this work [1], we perform a systematic analysis of neutron radiative β–decay in the framework of heavy baryon chiral perturbation theory (HBCHPT) and in the small scale expansion (SSE) (including explicit delta degrees of freedom), including all terms in $O(1/M)$, i.e., at next–to–leading order (NLO) in the small parameter ϵ. Here, ϵ collects all the small external momenta and quark (pion) masses, relative to the heavy baryon mass M, which appear when HBCHPT is utilized; in case of the SSE, such is supplemented by the $\Delta(1232)$–nucleon mass splitting, relative to the nucleon mass, as well. These systematic EFTs allows one to calculate the recoil-order corrections in a controlled way. In order to assess the size of the recoil-order corrections, we compare with the pioneering work of Ref. [2], in which such effects have been neglected. In that calculation, the standard parameterization of the hadronic weak current in terms of the weak coupling constants suffices to capture the hadron physics. No reference to photon emission from the effective four–fermion vertex is found in these papers. Here, we include all terms in $O(1/M)$, utilizing the framework of HBCHPT and the SSE for the actual calculations. In fact, the pertinent two– and four–point functions can be taken directly from Ref. [3], after relabelling the momenta and such.

To summarize the findings of [1]: We have computed the photon energy spectrum and photon polarization in neutron radiative β–decay in including all terms in $\mathcal{O}(1/M)$. The leading contribution to the photon energy spectrum has been calculated previously [2]; we agree with the expression in Ref. [2] for $\sum_{\text{spins}} |\mathcal{M}|^2$, though we disagree with their numerical results for the photon energy spectrum. Moreover, we find that the $O(1/M)$ terms are numerically quite small, generating contributions no larger than $\mathcal{O}(0.5\%)$, so that radiative neutron β–decay is quite insensitive to nucleon structure effects beyond those encoded in g_V and g_A — and offers no clear resolution of the muon radiative capture problem. On the other hand, we have found that nucleon structure effects have a similarly negligible role in the determination of the photon polarization, so that a precise measurement of the photon polarization may well offer a crisp diagnostic of non-SM effects. Such studies may complement other new physics searches. For example, the (pseudo-T-odd) transverse muon polarization $P_\mu^\perp$ in $K^+ \to \mu^+\nu\gamma$ decay is sensitive to large squark generational mixings in generic supersymmetric models — such charged-current processes are not constrained by flavor-changing-neutral-current (FCNC) bounds. Such mechanisms modify the photon polarization as well, and can also act to modify the $d \to u$ charged, weak current at low energies, to impact the photon polarization, as is our concern here. Finally, we note that the polarization of the photon in radiative B-meson decay, namely in $b \to s\gamma$ decay, is also left-handed in the SM, modulo $\mathcal{O}(1/M_B)$ corrections, estimated to be of order of a few percent; it is also sensitive to non-SM operators, as we have discussed here.

References:

[1] V. Bernard, S. Gardner, U.-G. Meißner and C. Zhang, Phys. Lett. B **593** (2004) 105 [Erratum-ibid. B **599** (2004) 348] [arXiv:hep-ph/0403241].

[2] Y. V. Gaponov and R. U. Khafizov, Phys. Atom. Nucl. **59** (1996) 1213 [Yad. Fiz. **59** (1996) 1270]; Phys. Lett. B **379** (1996) 7; Nucl. Instrum. Meth. A **440** (2000) 557.

[3] V. Bernard, T. R. Hemmert, and U.-G. Meißner, Nucl. Phys. A **686** (2001) 290.

*Also at HISKP, Universität Bonn

4 Accelerator Division

SPIN@COSY: Spin manipulation of vector and tensor polarized beams stored in COSY

M.A.Leonova[1], A.D.Krisch[1], V.S.Morozov[1], R.S.Raymond[1], D.W.Sivers[1], and V.K.Wong[1]
R.Gebel[2], A.Lehrach[2], B.Lorentz[2], R.Maier[2], D.Prasuhn[2], A.Schnase[2], and H.Stockhorst[2]
D.Eversheim[3], F.Hinterberger[3], H.Rohdjeß[3], and K. Ulbrich[3]
K.Yonehara[4]

Introduction

Many polarized beam experiments are performed in circular accelerators and storage rings such as the MIT-Bates Storage Ring, COSY, RHIC at Brookhaven and HERA at DESY. Frequent spin direction reversals can significantly reduce the systematic errors in such spin asymmetry measurements. Spin resonances induced by either an rf-solenoid or rf-dipole can produce such spin-flips in a well-controlled way. At high energy, the spin-flipping efficiency with an rf-dipole should be essentially independent of energy due to the Lorentz invariance of a dipole magnet's $\int B\,dl$; this is important for very high energy accelerators and colliders with polarized beams.

Spin manipulation studies of vertical polarized protons, vector and tensor polarized deuterons, and the investigation of higher order resonances were carried out by the international Spin@COSY collaboration. The presented results were achieved by utilizing a modified rf dipole with a new coil design to allow running at a higher current with further field enhancement by a surrounding ferrite box.

Experimental setup

The layout for SPIN@COSY is shown in Fig. 1. The polarized beam emerging from the H^-/D^- ion source was accelerated by the Cyclotron to COSY's injection energy. The Low Energy Polarimeter (LEP), between the Cyclotron and COSY, monitored the beam's polarization before injection into COSY.

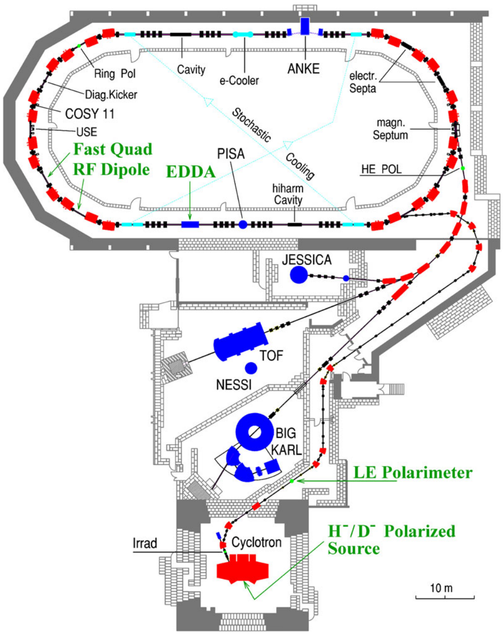

Fig. 1: Layout of the Cooler Synchrotron Storage Ring COSY, with its injector Cyclotron JULIC and polarized ion source. Also shown are, the rf dipole, the EDDA detector and the Low Energy Polarimeter.

The EDDA detector measured the beam polarization before or after the spin-manipulation. To maximize the spin flipping efficiency especially for deuterons the existing air-core copper-coil rf dipole was upgraded to increase the rf-dipole's strength. Basically its coil design was changed adding water-cooled coils to allow running at a higher current, and enclosing it in a ferrite box. The new system provides roughly 3.5 times higher integrated magnetic field of $\int B_{rms}dl$ = 0.54 T·mm compared to the rf dipole used in previous runs.

Spin manipulation of stored polarized protons

We studied the spin flipping of 2.1 GeV/c vertically polarized protons stored in COSY, by sweeping the frequency of a strong ferrite rf dipole through an rf-induced spin resonance. After finding the resonance's frequency, we varied the frequency ramp time Δt and frequency range Δf to maximize the spin-flip efficiency. At the rf dipole 's maximum strength and its optimum Δf and Δt, we used the multiple spin flip technique to measure a spin-flip efficiency of 99.92 ± 0.04%.

We determined f_r by linearly ramping the rf-dipole's frequency by $\Delta f/2 = \pm 2$ kHz around the calculated f_r; we then made ±2 kHz ramps next to each side of the previous frequency range until the beam was either spin-flipped or depolarized, as shown in Fig. 2. The data suggested that the resonance width was comparable to the ±2 kHz frequency ramps. Thus, we next studied $\Delta f/2 = \pm 1$kHz frequency ramps with different central frequencies. To map the resonance position more accurately, we then used. $\Delta f/2 = \pm 0.2$ kHz frequency ramps (see Fig. 2).

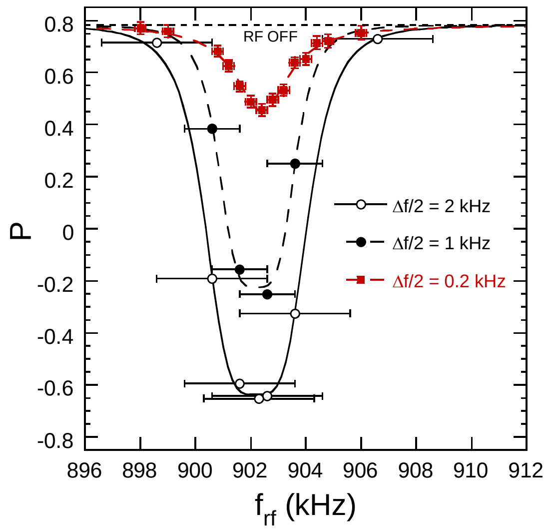

Fig. 2: The measured protons final-to-initial vector polarization ratio at 2.1 GeV/c is plotted against each ramp's frequency range Δf shown by a horizontal bar.

We then spin-flipped the proton beam by ramping the rf-dipole's frequency, with various ramp times Δt, through the frequency range $\Delta f/2$ = ±6 kHz, which seemed to safely cover the whole resonance; we measured the polarizations after each ramp. The measured data are plotted against the ramp time in Fig. 3; this suggested setting Δt near 100 ms. Since the spin-flip efficiency is never exactly 100%, the Modified Froissart-Stora Equation, Eq. (1), was earlier introduced to describe non-ideal single-flip data.

$$P_f = P_i\left\{(1+\eta)\exp\left[\frac{-(\pi\varepsilon f_c)^2}{\Delta f/\Delta t}\right]-\eta\right\} \qquad (1)$$

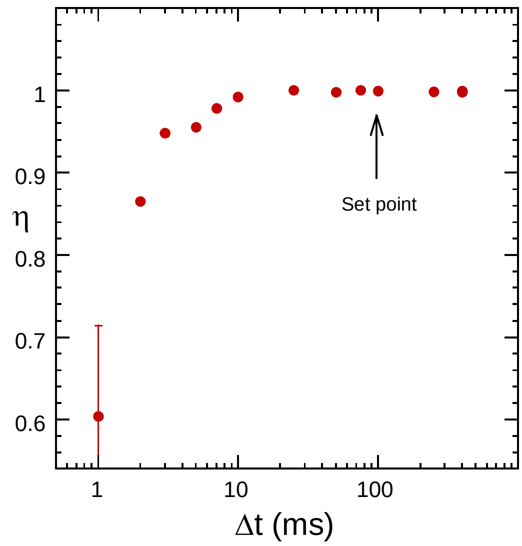

Fig. 3: The measured spin flip efficiency at 2.1 GeV/c is plotted against the rf-dipole ramp time Δt. The rf-dipole's frequency half-range $\Delta f/2$ was 6 kHz, and its $\int B_{rms}\, dl$ was 0.46 Tmm.

To more precisely determine the spin-flip efficiency, we then measured the polarization after 11 spin-flips, while varying the rf-dipole's *rms* $\int B_{rms} dl$, its ramp time Δt, and its frequency half-range $\Delta f/2$. This technique enhanced small changes in the spin-flip efficiency's dependence on the rf-dipole's parameters, because the 11th power of even a small single-spin-flip depolarization, is large.

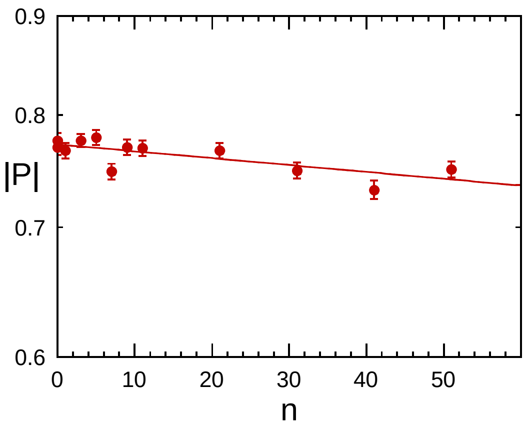

Fig. 4: The measured proton polarization at 2.1 GeV/c is plotted against the number of spin-flips. The rf-dipole's frequency ramp time Δt was 0.1 s; its frequency half-range $\Delta f/2$ was 6 kHz, and its $\int B_{rms} dl$ was 0.34 T·mm.

After setting Δt, Δf and $\int B_{rms} dl$ to maximize the spin-flip efficiency, we then measured it precisely by varying the number of spin-flips. The vertical polarization after 0, 1, 3, 5, 7, 9, 11, 21, 31, 41 and 51 spin-flips, was measured while keeping Δt, Δf and $\int B\, dl$ all fixed; these data are plotted against the number of spin-flips in Fig. 4. We fit these data using the measured $\hat{\eta}$ defined by:

$$P_n \equiv P_i(-\hat{\eta})^n, \qquad (2)$$

where P_n is the measured polarization after n flips. The fit gives a measured spin-flip efficiency of $\hat{\eta}$ = 99.92±0.04%. Note that, when the exponential in Eq. (1) goes to zero, the equation yields η = $\hat{\eta}$ for one spin-flip.

Spin manipulation of stored polarized deuterons

We also investigated the spin manipulation of a simultaneously vector and tensor polarized deuteron beam stored at 1.85 GeV/c in the COSY Cooler Synchrotron. We manipulated the deuteron's polarization by sweeping the frequency of the ferrite rf dipole through an rf-induced spin resonance and obtained a measured vector spin-flip efficiency of about 97 ± 1%. Moreover, the behavior of tensor polarization was studied in detail.

The February and December 2003 runs at 1.85 GeV/c used COSY's first stored polarized deuteron beam. We spin-flipped it by ramping the rf dipole's frequency through an rf-induced spin resonance to manipulate the polarization direction of the deuteron beam. We reduced the systematic errors by cycling the deuteron source through five states with nominal vector polarization values of 0, -2/3, -1/3, -1, +1. The vector and tensor polarizations were measured using p d elastic scattering events detected with the EDDA detector setup, making use of previously calibrated analyzing powers. The following procedure was used to optimize the rf-dipole's parameters for the highest spin-flip efficiency: we experimentally determined the resonance's frequency; then set the rf dipole's $\int B_{rms} dl$ to its maximum; and then varied its frequency ramp time Δt and frequency range Δf.

The rf dipole frequency was first centered at the spin resonance's approximate location of $f_r = f_c\ (1-|\nu_s|)$. We then ramped its frequency through ±100 Hz around the calculated f_r = 917.4 kHz; we next made ±100 Hz ramps on each side of the previous frequency range until the beam was depolarized. For these time-consuming studies, we cycled the deuteron beam through only the +1 and –1 vector polarized states. After each rf dipole ramp we measured the left-right deuteron scattering asymmetry, which was linearly proportional to the beam's vector polarization We then mapped the resonance by measuring the polarization, with the rf dipole at some fixed frequencies near 917.4 kHz. This mapping data showed a wide and shallow dip also centered at 917.4 kHz; its wide shape may be due to the rather weak rf dipole and the non-zero spin tune width.

After setting the rf dipole's $\int B_{rms} dl$ at its maximum and its frequency range at $\Delta f = \pm 100$ Hz, we spin-flipped the beam while varying its frequency sweep time Δt. The measured vector and tensor polarizations for all five deuteron spin states are plotted in Fig. 5; the curves show the fit to Eq. (3) for each polarization state.

$$\begin{aligned} P_V(\theta) &= P_V^i \cos(\theta) \\ P_T(\theta) &= P_T^i\left[\frac{3}{2}\cos^2(\theta)-\frac{1}{2}\right] \end{aligned} \qquad (3)$$

Notice that all five vector polarization curves cross zero at the same point near 8 s. Fig. 5 shows that the vector polarization was almost completely spin-flipped for the longest ramp times.

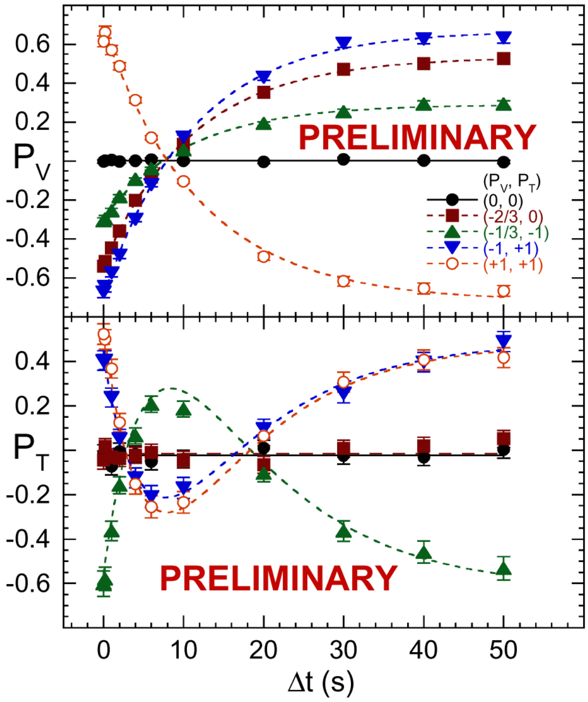

Fig. 5: The measured vector and tensor polarizations for the 5 deuteron spin states at 1.85 GeV/c is plotted vs. the rf-dipole's ramp time *Δt,* with *Δf/2* = 100 Hz. The curves are fits using Eq. (2).

The data in Fig. 5 suggest that increasing the ramp time even further would probably not significantly increase the spin-flip efficiency. This could be because the ±100 Hz frequency range did not fully overlap the resonance, which limited the maximum spin-flip efficiency. To analyze the data, we first subtracted from each asymmetry data point the unpolarized offset, shown by a solid line in Fig. 5, and then divided by its initial asymmetry. We then averaged these ratios for all four polarization states; the resulting vector and tensor spin flip efficiency are η_V= 96.4 ± 0.9% and η_T= 98.3 ± 0.9%; as expected they are consistent with each other. They give an overall spin-flip efficiency η = 97 ± 1% for the optimum ramp time.

Study of higher-order spin resonances

Finally, we examined higher-order spin resonances using 2.1 GeV/c vertically polarized protons stored in COSY. By changing the vertical betatron tune within the range 3.51 to 3.71, with fixed horizontal tune. The spin was totally spin-flipped when a first-order spin resonance was crossed; we also found partial depolarization near several third-order resonances and possibly near one second-order resonance (see Fig. 6). The analysis is ongoing, and the results will be presented at a later time.

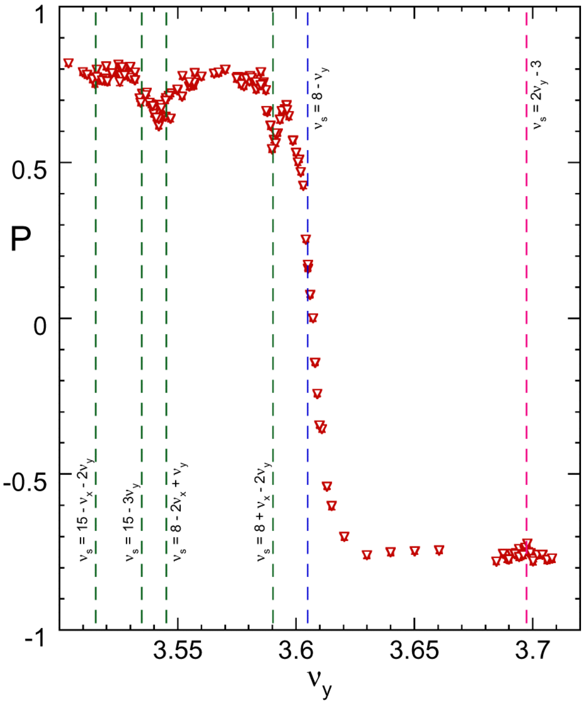

Fig. 6: The preliminary results for measured protons vector polarization 2.1 GeV/c is plotted against the vertical betatron tune of COSY. A total spin flip at the strong resonance at a tune of about 3.605 is clearly visible.

Summary and Conclusion

COSY provided a high beam polarization of above 80% for protons and up to 70% for deuterons at about 2 GeV/c beam momenta allowing us to perform precise spin flipping experiments. A remarkably high measured proton spin-flip efficiency of 99.92 ± 0.04% was achieved by using a strong ferrite-core water-cooled RF dipole. For polarized deuterons a high spin-flip efficiency of 97 ± 1 % was measured, and the dynamics of tensor polarization were studied in detail. The striking behavior of the spin-1 tensor polarization during spin-flips recently found at IUCF was confirmed. For higher order spin resonance studies, a well-elaborated procedure to move betatron tunes during the COSY cycle was developed and applied. As expected, a total spin-flip was observed at a very strong first-order intrinsic spin resonance. Third-order spin resonances were measured to be much stronger than the second-order spin resonance for our conditions.

Acknowledgements:

This research was supported by grants from the German BMBF Ministry.

[1] Spin Physics Center, University of Michigan, Ann Arbor, MI 48109-1120, USA
[2] Forschungszentrum Jülich, Institut für Kernphysik, Postfach 1913, D-52425 Jülich, Germany
[3] Helmholtz-Institut für Strahlen- und Kernphysik, Universität Bonn, D-53115 Bonn, Germany
[4] Dept. of Biological, Chemical, and Physical Sciences, Illinois Inst. of Technology, Chicago, IL 60616, USA

Characteristic Features of Electron Cooling at COSY

J. Dietrich, V. Kamerdzhiev, Yu. Korotaev[1], R. Maier, I.N. Meshkov[1], D. Prasuhn, A. Sidorin[1], H.J. Stein, H. Stockhorst

In June and September 2004 two weeks of beam time were dedicated to studies of some characteristic features of electron cooling at COSY. In this contribution results on the lifetime and the intensity dependence of the ion beam dimensions are reported. Stripping injection of H^- or D^- ions in combination with electron cooling allows to increase the stored ion intensity by repeated injections (transverse stacking). Fig. 1 shows a characteristic stacking procedure of 45 MeV protons with 7 injections every 20 s resulting in an equilibrium beam current of about 3.8 mA after 120 s. A transverse feedback system stabilizes the ion beam against vertical and horizontal coherent oscillations. Otherwise fast beam losses would limit the intensity below 1 mA [1]. The achieved stacked intensity is determined by the balance of newly injected protons and the beam losses between consecutive injections. There is a fast loss during the cooling time of about 10 s (see the time evolution of the neutral particle detector rate) followed by a slow loss which is obviously exponential, i.e. the higher the stored proton intensity the higher are these slow losses. No essential intensity gain is obtained when the time interval between injections is reduced to 10 s but the equilibrium is reached already after half the time, Fig. 2.

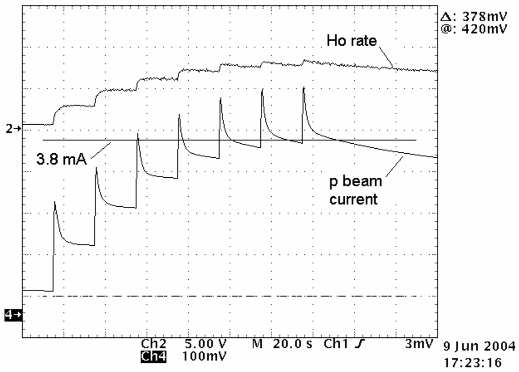

Fig. 1: Stacking of the proton beam intensity by 7 repeated injections every 20 s. Equilibrium is reached at 3.8 mA after 120 s. The time dependence of the neutral particles rate (H^0 rate) indicates that the proton beam is fully cooled in less than 10 s. Applied electron beam current 170 mA (1 inch beam diameter). Tunes: $Q_h = 3.61$, $Q_v = 3.66$.

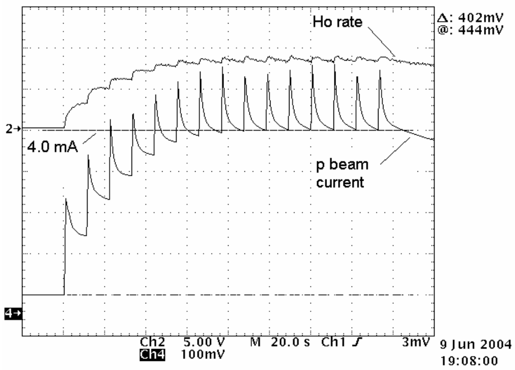

Fig. 2: Stacking by 15 repeated injections every 10 s. Equilibrium at 4.0 mA after 60 s.

The losses are of incoherent nature only since no betatron frequencies in the transverse Schottky spectrum were seen in the time interval covered by Fig. 1 and Fig. 2. However, slight horizontal oscillations suddenly occurred after the beam intensity had fallen below a sharp, reproducible threshold of 2.68 mA. The horizontal feedback was not fully implemented at that time [2].

Lifetime of the proton beam under cooling conditions

The continuation of the decay of the beam intensity after new injections are stopped was once more measured during the September beam time, here definitely free of transverse oscillation over the whole intensity range since also the horizontal feedback was fully operational. The decay of the beam within the following 1000 s is shown in Fig.3. The electron beam still continues beam cooling, maintaining small beam emittances. The closer analysis of the "instantaneous" lifetime

$$\tau_{inst} = I/(dI/dt) \qquad (1)$$

reveals a 1/e lifetime increasing from 400 s up to a more or less constant value of 800 s, see Fig. 4.

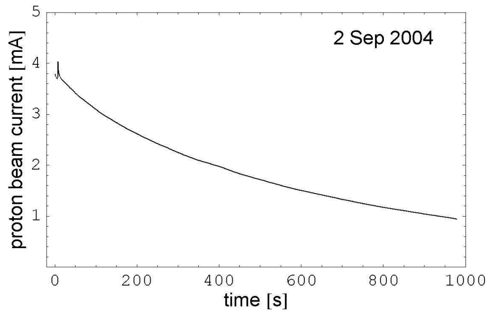

Fig. 3: Approximately exponential decay of the stacked proton beam intensity after the last injection. Electron current 170 mA. $Q_h = 3.620$, $Q_v = 3.645$.

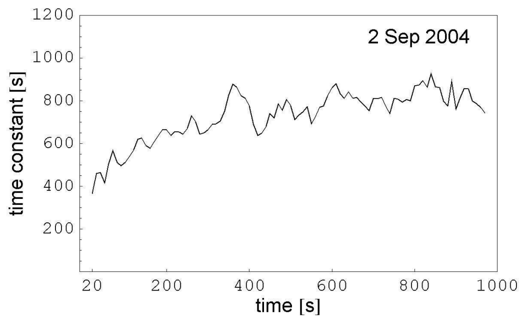

Fig. 4: Instantaneous time constant of the decay curve shown in Fig.3. The 1/e lifetime is shorter at higher proton intensities. The fluctuations are mainly caused by the numerical evaluation, Eq.(1).

The reasons for this surprisingly short lifetime as well as its intensity dependence are not quite clear. We present the result as an experimental fact without having at hand a conclusive explanation. A first candidate certainly to be considered is single Coulomb scattering on residual gas atoms with angles larger than the mean acceptance angle of the ring. The vacuum pressure around the COSY ring is typically a few 10^{-9} mbar which is by 2 orders of magnitude higher then in other storage rings. Despite

Influence of Electron Beam Neutralization on the Stability of Electron-Cooled Ion Beams

J. Dietrich, V. Kamerdzhiev, Yu. Korotaev[1], R. Maier, I.N. Meshkov[1], D. Prasuhn, A. Sidorin[1], H.J. Stein, H. Stockhorst

The stability of the antiproton beam at the HESR ring of the FAIR project (GSI) in presence of neutralizing ions inside the cooling electron beam is discussed in Ref. [1]. It is shown that even a few percents of neutralization can appreciably decrease the stability threshold. Residual gas ions trapped in the electron beam oscillate in the longitudinal magnetic field of the cooler solenoid and the transverse electric field of the electron beam with frequencies determined by

$$\omega = \sqrt{\omega_i^2\left(1-\eta_{neutr}\right)+\omega_B^2/4} \pm \omega_B/2\,, \qquad (1)$$

where $\omega_B = ZeB/Am_p$ is the cyclotron frequency of an ion with mass Am_p and charge Ze in the magnetic field B, $\omega_i^2 = Ze^2n_e/2Am_p$ is the ion plasma frequency in the electron beam with a density n_e.

The influence of electron beam neutralization on the ion beam stability was experimentally proved at HIMAC [2]. In the COSY electron cooler the natural neutralization η_{neutr} is rather high, about 0.37 [3]. Cooling experiments at COSY with 45 MeV protons (June and September 2004) attempted to clear the electron beam from one or the other ion species by resonant excitation of the ion oscillations with a transverse sinusoidal electric field. This field was applied to the position pick-ups in the cooling section, the so called "shaker". If the shaker frequency is equal to the ion oscillation frequency the ions leave the electron beam very fast. The diminished neutralization leads to a deeper space charge depression and, therefore, a lower electron beam energy observable by a decrease of the revolution frequency of the ions circulating in the ring. The original revolution frequency is readjustable by increasing the electron gun cathode potential. Fig.1 shows the necessary change of the electron beam energy in dependence on the shaker frequency.

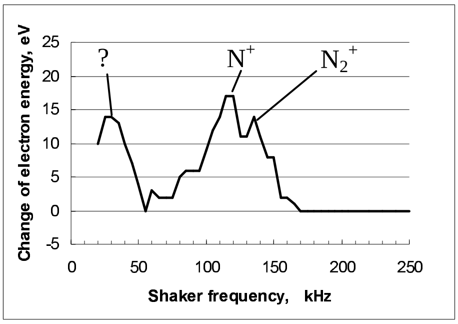

Fig.1: Spectrum of shaker frequencies. Electron beam current 170 mA (1 inch beam diameter), magnetic field in the cooling section 0.08 T, β = 0.299.

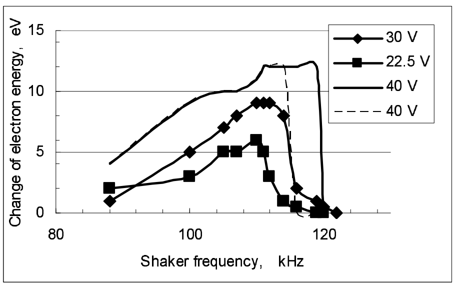

Fig. 2: Shape of the resonant peak between 90 and 120 kHz as function of the shaker voltage amplitude.

The measurements were performed at different shaker amplitudes ranging from 10 to 60 V. The width of the resonant peaks increases at higher voltages, Fig. 2. The peak shape is typical for a nonlinear resonance revealing a hysteresis behavior at the highest applied voltage of 40 V.. Increasing the shaker frequency, solid line in Fig. 2, the neutralization first decreases monotonically, but at a certain frequency it suddenly jumps back to the initial value. Decreasing the shaker frequency again, the opposite jump occurs at a smaller frequency, dashed line in Fig. 2.

The influence of the neutralization on the proton beam stability at COSY is well illustrated in Fig. 3. Without shaker or at nonresonant shaker frequencies a coherent instability leads to fast particle losses after 25 s, Fig. 3 a. Clearing the electron beam from one of the ion species, here presumably N^+ by applying a 114 kHz shaker frequency, the instability develops much later, i.e. after 65 s. Additionally, the ion loss rate is about 3 times smaller, Fig. 3 b.

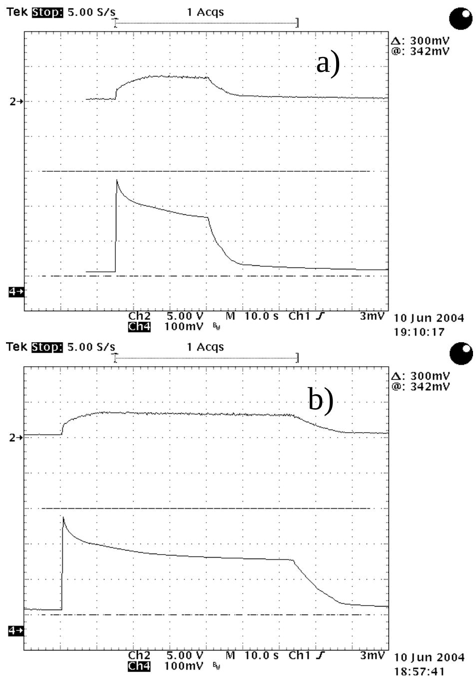

Fig. 3: Proton beam current (lower curve) and H^0 count rate (upper curve) versus time when no feedback is applied to stabilize the beam: a) Shaker off or nonresonant excitation, b) Excitation with the resonant frequency of 114 kHz. 100 mV/div correspond to 1 mA beam current

References:

[1] P. Zenkevich, A. Dolinskii and I. Hofmann, NIM A 532 (2004), 454.

[2] I.N.Meshkov et al., Ion lifetime at cooling stacking injection in HIMAC, HIMAC-087, May 2004.

[3] A. Sidorin, I.N. Meshkov, H.J. Stein, H. Stockhorst, Natural Neutralization in the Electron Beam of the COSY Electron Cooler, IKP Annual Report 2001.

[1] JINR, Dubna

Stable Longitudinal Collective Modes in an Intense Electron Cooled Proton Beam

H. Stockhorst

Longitudinal Schottky fluctuation spectra as e.g. observed at COSY are nearly Gaussian in shape as long as forces due to the beam-environment interaction acting back on a debunched proton beam are small. Increasing the particle interactions generates electromagnetic fields that induces collective motions of the beam as whole. As a result these correlations deform the longitudinal Schottky fluctuation spectra and furthermore may lead to beam instabilities [1]. The theoretical details of the electromagnetic fields produced by collective interactions of the beam with itself and its environment are usually quite complicated and require to solve Maxwell´s equations with boundary conditions of the underlying geometry of the beam surroundings. All these items can be covered by a coupling impedance which is in general a complex and frequency dependent quantity. It is possible to measure these impedances for high intense and cooled beams by analyzing the distorted Schottky fluctuation signals solely with a spectrum analyzer [2].

Figure 1 shows longitudinal Schottky spectra for an electron-cooled proton beam for different numbers of stored particles at injection momentum $p = 293.75\ MeV/c$. The spectra were recorded at the 5^{th} revolution harmonic with $5 \cdot f_0 = 2.441151\ MHz$ and $N = 6.4 \cdot 10^9$, $1.3 \cdot 10^{10}$, $2.6 \cdot 10^{10}$, $3.4 \cdot 10^{10}$, $4.8 \cdot 10^{10}$, corresponding to BCT readings *50 mV, 100 mV, 200 mV, 268 mV, 378 mV*, respectively. Clearly visible is the double structure lines with respect to the 5^{th} revolution harmonic.

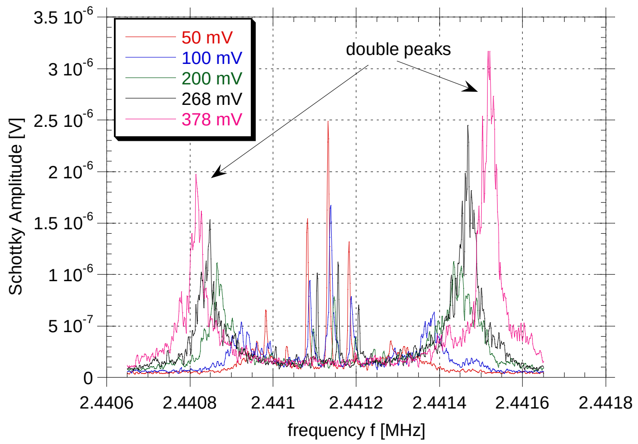

Fig. 1: Longitudinal beam spectrum at the 5^{th} revolution harmonic of an electron-cooled beam for different numbers of stored protons at injection energy. Besides the double peaks marked with arrows the spectrum contains also sharp lines resulting from transverse beam oscillations.

The peak distance versus stored particle number is displayed in figure 2. According to theory [1] this double peak structure can be explained by a longitudinal capacitive impedance $Z_{long}(f)$ which leads below transition energy to stable longitudinal oscillation modes with frequencies

$$f_n = nf_0 \pm \Delta f_n \tag{1}$$

determined by the frequency shift

$$(\Delta f_n)^2 = i\frac{e^2 N f_0^3 \eta Z_{long}(f) n}{\beta^2 E}. \tag{2}$$

N denotes the number of stored particles, e is the elementary charge and E is the total energy with corresponding kinematic β. The frequency slip factor is $\eta = 1/\gamma^2 - 1/\gamma_{tr}^2$ and is positive at injection energy.

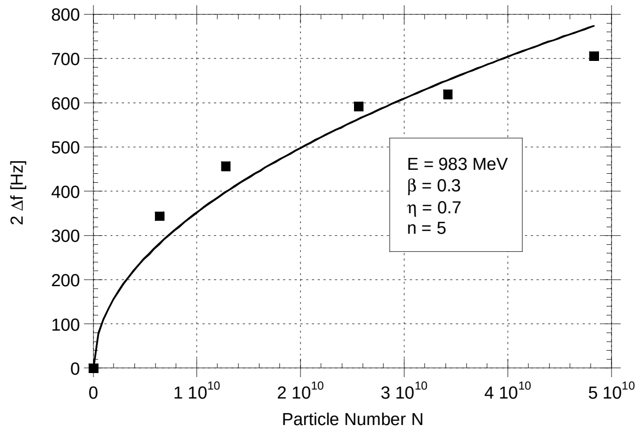

Fig. 2: Peak distance versus number of stored protons. The curve is a fit to the data according to eq. (2) assuming a pure capacitive impedance.

A fit according to eq. (2) to the data yields a capacitive impedance $Z_{long}(f) = -i\ 4.2\ k\Omega$ or normalized to the harmonic $n = 5$, $Z_{long}(f)/n = -i\ 840\ \Omega$. A rough estimate of the pure space charge impedance for round beams can be found from [3]

$$\frac{Z_{long}^{SC}(f)}{n} = -i\frac{Z_0}{2\beta\gamma^2}\left[1 + 2\ln\left(\frac{b}{a}\right)\right] \tag{3}$$

with the beam pipe radius b, the beam radius a and $Z_0 = 377\ \Omega$. For strongly cooled beams this impedance is significantly larger then $-i\ 570\ \Omega$ for $b \approx a$ and is thus larger then the measured coupling impedance. This outcome indicates that the electron cooler may have a damping effect on the two coherent modes resulting in a smaller impedance. However, further measurements especially covering a wide range of revolution harmonics are needed to study the damping effects of the electron cooler at COSY in more detail.

References:

[1] S. Chattopadhyay, "Some Fundamental Aspects of Fluctuations and Coherence in Charged-Particle Beams in Storage Rings", CERN 84-11

[2] W. Schwab, "Experimente zur Elektronenkühlung am Niederenergie-Antiprotonen-Speicherring (LEAR)", Kernforschungszentrum Karlsruhe, KfK 4673, Juni 1990

[3] U. Oeftiger, "Measurement of Beam Properties and Beam Environment in LEAR and COSY Using RF Excitation Methods", Institut für Kernphysik Jül-2977

Luminosity Considerations for Internal and External Experiments @ COSY

A. Lehrach, D. Prasuhn

Recently the WASA Collaboration, the Institut für Kernphysik of the FZ-Jülich, and the COSY team started to investigate the possibility to migrate and install the WASA detector at the Cooler-Synchrotron COSY [1], after the present nuclear and particle physics research program with the WASA detector has been completed at the CELSIUS ring of The Svedberg Laboratory. Different internal and external detector areas at COSY are considered [2]. Luminosity estimates for the WASA implementation at COSY are discussed in this paper.

Peak Luminosity

In 2003 the number of unpolarized protons at maximum momentum could be increased significantly up to $1.5*10^{11}$ particles [3]. This was achieved with single injection and without electron cooling. To get acceptable beam life times, internal targets have to be very thin or a powerful beam cooling system in needed. External targets are thicker by orders of magnitudes. In table 1 typical target thicknesses are summarized.

Table 1: Typical thickness of internal and external targets in medium energy hadron accelerator.

Type of target (internal)	Thickness [atoms/cm^{-2}]
Atomic beam	10^{12}
Atomic beam with storage	10^{14}
cellClusterPelletSolid	10^{14}
	10^{15}-10^{16}
	10^{16}-10^{18}
Type of target (external)	**Thickness [atoms/cm^{-2}]**
SolidLiquid hydrogen /	>5*10^{19}
Solid polarized (3.2mm)	
	2*10^{22}

In Fig. 1 the internal and external peak luminosity is plotted for different numbers of circulating or extracted particles in COSY versus target thickness.

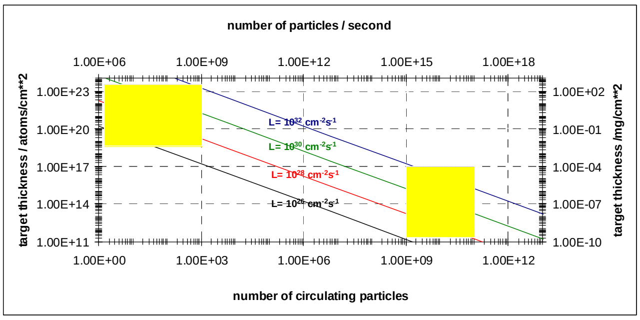

Fig. 1: Peak luminosity for internal and external experiments for typical target thicknesses at COSY. The internal luminosity is calculated for a particle revolution frequency of 1MHz in COSY (right yellow area), the external luminosity with an extraction time of 100s (left yellow area).

The peak luminosity at COSY is in the range of 10^{26}-10^{32}cm^{-2}s^{-1}, depending on the target thickness and number of circulating or extracted particles.

Average Luminosity

To calculate the average luminosity for COSY, machine cycles and beam preparation times have to be specified. In table 2 typical beam preparation times are summarized.

Table 2: Beam preparation time for different machine cycles.

Type of beam preparation	Time
Beam injection and accumulation	200ms
Acceleration	2 to 3s
Beam preparation for experiments	up to 3s
Magnet down ramp	2 to 3s
Distance between two cycles	1s
Cooling and single injection	10s
Cooling and stacking injection	up to 15min

The beam life time of internal beams passing through different targets are shown in table 3.

Table 3: Beam life time for circulating COSY beams .

Type of internal target	Time
Solid targets	ms to s
Pellet targets	minutes
Cluster targets	below 1h
Cluster targets with stochastic cooling	couple of hours
Atomic beam targets	10 to 100h
Without target	10 to 100 h

The average luminosity as function of the experimental (beam on target) time is given by:

$$\bar{L} = L_0 \frac{\tau[1-e^{-\frac{t_{exp}}{\tau}}]}{t_{exp}+t_{prep}},$$

where L_0 is the initial luminosity, τ the beam life time, t_{exp} the beam on target time per cycle and t_{prep} the beam preparation time.

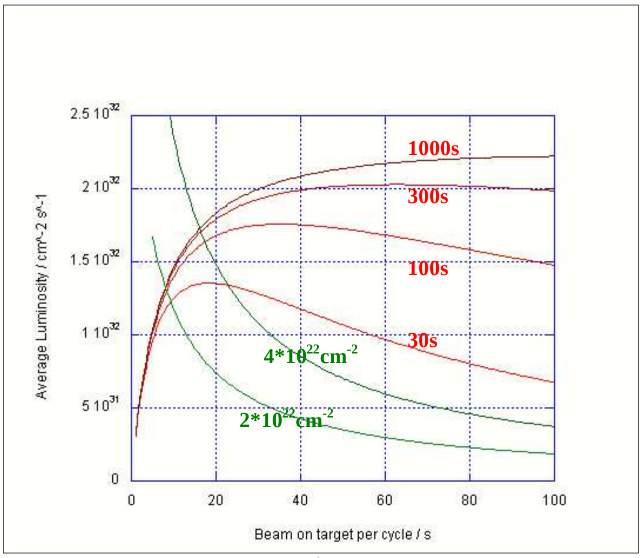

Fig. 2: Average luminosity for internal experiments with a pellet target thickness of $2.5*10^{15}$cm^{-2} (red lines), and external experiments with liquid target

thicknesses of 2 - $4*10^{22}cm^{-2}$ (green lines), 10^{11} circulating particles and a total beam preparation time of 7s. The average luminosity is plotted for different internal beam life times and external target thicknesses versus the beam on target time per cycle.

In Fig. 2 the average luminosity for internal and external experiments is plotted versus the beam on target time per cycle. In general, the extraction time should be short to get high external luminosity. Utilizing the slow extraction system of COSY, the spill structure gets worse for short extraction times. The internal luminosity strongly depends on the beam life time. Beam cooling is needed for cluster or even thicker targets to increase the beam life time. With a pellet target in COSY and without powerful beam cooling the beam life time is expected to be in the range of minutes, depending on the beam energy. The beam life time can be increased significantly with bunched beams to compensate for the mean energy loss of the beam [4].

References:

[1] Discussed at the FINUPHY Workshop on Advanced Electromagnetic Calorimetry and its Applications: Physics with a 4π Detector at COSY (FEMC04), January 26-29, 2004 Jülich.

[2] H. Schneider, private communication.

[3] See highlights of these proceedings.

[4] Calculations by H. Koch.

Beam Profile Measurements by Light Radiation of Excited Gas Atoms

J. Dietrich, N.I. Balalykin+, C. Böhme‡, V. Bykovsky+, V. Kamerdzhiev, I.N. Meshkov+, I. Mohos, A.N. Parfenov+, T. Weis‡

Interaction of an ion beam passing through a gaseous media results in atom excitation and / or ionization. The products of both processes can be used to determine the ion beams location and distribution. The methods based on registration of the ionization products (ions or electrons) are developed rather widely [1]. Another possibility is the registration of the light radiated by excited atoms.

One of the first attempts in application of light radiation of atoms excited by the beam particles was reported in [2]. The methods of construction beam position and profile monitors were proposed in [3, 4, 5]. The beam profile monitor setup has been proposed and preliminary measurements were performed at the Nuclotron in JINR Dubna [4] and COSY-Jülich [6]. Beam profile measurements were reported on the ICFA mini-workshop in Oak Ridge in 2002 [7].

Two main advantages are expected for using the light emission in order to measure the beam profile: First, the measurements are non-destructive, as only the residual gas is used. Second, the measurements are faster compared to the similar setup for detecting the electrons and ions being produced from the residual gas. But, usually in accelerators a good vacuum is needed and so only a very small amount of residual gas is present. Also the cross section for light emission is much lower compared to the production of electrons / ions. This leads to a small quantity of photons being available for detecting.

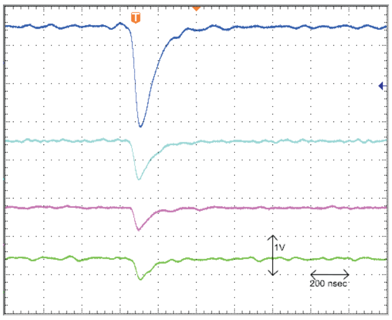

Fig. 1: Oscillogram picture of light signals registered at pressure of N_2 of 16 mbar, number of particles $5 \cdot 10^9$, energy 1.3 GeV. Bunch length $\approx 100 nsec$.

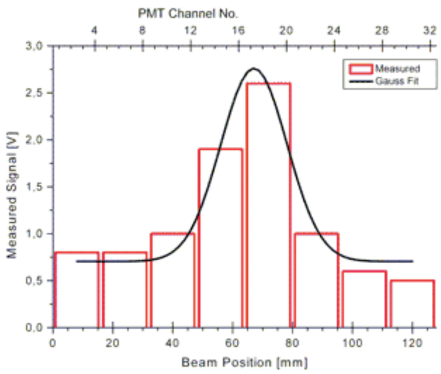

Fig. 2: Gauss fit of detected beam profile. For this experiment the 7^{th} and 8^{th} groups (right in picture) were darkened for visible light.

For the first experiments a chamber was constructed by JINR Dubna and installed at the JESSICA beamline, where the light at high gas pressure, up to atmospheric level, was detected. The light was detected with a Hamamatsu 32 channel linear array photomultiplier (PM), in which each 4 channels were combined, resulting in 8 groups for the read out. The complete electronic setup for control and readout of the PM was developed and build at the IKP, FZ-Jülich [8]. In Fig. 1 the signal readout for 4 groups is exemplary presented. In Fig. 2 the approximated beam profile, using all eight groups, is presented, assuming the beam distribution is a gaussian profile. Finally the beam was slightly shifted in the vertical plane. The measured profiles of the shifted and non-shifted beams are shown in Fig. 3.

With the first experiments we have found the principle of detecting the beam position through the emitted light of the residual gas is feasible. As the presented experiments didn't use much of the capabilities the PM has, approximation to typical storage ring pressures seems to be possible. In the presented setup measuring below 0,1 mbar was not feasible because of large background noise. In Fig. 2 the different amplitudes of the PM groups is shown. In this setup, the 7^{th} and 8^{th} group were shielded from visible light by a black paper. The level of background in this groups is not much lower compared to the open groups. This leads to the guess, mainly other ionizing radiation is the cause of the background. So one of the next objectives is to decrease this background.

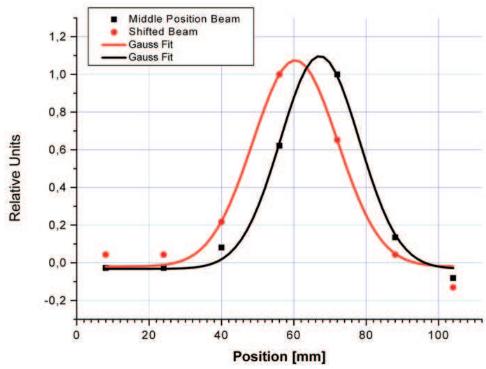

Fig. 3: Beam profiles in initial position (black) and shifted one (red).

References:

[1] V.Kamerdzhiev and J.Dietrich, IKP Annual Report 2001, Jl-3978.

[2] R.G. Bikmatov, L.G. Boriskin, V.I. Kudelaynen, I.N.Meshkov, V.V. Parkhomchuk, Atomnaya Energia, vol. 24, № 1, 1967.

[3] O.I. Brovko, I.N. Meshkov, A.N. Parfenov, Patent № 2212690, priority of 27.07.2001, Moscow, Russia.

[4] O.I. Brovko et al., Proc. of the Int. Workshop Rel. Nuc. phys: from hundreds of MeV to TeV. (Varna, BG, Sept. 10-16, 2001), pub. by JINR, 2001. vol. 1, pp.89-94.

[5] M.A.Plum et al., Nucl. Instr. Meth. A492 (2002), p.74.

[6] J.Dietrich et al., IKP Annual Report 2002, Jl-4052.

[7] M.Plum, 11th ICFA International Mini-Workshop on Diagnostics for High-Intensity Hadron Machines, Oak Ridge, Oct. 21.-23., 2002.

[8] I. Mohos, private communication.

+ JINR Dubna, Russia; ‡ University Dortmund, Germany

Modern Acceleration Cavities for Particle Rings

A. Schnase, on sabbatical [1]

The J-PARC complex [1], under construction in Tokai is planned to deliver high intensity protons at 3GeV to a neutron target and at 50 GeV to a target for neutrino studies. The synchrotron ring for 3GeV – RCS – (Rapid Cycling Synchrotron) will accelerate protons from 181MeV to 3 GeV in 20ms. The MR (Main Ring) will accelerate from 3 GeV to 50 GeV in around 2 seconds. In both synchrotron rings, acceleration cavities based on Magnetic Alloy (MA) are used, which require no tuning as compared to standard ferrite cavities [2], [3], [4].

Table 1: Main Parameters

	RCS	MR
Acceleration voltage	450 kV	280 kV
Acceleration frequency	0.94-1.67 MHz	1.67-1.72 MHz
Harmonic number	h=2	h=9 (h=18)
Energy	181-3000MeV	3-50GeV
Intensity	$5x10^{13}$ ppp	$3.3x10^{14}$ ppp
Average beam current	4~7A	11A
Number of cavities	11+1	6+1
Gaps per cavity	3	3
Voltage per gap	13.6kV	15.5kV

In future, it is planned to upgrade the H^--Linac to 400MeV. Then the RCS parameters will be slightly relaxed regarding the acceleration voltage.

The shunt impedance at each cavity gap is in the order of 800 Ohm. A peak power of 140kW has to be delivered by the power amplifier to each gap. Also the beam power and beam-loading compensation need a huge amount of RF-power. In each cavity, 3 gaps are in parallel and are driven by a push-pull tube amplifier. The DC power is provided by 1.2MW anode power supplies for 10-13 kV. Approximately half of the power is dissipated in the power tetrodes, the other half goes into the beam and the MA-loaded cavity structure.

Cavity development

In order to provide a reliable operation, the cavities need to be cooled so that no part will overheat.

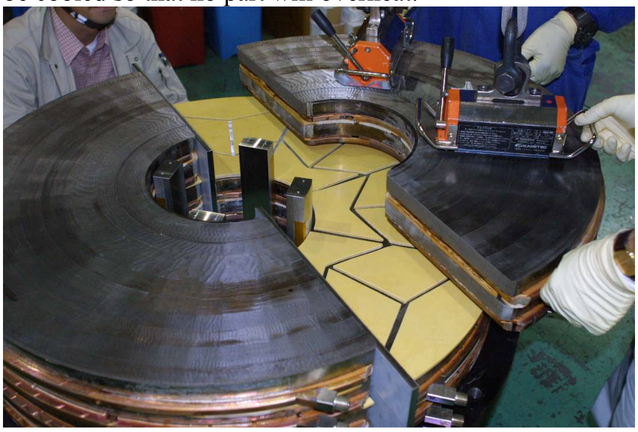

Fig.1 Stacking FineMet cores for the indirect cooled cavity

One way of cooling is "indirect-cooling" shown in fig. 1. The MA cores are bonded with BT-resin to copper cooling discs, which have water-cooling channels inside. A cavity structure of this type is shown in figure 2. In some cases the thermal contact of the MA cores to the cooling disc was weak on some point. Then local overheating could happen leading to further weakening of the heat transfer. Avoiding such problems a direct cooling design is favored for J-PARC. The water tanks before and after assembly of the cores are shown in figures 3 and 4. One cavity is a set of 6 tanks (fig. 5), to be connected to a tube amplifier.

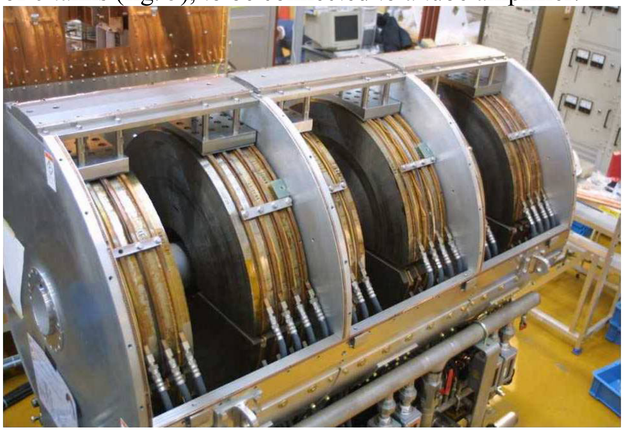

Fig.2 Assembly of a direct cooling cavity

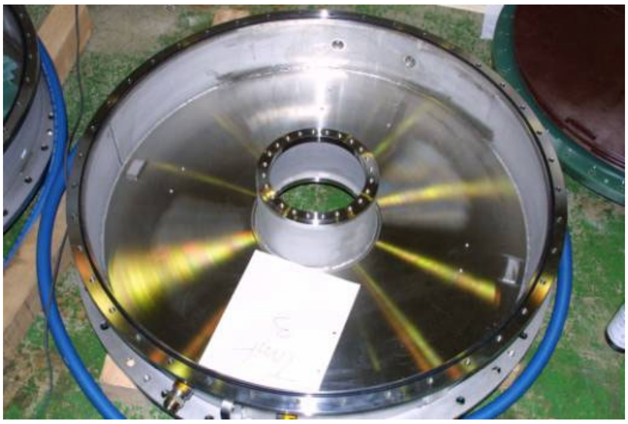

Fig.3 one tank of direct cooling cavity before assembly

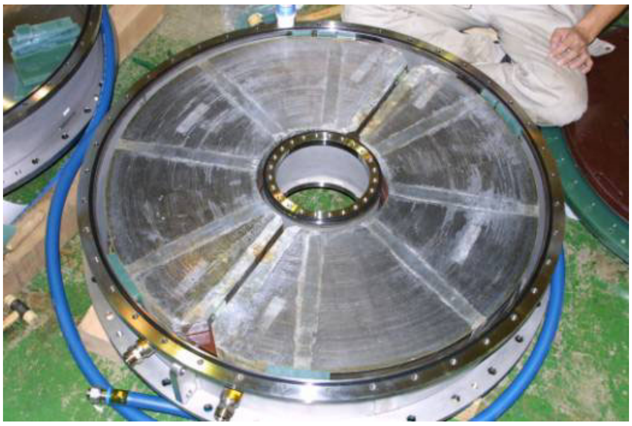

Fig.4 one tank of direct cooling cavity after assembly

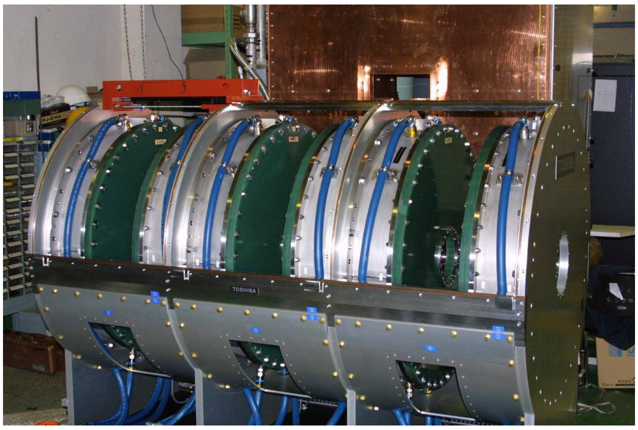

Fig.5 six tanks (3 gaps) assembled for direct cooling cavity

The structure in fig. 5 was improved by introducing design ideas of the VitroPerm cavity [5] in operation at COSY. Especially it is not necessary to put the tanks into a closed structure. Instead, the tanks are directly part of the cavity structure, as is demonstrated in figure 6.

Fig.6 the optimized cavity structure for direct cooling

Now, after taking out the beam pipe, each individual tank can be removed in case service is needed. Also alignment of the tanks is straightforward.

R&D Work for the RCS cavities

For the RCS cavity, a cut core technique is used to get an optimum Q value of 2. Such a cut is seen in fig.4. If the Q value is higher, it is not possible to cover (h=2) for acceleration and (h=4) for beam shaping within one cavity. If the Q value is too small, the cavity is too broadband and it is more difficult to compensate the beam loading at higher harmonics [3].

For Q=2, the distance between the 2 parts of each cut-core becomes less than 1 mm. Under this condition, we found, that the roughness of the cutting surface influences the local heat distribution. With water-jet cutting, the surface roughness was measured by laser scanning microscope to be in the order of 100-200 micron. Combined with tolerances and the thickness of the coating against corrosion, we could reach a Q-value of 3…4, but not 2. Preventing excessive heat on the cut surface is important, because the cooling water cannot easily find a way to go through such narrow gap space. There are 2 strategies to solve this problem: Hybrid cavity and grindstone cutting.

Hybrid cavity

We can combine 6 cut-cores set for a Q-value around 4 in the 2 center tanks with 12 un-cut cores for the 4 remaining tanks with a Q-value of 0.6 to reach the desired Q-value of 2. We will test this scheme before the grindstone cutting of the large cores has reached production status. We can set enough gap space for the cut cores in this scheme. With a PSPICE model of the cores and the tube amplifier we can simulate the behavior of the hybrid cavity.

Grindstone cutting

From the high power tests of the cavities filled with cut cores, we found the roughness on the cut surface was related to local heating. A better cut-surface quality is obtained by using grindstone cutting instead of water jet cutting, which reduces the roughness to approximately 10 micron. However, a high precision grindstone cutting machine able to cut 80…85cm cores did not exist in Japan. A company with experience in this field was asked to build such a machine. The construction of this grindstone cutting machine (fig. 7) for the large size cores finishes in spring 2005. Then we will confirm this cutting scheme after testing a cut core with 800 mm diameter.

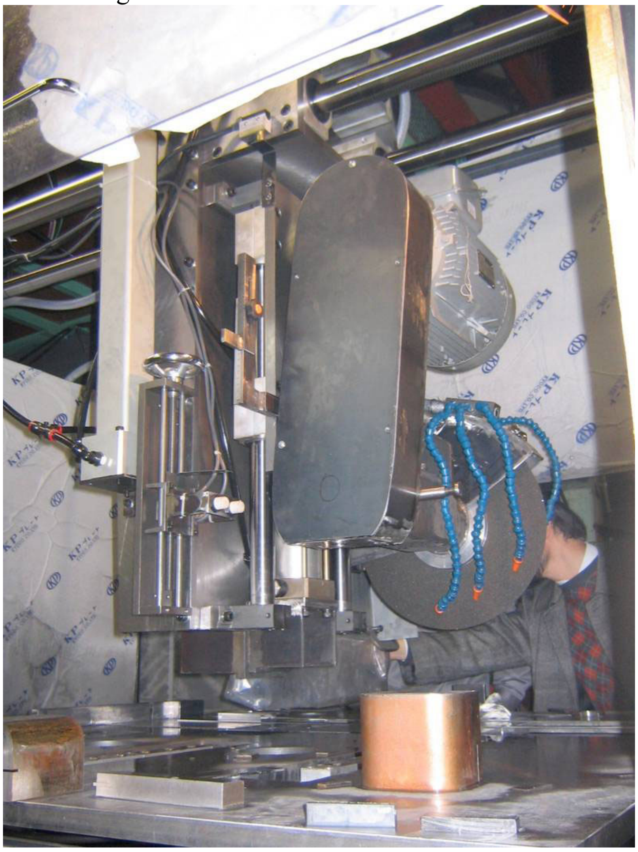

Fig.7 the grindstone cutting machine

Current status of RF system

Still, we are fighting the problem of local overheating of the cores. Therefore we analyze and optimize the water flow for cooling the MA cores. For the direct water cooling type cavity high power tests are performed at KEK with MR (Main-Ring) cavities to investigate optimum structures inside the water vessel. The RCS cavity has almost the same structure as the MR one except the size of the water vessel - the results are valid for both synchrotron rings. The 1st operational cavity for RCS will be delivered at the beginning of April 2005.

We found a model that relates the RF-power at the cavity to the temperature distribution in the cooling water. These results are fed back to the designing of the RCS cavity. In recent tests, we use fiber optic to inspect the cavities after high power test without the need for disassembly.

Currently for RCS 10 sets of tube amplifier, controller unit, anode power supply, and cavity are ordered from industry.

Final stage tube RF amplifier including controller
Construction completed: 9 sets
Under construction: 1 set
3 sets have performed and passed high power test.

Anode power supply
Construction completed: 8 sets
Under construction: 2 sets
7 sets have performed and passed high power test.

Driver amplifier
For the final stage tube amplifier, an input power of 7kW is required. The frequency range is 500kHz to 7MHz. A suitable driver amplifier, shown in fig.8, which was designed and constructed in the CERN-KEK collaboration for LHC-LEIR was tested. It is decided to use this design for the J-PARC Ring RF system.

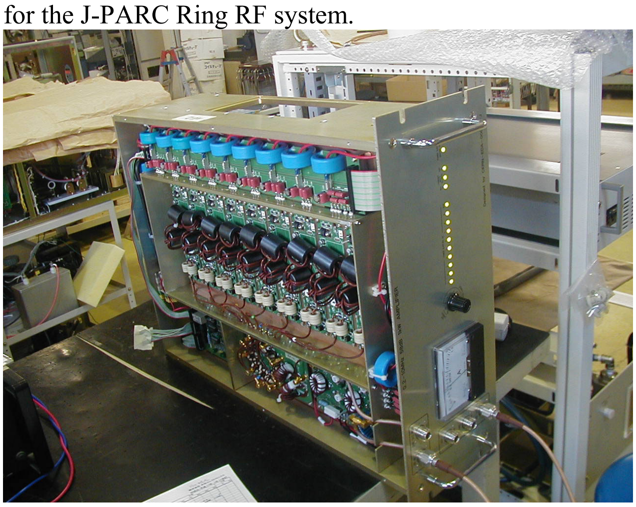

Fig.8 transistor driver 1kW designed by CERN / made in Japan.

For mass production, it was tried to construct the same amplifier module in Japan. It works well, so construction of operational driver amplifiers starts in May.2005. Nine 1kW modules with a 9:1 combiner are needed for RCS operation. The CERN 1 kW amplifier is very reliable, and it can keep running even when a FET in a 1 kW module gets broken. It has good linearity (slightly negative compression) and accepts reflected power, which is good for driving a vacuum tube control grid as load.

RF control system
At J-PARC, the linac and the 2 synchrotrons have to be synchronized to allow beam transfer with small losses. The clock frequency of the low-level systems for both rings is 36 MHz. This frequency is derived from a central 12 MHz high precision source which is also used as a reference for the Linac operating at 27*12 = 324 MHz.
The RF signal generator board based on DDS (Direct Digital synthesis) is under testing. The design of the amplitude feedback and the feed forward board for beam current compensation is finished. For RCS the RF low-level system operates with (h=2) for acceleration and (h=4) for beam shaping. Each cavity has its own independent amplitude controller for (h=2) and (h=4). The phase control between proton beam and cavities is based on the vector-sum of all cavity gap voltages.
The feed-forward system for beam-loading compensation works on harmonics (h=1…6). For each harmonic and each cavity, gain and phase offset are given by patterns.
The hardware of the low-level system is based on FPGA. For multi-harmonic operation, digital down-conversion in quadrature and filtering are the key elements. In contrast to communication applications, a small delay is crucial, as instabilities of the control loops can lead to beam loss, which is undesired-able for high intensity particle accelerators. Special tracking CIC filters have been developed combining selectivity with short delay.

Outlook
The schedules of manufacturing and installation are tight and a lot of detailed work is involved, before the commissioning phase will start. It is a challenge.

Acknowledgements
The author is very glad that he is given the chance to experience the exciting development of J-PARC in both laboratories, KEK in Tsukuba and JAERI in Tokai as a member of the J-PARC Ring RF group. We share our knowledge, contribute and learn at same time.

References
[1] http://jkj.tokai.jaeri.go.jp/
[2] C. Ohmori et.al., High Field Gradient Cavity for J-PARC 3 GeV RCS, EPAC 2004
[3] M. Yamamoto et.al., Dual Harmonic Acceleration with Broadband MA Cavities in J-PARC RCS, EPAC 2004
[4] T. Uesugi et.al., Direct-Cooling MA Cavity for J-PARC Synchrotrons, PAC 2003
[5] A. Schnase et.al., Experience with a VitroPerm cavity in COSY, IKP Annual report 2000

[1] J-PARC Ring RF group, Center for Proton Accelerator Facilities, Japan Atomic Energy Research Institute Tokai
2-4, Shirakata-Shirane, Tokai Village, Ibaraki 319-1195, Japan
e-mail: a.schnase@fz-juelich.de

Magnets, Alignment and New Installations

U. Bechstedt, G. Dolfus, R. Enge, P. Faber, G. Krol, G. Langenberg, H. Pütz,
B. Erkes, T. Sagefka, F. Scheiba

Besides many smaller activities we started intensive planning to bring the WASA detector from the CELSIUS ring at TSL Uppsala to COSY.

Magnets

In completion of the intensity upgrade program mentioned in last years report, we designed manufactured an installed an additional steering dipole magnet in the injection beam line near to the injection point. The position of the dipole is at the focus of all the different injection trajectories.
After measurement of the behavior of permanent magnet quadrupoles at cryogenic temperatures we continued to determine the influence of an outer magnetic field on the magnetization. Measurements were done in a superconducting solenoid at the University of Leipzig. Motivation for the measurements was the use of permanent magnet quadrupoles and dipoles in an Ioffe trap for the ATRAP experiment at CERN.
To perform all these magnetic measurements we calibrated quite a number of hall plates against an NMR probe in our test dipole magnet.
To get additional free space for the installation of the WASA detector it, especially for the upgrade of forward detectors, it would help if one could remove four correction dipole magnets presently installed at this location of the COSY ring. To allow for the removal of those dipoles we designed correction windings an installed them on four quadrupoles that are close to the positions of the correctors.
For the pupils` lab as well as the open house day of the research center we designed and built a number of different magnet experiments.

Installations

During 2003 there were no really big new installations. However, there has been a lot of smaller tasks and repair work.
At the cyclotron we installed new fore vacuum pumps for the cryo pumps.
After a water leak at one of the extraction steering magnets we had to service the turbo molecular pumps and dry out the fore pumps of the turbo pumps.
A leak at one of the membrane bellows of the beam stops in the injection beam line forced us to replace the bellow.
After we found a way to regenerate the ion sublimation pumps, we replaced the ion pumps in the first section of the injection beam line behind the cyclotron.
The same was done with the ion pumps in section four of the COSY ring.
The old RF system was taken out of the ring to prepare the place for the installation of the WASA detector.
An additional ion sublimation pump was installed at the ANKE facility.
At EDDA we had to replace the valve for the wire target because the target was lost and had blocked and damaged the valve. The linear motor was checked. Finally it turned out that the power supply for the motor had a fault.
The mass spectrometers in the COSY ring were tested and their ion sources were tuned. Nevertheless they show significant aging and should be replaced in near future.
A new visualization and control surface for the vacuum system was put into operation. A similar system is prepared for the cyclotron vacuum system.
The development of a fast shutter valve which was initiated by the thin vacuum windows at ANKE is close to completion. The mechanics of the valve was successfully tested. Closing time is in the range of 10 to 11 ms for an aperture of 150 mm in diameter.
For the atomic beam target at ANKE together with ZAT we found a solution to allow for a relatively quick change between cluster target and atomic beam target that will be installed in summer 2005.

Alignment

Most of the measurements at the COSY accelerator were related to the ANKE facility. The position of different detectors as well as the central spectrometer dipole had to be measured. Besides that a concept to measure positions to the tolerances required was developed. Two new reference points at the D2 were installed and measured, because one of the existing points will get lost with the installation of the atomic beam target.
Support of the institute for medicine was continued. The detectors for the PET of primates were set up an aligned at the final place in the institute.
Besides these activities we continued the support in the development of a measurement and alignment concept for the institute of plasma physics IPP.

Synchronisation of Function Generators at COSY

T.Vashegyi, N.Bongers, B.Dahmen, C.Deliege, D.Gehsing, K.Henn, M.Simon,, H.Zens

Ramp generation at COSY is done by so called function generators, which supply the dynamic power supplies with 24 bit digital values each µs.[1] Once started by an external trigger of the timing system the output of these values is clocked at 8 MHz by quartz oscillators located on the generator boards. The precision of these oscillators is fully sufficient for normal operation but the drift between them prevents special investigations at the end of long ramps, for example polarisation measurements. To overcome this limitation a new synchronisation hardware is designed for the synchronous operation of the function generators and other components of the control system at COSY. Based on the distribution of a central clock, the synchronisation together with the timing system will guarantee a highly synchronous operation of the connected components. The simple way of the distribution of the central clock enables the use of this continuous clock as a general clock on the whole area of the accelerator, not only for control components but for experiments and other hardware components too. .

The hardware components, are connected via a 10BASE-2 (Cheapernet) local area network, using a 50 Ohm coaxial cable and Media Attachment Units (MAU) at each node as the physical layer and the timing system uses a separated, distinguished network with the same hardware. This kind of coaxial physical layer with its simple bus structure, T-connections and isolated MAUs is working very reliable in our accelerator environment with a data rate of 10 Mbit/sec. The idea was to use this hardware to distribute a continuous 8 MHz clock signal to the function generators.

The central clock was realised as a VME-Board with a highly precise clock-source (a Rubidium Rival OCXO) , with three MAU interface *output* on the board for transmitting the precise clock-source and driving three bus structures at the same time. This enables a mixed star-bus-architecture where the three different Cheapernet-like coaxial buses are connected to one clock source. The number of coaxial buses is expandable - always by three buses - using more VME-boards in the same VME central clock crate. The MAU interfaces of the VME-boards are supplied by the same one OCXO clock-device source. The same type of VME-board can be used to connect a target VME-crate to a coaxial bus via an MAU interface input for receiving the central clock-signal and driving a spare VME-bus signal . Little hardware modifications have to be done for all those function-generator boards which have to be synchronised with the central clock, i.e. the local clock has to be replaced by the 8MHz clock signal from the back-panel (VME-bus P2-connector). To synchronise other fast VME-CPU- and VME-DSP-boards with the central clock in target crates - even with more 100MHz - the above mentioned hardware modifications have to be done combined with the replacement of the fast VME-board local oscillator by a PLL-clock-multiplier which one as an input the central clock from the target VME-bus uses.

References:

[1] K.Henn et. al. "Function Generation and Automatic Resynchronisation for the Dynamic Components of COSY", IKP Annual Report 1993

Overheating Protection And Monitoring System For The Electromagnetic Extraction Septum

U. Bechstedt, P. Birx, H. Borsch, G. Dolfus, T. Fest*, R. Hecker, K. Henn, K. Kruck, A. Richert, P. Richter*, D. Ruhrig, J. Schmitz, H. Schneider*, M. Simon

As observation of the temperature of the coils from the electromagnetic septum a local data acquisition system surveys the current and the two voltages (figure 1). All signals are galvanically insulated by buffer amplifiers. A digital-signal-processor (DSP) controlled system collects the different values, analyses them and, in case of overheating, it opens the interlock loop of the power converter.

In the main control room of COSY a graphical user interface (GUI) allows the remote access to the DSP system. In addition the actual current and voltages are monitored continuously.

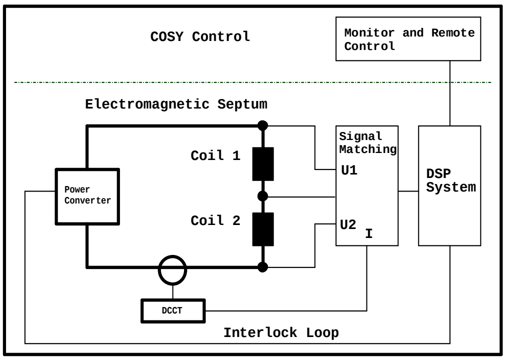

Figure 1: Schematic of the septum circuit

The observation of the temperature

Any change of temperature results in a variation of the resistor and an alteration of the voltage drop respectively. A special feature, the plausibility-check, proofs a proper signalling (interruption of a cable, unplugged connector).

The surveyor system operates in two different ways. While the power converter runs to the working point which is desired, it acts in mode "watch". In the control room the signals are observable by an operator and in case of exceeding the threshold of 70°C the power supply will be switched-off immediately. All signals are considered as absolute values. Additionally both voltages are compared to each other.

The second mode „limit" becomes active when the current is stable and the magnet has reached the thermal equilibrium. Voltages actually measured will be set as references.

In the mode „limit" these set-values classify the deviations between actual-values and the two reference-values. The calculation of the alarm thresholds takes place now. After exceeding these thresholds means by of a temperature variation of more than ± 1 K pulses will be generated. They are summarized in a counter. If a certain amount of counts is collected the DSP opens the interlock loop. Depending on the amplitude of the deviation varies the number of pulses. This means the bigger the deviation the faster the system indicates an over-temperature. It takes about 6 ms from the appearance of an overheating to the opening of the DSP-output-contact. Another 70 ms pass before a chain of relays releases the main circuit breaker internal the converter. Compared with the burn-out time of about 1.2 s this is sufficiently fast. By freewheel circuit the stored energy of the magnet turns over into heat.

The Remote Control

A special software allows the remote control of the DSP. It is integrated in the COSY control system. This program consists of two parts: Firstly a graphical user interface (figure 2) which is realised with TCL/TK and secondly a C - program which handles the communication between the DSP and the GUI. On the monitor all actual operating parameters of the septum are displayed continuously. Additionally commands can be set and the present status is shown. Thanks to the implanted memory function the last 300 ms before a switch-off occurred can be investigated afterwards.

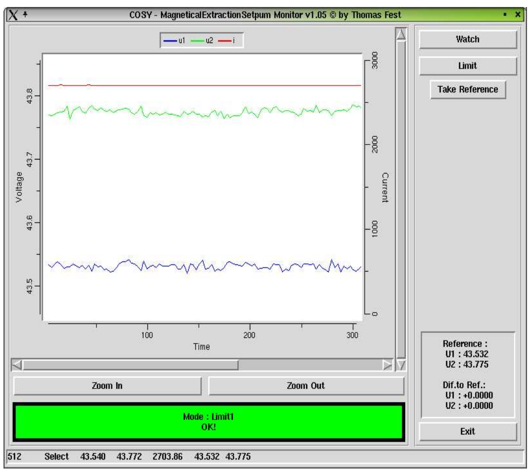

Figure 2: Monitor and control window

Operation of the Injector Cyclotron and Ion Sources at COSY/ Jülich

H. G. Böge, W. Bräutigam, R. Brings, O. Felden, N. Gad, R. Gebel, A. Kieven, P. von Rossen, N. Rotert

In 2004 the injector cyclotron did provide beams for 7408 hours for the accelerator facility COSY. The total time of operation since the start of operation in 1968 exceeded 206,148 hours in December 2004.
In addition to the main objective to feed beams to the cooler synchrotron COSY, beams at the internal and external target stations of the cyclotron had been used frequently for irradiations by external users, e.g. the institute for nuclear chemistry (INC), the Fraunhofer Gesellschaft (FHG), and companies like ACCEL and Cryoelectra. For ACCEL, the manufacturer of the superconducting cyclotron for medical applications at the Paul-Scherrer-Institute (PSI), support has been given for several septum deflector tests at our septum test facility. The common aim has been to develop a stable long-term operation of high-voltage beam deflectors.

Ion source operation

The operation of the ion sources showed no failures in 2004. The improved quality of the filament operation allowed operation of the filaments in excess of 1000 hours. The single filament source for unpolarized ions was replaced after 14 years of operation and 10530 hours of beam service for COSY by an improved version.
For polarized deuterons the intensity extracted from the cyclotron exceeded 1.2 μA, which is comparable to the routinely delivered intensities of polarized proton beams. The polarization scheme, as reported last year, for deuterons has been successfully extended to pure vector and tensor polarized states. Efforts aimed to provide an optimized sequence for polarized deuteron beams has been continued. The technical prerequisites for a fast and reliable change of the polarization state, the change of resonance frequency and magnetic field, have been realized at the end of the year and allowed to provide pure polarization states to experiments in December. The possibility and performance of additional combinations will be investigated.
The nuclear electronics of the low energy polarimeter in the injection beam line to the COSY has been extended by a set of simultaneously acquiring multi-channel analyzers. The amount of time for a single measurement has thus been reduced by a factor of four. Sources of systematic errors like pile up, background or low resolution are, therefore, under control and the precision of the measurements has been greatly enhanced.
In a very fruitful collaboration with the Institute for Nuclear Research (INR Troitsk, Russia) the optimization of ion source components resulted in an increased performance of the polarized ion source with respect to intensity and reliability. In the beginning of 2004 the electromagnetic hexapole magnets were replaced by a set of permanent magnets. The use of encapsulated hexapoles increased the intensity by 20 % and improved the vacuum conditions by a factor 2-3 to residual pressures below $4 \cdot 10^{-7}$ mbar. The optimization studies are partly funded by the European Community under the contract acronym HP-NIS (High Performance Negative Ion Sources).

Recent improvements

The availability of D^- operation of the COSY injector is dependent on a reliable septum operation. To allow uninterrupted service the power supply for the septum has been pulsed for operation over 25 kV. This mode of operation allowed the usage of an otherwise inoperable septum for deuterons due to increasing loss of isolation. After two years of operation the actual septum is still in use for deuteron operation. The time constant for the pulse from the power supply in the range of 100 ms required a pulse length over 400 ms with a remaining small deviation in the deflection angle. Benefiting from the good experience with transistor switches for pulsed operation of the ion sources a switching circuit for the voltage of the septum has been realized for voltages up to 65 kV. With this switch rise times of about 2 ms are realized. The pulse width has been reduced to a fraction of the former set-up. The quality of

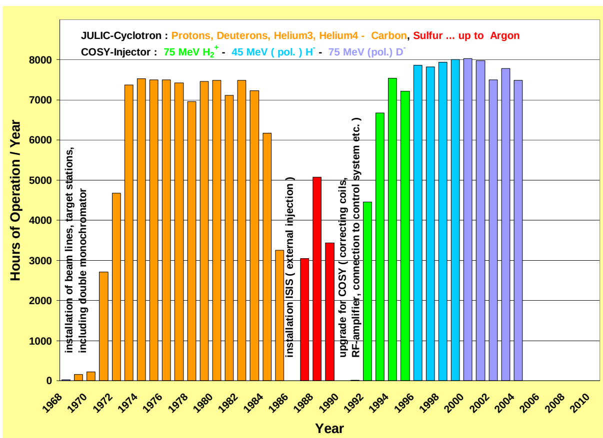

Fig. 1: Operation of the Cyclotron. At the end of 2004 the total operating time reached 206,148 hours.

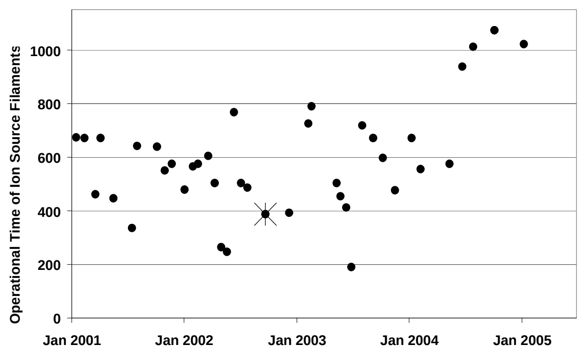

Fig. 2: Up-time of the filament driven ion sources since beginning of 2001. The asterisk marks the single failure of a filament during this period.

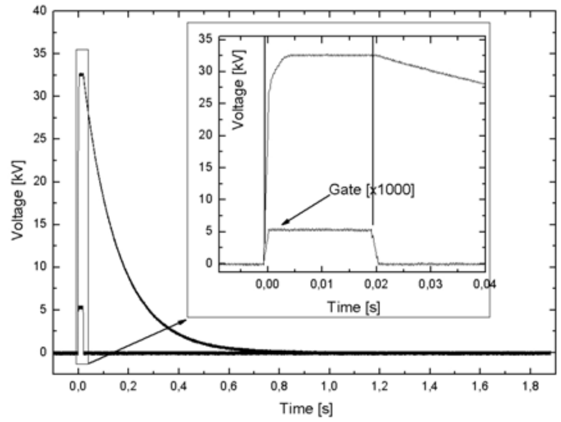

Fig. 3: Voltage pulse shape recorded at the septum test stand before installation at the cyclotron.

this pulsing scheme is depicted in fig. 3. After reaching the desired deflecting voltage the voltage is kept constant until the end of the gating pulse. The slow decay in the unloaded test condition decreases under real conditions due to the resistive load of the coated isolators of the septum deflector. The practical experience with beams in the injection beam line to COSY confirms this behavior.
In mid 2004 several magnet power supplies have been replaced. A new power supply for the main field with remote control close to the diagnostic systems of the cyclotron has been set in operation. During the shutdown period at the end of the year the exchange of the 12 power supplies for the correcting coils has been completed. Only 3 power supplies are now left with current shunts connected to the common water-cooling system with load depending temperature.
The upgrade of the vacuum system has proceeded. The replacement of oil containing fore-pumps of the cryo-pumps has been completed. The exchange of the two main turbo molecular pumps was postponed until the control system will be upgraded to a new release.

Aging and wear-out of cyclotron components

The cyclotron is in use since the mid 60s of the last century. Most of the systems were refurbished between 1980 and 1989. Again 20 years later wear-out of tubing, the loss of elasticity of vacuum and water seals becomes more likely.
The operation of the cyclotron in 2004 was interrupted for roughly 400 hours due to water leakages of internal and external magnet systems. The leakage of the internal vertical steering magnet caused water to flow into the main chamber of the cyclotron (cf. fig. 4). To regain the necessary vacuum conditions the pump system had to be dismounted, cleaned and dried in a time consuming procedure.
A damaged seal in the water distribution to the last solenoid in the injection path to the cyclotron made it necessary to dismount the injection column in the center of the cyclotron (see fig. 5). The quantity of water flowing down from the magnet damaged systems beneath. Therefore, control and regulation circuits for the inflector and the buncher had to be refurbished. The position control for the inflector, the tuning circuits for the buncher system and the focusing magnet “LV2” are partly inoperable and will need further attention. The missing function of these elements has been partly compensated by using different settings.

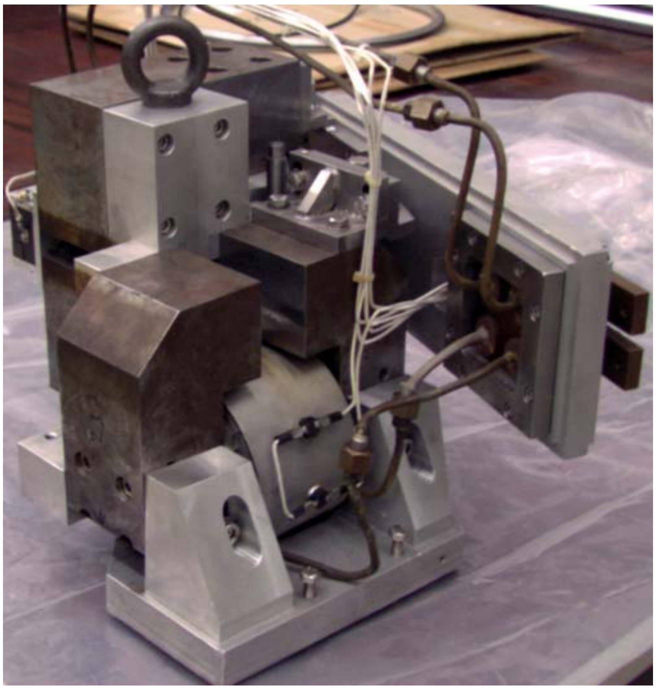

Fig. 4: Internal steering magnets at the exit of the cyclotron. The water leak had been caused by erosion of the copper tubes between the connectors and the encapsulated coil of the magnet.

Fig. 5: Dismounting of the magnetic solenoidal lens close to the magnetic center of the injector cyclotron. The lower part of the magnetic center with the last focusing solenoid “LM” of the source beam line was lifted through the floor of the cyclotron hall.

Velocity measurements of the pulsed atomic hydrogen beam of the COSY polarized ion source

A.S. Belov, O. Felden, R. Gebel and P. von Rossen

The intensity of polarized ion sources of atomic beam type is proportional to the intensity of the polarized hydrogen atomic beam produced by atomic beam apparatus if there is no limitation in an ionizer connected with the atomic beam intensity. It is known that in pulsed mode of operation it is possible to achieve a gain factor of ~2-3 in the polarized atomic hydrogen beam intensity in comparison with cw sources [1,2].

Introduction

The COSY polarized ion source works in pulsed mode of operation with a pulse duration of ~ 20 ms and a repetition rate of 0.5 Hz. The hydrogen dissociator of the polarized ion source provides pulsing of the RF discharge power and the gas supply system. The atomic beam apparatus produces polarized atomic hydrogen beam with an intensity of 7.5 10^{16} atoms /s in pulses with 20-100 ms downstream of the sextupole magnets [4]. Pulsed polarized ion sources of INR, Moscow and IUCF, Bloomington produced pulsed polarized atomic hydrogen beam with peak intensity of 2 10^{17} atoms /s with duration of ~2 ms. The COSY RF discharge dissociator works with typical RF power of 250-300 W which should be compared with 2-4 kW of INR and IUCF pulsed sources. However, simple increase of RF power and gas flux value does not lead to increase of the COSY polarized ion source's intensity probably because increasing of the RF power changes the velocity distributions of the atomic hydrogen beam produced by the dissociator. The test of this suggestion was one of the motivations for the present measurement of velocities of atomic hydrogen beam. A second motivation was connected with the need of information about velocity distributions for correct use of new permanent magnet sextupoles in the polarized ion source atomic beam part.

Description of the set-up and the measurements

The apparatus used consists of the RF discharge dissociator with a beam forming skimmer and a collimator, a chopper wheel, a time-of-flight mass spectrometer and a quadrupole mass spectrometer. In the present measurements only the TOF mass spectrometer was used but it is planned to use the quadrupole mass spectrometer in future too. The dissociator was identical to those used in the COSY polarized ion source. The rf discharge dissociator nozzle was cooled down to a temperature of 36 K with standard technique using a cryogenerator. Oxygen and nytrogen were injected into the dissociator tube to minimize the atomic hydrogen recombination. Molecular hydrogen gas flux into the dissociator tube was changed by changing the width of the pulse feeding the valve through which the molecular hydrogen was injected. The amount of gas injected was recorded in molecules per pulse. Real gas flux through the nozzle and pressure in the dissociator tube for the pulsed mode of operation changes during the pulse. The number of molecules per pulse can be determined from the pressure rise in the dissociator vacuum chamber and can be used for calculation of hydrogen molecules density in the dissociator tube.

The chopper wheel has two 3 mm wide slits on the opposite sides of the wheel. A collimator with a 3 mm slit was installed downstream the chopper wheel. The rotation frequency of the wheel was 100 Hz. The chopper produced triangular shaped pulses of the atomic or molecular hydrogen beam with an initial base duration of 170 μs and 85 μs FWHM. The start signal for the time-of-flight measurements was produced by a photodiode installed in the chopper collimator slit. The photodiode produced the start signal simultaneously with the atomic beam pulse production by the chopper by recording a light signal from the dissociator through the skimmer, the chopper wheel and the chopper collimator slit. Additionally a light diode-photodiode pair was installed on opposite side of the chopper wheel. The start signal produced by this photodiode was calibrated using the upper photodiode and was used for measurements of the velocity distribution of the molecular beam (in this case rf dissociator is off and upper photodiode does not produce a start signal).

The repetition rate of the dissociator pulses (0.5 Hz) and the rotation frequency of the chopper wheel (100Hz) differ significantly. To synchronize the dissociator pulses with the wheel rotation each 1/200 th from the start signals was used to trigger the dissociator apparatus.

The time-of-flight apparatus signals were recorded by the TOF mass spectrometer. The distance between the chopper wheel and the TOF mass spectrometer center was 38 cm.

The density of the atomic hydrogen beam versus gas flux into the dissociator tube was measured with the chopper wheel uninstalled. The results of the density measurements were used for calculation of a figure of merit of the atomic hydrogen beam (density / velocity squared) versus the gas flux into the dissociator tube.

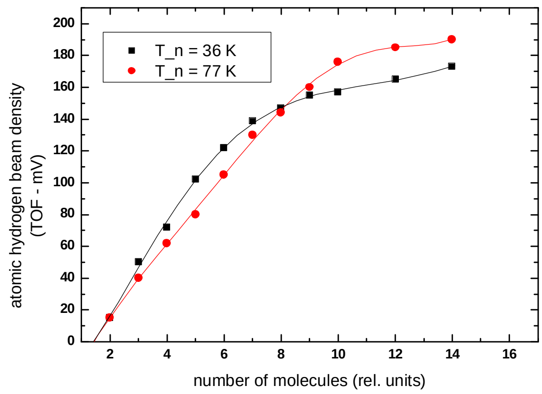

Figure 1. Atomic hydrogen beam density vs. gas flux into the dissociator in number of molecules per pulse.

Results

The results of the atomic beam hydrogen density measurements versus the number of molecules per pulse are shown in figure 1. The density of the atomic hydrogen beams was recorded for nozzle temperatures of 36 K and 77 K. Typical gas flux for COSY operation in units used is 7-10 u. In the present study the gas flux was increased up to 14 relative units. It was necessary to increase rf discharge power of the dissociator from 200 W for gas flux of 3 relative units to 500 W for maximum gas flux of 14 relative units.

The results show that the atomic beam density is increased with increase of the molecular hydrogen gas flux into the dissociator tube up to 14 relative units for both 77 K nozzle temperature and 36 K nozzle temperature showing that there is not still strong attenuation of the beams due to scattering with residual gas with the gas flux increase or due to another limitations.

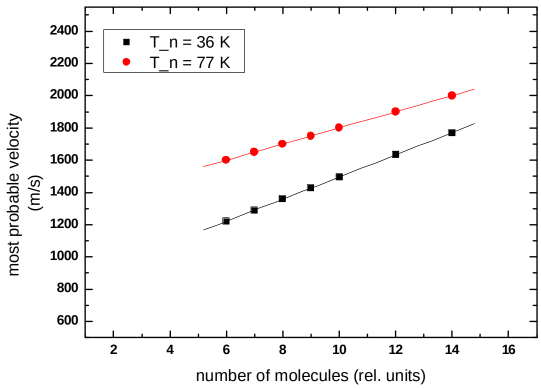

Figure 2. Most probable velocity of atomic hydrogen beam vs. number of molecules per pulse for nozzle temperatures of 36 K and 77 K.

Figure 2 shows results of atomic hydrogen beam velocity measurements. The most probable velocity is shown versus the number of molecules per pulse for nozzle temperatures of 36 K and 77 K. The RF discharge power was changed accordingly to the gas flux by the same way as in the atomic beam density measurements. The most probable velocity increases with increase of gas flux (and respective increase of RF discharge power) significantly. For a nozzle temperature of 36 K most probable velocity increases from 1200 m/s for low gas flux to 1900 m/s for highest gas flux used in the measurements. For 77 K the most probable velocity changes respectively from 1600 m/s to 2000 m/s. For high gas fluxes the influence of the nozzle temperature on the atoms velocity becomes nonessential showing non complete cooling of atoms in the dissociator nozzle.

This velocity change is important for the design of an optimal separating magnet system. For the magnets design a figure of merit n_H / V_{mp}^2 (here n_H is density and V_{mp} is most probable velocity) can be used because the acceptance angle of the separating magnets is inversely proportional to the atoms temperature or velocity squared. Figure 3 shows the figure of merit calculated from results shown in figure 1 and figure 2. Linear extrapolation of the velocity measurements data shown in figure 2 by solid lines were used for the figure of merit calculation. For the 36 K nozzle temperature the figure of merit reaches its maximum value at low gas fluxes in spite of density increase with increase of gas flux. For a nozzle temperature of 77 K the figure of merit has maximum at higher gas fluxes but its absolute value is lower than for the nozzle temperature of 36 K.

The maximum for the figure of merit is reached for gas fluxes where atomic beam density does not reach its maximum value. It is evident that better cooling of atomic hydrogen flux should provide higher figure of merit for higher gas fluxes and by this way higher intensity of polarized atomic hydrogen beam will be achievable.

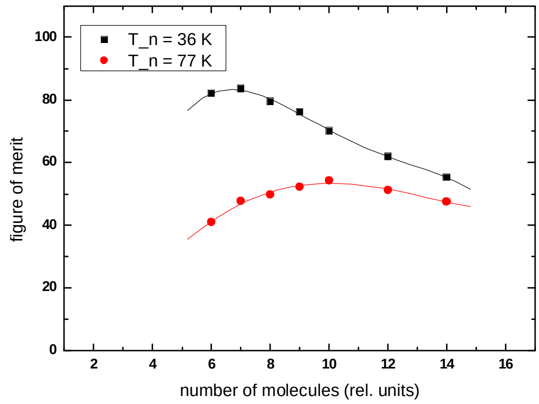

Figure 3. Figure of merit for atomic hydrogen beam for nozzle temperatures of 36 K and 77 K vs. number of molecules per pulse

Conclusion

The density of atomic hydrogen beam produced by rf discharge dissociator can be increased for pulsed mode of operation by increasing the gas flux and respective increase of rf discharge power level. However, the mean velocity of hydrogen atoms in the beam produced increases with the gas increase demonstrating non complete cooling of atomic hydrogen beam in the nozzle. This is one of the limitations for polarized atomic hydrogen beam in the COSY polarized ion source. The limitation can be overcome partially by using a nozzle cooling system producing a more complete cooling of the atomic hydrogen for high level gas flux and rf discharge power in the pulsed hydrogen dissociator. A factor of 2 in intensity increase is expected after designing and use of the rf dissociator with new nozzle accommodator system.

Acknowledgements

We would like to thank N. Rotert and A. Kieven for help in the experimental set-up assembly.

References

[1] A. S. Belov, S. K. Esin, S.A. Kubalov et. al., Nucl. Instr. And Meth. In Physics Res. A255 (1987) 442-459.

[2] V. P. Derenchuck and A. S. Belov, “A multimilliampere polarized and unpolarized negative ion source for IUCF”, In Proc. of the 2001 Particle Accelerator Conference, Chicago, USA, 2001, p.p. 2093-2095.

[3] COSY polarized ion source, atomic beam intensity $7.5 \cdot 10^{16}$ atoms/s

Magnetic Spectrograph BIG KARL

R. Jahn, F. Hinterberger, K. Kruck, M. Lesiak, H. Machner, R. Maier, W. Derissen, P. v. Rossen, R. Siudak, R. Tölle,
GEM-, HIRES-, and MOMO-Collaboration

Experiments were performed by GEM, HIRES, and ENSTAR, HIRES has been able to extend its database and its analysis is in progress. The original goal in terms of the range of settings could not achieved due to a water leak inside the injector cyclotron. Fortunately, the COSY-crew was able to complete the formidable and laborious task fast enough to deliver beams for some crucial measurements.

The ENSTAR detector made its first successful measurements together with BIG KARL. All modules of the detector are operational. They are arranged in a cylindrical arrangement of scintillators in three layers around the target and beam pipe. The proposed experiments foresee the coincident measurements of ^{3}He analysed in BIG KARL and the decay products of η-mesic nuclei in the ENSTAR detector.

The GEM beam time close at the end of the year was plagued by external interference, which prevented taking useful data. Nevertheless, during this run COSY again demonstrated that it is able to deliver high quality polarized deuteron beams, whose polarization can be varied in a broad range choosing between all kinds of combinations of vector and tensor polarizations.

To have the opportunity to study effects due to vertical vector polarizations a much larger horizontal acceptance angle is needed in case of the spectrograph. Fig. 1 shows the arrangement of the spectrometer with its three entrance quadrupoles.

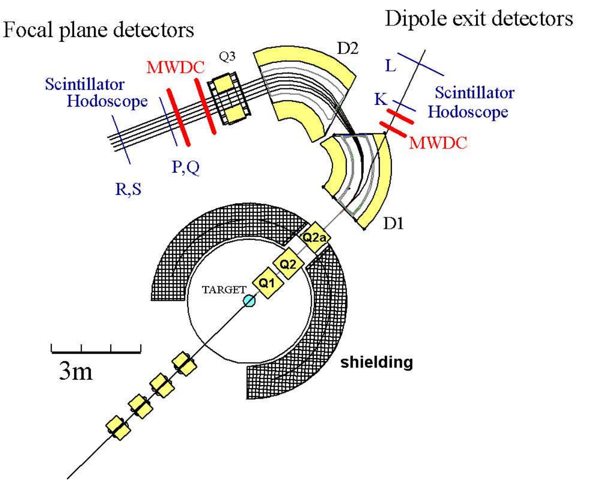

Fig. 1: BIG KARL with its detector systems for the focal plane and for the auxiliary detection plane behind dipole 1

In the standard high resolution mode the first quadrupole is vertically focusing. This implies that it is defocusing in the horizontal plane and results in a horizontal acceptance that is approximately a factor of four smaller than that of

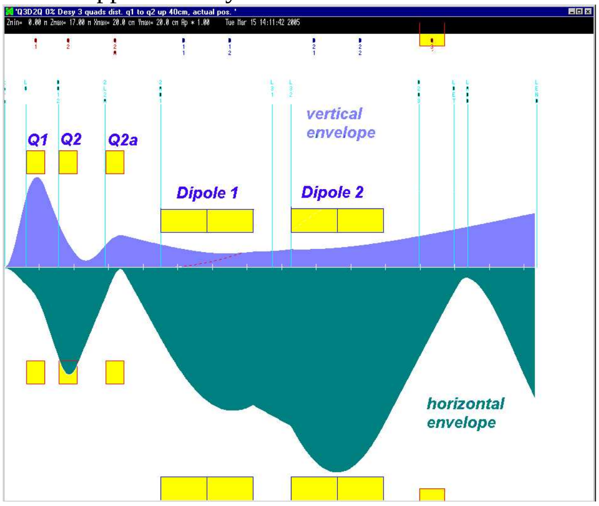

Fig. 2: Envelope structure in the spectrograph in the standard high-resolution mode

the vertical plane. The envelopes resulting from such a setting are depicted in fig. 2.

After the defocusing action of Q1 the horizontal envelope size rises sharply in Q2 and even exceeds the aperture of the pole tips. But the use of a so-called "butterfly" vacuum chamber give enough space to transport the entire envelope.

Fig. 3 shows the situation if one starts with horizontal focusing using Q1 and does the vertical focusing with Q2. The envelopes shown are based on a beam spot size of 2

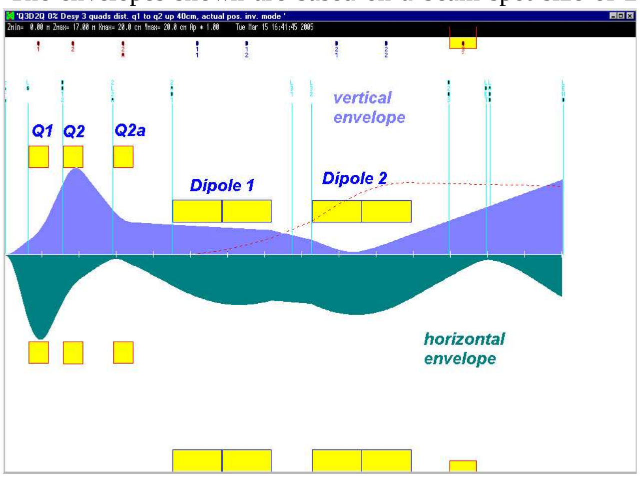

Fig. 3: Envelope structure in the spectrograph in the standard high-resolution mode

mm by 2 mm, with a horizontal angular range of ±100 mrad and ±22 mrad for the vertical plane.

H.Borsch, J.Göbbels, O.Felden, K.Krafft

Personal Dose Survey at IKP

In 2004 145 Persons (with only small fluctuations) of the IKP have been under radiation protection survey. They are equipped with official film badges and Pencil-dosimeters. 84 of these persons plus 9 external experimentalists from universities, which have access to the inner hall during operation of COSY, wear film badges for neutron dosimetry in addition [1]. In the second half of 2004 the MPA (Material-Prüfungsamt) which is responsible for the analysis of the badges changed the material and analyzing-algorithm for the neutron badges. Within this, some badges showed doses up to about 2,3mSv while in the past the doses always had been around or mostly below the detection limit. In spite of looking at the other personal dosimeters (film badge and pencil-dosimeter), the working modes of COSY and the values from the 50 neutron monitors installed around COSY and inside the inner hall the measures from the MPA could not be reconstructed.

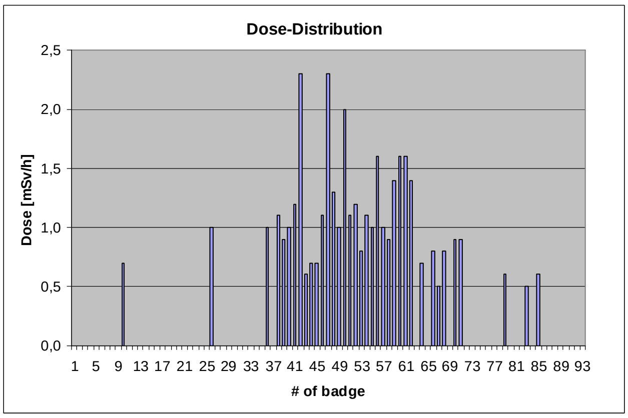

Figure 1 : Dose Distribution of the neutron badges. The badges are sorted by production number.

The dose distribution (figure 1) shows that the doses occur in one block instead of being uniformly distributed. This in combination with the data from the other dosimeters and neutron monitors give a strong hint that the new material, the production process or the analyzing-algorithm failed.

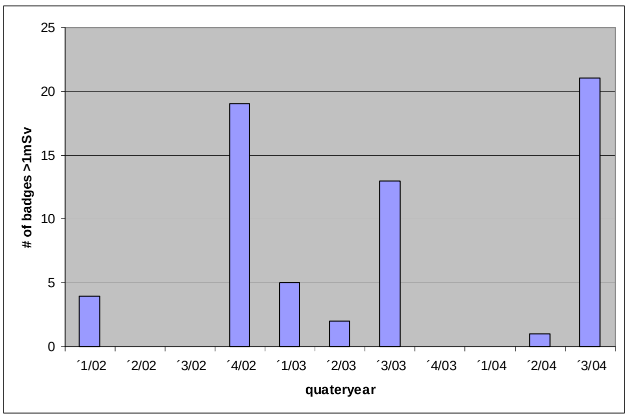

Figure 2 : Number of badges >1 mSv/quateryear from ´1/2002 to ´3/2004

By that we rejected these values as we have done in the 4th quarter of 2002 and the third quarter of 2003. Both times MPA changed their analyzing algorithm, which lead to an increase of dosimeters with values of 1 mSv or above (fig. 2) which was not in agreement to our data. After correction of the algorithm the data matched.

Upgrade of the personal safety system

In 2003 we started to upgrade our personal safety system. Starting point was idea to run the cyclotron as a standalone machine for doing research for other institutes e.g. Institute for nuclear chemistry (INC), Frauenhofer Institute or other industrial companies. By that we decided to separate the personal safety systems (PSA) of the cyclotron and COSY. The PSA bases on programmable logic systems (PLS). After Siemens announced that the support of the S5-System, which was the used PLS, runs out we switched over to S7. In 2003 we first separated all information concerning COSY to the old existing PLS (S5) while the data from the cyclotron were connected to a second PLS (S7-300) installed nearby the cyclotron [1]. In the beginning of 2004 we then replaced the old S5-System running at COSY by a S7-400. The systems are connected via profibus (fig.3), a standardized communication protocol, as before.

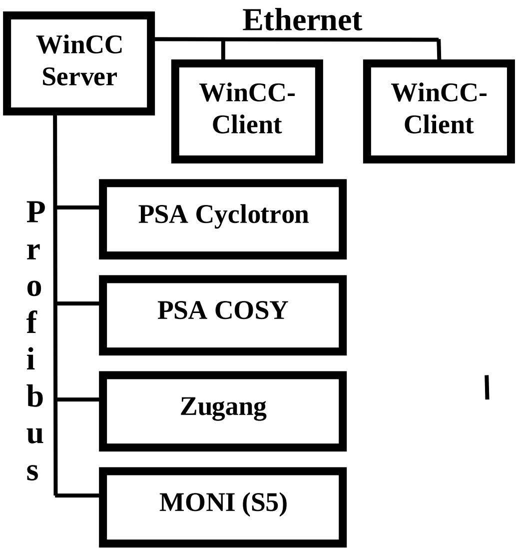

Figure 3: overview of the personal safety and radiation survey systems

By watchdog functions both machines check each other. In case one fails the other machine stops the COSY-beam immediately by driving beam-stoppers. In October 2004 we then changed the S5-System controlling the access to the inner hall during beam operation [1,3]. There also a S7-400 (Zugang) is running now. This machine is connected to the profibus and checked by the safety system. In case of a failure the beam will be stopped as described above. At least there is one S5-PLS (MONI) measuring the beam-losses in order to look at the radiation levels outside of COSY. In case of overcoming the limits given by the authorities the beam is switched of. We will change this system to S7 in 2005.

All important data from the different System, e.g. number of people inside the inner hall, actual dose levels or

Pulsed operation of the superconducting HWRs

R. Eichhorn, H. Singer, R. Stassen

The concept of a new injector for COSY was based on a pulsed operation at a repetition rate of 2 Hz and a beam duration of 500 µs, having some impact on the cavity operation and control. The adjustable coupler [1] as well as the mechanical tuner have been adapted to the vertical bath cryostat, thus tests according to the nominal operation condition in the injector scheme can be performed. High power tests of the whole RF-system including the RF main-coupler, ceramic-window and power amplifier had been tested together with the cavity up to 3kW. Fig. 1 shows an example of an operation with 1kW pulsed power and CW base-level of about 30W. The field level in this constellation was about 7.3 MV/m.

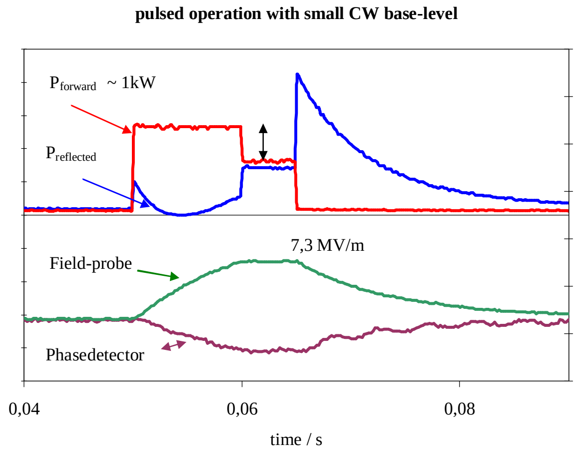

Fig. 1: Pulsed operation

After filling the cavity to an accelerating field of 7.3MV/m the forward power has been reduced by 6 dB to reach a constant flat-top level. Similar measurements of the Type I prototype showed an excitation of a mechanical resonance, which could hardly be compensated by the control-system.

Lorentz Force Detuning

The high electromagnetic fields causes pressures on the cavity walls. The forces lead to deformations of the walls resulting in a frequency shift of the resonance.

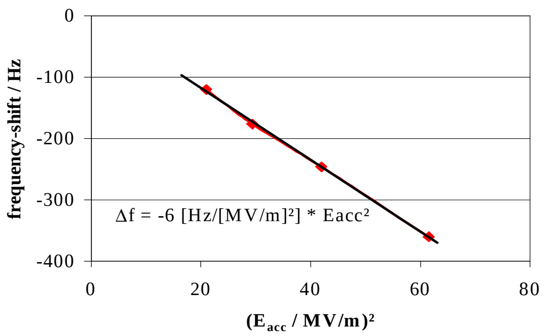

Fig. 2: Determination of the LFD-constant.

Both the magnetic field at the top and bottom part of the cavity as well as the electric field at the beam-tubes part will lower the resonant-frequency. Fig. 2 shows the measurement of the Lorentz force-detuning (LFD) and the linear approximation for the Type II prototype. The resulting LFD-constant of 6 Hz /(MV/m)² is about six times higher compared to the simulations [2]. Prototype Type I even showed a LFD-constant of 10 Hz/(MV/m)², which is far beyond the design value of a compensation-scheme by the fast Piezo-tuning-system. Nevertheless different compensation curves have been tested at lower accelerating field-levels and have proved the principle of work of an installed fast Piezo-tuner outside the cryostat.

Mechanical resonances

Mechanical resonances play an important role in the pulsed operation of a superconducting cavity.

Two methods has been used to measure the mechanical resonances of the prototypes. A rough estimation can be found by a fast fourier transformation of the RF-phase signal after an excitation of the cavity using a step-function at the fast Piezo-system. The most significant mechanical resonance has been found at 230 Hz for the Type II prototype. Fig. 4 shows the corresponding results of prototype Type I with an additional mechanical resonance at 48Hz.

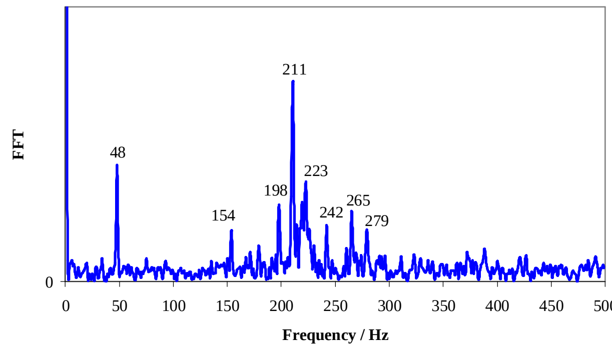

Fig. 4: Mechanical resonances of Type I prototype.

The mechanical behaviour of prototype Type I is much worse compared to Type II. Thus the results of the measurements prefer a fabrication according to Type II, although the additional costs using a thick niobium plate to built the endplates is pretty higher.

I/Q control system

The whole control-system including the stepper-motor to adjust slow changes of the resonant-frequency has been tested in a pulse scheme according the COSY Linac project but at field levels of about 1-2 MV/m to prevent the excitation of mechanical resonances. After an rough adjusting of the control parameters we reached immediately an amplitude-stability of +/-0.6% and a phase-stability of+/-1.4°.

References:

[1] G. Schug et al., The adjustable RF main coupler for the superconducting COSY Linac cavities, IKP Annual Report 2002, Jülich, Jül-4052

[2] E. Zaplatin, results of ANSYS simulations, private communication

Warm measurements of the superconducting Half-Wave Resonators

R. Eichhorn, F. Esser[1], B. Laatsch[1], G. Schug, H. Singer, R. Stassen

Two prototypes of the 160MHz Half-Wave Resonators (HWRs) – foreseen in the COSY-Linac design - have been built at different companies. The fabrication differs slightly concerning the top and bottom parts of the cavities and the welding procedure of the single components. Exemplarily Fig. 1 shows the layout of prototype Type I with round shaped top- and bottom plates. The second prototype with machined 2cm thick niobium-plates resulting in an elliptical shape for the endplates will be called Type II.

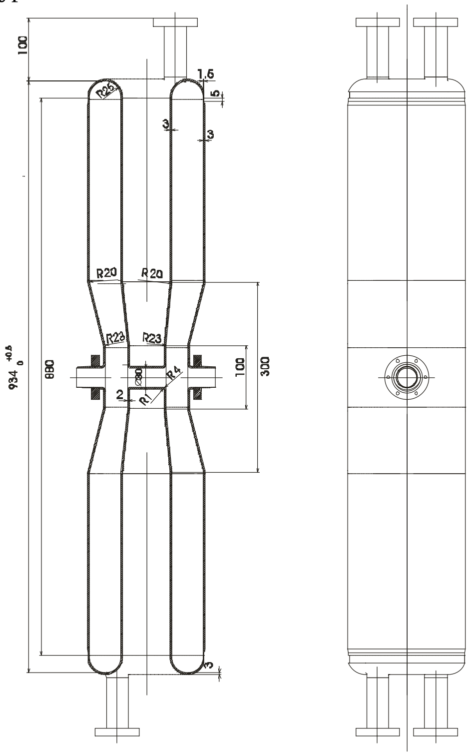

Fig. 1: Layout of the prototype cavity with round shaped top and bottom plate.

The comparison of the first measured 10 Eigenmodes with the simulation results [2] verifies the use of the calculated R/Q-value to determine the accelerating-field E_{acc} during the cold RF-measurements.

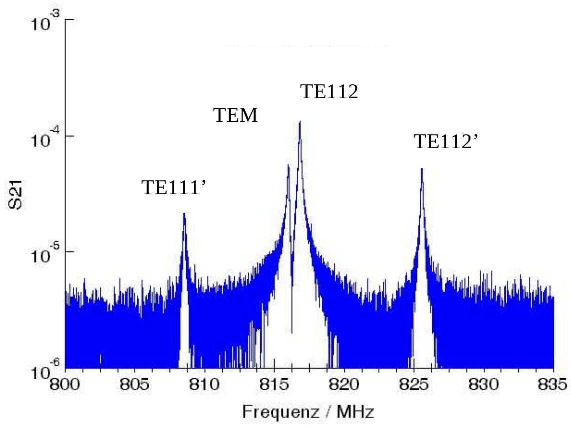

Fig. 2: 6^{th} -9^{th} Eigenmodes of the HWR-Prototype Type II.

Even the non degradation of the first TE-modes caused by the deformation near the beam-ports to adjust the necessary ß-value can be separated (Fig. 2). The accuracy between the measured and calculated resonances is within 1%, mostly better than 0.5%.

Change of resonant frequency

The control of the resonant frequency after each step during the manufacturing, preparation and starting procedure (pumping and cool-down) to perform a cold-testing allows a good estimation of the final frequency range during a series production. The results during the starting procedure are summarized in table 1.

Table 1: Comparison of calculated and measured change of the resonant frequency:

	Calculated	Measured
f_o at RT	--	160,4 MHz
Δf after pumping	- 32 kHz	- 50 kHz
Δf after cool down	+ 270 kHz	+ 260 kHz
Tuning sensitivity	140 kHz / mm	120 kHz / mm

Field-profile measurements

The first prototype delivered by ZANON (Type II) without chemical preparation has been used to determine the field-profile along the beam-axis. Fig. 2 shows the on-axis bead pull measurement compared to the electromagnetic simulation.

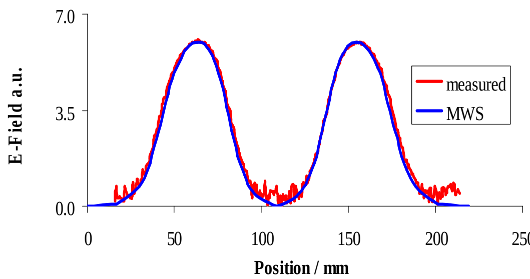

Fig.2: Comparison of measured and calculated field-profiles.

The homogenity of the electrical field in the accelerating gap had been demonstrated by a 6 mm off-axis bead pull measurement. The changes in the field-profiles are within the accuracy of the RF measurement-system.

References:

[1] R. Stassen et al., Superconducting RF activities at FZ-Juelich, SRF2003 Lübeck

[2] MicroWaveStudio, electromagnetic simulation software, http://www.cst.de

[1] ZAT, Forschungszentrum Jülich

Cold measurements of the superconducting Half-Wave Resonators

R. Eichhorn, F. Esser[1], B. Laatsch[1], G. Schug, H. Singer, R. Stassen

The two prototypes of the 160MHz Half-Wave Resonators (HWRs) have been tested in the vertical bath cryostat [1]. A resonant frequency control loop consisting of a precise phase detector and a controllable RF-source allows measurements at critical coupling. This critical coupling is preferred to perform a Q_0-E_{acc} measurement with highest accuracy.

Surface treatment of the cavity

A commercially available standard procedure has been used to get a chemical preparation of both prototypes. The special high-pressure water-rinsing through all access ports at the bottom and top flanges of the HWR prototype guaranteed an optimized cleaning of the surfaces. Details of the preparation are summarized in the following list:

- 60µm BCP chemical etching in a temperature-controlled closed loop operation
- 60µm BCP after a 180° rotation of the cavity
- HPR through all of the four access-ports
- Drying by pumping
- Baking at 100° C for 4 hours
- Pumping to $1*10^{-5}$ mbar
- The cavity, prepared in this manner, was cooled down to 4 K in a vertical bath cryostat without further pumping of the cavity vacuum.

In the first RF-measurements [2], performed after the chemical preparation a first multi-pacting (MP) level occurred at the low RF level of about 2mW and a loaded Q_L of 1E7. This MP barrier is located at the flat region near the beam ports. It needed at least about 2 weeks of different conditioning methods before the MP barrier was exceeded. Further multi-pacting levels of the Type II prototype has not been observed up to an accelerating gradient of more than 7 MV/m. The first measurement of the cavity performance, taken at CW-operation is presented in Fig. 1. The cavity quenched at 6.2 MV/m at CW-operation, but reached up nearly 8 MV/m at pulsed mode.

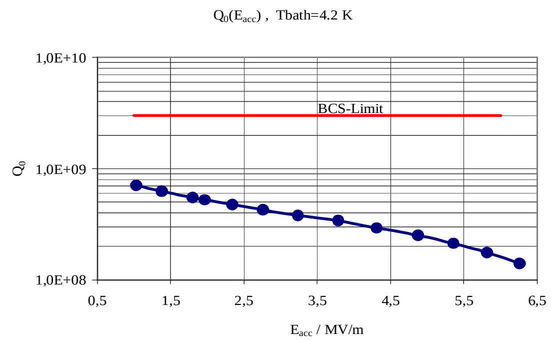

Fig.1: Q_0-E_{acc} measurements of the HWR prototypes

Taking into account the limiting shielding of the magnetic earth-field and a resulting resistance of the surface by the preparation the cavities the theoretical possible Q_0-value has been reached at low accelerating-fields.

While operating the cavity at high field, a huge dose of x-rays has been measured. The x-ray spectrum verifies the existence of high field-levels by an independent measurement. The center energy of 200 keV corresponds roughly to the accelerating field-gradient of 6 MV/m.

Due to the round shaped endplates of Type I additional MP-levels had been found while testing the second cavity. This MP-levels had been easily conditioned within some minutes. Both cavities have shown similar results concerning the electromagnetic behaviour.

Tuning the cold cavity

The mechanical tuner [3] designed by ZAT was ready to be used during the cold tests and didn't showed any failure. The tuning ranges of both the slow stepper motor driven and the fast piezo system correspond to the calculated values. The control system of the stepper motor tuner has been tested after changing the coupling strength to a loaded Q_L = 3E6 and switching to a generator driven operation.

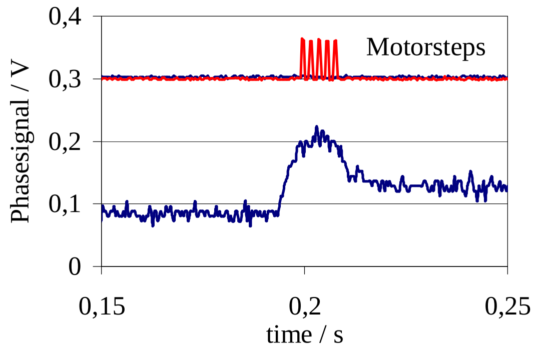

Fig. 2: Stepper motor control after a 10Hz jump of the generator frequency

Fig. 2 represents the fast response of the control system after changing the generator frequency of 10Hz. The system comes into operation when the phase changes more than +/- 15° compared to the desired operating frequency. All slow changes of the resonant frequency like the changes by the variations of the pressure in the lHe-system had been successfully compensated by the resonant frequency control loop.

Some nonadvantageously behaviour like the small hysteresis of the tuner system need more investigations during the next cool down period.

References:

[1] R. Eichhorn, H. Singer, R. Stassen, Set-up and first cool-down of the vertical bath cryostat for cavity testing, IKP Annual Report 2003

[2] R. Stassen, R. Eichhorn, F.M. Esser, B. Laatsch, R. Maier, G. Schug, R. Toelle, First results of pulsed superconducting half-wave resonators, Proc. of EPAC 2004, Lucerne, Switzerland

[3] R. Eichhorn, F.M. Esser, B. Laatsch, G. Schug, H. Singer, R. Stassen, E. Zaplatin, Development of a pulsed light-ion accelerator module based on half-wave resonators, Proc. SRF2003 Lübeck

[1] ZAT, Forschungszentrum Jülich

5 Preparations for FAIR

Study of strangeness -2 baryonic states at FLAIR

A. Gillitzer, D. Grzonka, K. Kilian, W. Oelert, J. Ritman, T. Sefzick

At the future FAIR project of the GSI low energy antiprotons will be available at FLAIR, the **F**acility for **L**ow **e**nergy **A**ntiproton and **I**on **R**esearch. Within the FLAIR LOI [1] it is proposed to study the production of strangeness S = -2 baryonic states based on ideas proposed for LEAR [2].

Studies of the baryon-baryon interaction are a basic tool for investigations of the strong interaction. While for the NN-system an extended data base exists the hyperon sector is much less explored and studies of strangeness S = -2 systems are practically limited to searches for the H-particle, a system of B = 2, S = -2 first proposed by Jaffe [3] which up to now was not proven to exist. The cascade hyperons Ξ are normally used as entrance into the B = 2 systems with S = -2. Slow Ξ particles can go into interacting ΞN systems which may couple to YY or the H particle.

The proposed experiment for the observation of strangeness -2 baryonic states is based on the production of Ξ-baryons in the special condition of recoil-free kinematics where in a fixed target experiment: a+b → c+d the reaction product with S = -2 has zero momentum in the laboratory system.

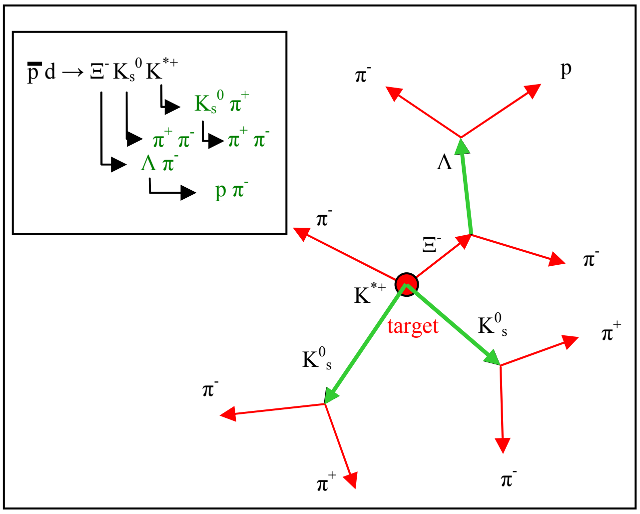

Fig. 1: Sketch of a suitable reaction channel to study the production of Ξ. The primary produced K^{*+} decays within a few fermi into a K_s^0 and a π^+ resulting in three delayed decays which allows to create a very clean trigger signal via multiplicity increase.

To perform such recoil-free kinematics for the Ξ production a $\bar{K}^*$ "beam" is particularly suitable if the $\bar{K}^*$ momentum is about 160 MeV/c for m_{K*} = 982 MeV/c. The $\bar{K}$* momenta resulting from an antiproton annihilation at rest via the: $\bar{p}\,p \rightarrow \bar{K}^* K^*$ reaction amount to about 290 MeV/c at the nominal K* mass. We see that $\bar{p}\,p$ annihilation at rest provides in a first step the necessary $\bar{K}^*$ "beam" for recoilless Ξ production on a further nucleon.

The studies will begin with the Ξ production. The most suitable reaction channel is: $\bar{p}\,d \rightarrow \Xi^- K_s^0\ K^{*+}$ which results in 8 charged particle tracks in the exit channel. A sketch of this reaction channel is shown in fig. 1. The event identification and kinematical complete reconstruction works via the geometry of the particle tracks. Such techniques have been applied successfully by the PS185 collaboration at CERN and are in use at the COSY TOF experiment. From the charged pions the decay vertices of the K_s^0 are reconstructed and with the known target vertex their tracks are determined. The Λ track is given from the vertices reconstructed from the (p, π^-) and (Ξ^-,π^-) tracks. With this information all momentum directions of all particles are known and applying a mass hypothesis for the detected and the reconstructed particles the events are completely reconstructed.

Fig. 2 shows a schematic drawing of the detector set-up.

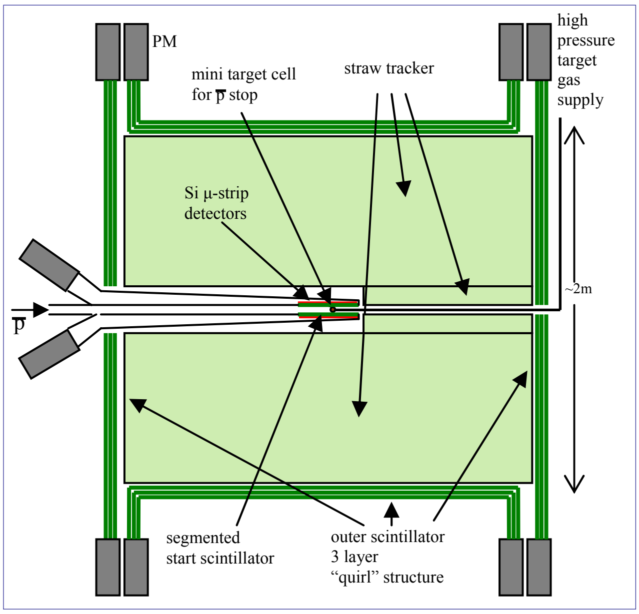

Fig. 2: Sketch of the detection set-up with two scintillator layers, the first one close to the target and the second one at a distance of about 1 m, in between tracking detectors are installed.

The next step in the experimental programme will be the study of the Ξ-N, Λ-Λ or H systems. Here ^{3}He has to be used as target gas. The particle configuration in the exit channel is similar. Only an additional proton appears in the exit channel. A further extension of the programme will be the production of double hypernuclei. With the technique of recoil-free kinematics the Ξ can also be produced and deposited in more extended nuclei. A highly efficient production of double hypernuclei is expected with this method.

References:

[1] FLAIR LOI, http://www-linux.gsi.de/~flair.
[2] K. Kilian, Proc. 4th LEAR Workshop (1988) 529;
K. Kilian et al., Memorandum PSCC CERN (1990).
[3] R.L. Jaffe, Phys. Rev. Lett. 38 (1977) 195.

The Design of the Micro Vertex Detector for PANDA experiment

T. Stockmanns

The Micro Vertex Detector (MVD) plays a major in the PANDA experiment [1] to identify open charm and strangeness by detecting secondary decays of particles displaced from the primary interaction point. These decay lengths differ for charmed mesons and baryons from several 10 μm up to strange hadrons with decay lengths of several cm. To efficiently track the ionizing particles in the solenoidal magnetic field of the detector five sensitive layers are foreseen. Due to the high occupancy and the radiation dose close to the interaction point at least the innermost layers have to be pixel detectors. For the outer layers strip detectors could be used which have the advantage of a smaller radiation length and less readout channels.
The requirements for the MVD can be sorted in four groups:

- spatial resolution

  The spatial resolution should be better than 100 μm along the beam axis (z-direction) to recognize $D\overline{D}$ events as decay products of $c\overline{c}$ resonances. In addition the resolution in r/ϕ direction should not be sufficiently worse for a good momentum measurement.

- timing resolution / readout speed

  The PANDA experiment runs with a DC beam with an annihilation rate of 10^7 interactions s^{-1}. Therefore a timing resolution better than 100 ns is necessary to assign individual hits in the detector to a single interaction. Without a hardware trigger, as it is planed for PANDA, all generated hits have to be transferred to the off-detector electronics within a reasonable time ($< 100\ \mu$s) for the first software trigger stage.

- radiation tolerance

  The MVD is the innermost subdetector directly positioned around the interaction point. This leads to the highest radiation dose within the detector with $1 \cdot 10^{13} n_{eq}/cm^2$ over the full lifetime of the experiment. Thus all components of the micro vertex detector have to be operative up to this level.

- material budget

  To minimize multiple scattering and photon conversion in the MVD the radiation length should be as small as possible. As a realistic goal an upper limit of 4% x/X_0 was chosen.

Nowadays hybrid pixel detectors, which consist out of a large silicon sensor and several individual readout chips, are widely used in all kinds of medium and high energy physics experiments. Especially the LHC experiments put a lot of effort into the development of radiation tolerant silicon sensors and readout electronics. With the limited manpower available at the moment the baseline solution for the PANDA detector is to adopt either the ATLAS [2] or the CMS [3] pixel module to the slightly different requirements of the PANDA experiment. These detector modules are sufficiently radiation tolerant, offer a good timing information of 25 ns and and have a moderate spatial resolution with pixel sizes of 50 x 400 μm^2 for ATLAS and 100 x 100 μm^2 for CMS. Their main drawback is the hight material thickness in the order of 1 % x/X_0 per layer.
A more advanced option is a complete redesign of the readout electronics in a new process technology which offers several advantages from a better spatial resolution over a good time measurement to an improved charge information.
A third option is the use of monolithic active pixel sensors[4, 5]. In this quite new technology sensor and readout electronic are combined on one substrate which gives a very thin sensors with a spatial resolution of a few μm. This technology still does not have the necessary radiation tolerance nor the desired time resolution but many groups are working in this field and some progress can be expected with the next few years.
For a first layout of the MVD a combination of an ATLAS-like pixel module with a 4 x 2 cm^2 silicon sensor and 10 front end chips and a strip detector with a double-sided 6 x 2 cm^2 silicon sensor with four readout chips situated at the side of the strip sensor were taken. Figure 1 shows a perspective view of the MVD detector without the five disks in the forward direction.

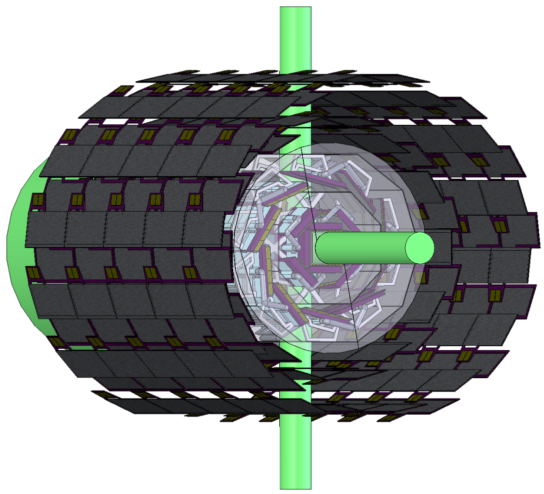

Fig. 1: Side view of the MVD without forward disks

In the forward part of the detector the innermost layer is situated directly at the beam pipe and consists of four modules which are slightly tilted towards the interaction point. The holes at the edges of the modules are closed by the second layer of pixel detectors which are turned by 45 in respect to the first layer. The backward region and the sides of the target pipe are covered by eight modules, six at the side and two at the bottom and top. The third and last pixel layer is build out of ten staves with six modules each. The pixel orientation in this layer is perpendicular to the pixel orientation of the other two layer to improve the longitudinal resolution of the pixel detector.
Two additional layers of strip detectors accomplish the barrel part of the MVD. In the forward direction five disks are used to track particles with low transverse momenta. The three

R&D work (2005-2008) for the High-Energy Storage Ring

R. Maier for the HESR Consortium

The High Energy Storage Ring (HESR) [1] is dedicated to the field of high-energy antiproton physics with high quality beams over a broad momentum range from 1.5 to 15 GeV/c. The design work for the HESR is organized in a consortium with scientists from FZ Jülich, GSI Darmstadt and TSL Uppsala. In this paper an overview of the R&D work is given. Further details can be found in the Technical Report of the FAIR facility [2].

Introduction

The R&D work is performed according to the importance for the HESR project (see Tab.1). Feasibility demonstration is assigned to be the highest priority, followed by design choice and reliability, start of production, and desirable technical / cost optimization. Prototype development (except magnets) is already partially funded by the European Community (EC) with more than 1.2 M€ via a FP6 Design Study, referred to as DIRAC subproject HESR. This design study work will cover the years 2005-2007. It addresses the high energy electron cooling, pickup development for stochastic cooling, suitable injection scheme and RF cavity.

R&D needed for feasibility demonstration

Beside the key questions of magnetized electron and high-bandwidth stochastic cooling the rather high initial beam emittance of the injected beam from the RESR is of major concern. To keep the R&D efforts for the HESR at a justifiable level further investigation on the achievable equilibrium parameters in RESR is necessary. Highest priority (priority 1) is assigned to the electron cooler related R&D. The R&D in this field has been already initialized (DIRAC-HESR). The associated R&D is done in collaboration between the DIRAC-HESR partners and other partners like FNAL, Novosibirsk. The main issue is the reliable operation of a high brilliance electron beam in a high voltage environment. High voltage stabilization techniques used in atomic mass spectroscopy can be used to stabilize the electron beam high voltage. Pre-cooling by broad-band stochastic cooling can be a solution to avoid antiprotons outside the electron beam. This work (priority 2) will be partially funded by the EC (DIRAC-HESR).

Priority 2 is also assigned to the development of a stochastic cooling system (2 bands up to 8 GHz). This puts additional requirements on the lattice. First design considerations suggest that stochastic cooling at higher energies (above ~8 GeV) is favorable. Of particular interest is to investigate under which conditions efficient stochastic cooling below 8 GeV would be possible. The pickup development is partially funded by the EC (DIRAC-HESR). Furthermore a prototype for the multi harmonic RF cavity is also being developed with partial funding by the EC (DIRAC-HESR) (priority 2). R&D for a curved super-conducting magnet is assigned priority 1. As the beam travels on a curved path inside the dipole (which in the current design is straight) leads to certain disadvantages: The effective beam pipe aperture is reduced and the impact of higher order field components is more severe. Curving the magnet according to the beam path curvature (13.9 m) would be advantageous. The R&D program shall investigate the possibility and the perspectives of a highly curved dipole magnet. The impact of the results on beam instabilities and stochastic cooling has to be discussed and compared to the short straight magnets.

R&D needed for realization

The super-conducting straight magnets need careful R&D work, even if 'only' the RHIC D0 magnets have to be shortened. Prototypes have to be built (priority 2). The injection is in principle state of the art but the development of low impedance kickers is of importance for an effective injection (priority 2). Broad-band amplifiers for beam feedback have to be designed with low impedance (priority 3). Alignment and assembly issues for bent cryostats will be investigated (priority 3). The optimum number of magnets per cryostat segment has to be found for the final design (priority 4). A design for super-conducting combined function magnets to save space in the ring should be worked out (priority 3).

References:

[1] An International Accelerator Facility for Beams of Ions and Antiprotons, Conceptual Design Report, GSI Darmstadt, November 2001, see http://www.gsi.de/GSI-Future/cdr/
[2] FAIR Project (subproject HESR), Technical Report, to be published in 2005

Table 1: Gantt diagram with R&D ranking and milestones

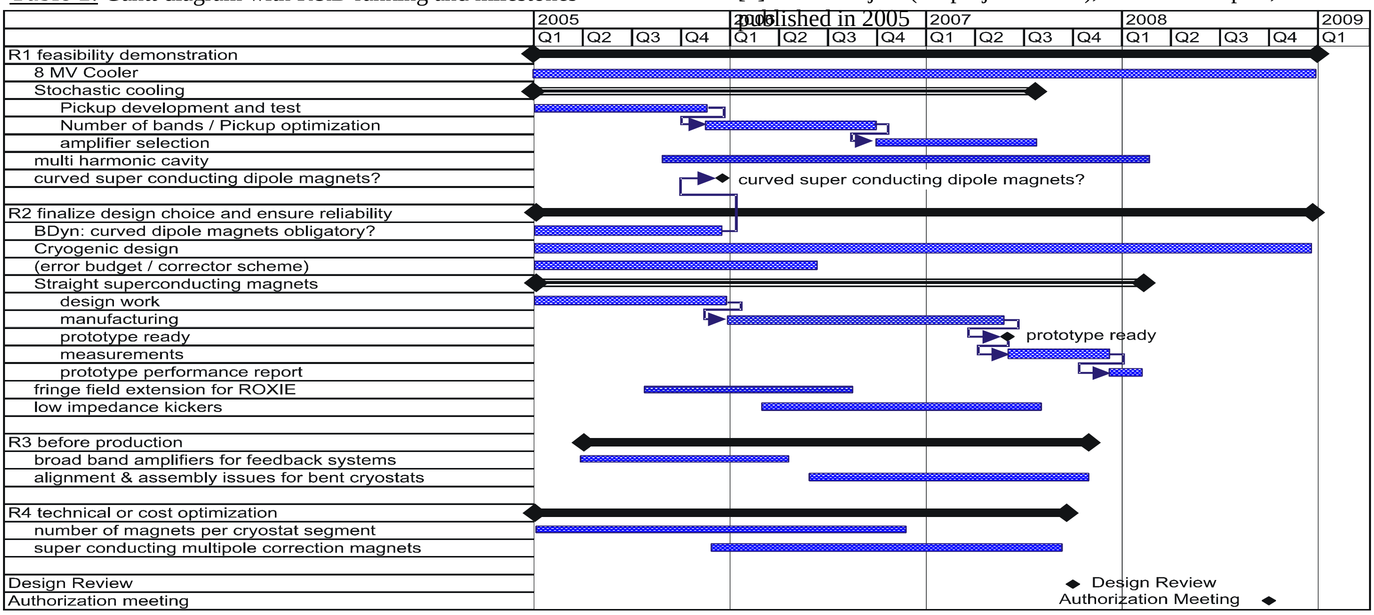

Polarized Beams in the High-Energy Storage Ring

A. Lehrach, R. Maier, D. Prasuhn

Introduction

The High-Energy Storage Ring (HESR) of the future GSI Facility for Antiproton and Ion Research (FAIR) [1] is proposed as a storage ring for antiproton physics with high quality beams over a broad momentum range from *1.5* to *15GeV/c*. An important feature of this new storage ring is the combination of phase space-cooled beams with internal targets. In 1992 an experiment at the Test Storage Ring (TSR) at the MPI Heidelberg proved the feasibility to polarize a *23MeV* proton beam by spin-dependent interaction of the stored beam with an electron-polarized hydrogen target [2]. A Letter-of-Intent has been submitted by the PAX collaboration [3] proposing to utilize this technique to provide a polarized antiproton beam for the FAIR project. A dedicated Antiproton-Polarizer Ring with a large acceptance angle is needed in order to polarize antiprotons to a high polarization degree of *30* to *40%* [4]. To perform spin-physics experiments with antiprotons, the polarized beam would have to be accelerated in the HESR.

Depolarizing Spin Resonances

Spin motion in an external electro-magnetic field is governed by the so-called Thomas-BMT [5], leading to a spin tune of $\nu_{sp}=\gamma G$. G is the anomalous magnetic moment of the particle and $\gamma=E/m$ the Lorentz factor. The G-factor is quoted as *1.792847337(29)* for protons, *1.800(8)* for antiprotons (see Particle Data Booklet). In a strong-focusing ring like the HESR Imperfection and Intrinsic spin resonances can depolarize the beam. In total *25* Imperfection resonances ranging from $\gamma G=4$ to 28, and *50* Intrinsic resonances from $\gamma G=16\text{-}Q_y$ to $16+Q_y$ have to be crossed during acceleration, where $Q_y\approx 12.2$ is the vertical betatron tune for a 6-fold symmetry lattice of the HESR [6]. The resonance strength depends on orbit excursions for Imperfection resonances, respectively focusing structure of the lattice and beam emittance for Intrinsic resonances and is ranging from 10^{-2} to 10^{-6} for the expected beam parameter. Due to coupling introduced by the *15Tm* solenoid of the Electron Cooler also strong coupling spin resonances are excited. The large number of resonances in the HESR makes it very hard to apply techniques of individual manipulation of single spin resonances. Siberian snakes seem to be to only option to guarantee a setup with low polarization losses.

Siberian Snake with Combined Fields

In the HESR momentum range it is difficult use a RHIC-type [7] helical dipole snake due to large orbit excursions as shown in the upper left plot of Fig. 1. A solenoidal field would require pretty high integrated field strength. Therefore a magnet system with a combination of both field types was investigated, consisting of four RHIC-type helical dipole magnets with a maximum field of *2.5T* and a *15Tm* solenoid (see upper right plot in Fig. 1). To provide a full spin flip in the whole momentum range the snake magnets have to be ramped according to the values given in the lower left plot, where *s* is the solenoid and *d1*, *d2* are the two helical dipole field values. The resulting spin motion at *15GeV/c* is shown in the lower right plot (Fig.1).

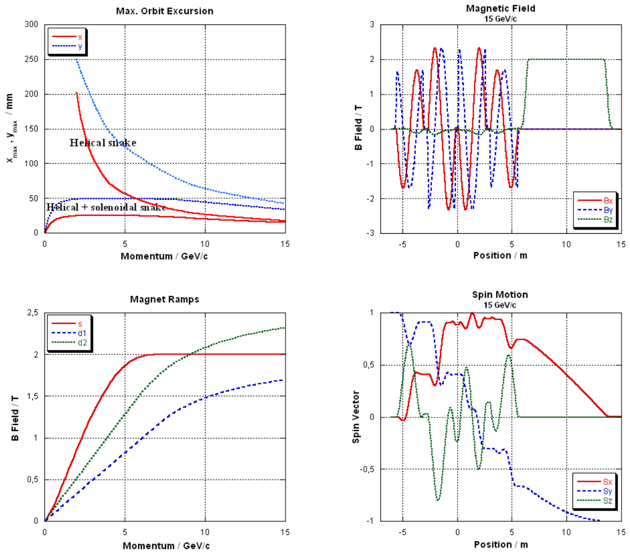

Fig. 1: Calculations for the layout of a full Siberian snake with combined magnetic fields

This magnet system provides a full spin flip in the whole momentum range by keeping the maximum closed orbit excursion below *5cm*. Spin rotation induced by the DC Cooler solenoid at any possible field level can be compensated by the rampable *15Tm* snake solenoid, if snake and Cooler are installed in the same straight section. A second scheme proposed by Y. Shatunov utilizes four solenoids together with two groups of four skew quadrupoles. It could serve as a partial or full Siberian snake, doesn't excite orbit excursion and compensated for transverse phase space coupling [8].

Conclusion

The most serious drawback of a Siberian snake with combined field scheme is large orbit excursion in the snake. Good field quality of super-conducting ring magnets in order to keep the strength of higher-order spin resonances small combined with high flexibility of the lattice allowing for betatron tunes close to integer are essential to apply a partial Siberian snake. A decision for one of the proposed snake solutions should be taken after intense particle and spin tracking including field errors and technical layout of the snake magnets.

References:

[1] GSI Future Project, Conceptual Design Report, November 2001, http://www.gsi.de/GSI-Future/cdr/

[2] F. Rathmann et al., Phys. Rev. Lett. 71, 1379 (1993)

[3] PAX collaboration, Letter-of-Intent, January 2004, http://www.gsi.de/documents/DOC-2004-Jan-125-1.ps

[4] F. Rathman et al., hep-ex/0410029, accepted for publication in Phys. Rev. Lett.

[5] L.H. Thomas, Phil. Mag. 3, 1 (1927); V. Bargman, L. Michel, V.L. Telegdi, Phys. Rev. Lett. 2, 43 (1959)

[6] Y. Senichev et al., Lattice Design Study for HESR, Proc. of the European Accelerator Conference (2004), p.653

[7] See http://www.agsrhichome.bnl.gov/RHIC/Spin

[8] A. Lehrach et al., Proc. of 16th International Spin Physics Symposium, Spin2004, Oct. 10-16, 2004, Trieste, to be published

Perturbation of the HESR lattice due to the Electron Cooling Insertion

A.U. Luccio[1], N.L. D'Imperio[1], A. Lehrach[2]

The antiproton beam in the 1.5-15 GeV/c storage ring HESR, (FAIR complex at GSI [1]), will utilize electron cooling. The e-beam generates a radial electric field that produces a strong defocusing of the antiproton beam in both transverse planes. Main parameters are: electron beam current I = 0.1 to 1 A, antiproton beam energy factor γ= 1.9 to 16. The bare HESR lattice is shown in Fig.1.

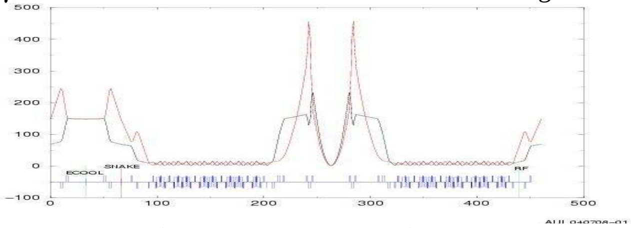

Fig. 1: Bare 4-fold symmetry lattice of HESR [3]

Electron cooling is done in a 30 m long straight section. The (round) beam envelope functions in this section vary from ~ 150 m at both ends to ~ 148 m in its center. The electron beam shape should match the Gaussian profile of the beam, with an r.m.s cross section (σ_L, Raleigh length) $\sigma_T(z) = \sigma_T(0)$ [$1 + (z/\sigma_L)^2$]. Assume the electron beam has a transverse Gaussian density. The antiproton beam size starts larger than the e-beam, then during cooling becomes equal to the e-beam size. The static electron beam potential is given by $\Phi(x,y,z)=(\mu_o c/2\pi\beta)I \exp[-(x^2+ y^2)/2\sigma_T^2]$ where $\mathbf{E}=-\Delta\Phi$ is the e-beam electric field.

We did: (1) Integrate the eq. of motion of many antiprotons through the e-cooling section, to calculate a transfer map; (2) insert the map in MAD[2]; (3) run MAD to find the perturbation to the lattice; (4) correct the lattice with available quadrupoles.

Phase space figure matching

While the antiproton-beam shrinks, an increasing larger fraction of it is defocused, producing distortions of the phase space. The process is not conservative and the emittance increases. A complete treatment would involve high order non symplectic maps. Here, we limit to first order: (1) propagate a number of particles; (2) match the starting and final phase space with an r.m.s. ellipse;(3) find the linear transformation of the starting ellipse that brings it to coincide with the final $\gamma x^2+2\alpha xx'+\beta x'^2=\varepsilon$. The Courant-Snyder parameters α, β, γ, ε, are found from the dispersion matrix of the transverse distribution.

High energy

At high HESR energy, I_e=1 A, variable defocusing during e-cool is illustrated in Fig.2 by tracking 1000 Gaussian random particles through the e-beam. The defocusing lens (in both planes) equivalent to the e-beam is increasingly stronger as the beam shrinks. The effect is small. The lens can be represented by the coefficients of a simple rotation that brings the starting upright ellipse to coincide with the final rotated ellipse. Resulting tunes from MAD for four cases of low energy, high I_e were

σ_a/σ_e	no ecool	1.6	1.2	0.8
ν_x	8.188	8.159	8.157	8.155
ν_y	8.135	8.106	8.104	8.101

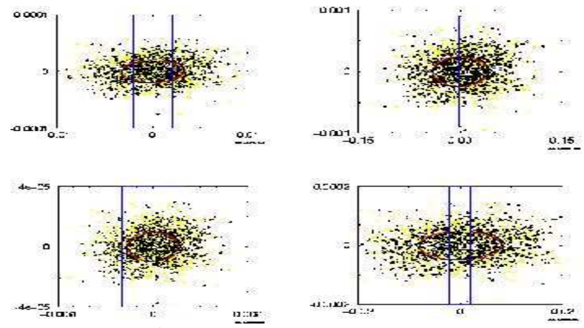

Fig. 2: Initial and final transverse phase space. High Energy

Low energy, high e-current

Resulting tunes for tracking at low energy, γ=4, and high electron current, Ie = 1 are

σ_a/σ_e	inf	10	4	2	1
ν_x	7.869	7.805	7.797	7.780	7.707
ν_y	8.178	8.215	8.227	8.235	8.256

At this beam energy the lattice must be deeply retuned, because the tune is brought close to the integer 8, where the lattice is unstable. Tracking point on ellipses yield the phase space of Fig.3.

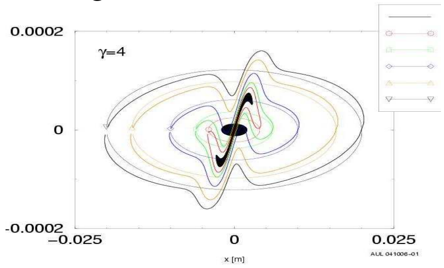

Fig. 3: Labels indicate σ_a/σ_e ratio

Low energy, lower e-current

For low energy, decreasing the e-beam current to 500 mA, yields a more manageable tune shift

σ_a/σ_e	inf	10	4	2	1
ν_x	8.170	8.135	8.120	8.098	7.993
ν_y	8.146	8.153	8.165	8.179	8.192

Conclusions

Preliminary results show that HESR e-cooling has large lattice effect at electron currents ~1 A or at anti proton energies below γ=10. To achieve a fast cooling at low energies may prove difficult. In a later stage a rectangular transverse e-beam distribution will also be considered in the simulations.

References:

[1]www.gsi.de/zukunftproject/beschleinigeranlage_e.html
[2] H.Grote and F.Ch.Iselin The MAD program, vers.8.19, Tech.Report CERN/SL/90-13
[3] Y. Senichev et al., Lattice Design Study for HESR, Proc. of the European Accelerator Conference (2004).

[1] Brookhaven National Laboratory, Upton NY 11973, USA
[2] Forschungszentrum Jülich, 52425 Jülich, Germany

Studies of the Effect of Longitudinal Impedances on the HESR

A. Lehrach[1], A.U. Luccio[2]

Longitudinal Impedance

The effect of longitudinal ring impedance utilizing the tracking code *SIMBAD* was studied [1,2]. Longitudinal impedances are treated as follows. The longitudinal frequency components of the beam, represented by a "herd" of macro particles are obtained by FFT. To do this, the longitudinal distribution of the macros is first binned in a number N_{bin} of longitudinal bins. The spectrum of the beam is then represented by $N_{bin}/2$ frequency components of amplitude I_n and phase ϕ_n (see Fig. 1). A table of longitudinal impedances is read, listing the real and imaginary components of each Z_n/n vs. an integer n, where $n=1$ represents the frequency of the fundamental harmonic of the synchrotron (see also Fig. 1). For each value of n the value of the impedance amplitude Z_n and phase χ_n are calculated as

$$\begin{cases} Z_n = \sqrt{\mathrm{Re}(Z_n)^2 + \mathrm{Im}(Z_n)^2} \\ \chi_n = \arctan\dfrac{\mathrm{Im}(Z_n)}{\mathrm{Re}(Z_n)} \end{cases}$$

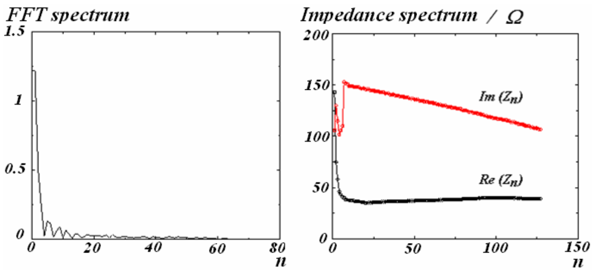

Fig. 1: Longitudinal FFT spectrum of the beam (left) and longitudinal impedance table (right)

The longitudinal impedance (LI) energy kick on the *i-th* macro of the herd is given by

$$\delta(eV) = I_n |Z_n| \cos(\phi_i + \phi_n + \chi_n)$$

with ϕ_i the phase of the individual macro. This energy kick can be applied at the passage through any section of the vacuum chamber where the impedance table is supposed to be, and conversely will show what is the highest value for the longitudinal impedance to achieve a given momentum spread.

Effect of Longitudinal Impedances

At the time the simulation was done we did not have clear ideas how the HESR vacuum chamber will be structured and consequently we did not have a specific impedance table and decided to use the table from Fig. 1 as a first guess; multiplying its impedance values by 10, 100, 1,000, respectively (scaling of equilibrium momentum spread with impedance values). For this very first study we utilized a 4-fold symmetry lattice of the HESR [3], tracking 10000 macro particles with a particle charge of 10^{11}. The longitudinal phase space was divided into 128 bins with an initial distribution spread over 360° and $\Delta p/p = 10^{-5}$ (rms). We repeated the tracking for four different beam energies, and with different bunch lengths at the same total current.

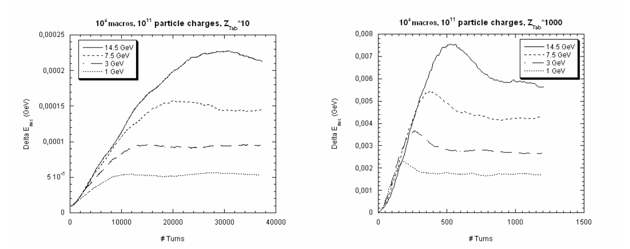

Fig. 2: r.m.s. value of ΔE for different longitudinal impedances and energies

From the final values of energy spread ΔE as plotted in Fig. 2 we obtained final values for momentum spread versus multiplication factor of the utilized impedance table as can be seen in Fig. 3 (left plot). Fitting the data in Fig. 3 showed that it is feasible to reach $\Delta p/p$ values in the range of 10^{-5} for the impedances used from impedance table. Since the HESR is a storage ring with many additional insertions like installation for experiments and cooling, longitudinal impedance could be a limiting factor for beam quality. Analyzing the results in Fig. 2 one can identify three regions: the initial region, where the beam starts to grow, a linear region in between and final region, where the distribution reaches equilibrium. The results of the fits in the linear region for different ring impedances and beam energies are shown in Fig. 3 (right plot). As expected the growth rate scales linearly with the impedances and shows some differences for various energies.

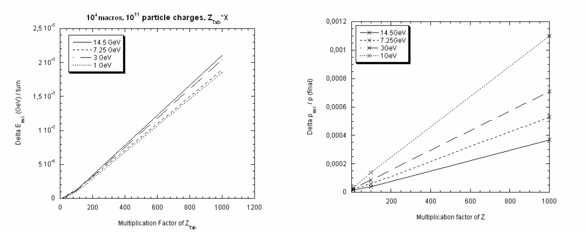

Fig. 3: Final rms value of the Δp/p (left) and increase of rms energy spread per turn (right) for different ring impedances and beam energies

All calculations were made on the new parallel supercomputer JUMP at the John von Neumann-Institute for Computing at the Forschungszentrum Jülich.

References:

[1] SIMBAD code by A.U. Luccio and N. D'Imperio (BNL), based on the ORBIT code by J. Galambos, S. Danilov, D. Jeon, J. Holmes, D. Olsen, J. Beebe-Wang, and A. Luccio, Proc. of the Particle Accelerator Conference (1999), p 3143

[2] A.Lehrach, AU. Luccio, SIMBAD Studies of the Effect of Impedances on the HESR, Proc. of the 33rd ICFA Advanced Beam Dynamics Workshop, High Intensity & Brightness Hadron Beams, October 18-22,2004, Bensheim, Germany

[3] Y. Senichev et al., Lattice Design Study for HESR, Proc. of the European Accelerator Conference (2004), p.653

[1] Forschungszentrum Jülich, 52425 Jülich, Germany
[2] Brookhaven National Laboratory, Upton NY 11973, USA

Radiation Protection at the HESR

O. Felden

Introduction

Aspects concerning the radiation protection have to be considered at the earliest stage of an accelerator project as they define boundary conditions that have to be met by federal law. Crucial areas are interaction points and regions that are foreseen for dumping the beam. Careful planning is not only necessary for radiation protection but also for minimizing the cost for shielding.

Skyshine

During the operation of an accelerator a significant amount of the dose rate in the vicinity the machine is produced by neutrons scattered on nuclei of the air. This phenomenon is called skyshine. The skyshine-dose can be calculated by using the following formula, which has been described by Alsmiller et al. in “Skyshine at neutron energies ≤ 400 MeV” [1].

$$\Delta \dot{D} = 2\cdot\pi\cdot\int_{\delta_n}^{\delta_{n+1}} (0.25\cdot Y_m(\delta)+0.5\cdot Y_m(\pi/2)+0.25\cdot Y_m(\pi-\delta))\cdot\cos\delta\cdot$$
$$\prod_{j=1}^{a} \cdot e^{-d_j\cdot\mu_{j_m}/\sin\overline{\delta_n}}\cdot I_m(\cos\Phi,r)\cdot J_P\cdot d\delta\cdot\Delta E$$

With

$\Delta\dot{D}$: Dose rate in the energy interval ΔE_m and the angular interval $\Delta\delta_n$

δ_n, δ_{n+1}: Boundary angles of the angular interval looked at

$Y_m(\delta)$: Neutron distribution function (from [3]) in the energy interval $E_m \le E \le E_{m+1}$

E_m, E_{m+1}: Boundary Energies of the interval $E_m \le E \le E_{m+1}$

d_j: Thickness of the top shielding material j

μ_{j_m}: Removal coefficient of the used top shielding material j for the energy interval $E_m \le E \le E_{m+1}$

$\overline{\delta_n}$: Average angle of the interval $\delta_n \le \delta \le \delta_{n+1}$

$I_m(\cos\Phi, r)$: “neutron importance function” (from [1]) for the neutron energy difference $E_m \le E \le E_{m+1}$

J_P: Loss rate of antiprotons

ΔE_m: Energy difference in the interval $E_m \le E \le E_{m+1}$

The overall dose rates in a distance r from the source of radiation are obtained by summing over all energies and angular intervals.

In fig. 1 the skyshine dose rates for a point-like loss of $2\cdot10^7$ p/s are shown in dependence of the distance r.

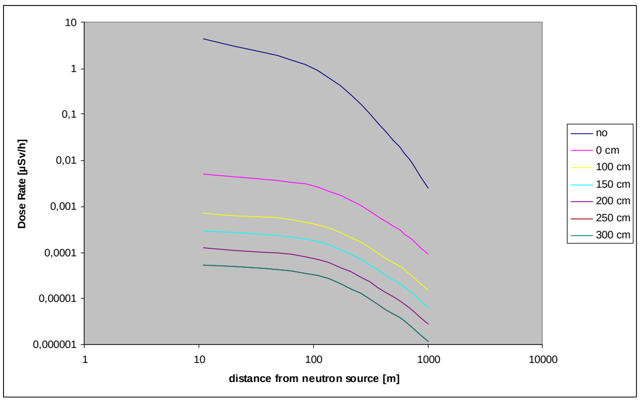

Figure 1: Dose rate in dependence of the distance r from the neutron source and different thicknesses d of the top shielding made from 100cm concrete plus the given numbers of earth-shielding in cm. The dark blue line (no) shows the dose rate without any shielding.

The investigation shows that it is necessary to have a top-shielding above the accelerator to reduce the dose rate at the fence of the research center. Assuming as the shortest distance between the HESR (source of radiation) and the fence to be 20m, i.e. the point where the dose rate must not exceed 1mSv/year or 0.12µSv/h, one needs a necessary top shielding of 40cm concrete.

Radiation shielding

The upper and lower boundary for shielding are defined by two scenarios. One is a line-source like loss, in which beam losses take place all over the ring with equal probability and the other scenario is the loss of the entire beam at one point. The real occurrence of losses will be within these boundaries. The maximum production rate of antiprotons for the HESR is in the order $2\cdot10^7$ p/s. This number represents the maximum average loss rate in the accelerator, respectively at the experimental setup under normal conditions. If by accident the entire beam is lost the number of instantaneously dumped antiprotons can go up to $5\cdot10^{11}$ particles or averaged $14\cdot10^7$ p/s.

The necessary lateral shielding of high-energy accelerators can be estimated by using the “Moyer-model”. R.G. Stevenson described a well-suited formula for these calculations [2].

In principle the model was developed to calculate the shielding for proton accelerators but can be applied at high energies for antiprotons in the same way.

The dose per stopped anti-proton outside of the shielding derived from this formula is:

$$H = H_0\cdot r^{-2}\cdot e^{(-\beta\cdot\delta)}\cdot\prod_{i=1}^{n} e^{\frac{-x_i}{\rho_i}}$$

With

H: Dose per stopped Antiproton outside of the shielding

$H_0(E_p)$: normalized Dose, which depends on the energy of the primary antiproton. Its value is $3.5\cdot10^{-12}$ Sv·m² for 22GeV primary energy [2].

r: Distance from the source of radiation

β: Constant, the best value established by Stevenson [2] is 2.3.

δ: Angle towards beam direction

x_i: Thickness of shielding material i

ρ_i: Relaxation length of the shielding material i

n: Number of different shielding materials

Because of the superposition of the radiation fields from the other accelerators, GSI demanded that the dose-rate at the outer HESR-shielding must not exceed 0.5µSv/h. Taking that number the calculation of the line-source like losses require a minimum lateral shielding of 1m concrete and about 0.5m earth. In case of the point-like loss it requires a maximum lateral shielding of 1m concrete and 4m earth. The real losses and hence the required shielding will be within these to boundaries.

To reduce halo-effects at the experiment and at the electron-cooler it is foreseen to install two scrappers, one behind the electron-cooler, the other behind the PANDA-Detector. Particles passing through the scrappers will loose some energy, which leads to their loss in the arc section. This will induce a higher dose rate in the arc section compared to the straight sections. An estimated loss of 70% of the particles in one of the bending sections requires a shielding of 1m concrete and 2.5m earth to stay below the dose-rates limit.

Another issue, which has to be looked at, is the dose rate at the fence of the research center. Here the dose-rate must not exceed 1mSv/year or 0.12µSv/h. The distance between the source of radiation and the fence has not been finalized. Assuming a distance of 20m and a lateral shielding of 1m concrete and 2.5m earth in the bending sections this condition can be fulfilled, too. In case of a permanent point-loss, which is highly unrealistic the shielding would have to be 1m concrete and 3.2m earth. In case of a later upgrading program in which the loss rates exceed the given values by a factor of 10 the shielding would have to be strengthened with 1.2m earth.

Special attention has to be paid to the shielding of the electron-cooler-section. The losses in this section are estimated to be max. 2mA at 8MeV. In order to reach the required 0.5µSv/h Dose-rate outside the building the shielding must be of 1m concrete plus 4.7m earth in case of equal losses all over the 30 m cooling length. In case of a point-like loss it has to be 1m concrete plus 5.3m earth. Because of this large amount of shielding one could take into consideration using a thinner shielding in combination with a monitoring system that would be part of the interlock of the electron-cooler. By lowering the losses by a factor of 10 the earth-shielding can be reduced by 40cm.

[1] Alsmiller, R.G.Jr.: Skyshine at neutron energies ≤ 400 MeV, ORNL-TM-7512 (1980)

[2] Stevenson, G.R. et al.: Determination of transverse shielding for proton accelerators using the Moyer model, Health physics Vol. 43(1) pp13-29 (1982)

[3] Probst, H.J.: Strahlenschutzrechnungen für COSY, unpublished (1992)

6 Technical Developments

First Polarization Measurement of Hydrogen Atoms Effusing from a Storage Cell into the Lamb-Shift Polarimeter and the Removal of the Components of the Polarized Target to COSY

R. Engels, K. Grigoryev[a], P. Jansen[b], F. Klehr[b], H. Kleines[c], M. Mikirtytchiants[a], F. Rathmann, J. Sarkadi, H. Seyfarth, and A. Vassiliev[a]

From next year on the polarized internal target (PIT) allows experiments with a polarized target at ANKE. For this purpose a T-shape storage cell[1] in the COSY beam line will be filled with polarized hydrogen or deuterium atoms, produced with an atomic beam source (ABS). The polarization should be measured when a sample of this atoms went through a sampling tube into a Lamb-Shift polarimeter[2].

The mayor problem for the polarization measurement is the very small number of less than 10^{13} atoms/s reaching the ionizer of the LSP. Therefore, the amount of polarized protons (deuterons) is in the order of 100 pA and about 10 times smaller compared to background ion beam produced from residual gas. But with a chopper between sampling tube and ionizer and a special amplifier the signal of the polarized atoms was separated and the polarization could be measured. In Fig. 1 the polarization is shown as a function of the current in the wienfilter coils, when the polarization vector was rotated. Even after some corrections the absolute value of the polarization is smaller than expected. This point at some other effects, which decrease the asymetry of the Lyman peaks. For example it could be shown, that most atoms do not recombine after they leave the storage cell and enter the vacuum chamber. After some wall collision this atoms are unpolarized and then they reached the LSP, when the chopper was open.

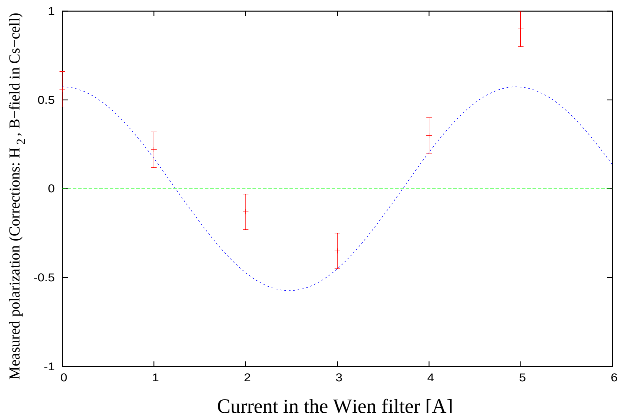

Fig. 1: The measured polarization along the beam line, when the quantization axis is rotated on the vertical magnetic field in the spinfilter.

In autum the movement of all PIT components to COSY starts. All infrastructure components, developed together with Zentralabteilung Allgemeine Technologie of FZJ, and the slow control system of ABS and LSP, developed with Zentralinstitut für Elektronik of FZJ, are available. ABS and LSP have been transferred to the "LKW-Schleuse", a separate area within the COSY hall outside the accelerator tunnel. The photograph in Fig. 2 shows the assembly there. The vertical ABS is mounted in the new horizontal frame, which is carried by two support posts. The LSP is horizontally mounted in a support, which allow one to change the height. In the lower position, with the ionizer mounted vertically and followed by a 90 $^\circ$ deflector, the direct beam from the ABS can be studied, whereas in the higher position, with the ionizer mounted horizontally, investigations of gas samples extracted from test cells fed by the ABS becomme possible. All the supply units are assembled on a moveable platform. Thus, a few crane movements only are needed to transfer the ABS in its support bridge, LSP, and supply units to and from the ANKE target place.

Between the beam-times, where ABS and LSP are used at ANKE, these instruments are employed in the LKW-Schleuse combined with an an additional device, developed at the St. Petersburg Nuclear Physics Institute (PNPI) in Gatchina in the framework of an International-Science-and-Technology-Center (ISTC) project. This worldwide unique combination of ABS, the PNPI chamber with exchangeable test cells in a strong magnetic field produced by a superconducting magnet, and the LSP for polarization analysis, will allow hitherto inaccessible studies of the recombination process polarized hydrogen or deuterium atoms on various wall materials as function of the wall temperature and of the nuclear polarization maintained in the recombined molecules.

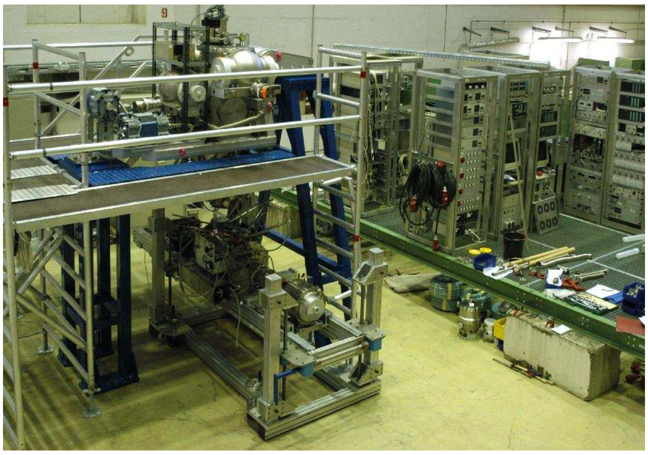

Fig. 2: The experimental setup in the "LKW-Schleuse" of the COSY hall: The ABS (vertical) in its horizontal support bridge, the LSP (horizontal) in the lower support system, and the ISTC chamber underneath the ABS. On the right-hand side the moveable platform (green) with the equipment for ABS and LSP is shown.

In parallel a new LSP was designed together with R. Gebel to measure the polarization of the deuteron beam from the polarized source at COSY. With this device it will be possible to tune the transition units of the ABS online. Therefore, the time to optimize the COSY beam polarization can be minimized.

References:

[1] K. Grigoriev et al., contribution to this report.
[2] R. Engels et al., Rev. Sci. Instrum., Vol 74 (2003) 4607.

[a] St. Petersburg Nuclear Physics Institute, Gatchina, Russia.
[b] Zentralabteilung Technologie, FZ Jülich.
[c] Zentrallabor Elektronik Technologie, FZ Jülich.

Observation of hydrogen and nitrogen pellets at the ANKE pellet target*

W.Borgs, M.Büscher, A.Bukharov[a], V.Chernetsky[b], V.Chernyshev[b], P.Fedorets[b], A.Semenov[a]

During 2004 several pellet-target test runs have been performed according to the final stage of ISTC[1] project #1966. The target comprising a cryostat with the pellet generator and the dumping system is currently installed in the COSY accelerator hall (Fig. 1) in a support construction which can later be moved to an internal target place of COSY.

Fig. 1: The pellet-target test-setup in the COSY hall.

In a pellet target a continuous flow of droplets is generated by injecting a liquefied gas through a thin vibrating nozzle into a triple-point chamber (TPC), where temperatures and pressures close to TP conditions for the particular target material are maintained. These droplets freeze and form the pellets when they pass through a sluice (length ∼5 cm, inner diameter ∼0.6 mm) into vacuum. The tests in 2004 focused on the optimization of nozzle and sluice components.

In order to develop technologies for bulk production of nozzles, two different nozzle types have been tested. About 20 capillary glass nozzles glued into brass or steel housings with outlet diameters ranging from ł = 8 to 45 μm have been produced. 10 of these were tested for liquid jet generation as well as stainless steel nozzles with ł = 25 and 38 μm. All nozzles provided stable generation of liquid hydrogen and nitrogen jets, while the jet velocities are roughly two times larger for the glass nozzles. The process of jet and droplet formation can be observed with a fast CCD camera which is installed close to a window in the TPC, see Fig. 2.

Due to the cooling and warming time of the target cryostat, about 3 days are needed for testing each nozzle. Thus a dedicated test cryostat has been assembled at ITEP in order to minimize the time for nozzle tests during target operation at the FZJ. New nozzles produced in Russia will be tested and selected before being transfered to the Germany.

For observation of frozen corpuscles a second CCD camera has been installed close to quartz glass window of the first vacuum chamber and focused on the outlet of sluice from the TPC. To observe 30 μm pellets the optical magnification must not be less than a factor 50. Due to the sensitive time of the CCD (∼ 5 μs) the pellets are currrently observed as short

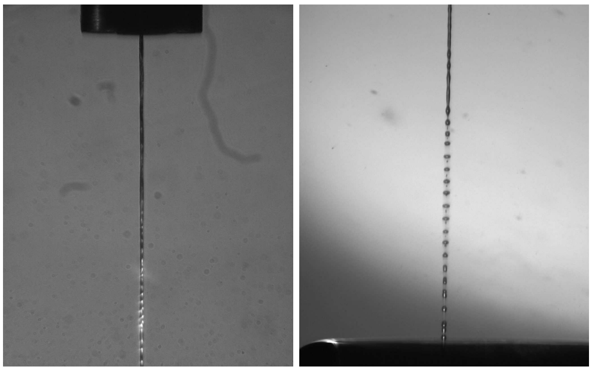

Fig. 2: Injection of an H_2 jet through a steel nozzle with ł = 38 μm into the TPC (left). Breakup of a jet into droplets before the sluice to the first vacuum chamber (right).

tracks with lengths depending on their velocities (Fig. 3). The frequency of pellet detection is 300 Hz, at 3 kHz for the droplet generation. The measured pellet velocity is about 30–50 m/s which is close to the expected value. The information from the CCDs is written to disk for subsequent analyses.

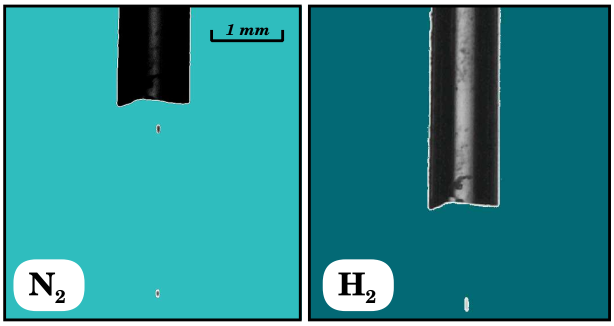

Fig. 3: N_2 and H_2 frozen pellets with ł ∼ 30 μm (ł$_{\rm nozzle}$ = 18 μm) behind the sluice to the vacuum chamber.

During the November/December test runs long-term stability of liquid jet generation has been achieved. In the vacuum chamber stable generation of hydrogen and nitrogen pellets with different diameters has been obtained and observed, see Table 1. The tests were carried out during 10 days of permanent target operation. Since hydrogen and nitrogen pellets have been generated for many hours the target demonstrated its reliability for installation at the internal beam of COSY.

Table 1: Main results of the nozzle tests.

Nozzle type	Nozzle ł	Target material	Pellet ł
Steel	25 μm	H_2	50 μm
	38 μm	H_2	70 μm
	38 μm	N_2	70 μm
Glass	10 μm	H_2	$<$ 20 μm
	18 μm	H_2	30 μm
	18 μm	N_2	30 μm
	40 μm	H_2	70 μm

[1] International Science and Technology Center, Moscow, http://www.istc.ru

[a]MPEI, Moscow, [b]ITEP, Moscow

*Supported by grants RFFI03-02-04013, RFFI02-02-16349, DFG-436RUS-113/733, ISTC#1966.

Polarized Target for the TOF - Detector

H. Dutz[1], J. Heckmann[2], Ch. Hess[2], F. Klein[1], W. Meyer[2], A. Raccanelli[1],
E. Radtke[2], G. Reicherz[2]
[1] Physikalisches Institut Universität Bonn
Nussallee 12, 53115 Bonn
[2] Institut für Experimentalphysik I, Ruhr-Universität Bochum
Universitätsstr. 150, 44780 Bochum

With the increasing experimental evidence for an exotic baryon with strangeness S=+1, the Θ^+ (1540), forthcoming activities are trying to pin down the quantum numbers of the Θ^+. In particular the parity $\pi(\Theta^+)$ of this state is so far not determined experimentally and the theoretical predictions allow for both possibilities. It is thus of utmost importance to determine $\pi(\Theta^+)$ to further constrain the internal dynamics and structure of this exotic state. In the near future it is planned to measure the spin correlation coefficient A_{xx} at COSY to determine the parity of the Θ^+ from the reaction $\vec{p}\vec{p} \longrightarrow \Sigma^+\Theta^+$ near its production threshold. The measurement of A_{xx} requires transverse polarized protons in the initial state provided by a polarized beam and a polarized target, respectively [1].

There can be significant technical problems in the use of a polarized target for the proposed experiment. To detect the charged particles of the nominal process exiting the target with a reasonable efficiency, the first detector components must be placed as close as possible to the interaction vertex, which limits the outer diameter of the target refrigerator. In order to achieve the necessary statistical precision, one must have a reasonably thick target with a high polarization. The target material should also be resistant to localized beam heating and radiation damage to avoid depolarizing the sample unevenly, particularly in the region of the beam.

To obtain a reasonable counting rate in the case of a limited beam intensity, a wide opening angle with the ability to place detector components as close as possible to the target material is needed. This can be achieved with the concept of the frozen spin target [2]. The operation of the frozen spin target is based on the experimental fact that the nucleon polarization relaxation time T_1 is a very strong function of the temperature and the magnetic field. T_1 characterizes the polarization decay after switching off the dynamic nuclear polarization (DNP) mechanism. Once the target material is optimally polarized at a high and uniform field (e.g. 2.5 Tesla) and at a temperature in the range from 0.2 to 0.4 K ('continuous mode'), the microwaves are switched off and the polarization is frozen at temperatures around 60 mK ('frozen spin mode'). Due to the very long T_1 at these temperatures, the field in the target region can be significantly reduced to a value of 0.3 - 0.6 T ('holding field') where the polarization decay is still acceptable. An appropriate setting of external holding magnets allows different orientations of the target polarization and provides good experimental access. The disadvantage of the external holding coil arrangement is the large size and strong fringe field of the superconducting magnets. Therefore such frozen spin targets cannot be operated in combination with detection systems, where detector components are placed close to the target refrigerator. To overcome this problem, a new type of a small superconducting 'holding magnet' has been built by the Bonn polarized target group [3]. The superconducting wire has been wound on the inner cooling shield of the vertical ^{3}He/^{4}He-dilution refrigerator around the target area.

That this is a reliable technique also under experimental conditions has been demonstrated by our group with the PS185 experiment to measure the spin transfer parameter D_{nn} in the hyperonproduction ($\bar{p}p\uparrow \longrightarrow \Lambda\bar{\Lambda}$) at the antiproton accelerator LEAR (CERN) in 1996 [4, 5, 6]. A miniaturized butanol block target sample of 0.24 cm^3 [7] was used in the modified vertical dilution refrigerator with a tiny 'split-pair'-like internal holding magnet, [8], which maintained the polarization in a field of 0.58 T and gave an open geometry of 4π in the CMS-system. Due to the small size of the arrangement of the superconducting coils the field at short distances axial and radial from the center of the magnet diminishes to about 10^{-3} Tesla. This allows the placement of detector components directly around the vacuum jacket of the dilution refrigerator. A maximum proton polarization of about $\pm 70\%$ has been reached in a polarizing field of 2.5 Tesla, typical relaxation times of $\tau \sim 100$ h led to an average polarization magnitude over the entire data taking period of about 62%.

Since indeed both experiments, the planed parity measurement of the Θ^+ at COSY and the D_{nn}-measurement at PS185/3, are comparable in various demands, we propose to combine the existing frozen spin target used at the PS185/3 experiment with a new TOF-start counter setup [9]. But with respect to the special boundary conditions of the experimental area at COSY and the TOF-detector as well as the experimental requirements of the scattering observable, the target has to be partially modified and adapted to the detector setup. The mechanical structure containing the main target components like the dilution refrigerator and the superconducting polarization magnet, placed in front of the TOF-detector arrangement has to be renewed. The frame will consist of three parts. The first part supports the necessary vacuum pumps and electronics next to and above the detector and target systems. The second part supports the cryostat assembly, and will be mechanically independent of the first to lessen vibration which would cause heating and stress to the target refrigerator. The cryostat will be held from above by vacuum-tight bellows and clamps attached to the support frame to leave the target area free for the start-detector components. The third one takes care of the movement of the polarization magnet to polarize or repolarize the target in the 'continuous mode' and for the data taking ('frozen spin mode'). The start-detector components will be placed on a separated frame which allow to accurately move the detectors in and out of the target region for the data taking. First design studies have shown that such a complex mechanical structure can be placed in between the existing TOF-detector and the last beam defining elements of the accelerator ('Brandenburger Tor').

The second main modification on the target system concerns the target material itself. To get a reasonable luminosity and a high acceptance for the reconstruction of the nominal process, the beam intensity has to be maximized and the beam spot on the production target to be minimized. We expect an intensity of 10^7 protons/sec at a beam spot of about 1 mm^2. Under this conditions the butanol block target scheme used at PS185/3 is a non appropriate solution. It fails with regard to the radiation resistance, which is limited to about 10^8 $protons\ sec^{-1} cm^{-2}$, a poor heat conductance and a high Kapitza resistance of the amorphous material. With an assumed bath temperature of about 60 mK, the last point causes a temperature increase in the beam spot to more than 100 mK leading to relaxation times of only a few hours [10]. The discussions led to ^6LiD or ^7LiH as target material. The advantages of the Lithium isotopes are a good radiation hardness, high relaxation times at moderate temperatures ($\tau \sim 50$ $days$ at ~ 90 mK and 0.5 $Tesla$), easy handling and a preparation at room temperature [11]. It is planned to use a target sample with 4 layers of ^7LiH with a diameter of 6 mm and a total thickness of 4 mm and we expect a proton polarization of about $\sim 70\%$ at 5 $Tesla$. [12]. The preparation of the material and measurements of the polarization behavior will be done at the Bochum polarized target laboratory. In the meantime the complete target setup will be installed and tested at the Bonn University. As soon as all components including the target material are running with the expected parameters (high polarization and long relaxation times) the system will be moved to the IKP and installed at the TOF experimental area at COSY.

[1] C. Hanhart et al., hep-ph 0312236v2 (2004).
[2] T.O. Niinikoski and F. Udo, Nucl. Instr. and Meth. **134** (1976) 219.
[3] H. Dutz et al., Nucl. Instr. and Meth. **A356** (1995) 111.
[4] M. Plückthun, PhD-thesis, Universität Bonn, BONN-IR-1998-4 (1998).
[5] B. Bassalek et al., Phys. Rev. Lett. **89** (2002) 212302.
[6] H. Dutz et al., to be published in Nucl. Instr. and Meth.
[7] M. Plückthun et al., Nucl. Instr. and Meth. **A400** (1997) 133.
[8] R. Gehring et al., Nucl. Instr. and Meth. **A418** (1998) 233.
[9] H. Dutz, Workshop on Hadron Physics at COSY (HPC 2003), Bad Honnef (2003).
[10] A. Raccanelli, 'Polarized Nucleon Targets for Europe' (JNR8 Sixth European Framework Program), Bochum (2004).
[11] St. Goertz et al., Nucl. Instr. and Meth. **A425** (1995) 20.
[12] J. Ball, Nucl. Instr. and Meth. **A526** (2004) 7.

Gold Fingers Cryogenic Target for External COSY Experiments

S. Abdel-Samad, M. Abdel-Bary, K. Kilian, J. Ritman and J. Uehlemann
for the COSY-TOF-collaboration

A very small and very light liquid hydrogen/ deuterium target has been developed for background-free pp and pd interaction studies at COSY [1]. The target has a long, thin heat conductor, which was first made as metallic conductor from copper, then aluminum and finally we now use an extremely light stainless steel heat pipe of 0.1 mm wall thickness [2, 3]. Isolation against heat radiation was done by a stack of very light aluminized Mylar foils (superisolation). As further improvement, we show that small enough heat load to the cold parts can also be achieved by coating the target finger and the heat pipe (Fig. 1) with a thin polished gold layer. The radiation heat load is described by the black body radiation formula:

$$P = \sigma A \varepsilon (T^4_{outside} - T^4_{surface}), \qquad (1)$$

Where σ is the Stefan-Boltzmann constant = (5.67×10^{-8} W m^{-2} K^{-4}), A is the surface area (76.93 cm^2), ε is the emissivity of the surface (stainless steel = *0.4,* aluminum = 0.22 and polished gold = 0.02), $T_{surface.}=15$ K, $T_{outside}=300$ K.

With gold the radiation heat load is reduced from 1400 mW on the non-isolated stainless steel surface system to 70 mW. It is reduced further to 0.05 mW by using an aluminum heat shield at ~ 50 K around the cold parts at 15 K. The heat load can be reduced further without changing the geometry by coating both sides of the aluminum shield with a thin gold layer. The new very slim "gold finger" target showed safe and stable performance during a 6 weeks long run.

Table 1: The radiation heat load to the heat pipe and the target finger without and with gold coating

Radiation heat load to the heat pipe and target at 15 k	Heat load (W)
without super isolation and without coating	1.42
with gold coating of the heat pipe and the target appendix	0.07
with gold coating heat pipe-target appendix and 1 mm Al heat shield at 50 K around the heat pipe	0.00005

The advantages of using an aluminum heat shield around the gold coated heat pipe are:

1. further strong reduction of the heat load to the cold parts because the Al shield (connected to the first stage of the cooling machine) is at ~ 50 K. The radiated heat to the cold parts is reduced by factor 1400.
2. there is no super isolation which gives better access for detectors.
3. improved vacuum around the target by reducing the degassing between the super isolation layers.

Even without aluminum heat shield the gold coated target system works well with stable working conditions [4].
The cool down time of the gold coated heat pipe and target with liquid hydrogen is shown in Fig. 2. T1, T2, T3, T4 are the temperatures on the aluminum condenser of the heat pipe, target appendix, aluminum shield at the first stage, end of the aluminum shield, respectively.

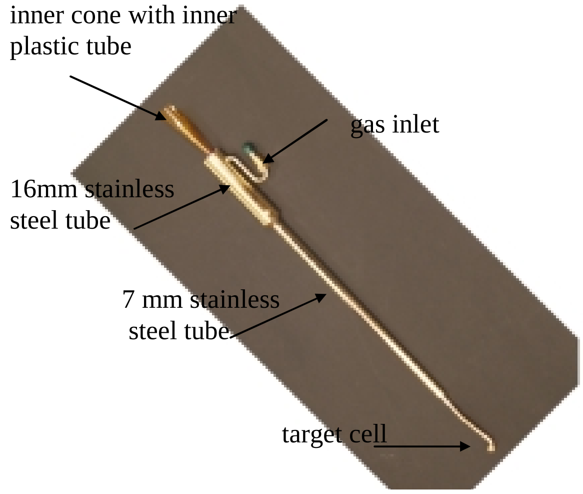

Fig. 1: Gold coated heat pipe and target appendix.

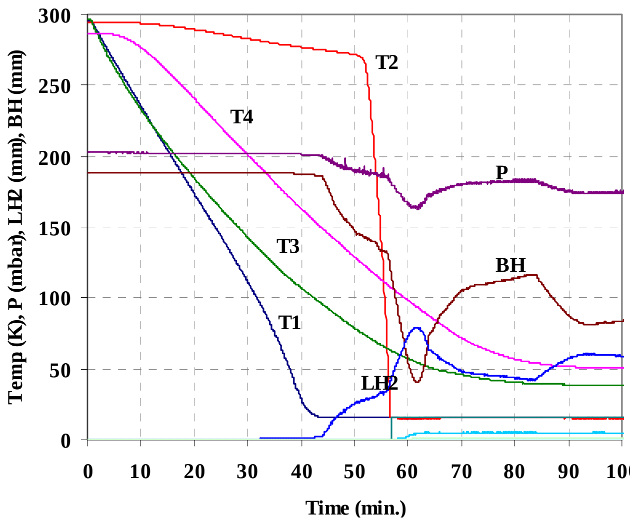

Fig. 2 Cool down time of the gold coated heat pipe and target with liquid hydrogen (without heat shield)

References:

[1] s. Abdel-Samad, M. Abdel-Bary, and K. Kilian. NIM 495 (2002)1-7.
2] S. Abdel-Samad, PhD. Thesis FZJ/RWTH Aachen (2001)
[3] M. Abdel-Bary, PhD. Thesis FZJ/RWTH Aachen (2004)
[4] s. Abdel-Samad, M. Abdel-Bary, K. Kilian, J. Ritman, to be published in NIM A.

Residual gas analysis in the TOF high vacuum tank

S. Abdel-Samad, M. Abdel-Bary, K. Kilian, J. Ritman and J. Uehlemann
for the TOF-Collaboration

Residual gas in the TOF vacuum system refers to those gases remaining in the vacuum chamber during the normal operation. Although these gases may be present in small amounts, their presence is very significant to the reaction between the COSY proton beam and the liquid hydrogen target where a low level of background from residual gases is a prerequisite to success [1,2]. Since the liquid hydrogen target at 15 K acts as a cryopump, the target area has to be in a high vacuum < $1*10^{-6}$ mbar. All residual gases except hydrogen and helium condense and freeze on the windows of the liquid hydrogen target. As a result it increases the background during the reaction between the COSY beam and the target. These condensates have to be removed from the target windows by heating the target cell from 15 K up to room temperature.

The residual gas composition in the TOF vacuum system has been measured with a quadrupole mass spectrometer [3]. The partial pressure spectrums of the condensed gases on the liquid hydrogen target are also measured. The residual gas analysis as shown in Fig. 1 shows that the majority of the condensates on the target windows after operating the vacuum for 21 days are nitrogen, oxygen and water vapor. A fast heating is used to clean the target where only the window region of target cell is heated from the cold operating temperature to room temperature until the condensates disappear. The fast heating cycle takes about 1 minute for heating and 5 minutes for cooling down again and for vacuum improvement due to the residual gases [4,5]. In Fig. 2 shows the residual gases and all outgassing spectrum during fast heating and cleaning the full gas hydrogen target in the small TOF tank at $6.6*10^{-7}$ mbar after 21 days operation of the vacuum system. The three spectrums the figure are for the outgassing of oxygen, nitrogen and water vapor

Table 1 summarizes the residual gases and all outgassing from the target windows

Mass spectrum Atomic Mass Unite (AMU)	Gas type
1,17,18	H^+, HO^+, $H2O^+$
2	$H2^+$
14, 28	N^+, $N2^+$
16, 32	O^+, $O2^+$
40	Ar^+
12, 44	C^+,$CO2^+$

The appearance of masses 28, 32 in the ratio of N_2 and O_2 in air (about 4:1) usually signifies a leak in the vacuum system, but such ratios are not shown in the mass spectrum this means there is no observable leak in the system. In Fig.2 one see the characteristic strong peaks at 1 and 18 AMU (water vapor at 160 K , partial pressure 4.0 E-9 mbar and 2.0 E-7 mbar respectively) - at 8, 16 and 32 AMU (oxygen at 130 K , partial pressure 7.0 E-12 mbar, 3.3 E-9 mbar and 5.2 E-8 mbar respectively) – at 14 and 28 AMU (nitrogen at 30 K , partial pressure 1.2 E-8 mbar and 1,9 E-7 mbar respectively) – at 19 AMU (fluorine at 160 K , partial pressure 2.1 E-9 mbar) – at 20 and 40 AMU (argon at 130 K , partial pressure 3.0 E-11 mbar and 1.3 E-9 mbar respectively).

The present investigations show that the fast heating process for the target cleaning is very effective. It shows the degassing of water vapor, nitrogen and oxygen with high peaks. It is clear that the deposited layer of water vapor, nitrogen and oxygen is removed during the target

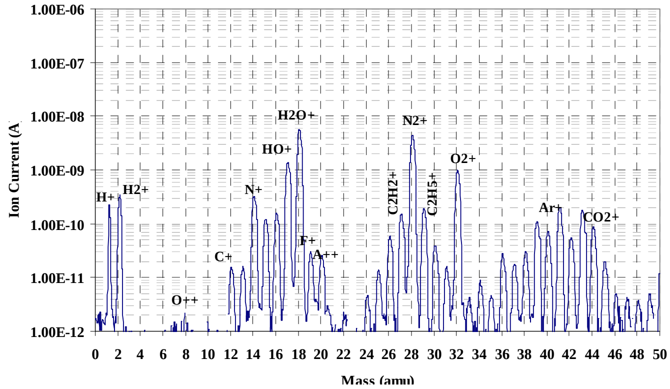

Fig. 1 The residual gases in the small TOF tank after 21 days from starting the vacuum system with full liquid hydrogen target.

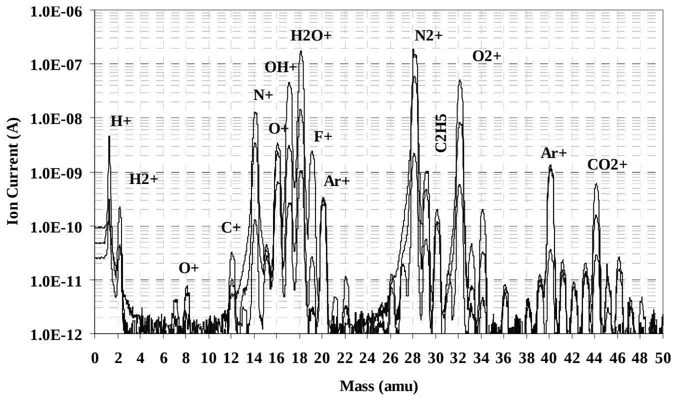

Fig. 2 The residual gases and all outgassing spectrum during fast heating and cleaning the full gas hydrogen target in the small TOF tank after 21 days from starting the vacuum system.

cleaning with the fast heating process. This cleaning cycle is needed to be done every 2 days.

References:

1. Hassan A, Brinkmann K-Th, Kuhlmann E, Kilian K, Oelert W, Roderburg E. NIM A425 (1999)403 - 408.
2. Abdel-Samad S, Abdel-Bary M, Kilian. NIM A495 (2002) 1-7.
3. Pfeiffer Vacuum. QMS 200 Quadrupole mass spectrometer Prisma. Germany (1999).
4. Abdel-Samad S. Ph.D. thesis, FZ Juelich/Aachen University, Germany (2001).
5. Abdel-Bary M, Abdel-Samad S, Kilian K. Accepted paper NIM A.

Studies of an External Cryotarget for WASA at COSY

S. Abdel-Samad, M. Abdel-Bary, K. Kilian, J. Ritman and J. Uehlemann
for the TOF-Collaboration

WASA ("Wide Angle Shower Apparatus") has been designed and built for use as an internal beam setup with the CELSUS accelerator. It consists of Central Detector, Forward Detector, Pellet Target and Zero-Degree Spectrometer [1]. WASA will come to COSY, and there are two possibilities to install WASA: either as an external experiment with the Time of Flight Spectrometer (TOF) or as an internal experiment in the COSY ring.

The most crucial questions concerning an external target for WASA at COSY during the WASA meeting in December 2003 and also during the WASA workshop FEMC04 in January 2004 were: Is it possible to build a LH2/D2 target compatible with WASA within the next two years? Who will build it and how long does this take? What are the necessary modifications (beam- and target-tube) to WASA?

We were able to prove that our standard cryotarget with 0.9 µm Mylar windows can be used. In the existing WASA detector system no changes at all are needed. In the vacuum system one needs only minor changes (outside of the detectors) in order to insert a horizontal heat conductor of 1.2 m length. The horizontal part can not be our standard heat pipe but must be a > 1m long metallic conductor. We succeeded in a quick test to run with a 100 cm long aluminum conductor (1.5 cm diameter) and a 32 cm long heat pipe (7 mm diameter). Our standard cold heads have already sufficient cooling power and provided the required low temperature of 15 K for LH_2 and 18 K for LD_2 in 1.3 m distance from the cold head. The cool down time from room temperature to the operating temperature of LH_2 and LD_2 is governed by the comparatively large heat capacity of the Al conductor.

An external target at COSY can take full advantage of the very small external beam cross section and the resulting very small target – beam overlap of only a few mm^3 or less. A similar LH_2/LD_2 target construction as currently used at TOF and BIG KARL can be made within few weeks. The WASA detection system does not need to be modified. The only change to the internal target operation is an additional flange on the existing vacuum tube as indicated in Fig. 1.

A luminosity of $L = 10^{32}\ cm^{-2}s^{-1}$ can be reached with 5.10^{10} (unpolarized) particles in COSY, an extraction cycle of 20 s and a LH_2/LD_2 target of 10 mm length (taking into account 5s for beam preparation). For higher intensities or shorter cycles the target can be shorter too.

Experimental results with LH_2/LD_2 target for external installation of WASA at COSY

With the standard cold head and standard heat pipe and target [2-4] in addition to a 1 meter aluminum heat conductor we made a working prototype. We succeeded to cool down the target from room temperature to the liquid temperature of LH_2 and LD_2 and to have enough liquid in the target cell with stable working conditions (Fig. 2). It is possible to use LH_2/LD_2 target with the existing WASA detection system with only very small modifications in the inlet vacuum tube. Future developments and tests may concern the shape of the aluminium conductor and the cool down time.

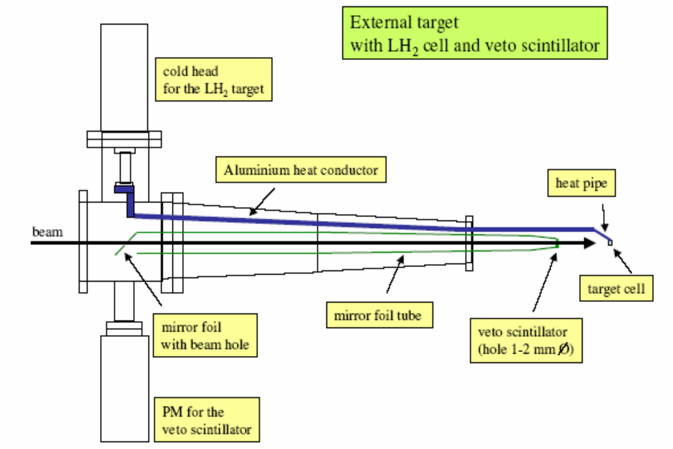

Fig.1 Schematic drawing of the LH2 target instillation in WASA at COSY. Only the inlet for the heat conductor from the cold head has to be added to WASA.

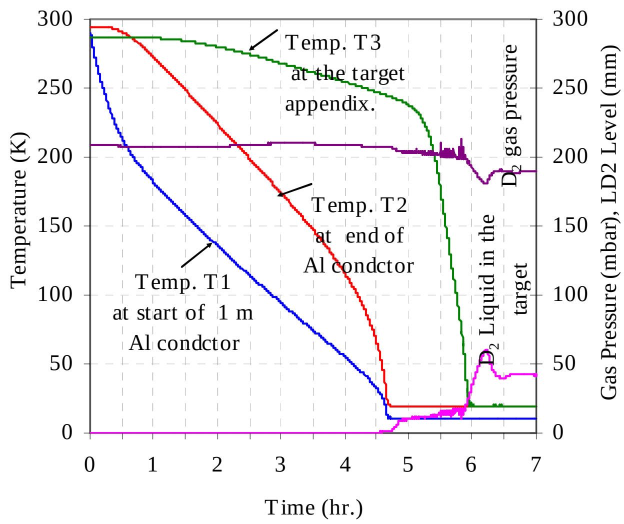

Fig. 2 Temperatures during cooling down of cold head, 1 meter aluminium heat conductor and target cell at the end of the 7 mm diameter heat pipe with deuterium filling.

References

[1] WASA home page: http://lora.tsl.uu.se/wasa/
[2] S. Abdel-Samad, et al., Nucl. Instr. and Meth. in Phys. Res. A495 (2002) 1.
[3] S. Abdel-Samad, Ph.D. thesis, FZ Juelich/Aachen University, Germany (2001).
[4] M. Abdel-Bary, Ph.D. thesis, FZ Juelich/Aachen University, Germany (2004).

Laboratory for Semiconductor Detectors

D. Protić, G. Fiori, T. Krings, H. Metz, K. Schwill

Increasing interest perceived world-wide has stimulated research and development of large-volume Si(Li) detectors. Well established techniques for creating position-sensitive structures on both contacts have been applied to construct two-dimensional devices. These detectors break into new fields of applications in position-sensitive detection of photons and charged particles.
Many Si(Li) detectors with a diameter of 4-inch and thicknesses between 5 mm and 10 mm have been processed by means of the reproducible Li-drift technique developed last years. Two of 10 mm thick detectors and several thinner detectors received position-sensitive structure (strips) on both contacts.
Excellent results achieved with the 10 mm thick detectors spurred us to develop even thicker detectors. A 20 mm thick diode with a diameter of 102 mm is being drifted. More than half of the thickness has been already Li-compensated.

Another possibility to enlarge the volume is using slices of larger diameter. According to the world leading company producing Li-driftable p-type silicon, TOPSIL (Denmark), there are some problems if the diameter exceeds 4-inch. In collaboration with TOPSIL we are currently testing the Li-driftability of several 5-inch slices. Each of the slices was cut from the different part of the silicon ingot. Definite correlation between the Li-driftability and the position inside the ingot has been found. In any case, we hope to start with fairly good (Li-driftable) 5-inch p-type silicon slices. These investigations will be extended also to 6-inch material. Even more, we will try to improve the Li-driftability of bad slices through various annealing and gettering techniques.

For the ANKE vertex group additional 3 Si(Li) detectors were built. The detectors are 5.1 mm thick and have the same position-sensitive structure on both contacts: 96 strips on 64 mm x 64 mm active area, orthogonally positioned. The group has been supported in preparation of the vertex telescopes and the chip-based readout electronics (mounts, connections, glueing, bonding, etc.). Of course, the availability of ca. 10 mm thick position-sensitive Si(Li) detectors will be exploited for constructing improved vertex telescopes being able to stop particles of higher energies. A couple of detectors are already at different preparation stages.

First 10 mm thick Si(Li) orthogonal-strip detector (32 strips with a pitch of 2.0 mm on each contact) has been delivered to Lawrence Livermore National Laboratory. This detector is now being used as the scatter detector of their Si+Ge Compton Camera [1-3]. By combining two-dimensionally segmented detectors having 2.0 mm wide strips with appropriate pulse-shape processing it is possible to obtain three-dimensional position information of interactions to an accuracy of about 0.125 mm^3.

Large-volume Si(Li) position-sensitive detectors are also very attractive for spectroscopy of light-particle target recoils which is planned to be realised in frame of the EXL-collaboration. Our laboratory is involved in submitting the Technical Proposal for the FAIR project at GSI-Darmstadt (January 2005).

A world-wide collaboration conducted by Prof. Walenta from University of Siegen is working on a Compton Camera research project named C-Camed. Our large-volume Si(Li) orthogonal-strip detectors will be an important contribution to this project. The proposal "High sensitivity molecular imaging with the Compton Camera for targeted cancer therapies" is submitted (November 2004) to the FP6-2004-LIFESCIHEALTH-5 program of EU.

Fully equipped detector system "Germanium wall" (Quirl-detector followed by three 17 mm thick ΔE-detectors) was employed at two GEM-experiments (April and November 2004). Seriously radiation damaged detectors were thoroughly regenerated before every experiment. The detector system was every time installed, prepared for measurements and maintained during and after the experiments by our group.

An unique two-dimensional microstrip germanium detector was developed and constructed for x-ray spectroscopy of highly-charged heavy ions [4, 5].

Several IKP-groups were supported by our laboratory through various service, among other things

- Ceramic resonators of COSY-group were covered with well defined evaporated germanium layers.
- A series of Cs-ovens for ATRAP-experiment were covered with evaporated gold layers.
- Several copper tubes for LH_2-target were covered with evaporated gold films.

References:

[1] "Large-Volume Si(Li) Orthogonal-Strip Detectors for Compton-Effect-Based Instruments", contribution to this report.

[2] D. Protić, E. L. Hull, T. Krings, K. Vetter, "Large-Volume Si(Li) Orthogonal-Strip Detectors for Compton-Effect-Based Instruments", presented at IEEE NSS 2004, Rome, Italy, Oct. 16-22, 2004

[3] K. Vetter, M. Burks, E. Hull, L. Mihailescu, T. Niedermayr, D. Protić, T. Krings, P. Luke, C. Tindall, "A Compact Si+Ge Compton Camera", presented at IEEE NSS 2004, Rome, Italy, Oct. 16-22, 2004

[4] "Two-Dimensional Microstrip Germanium Detector for X-Ray Spectroscopy of Highly-Charged Heavy Ions", contribution to this report.

[5] D. Protić, Th. Stöhlker, T. Krings, I. Mohos, U. Spillmann, "Two-Dimensional Microstrip Germanium Detector for X-Ray Spectroscopy of Highly-Charged Heavy Ions", presented at IEEE NSS 2004, Rome, Italy, Oct. 16-22, 2004

Two-Dimensional Microstrip Germanium Detector for X-Ray Spectroscopy of Highly-Charged Heavy Ions

D. Protić[1], Th. Stöhlker[2], T. Krings[1], I. Mohos[1], U. Spillmannn[2]

New possibilities are opened utilizing position-sensitive germanium detectors in the X-ray spectroscopy of highly charged heavy ions at GSI-Darmstadt [1]. The recent experiments revealed the need for two-dimensional strip detectors with their inherent advantages concerning spectroscopy and imaging capabilities as well as polarization sensitivity.

Very recently a new method for producing position-sensitive structures on germanium detectors having amorphous Ge contacts (a-Ge contacts) was presented [2, 3]. The method is based on the well established technique for manufacturing position-sensitive germanium and silicon detectors by means of photolithography and subsequent plasma etching of grooves through implanted contacts [4, 5]. Using this technique a one-dimensional 200 strip detector [6] and a 4x4 planar pixel detector [1], both made from high-purity germanium, were manufactured in the Laboratory for Semiconductor Detectors at IKP and successfully applied at GSI for the spectroscopy of atomic transitions in the hard X-ray regime above 15 keV and for polarization studies [1].

For the first prototype a germanium diode (70 mm x 41 mm, 11 mm thick) with a boron implanted p^+-contact on the junction side and a blocking a-Ge-contact on the other side was prepared. A 128 strip structure on an area of 32 mm x 56 mm with a pitch of 250 µm, surrounded by a guard-ring, was defined by means of photolithography on the implanted p^+-contact. On the a-Ge-contact only 48 strips with a pitch of 1167 µm, also surrounded by a guard-ring, were created using the same techniques as for the p^+-contact.

The detector is mounted in a cryostat (Fig. 1) which will enable any orientation of the detector in respect to a photon source. A view of the detector holder and the connection to the preamplifiers placed outside the vacuum system is shown in Fig. 2.

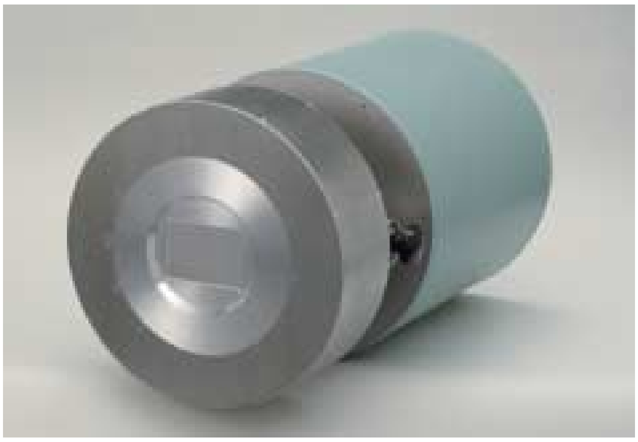

Fig. 1: View of the detector system. The detector is placed behind a 0.5 mm thick Be-window. The LN_2-dewar allows operation of the detector in any orientation without LN_2 spillage even when the dewar is full.

Fig. 2: View of the Ge-detector and one half of the preamplifiers with open cryostat cap.

In June 2004 the detector system was delivered to GSI. There it will be used to perform:

- High resolution X-ray spectroscopy for precise tests of quantum electrodynamics (QED) in the heaviest one- and two-electron systems such as hydrogen- and helium-like uranium
- Polarization studies for hard X-rays exploiting 3D capability of the detector and the Compton effect

References:

[1] Th. Stöhlker et al., "Applications of Position Sensitive Germanium Detectors for X-ray Spectroscopy of Highly-Charged Heavy Ions", NIM B 205, pp. 210-214, 2003

[2] D. Protić and T. Krings, "Detection characteristics of Ge detectors with microstructured amorphous Ge contacts", IEEE Trans. Nucl. Sci., vol. 51, pp. 1129-1133, June 2004.

[3] D. Protić and T. Krings, "Microstructures on Ge detectors with amorphous Ge contacts", IEEE Trans. Nucl. Sci., vol. 50, pp. 998-1000, August 2003.

[4] D. Protić and G. Riepe, "Thick silicon strip detectors", Nucl. Instrum. Methods, vol. 226, pp. 103-106, 1984.

[5] D. Protić and G. Riepe, "Position-sensitive germanium detectors", IEEE Trans. Nucl. Sci., vol. NS-32, pp. 553-555, February 1985.

[6] D. Protić et al., "A micro-strip germanium detector for position sensitive X-ray spectroscopy", IEEE Trans. Nucl. Sci., vol. 48, pp. 1048-1052, August 2001.

[1] FZJ-IKP
[2] GSI, Darmstadt

Large-Volume Si(Li) Orthogonal-Strip Detectors for Compton-Effect-Based Instruments

D. Protić[1], E. L. Hull[2], T. Krings[1], K. Vetter[2]

Recent developments of large-area Si(Li) orthogonal-strip detectors have revealed their capability for applications in Compton-effect-based instruments. Some inherent advantages of silicon such as the dominance of Compton scattering in photon interactions and operation at room or somewhat lower temperature combined with the availability of large-volume Si(Li) detectors could stimulate the development of powerful Compton instruments. Several diodes 10 mm in thickness with a diameter of 102 mm were fabricated in the Laboratory for Semiconductor Detectors at IKP. Two 10 mm thick diodes were cut to form a 74 mm x 74 mm square with slightly rounded corners.

The same position-sensitive structure, 32 strips with a pitch of 2 mm, was produced on the thin Li-diffused n-contact and boron-implanted p^+-contact by means of photolithography and plasma etched grooves [1, 2]. The position-sensitive area of 64 mm x 64 mm is surrounded by a 5 mm wide guard-ring. The position-sensitive volume of the detector is 40 cm^3 (!) [3].

The first of these 10 mm thick Si(Li) orthogonal-strip detectors is now being used as the scatter detector of the Compact Si+Ge Compton Camera [4] at LLNL, which is shown in Fig. 2. Energy resolutions [FWHM] between 1.5 and 2.0 keV could be achieved at LN_2-temperature when all channels were operated [4]. By combining two-dimensionally segmented semiconductor detectors such as Si, Ge or CdZnTe with pulse-shape processing it is possible to obtain three-dimensional position information of interactions to an accuracy of about 0.5 mm at 122 keV with a "pixel" size of 2 mm.

- Large-volume Si(Li) orthogonal-strip detectors could significantly enhance the development of Compton-effect-based instruments for different applications such as
  - Medical Imaging
  - High-energy Astrophysics
  - Compton Polarimetry (SPARC collaboration, GSI-Darmstadt)
  - Monitoring of Nuclear Waste
  - Homeland Security
- A proposal C-CAMED (High sensitivity molecular imaging with the Compton Camera for targeted cancer therapies), in which the large-volume Si(Li) strip detectors play an important role, is submitted by Prof. Walenta to EU (FP6-2004 LIFESCIHEALTH-5).
- Such detectors will be also used in EXL-experiments (GSI-Future project) to measure the position and energy of charged particles.
- Supposing the commercial availability of driftable p-type silicon we have not found any other reason that could prevent the realization of even thicker Si(Li) detectors. Furthermore, in collaboration with the supplier of silicon TOPSIL we are looking for good driftable material having 5" and 6" in diameter.
- 20 mm thick diodes with a diameter of 102 mm have been in Li-drift process for several weeks.

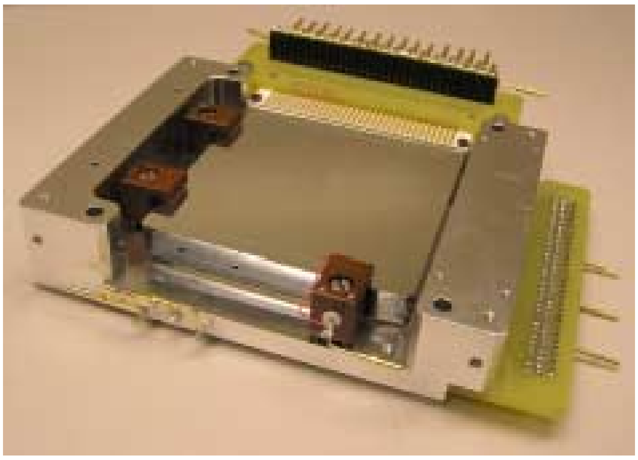

Fig. 1: The Si(Li) detector (9.7 mm thick) mounted in the LLNL holder. The testboards will be replaced by ceramic PCBs (printed circuit boards) at LLNL.

Fig. 2: The Compact Si+Ge Compton Camera at LLNL consisting of the double-sided strip Si(Li) detector (shown in Fig. 1) and a double-sided strip HPGe detector.

References:

[1] D. Protić and G. Riepe, "Thick silicon strip detectors", Nucl. Instrum. Methods, vol. 226, pp. 103-106, 1984.

[2] D. Protić, T. Krings and R. Schleichert, "Development of double-sided microstructured Si(Li) detectors", IEEE Trans. Nucl. Sci., vol. 49, pp. 1993-1996, August 2002.

[3] D. Protić, E. Hull, T. Krings and K. Vetter, "Large-Volume Si(Li) Orthogonal-Strip Detectors for Compton-Effect-Based Instruments", presented at the IEEE Nuclear Science Symposium, Rome, 2004

[4] K. Vetter, M. Burks, E. Hull, L. Mihailescu, T. Niedermayr, D. Protić, T. Krings, P. Luke and C. Tindall, "A Compact Si+Ge Compton Camera", presented at the IEEE Nuclear Science Symposium, Rome, 2004

[1] FZJ-IKP

[2] LLNL, USA

Electronics Laboratory

C.Berchem, N.Dolfus, W.Ernst, R.Nellen, J.Sarkadi, H.Schiffer, T.Sefzick

The activities of the IKP Electronics Laboratory can be assigned to mainly the following three topics:

Electronics and Data Acquisition for experiments

For the straw chamber project at TOF further development of pre–amplifiers and signal conversion circuitry took place. The production of 50 pre–amplifiers boards was supervised and the delivered boards were checked for meeting the requirements. Moreover, the readout prototype system, which is used in the straw chamber development laboratory, was upgraded from 256 to 1000 readout channels.

For the ANKE multi-wire proportional chambers which are under development oversized printed circuit boards needed to contact the individual wires were designed and ordered for production. These chambers will be read–out using a CMP16/F1 based system, consisting of a combined shaper amplifier and discriminator (CMP16) and a time stamper (F1). Tests of the CMP16 chip were continued and resulted in the production of the first 20 fully equipped printed circuit boards. A testing system for wire chambers with up to 1000 channels was developed, set–up, and tested. Due to supplementary requirements, the fully developed low–voltage, high–current ($\pm$5V, 2A) power supplies for the spectator detector, working at high voltage offsets without showing significant leakage currents, were re–developed, in order to meet financial conditions. The system for glueing ceramic plates and flexible circuit boards together was enhanced by a data acquisition system to monitor the temperature during the glueing process.

In the ATRAP-II experiment a scintillating fiber hodoscope, consisting of appr. 1800 channels read out by 16-fold multianode photomultipliers followed by pre–amplifiers, will be used. Time measurement of the signals is based on a RAL111 system. The required readout boards, manufactured externally, were fully tested and calibrated. The photomultipliers together with the pre–amplifiers were mounted into μ metal housings, were tested, and calibrated. Low–voltage power supplies for the pre–amplifiers and the readout system were built. Mechanical components, needed for installation on site at CERN, were developed. 16-channel ECL-NIM and NIM-ECL converters, meeting the special requirements of the experiment, were tested after external production. The complete system awaits installation on site.

For the TOF experiment adapter cables interfacing from coaxial connectors to 34–fold flat ones were made available. The control system of the liquid hydrogen target was improved.

The production of new delay cables for the GEM experiment was supervised, the cables were tested and delivered. In addition a discriminator crate, originally supplied by the ZEL as a prototype, was completely overhauled.

The positioning system of the crystal spectrometer at the pionic hydrogen experiment at PSI was tested and adjusted. The stepping motor and piezoelectric positioning system was repaired. The apparatus was improved by temperature und pressure measurements. The new crystal spectrometer has been set–up in the so–called south hall in the cyclotrone building.

Porting the Simatic S7 vacuum control system at the TOF experiment to the new WinCC version was completed. This included rewriting of user interface applications and structural changes in the STEP7 software. Moreover, continuous support was necessary to ensure the operation of the liquid hydrogen target at TOF.

Advanced measurements for the development of a microphone based implosion monitor system igniting quick-action valves at accelerators were performed for IKP1 and resulted in a publication.

A S7–300 PLC based target positioning system for movement of a double xy-table at the atomic beam source (ABS) at ANKE was developed. The user interface was prepared in WinCC. Specifications for a interlock system needed to protect detectors against damage in case of severe target failures were determined. The required hardware and software were produced and await testing. The whole ABS system was moved from a laboratory into the COSY hall.

COSY diagnostics

Maintenance was provided for the multi–wire chambers for beam diagnostics in the extraction beamlines und for the viewer cameras.

A system for motion and position measurement of the beam position monitor at the ANKE experiment was improved by a remote control system.

Computer network

In buildings 09.6 and 09.7 the fibre wire infrastructure has been established. After planning and measurements the installation of wireless LAN access points in the institute, COSY, and cyclotron buildings awaits completion. To meet short term requirements (PANDA collaboration meeting) some access points have already been installed in meeting rooms. The ongoing gradual switch–over from 10 Base-2 to 100 Base-FX computer links was slowed down due to financial cuts but is continued. Frequent support was granted to ensure continuous operation of the existing networks.

Miscellaneous

Like every year substantial support was given with regard to short term maintenance and repair or replacement of electronics. In some cases the urgent demand didn't allow a time-consuming outside repair procedure, in other cases the manufacturer doesn't even exists anymore, but the electronics can not be replaced easily, or the manufacturer was unable to perform the repair. Support of the so–called ZEL discriminators has been taken over.

Prototypes and small series of cables or electronics, for which an outside production would not have been reasonable, were delegated to infrastructure facilities or done here, mainly by trainees and student auxiliary workers.

The standard data acquisition systems at several COSY experiments were taken care of to assure stable operation during several beamtimes.

In addition, some members of our laboratory supported experiments by taking over shifts at beamtimes, mainly at COSY-11 and at the pionic hydrogen experiment at PSI.

Regarding S7 systems continuous support was given to the radiation safety division and to the cyclotron group.

ZEL - IKP developments for Detection Systems

A. Ackens, U.Clemens, H.Gorke, W.Erven, H.Gutschmidt, G. Kemmerling, H. Kleines, H.-W. Lövenich, D.Mäckelburg, J. Majewski, P. Wüstner, J. Zimmermann, K. Zwoll
D. Gotta[*], W. Oelert[*], H. Ohm[*] R. Schleichert[*]: [*] IKP

Introduction

The experimental capabilities of the IKP are greatly enhanced by members of the ZEL, who contribute a wealth of experience and know-how in the field of dedicated electronics for data taking as well software expertise to find solutions for difficult problems in data acquisition and analysis. Some of outstanding results that have been achieved are presented.

Pionic atoms

For the measurements of exotic atoms with a pnCCD-detector, a cPCI-sequencer board has been developed. It generates much faster timing sequences (10 ns) for the control of the CAMEX frontend chips, which are coupled to this detector. In order to facilitate the testing of these frontend chips, a multi-power supply has been developed. in addition. It delivers 48 voltages, which are programmable in height and ramp via PC104 and 8051 Microcontroller.

Precision time information

A high-performance readout system for precise measurements of time information based on the LVDS standard has been developed. It will be used for the TOF straw detectors (ca. 14000 channels) and the ANKE MWPC (ca. 120 channels). The system comprises crates with LVDS backplane, crate controllers and TDC-boards with F1-chips for the measurement of time information. Within the crate a data transfer rate of 80 Mbyte/s may be achieved via the LVDS bus. Data transfer from the controller to the host system is implemented as an optical link, based on the SIS1100 Gigabit interface. The TDC boards are equipped with 8 F1-chips each, which are able to readout in total 64 channels in common stop mode. A time resolution of 120 ps has been achieved with the F1-chips (cf. fig. 1).

Fig. 1: TDC-board with 8 F1-chips. 64 channels in common stop mode, resolution 120 ps.

ANKE vertex detector

For the vertex detector of the ANKE experiment, a readout system based on the LVDS standard is under development. It uses a LVDS-sequencer board, which is able to generate the necessary timing sequences for the readout of the VA 32 frontend-chips of the detectors. Additionally, the board is equipped with an ADC piggy-pack for the digitization of the analog signals (see fig. 2). It is envisaged to use the system in March 2005 at the ANKE experiment.

Fig. 2: LVDS-Sequencer with ADC piggy-pack

Readout for ATRAP

The readout system for the photomultipliers of the ATRAP-experiment has been finished. It comprises master/slave control modules for a sequential readout of crates and modules dedicated for the readout of the RAL-111 chips (cf. fig. 3). Data transfer between crates and the host computer is done via HOTLink to a PCI-module. Altogether, 120 modules have been produced from which 30 modules are already used in the current phase of the experiment.

Fig. 3: Master control module with HOTLink interface

A Councils

A.1 Scientific Council

Prof. J.P. Blaizot	CEA Saclay, FR	
Prof. P. Braun-Munzinger	GSI Darmstadt, DE	Chairperson
Prof. D.F. Geesaman	Argonne National LAboratory	
Prof. H. Halling	ZEL, FZ-Jülich, DE	
Prof. M. Harakeh	KVI Groningen, NL (Chairman PAC)	
Prof. D. von Harrach	Universität Mainz, DE	
Prof. E. Hilger	Universität Bonn, DE	
Prof. Y. Nagai	RCNP, JP	
Prof. A.W. Thomas	Thomas Jefferson National Lab, U.S.A.	
Dr. D. Trines	DESY Hamburg, DE	

A.2 Program Advisory Committee

Prof. H. Freiesleben	TU Dresden, DE	
Prof. B. Friman	GSI Darmstadt, DE	
Prof. M. Garçon	CEA Saclay, FR	
Prof. M.N. Harakeh	KVI Groningen, NL	Chairperson
Prof. T. Johansson	Uppsala Universitet, SE	
Prof. R. Landua	CERN, CH	
Prof. V. Metag	Universität Gießen, DE	
Prof. W. Meyer	Universität Bochum, DE	
Prof. W.T.H. van Oers	University of Manitoba, CA	
Prof. E. Oset	Universitat de Valencia, ES	
Prof. E. Radermacher	CERN, CH	
Prof. C. Schaerf	INFN Roma II, IT	

B Personnel

Scientific Staff

Msc. M.-M. Abdel-Bary (E1)

Dr. Abdel Samad (E1)

DP S. An (GG)

Prof. Dr. G. Baur (TH) (a.o. Prof. Univ. Basel)

Dr. U. Bechstedt (GG)

DP A. Bogdanov (GG) until Jul., 2004

DP V. Bollini (E1) (until Feb. 5, 2004)

Dr. K. Bongardt (GG)

DI N. Bongers (GG)

DI W. Borgs (E2)

DI W. Bräutigam (GG)

DI R. Brings (GG)

DP A. Bubak (E1) (until Feb. 19, 2004)

Dr. M. Büscher (E2)

DP D. Chiladze (E2)

R. Czyzykiewicz (E1)

Dr. habil. J. Dietrich (GG) (PD Univ. Dortmund)

Dr. A. Djalois (E1)

DP A. Dzyuba (E2)

Dr. R Eichhorn (GG)

Dr. R. Engels (E2)

DI F.-J. Etzkorn (GG)

Dr. K. Fan (GG)

Dr. P. Fedorets (E2) (since Sep., 2004)

Dr. O. Felden (Rs)

Prof. Dr. D. Filges (E1) (apl. Prof. Univ. Wuppertal) (until Jan 31, 2004)

DP M. Frink (TH) (until Oct. 31, 2004)

Dr. W. Gast (E1)

Dr. R. Gebel (GG)

Dr. habil. A. Gillitzer (E1) (PD Univ. Bonn)

Dr. habil. F.Goldenbaum (E1) (PD Univ. Wuppertal)

Dr. habil.D. Gotta (E2) (PD Univ. Köln)

Dr. F. Grümmer (TH)

Dr. D. Grzonka (E1)

Dr. habil. J. Haidenbauer (TH) (PD Univ. Graz)

Dr. C. Hanart (TH)

Dr. M. Hartmann (E2)

Dr. V. Hejny (E2)

DI K. Henn (GG)

DP V. Kamerdjiev (GG)

DP I. Keshelashvili (E2)

Prof Dr. K. Kilian (E1) (until Jul. 31, 2004)

DP D. Kirillov (GG) (since Oct. 19, 2004)

Dr. V. Kleber (E2)

Dr. St. Kliczewski (E1)

Prof. Dr. S. Krewald (TH) (apl. Prof. Univ. Bonn)

Th. Krings (Dt)

DI K. Kruck (GG)

Dr. P. Kulessa (E2)

Dr. A. Lehrach (GG)

DP V. Lenski (TH) (since Mar. 8, 2004)

DI B. Lensing (E1) (until Aug. 6, 2004)

DP V. Leontyev (E2)

DP M. Lesiak (E1) (since Sep. 1, 2004)

DP E. Lieder (E1) (until Oct. 31, 2004)

Dr. B. Lorentz (GG)

Prof. Dr. H. Machner (Prof. Univ. Duisburg-Essen)

Dr. Y. Maeda (E2)

Prof. Dr. R. Maier (GG) (Prof. Univ. Bonn)

DI J. Majewski (E2) (Jun. 1 to Dec. 31, 2004)

Dr. S. Martin (GG)

Prof. Dr. U.-G. Meißner (TH) (Prof. Univ. Bonn)

DI I. Mohos (GG)

Dr. H.-P. Morsch (E1)

Dr. P. Moskal (E1)

DP A. Mussgiller (E2)

Dr. M. Nekipelov (E2)

Prof. Dr. N. N. Nikolaev (TH)

Dr. K. Nünighoff (E1)

Prof. Dr. W. Oelert (E1) (apl. Prof. Univ Bochum)

Dr. H. Ohm (E2)

DI N. Paul (E1)

DP F. Pavlov (TH)

DP B. Piskor-Ignatowicz (E1) (since Mar., 1, 2004)

L. Platter (TH)

Dr. H. Polinder (TH) (since Jun., 14, 2004)

Dr. D. Prasuhn (GG)

DP D. Protic (Dt)

Dr. habil. F. Rathmann (E2) (PD Univ. Erlangen)

DI A. Richert (GG)

Prof. Dr. J. Ritman (E2) (Prof. Univ. Bochum) (since Sep., 17, 2004)

Dr. E. Roderburg (E1)

Dr. P. v. Rossen (GG)

DP T. Rozek (E1)

DI J. Sarkadi (Ec)

DP F. Sassen (TH)

Dr. H. Schaal (E1)

Dr. S. Schadmand (E1) (since Sep. 1, 2004)

Dr. W. Schäfer (TH) (until Dec. 31, 2004)

Dr. R. Schleichert (E2)

Dr. A. Schnase (GG)

DP S. Schneider (TH) (until Apr. 30, 2004)

DI H. Schneider (GG)

DI G. Schug (GG)

Dr. Th. Sefzick (Ec)

DI E. Senichera (GG) (since Apr. 1, 2004)

Dr. Y. Senichev (GG)

Dr. A. Sibirtsev (TH) (until Oct. 31, 2004)

DI M. Simon (GG)

DP A. Sokolov (E1) (since Aug. 1, 2004)

DI R. Stassen (GG)

Dr. H.-J. Stein (E2)

G. Sterzenbach (E1)

Dr. H. Stockhorst (GG)

Prof. Dr. H. Ströher (E2) (Prof. Univ. Köln)

Prof. Dr. J. Tang (GG) (until Mar. 12, 2004)

Dr. R. Tölle (GG)

DP A. Ucar (E1)

DP Y. Valdau (E2)

DI T. Vashegi (GG)

DP N. Vasiukhin (GG)

DP P. Vlasov (E1) (since Sep. 3, 2004)

Dr. K.-H. Watzlawik (E2)

J. Wimmer (E1)

DP P. Winter (E1)

Dr. P. Wintz (E1)

Dr. A. Wirzba (TH) (since Aug. 16, 2004)

DI J.-D. Witt (GG)

Dr. M. Wolke (E1)

DP A. Wronska (E2) (until Aug. 30, 2004)

Dr. E. Zaplatin (GG)

DP D. Z. Zhang (E1) (since Oct. 10, 2004)

B.1 Technical and Administrative Staff

C. Berchem (Ec)

P. Birx (GG)

H.-G. Böge (GG) (until Nov. 30, 2004)

M. Böhnke (GG)

J. Borsch (GG)

J. But (Ws)

M. Comuth (Ad)

W. Derissen (Cd)

N. Dolfus (Ec)

G. D‘Orsaneo (E2)

R. Dosdall (E1) (since Sep., 2004)

B. Dahmen (GG)

C. Deliege (GG)

R. Enge (GG)

J. Engel (GG) (until Dec. 31, 2004)

B. Erkes (GG)

W. Ernst (Ec)

K. Esser (Ad)

H.-P. Faber (GG)

G. Fiori (Dt)

H.-W. Firmenich (Ws)

N. Gad (GG)

D. Gehsing (GG)

J. Göbbels (Rs)

H. Hadamek (Ws)

R, Hecker (GG)

E. Heßler (Cd)

M. Holona (Ws)

H.-M. Jäger (E1)

H. J. Jansen (Ws)

R. Jansen (Ad) (until Jul., 2004)

M. Karnadi (E2)

A. Kieven (GG)

K. Krafft (Rs)

Ch. Krahe (Ws)

M. Kremer (Ws)

G. Krol (GG)

M. Küven (Ws)

K.-G. Langenberg (GG)

G. Lürken (Ec)

H. Metz (Dt)

S. Müller (Ad)

R. Nellen (Ec)

H. Pütz (GG)

G. Roes (Ad)

N. Rotert (GG)

D. Ruhrig (GG)

T. Sagefka (GG)

F. Scheiba (GG)

H. Schiffer (Ec)

J. Schmitz (GG)

F. Schultheiß (Ws)

K. Schwill (Dt)

H. Singer (GG)

D. Spölgen (E2)

J. Strehl (Ws)

V.N. Tika (E1) (until Apr. 30, 2004)

J. Uehlemann (E1)

P. Wieder 9E2)

H. Zens (GG)

Ad = Administraion
Cd = Construction
Dt = Detectors
E1 = IKP-1
E2 = IKP-2
Ec = Electronics
GG = Accelerator Division
Rs = Radiation Safety
TH = Theory
Ws = Workshop

C Publications 2004

1. Experiment

1. **Determination of the $\bar{K}^0 d$ scattering length from the reaction $pp \to d\bar{K}^0 K^+$**
   A. Sibirtsev, M. Büscher, V.Yu. Grishina, C. Hanhart, L.A. Kondratyuk, S. Krewald, U.-G. Meißner
   Phys. Lett. B **601** *(2004) 132*

2. $a_0^+(980)$ **resonance production in the reaction $pp \to d\pi^+\eta$ close to the $K\bar{K}$ threshold**
   P. Fedorets, M. Büscher, V.P. Chernyshev, S. Dymov, V.Yu. Grishina, C. Hanhart, M. Hartmann, V. Hejny, V. Kleber, H.R. Koch, L.A. Kondratyuk, V. Koptev, A.E. Kudryavtsev, P. Kulessa, S. Merzliakov, S. Mikirtychiants, M. Nekipelov, H. Ohm, R. Schleichert, H. Ströher, V.E. Tarasov, K.-H. Watzlawik, I. Zychor
   subm. to Phys. Atom. Nucl. [Yad. Fiz.] [arXiv:nucl-ex/0501027]

3. **Near-threshold production of ω mesons in the $pn \to d\omega$ reaction**
   S. Barsov, I. Lehmann, R. Schleichert, C. Wilkin, M. Büscher, S. Dymov, Ye. Golubeva, M. Hartmann, V. Hejny, A. Kacharava, I. Keshelashvili, A. Khoukaz, V. Komarov, L. Kondratyuk, N. Lang, G. Macharashvili, T. Mersmann, S. Merzliakov, A. Mussgiller, M. Nioradze, A. Petrus, H. Ströher, Y. Uzikov, B. Zalikhanov
   Eur. Phys. J. A **21** *(2004) 507*

4. **Inclusive K^+-meson production in proton-nucleus interactions**
   M. Büscher, V. Koptev, M. Nekipelov, Z. Rudy, R. Schleichert, H. Ströher, Yu. Valdau, S. Barsov, M. Hartmann, V. Hejny, V. Kleber, N. Lang, I. Lehmann, N. Lang, S. Mikirtychiants, H. Ohm
   Eur. Phys. J. A **22** *(2004) 301*

5. **Measurement of the analyzing power in $\vec{p}d \to (pp)n$ with a fast forward $^1S_0$-diproton**
   S. Yaschenko, S. Dymov, V. Komarov, G. Macharashvili, F. Rathmann, S. Barsov, M. Hartmann, R. Gebel, A. Kacharava, A. Khoukaz, P. Kulessa, A. Kulikov, V. Kurbatov, N. Lang, I. Lehmann, B. Lorentz, T. Mersmann, S. Merzliakov, S. Mikirtytchiants, A. Mussgiller, M. Nioradze, H. Ohm, D. Prasuhn, R. Schleichert, H. Seyfarth, E. Steffens, H.J. Stein, H. Ströher, Yu. Uzikov, B. Zalikhanov, N. Zhuravlev
   Phys. Rev. Lett. **94** *(2005) 072304*

6. **Spectator detection for the measurement of proton-neutron interactions at ANKE**
   I. Lehmann,S. Barsov, R. Schleichert, C. Wilkin, M. Drochner, M. Hartmann, V. Hejny, S. Merzliakov, S. Mikirtychiants, A. Mussgiller, D. Protic, H. Ströher, S. Trusov, P. Wüstner
   Nucl. Instr. Meth. A **530** *(2004) 275*

7. **Experimental study of $pp\eta$ dynamics in the $pp \to pp\eta$ reaction**
   P. Moskal, H.H. Adam, A. Budzanowski, R. Czyżykiewicz, D. Grzonka, M. Janusz, L. Jarczyk, B. Kamys, A. Khoukaz, K. Kilian, P. Kowina, K. Nakayama, W. Oelert, C. Piskor-Ignatowicz, J. Przerwa, T. Rozek, R. Santo, G. Schepers, T. Sefzick, M. Siemaszko, J. Smyrski, S. Steltenkamp, A. Tächner, P. Winter, M. Wolke, P. Wüstner, W. Zipper
   Phys. Rev. C **69** *(2004) 025203*

8. **Total and differential cross sections for the $pp \to pp\eta'$ reaction near threshold**
   A. Khoukaz, I. Geck, C. Quentmeier, H.H. Adam, A. Budzanowski, R. Czyżykiewicz, D. Grzonka, L. Jarczyk, K. Kilian, P. Kowina, N. Lang, T. Lister, P. Moskal, W. Oelert, C. Piskor-Ignatowicz, T. Rozek, R. Santo, G. Schepers, T. Sefzick, S. Sewerin, M. Siemaszko, J. Smyrski, A. Strzałkowski, A. Täschner, P. Winter, M. Wolke, P. Wüstner, W. Zipper
   Eur. Phys. J. A **20** *(2004) 345*

9. **Energy dependence of the Λ/Σ° production cross section ratio in p-p interactions**
   P. Kowina, M. Wolke, H.H. Adam, A. Budzanowski, R. Czyżykiewicz, D. Grzonka, J. Haidenbauer, M. Janusz, L. Jarczyk, A. Khoukaz, K. Kilian, P. Moskal, W. Oelert, C. Quentmeier, C. Piskor-Ignatowicz, J. Przerwa, T. Rożek, R. Santo,G. Schepers, T. Sefzick, M. Siemaszko, J. Smyrski, S. Steltenkamp, A. Strzałkowski, P. Winter, P. Wüstner, W. Zipper
   Eur. Phys. J. A **22** *(2004) 293*

10. **Drift chamber with a c-shaped frame**
    J. Smyrski, Ch. Kolf, H.-H. Adam, A. Budzanowski, R. Czyzykiewicz, D. Grzonka, M. Janusz, L. Jarczyk, B. Kamys, A. Khoukaz, K. Kilian, W. Oelert, C. Piskor-Ignatowicz, J. Przerwa, T. Rozek, R. Santo, G. Schepers,T. Sefzick, M. Siemaszko, A. Taschner, P. Winter, M. Wolke, P. Wustner, W. Zipper
    Nucl. Instr. Meth. A, in print [arXiv:nucl-ex/0501023]

11. **A precision measurement of pp elastic scattering cross-sections at intermediate energies**
Albers,D., Bauer,F., Bisplinghoff,J., Bollmann,R., Büßer,K., Busch,M., Daniel,R., Diehl,O., Dohrmann,F., Engelhardt,H. P., Ernst,J., Eversheim,P. D., Gasthuber,M., Gebel,R., Greiff,J., Groß,A., Groß-Hardt,R., Heider,S., Heine,A., Hinterberger,F., Hüskes,T., Igelbrink,M., Jeske,M., Langkau,R., Lindlein,J., Maier,R., Maschuw,R., Mosel,F., Prasuhn,D., Rohdjeß,H., Rosendaal,D., von Rossen,P., Scheid,N., Schirm,N., Schulz- Rojahn,M., Schwandt,F., Schwarz,V., Scobel,W., Thomas,S., Trelle,H.-J., Weise,E., Welinghausen,A., Woller,K., Ziegler,R.
Eur. Phys. J. A **22** *(2004) 125*

12. **Evidence for a narrow resonance at 1530 MeV/c^2 in the $K^\circ p$ system of the reaction $pp \rightarrow \Sigma^+ K^\circ p$ from the COSY-TOF experiment**
M. Abdel-Bary, S. Abdel-Samad, K.Th. Brinkmann, H. Clement, E. Doroshkevich, M. Drochner, S. Dshemuchadse, A. Erhardt, W. Eyrich, D. Filges, A. Filippi, H. Freiesleben, M. Fritsch, J. Georgi, A. Gillitzer, D. Hesselbarth, R. Jakel, B. Jakob, L. Karsch, K. Kilian, H. Koch, J. Kress, E. Kuhlmann, S. Marcello, S. Marwinski, R. Meier, P. Michel, K. Moller, H. Mortel, H.P. Morsch, N. Paul, L. Pinna, C. Pizzolotto, M. Richter, E. Roderburg, P. Schonmeier, W. Schroeder, M. Schulte-Wissermann, T. Sefzick, F. Stinzing, G.Y. Sun, A. Teufel, A. Ucar, G.J. Wagner, M. Wagner, A. Wilms, P. Wintz, St. Wirth, P. Wüstner
Phys. Lett. B **595** *(2004) 127*

13. **Detailed comparison of the $pp \rightarrow \pi^+ pn$ and $pp \rightarrow \pi^+ d$ reactions at 951 MeV**
M. Abdel-Bary, A. Budzanowski A. Chatterjee, J. Ernst, P. Hawranek, F. Hinterberger, V. Jha, K. Kilian, S. Kliczewski, D. Kirillov, D. Kolev, M. Kravcikova, T. Kutsarova, M. Lesiak, J. Lieb, H. Machner, A. Magiera, R. Maier, G. Martinska, S. Nedev, J. Niskanen, N. Piskunov, D. Prasuhn, D. Protic, P. von Rossen, B.J. Roy, I. Sitnik, R. Siudak, M. Smiechowicz, R. Tsenov, M. Ulicny, J. Urban, G. Vankova, C. Wilkin
Phys. Lett. B **610** *(2005) 31*

14. **A precision experiment determining the η meson mass**
M. Abdel-Bary, A. Budzanowski A. Chatterjee, J. Ernst, P. Hawranek, R. Jahn, V. Jha, K. Kilian, S. Kliczewski, D. Kirillov, D. Kolev, M. Kravcikova, T. Kutsarova, M. Lesiak, J. Lieb, H. Machner, A. Magiera, R. Maier, G. Martinska, S. Nedev, N. Piskunov, D. Prasuhn, D. Protic, P. von Rossen, B.J. Roy, I. Sitnik, R. Siudak, M. Smiechowicz, H. J. Stein, R. Tsenov, M. Ulicny, J. Urban, G. Vankova, C. Wilkin
subm. to Phys. Lett. B

15. **PISA — an experiment for fragment spectroscopy at the internal beam of COSY: application of an axial ionization chamber**
R. Barna, V. Bollini, A. Bubak, A. Budzanowski, D. De Pasquale, D. Filges, S. Förtsch, F. Goldenbaum, A. Heczko, H. Hodde, A. Italiano, L. Jarczyk, B. Kamys, J. Kisiel, M. Kistryn, St. Kistryn, St. Kliczewski, P. Kulessa, H. Machner, A. Magiera, J. Majewski, W. Migdał, H. Ohm, N. Paul, B. Piskor-Ignatowicz, K. Pysz, Z. Rudy, H. Schaal, R. Siudak, E. Stephan, D. Steyn, R. Sworst, T. Thovhogi, M. Wojciechowski, W. Zipper
Nucl. Instrum. Meth. A **519** *(2004) 610*

16. **Parameterization of the total cross-section for (p,^{7}Be) reaction**
A.Bubak, B. Kamys, M.Kistryn, B.Piskor-Ignatowicz
Nucl. Instrum. Meth. B **226** *(2004) 507*

17. **Ice moderator experiments at very low temperatures**
K. Nuenighoff, Ch. Pohl, V. Bollini, A. Bubak, H. Conrad, D. Filges, H. Glueckler, F. Goldenbaum, G. Hansen, B. Lensing, R.-D. Neef, N. Paul, D. Prasuhn, K. Pysz, H. Schaal, H. Soltner, H. Stelzer, H. Tietze-Jaensch, W. Bernnat, J. Keinert, M. Mattes, W. Ninaus, S. Koulikov, A. Smirnov, M. Wohlmuther
Eur. Phys. J. A **22** *(2004) 519*

18. **First laser-controlled antihydrogen production**
C.H. Storry, A. Speck, D. Le Sage, N. Guise, G. Gabrielse, D. Grzonka, W. Oelert, G. Schepers, T. Sefzick, H. Pittner, M. Herrmann, J. Walz, T.W. Hänsch, D. Comeau, and E. A. Hessels
Phys. Rev. Lett. **93** *(2004) 263401*

19. **Observations of cold antihydrogen**
J.N. Tan, N.S. Bowden, G. Gabrielse, P. Oxley, A. Speck, C.H. Storry, M. Wessels, D. Grzonka, W. Oelert, G. Schepers, T. Sefzick, J. Walz, H. Pittner, T.W. Hänsch, E.A. Hessels
Nucl. Instr. Meth. B **214** *(2004) 22*

20. **Aperture method to determine the density and geometry of anti-particle plasmas,**
P. Oxley, N. S.Bowden, R. Parrott, A. Speck, C. Storry, J.N. Tan, M. Wessels, G. Gabrielse, D. Grzonka, W. Oelert,

G. Schepers, T. Sefzick, J. Walz, H. Pittner, T.W. Hänsch, and E. A. Hessels
Phys. Lett. B **595** *(2004) 60*

21. **First measurement of the velocity of slow antihydrogen atoms,**
G. Gabrielse, A. Speck and C.H. Storry, D. Le Sage, N. Guise, D. Grzonka, W. Oelert, G. Schepers, T. Sefzick, H. Pittner, J. Walz, T.W. Hänsch, D. Comeau, E.A. Hessels
Phys. Rev. Lett. **93** *(2004) 073401*

22. **Precision spectroscopy of light exotic atoms**
D. Gotta
Prog. Part. and Nucl. Phys. **52** *(2004) 133*

23. **On the characterization of a Bragg spectrometer with X-rays from an ECR source**
D.F. Anagnostopoulos, S. Biri, D. Gotta, A. Gruber, P. Indelicato, B. Leoni, H. Fuhrmann, L.M. Simons, L. Stingelin, A. Wasser, J. Zmeskal
Nucl. Instr. Meth. A, to be published

24. **Studies of multi-nucleon transfer reactions in ^{90}Zr(^{18}O,X) and ^{90}Zr(^{16}O,X)**
V. Jha, B. J. Roy, A. Chatterjee, H. Machner
Eur. Phys. J. A **19** *(2004) 347*

25. **Exclusive η production in proton induced reactions**
F. Balestra, Y. Bedfer, R. Bertini, L.C. Bland, A. Brenschede, F. Brochard, M.P. Bussa, Seonho Choi, M.L. Colantoni, R. Dressler, M. Dzemidzic, J.-Cl. Faivre, A. Ferrero, L. Ferrero, J. Foryciarz, I. Frohlich, V. Frolov, R. Garfagnini, A. Grasso, S. Heinz, W.W. Jacobs, W. Kuhn, A. Maggiora, M. Maggiora, A. Manara, D. Panzieri, H.-W. Pfaff, G. Piragino, A. Popov, J. Ritman, P. Salabura, V. Tchalyshev, F. Tosello, S.E. Vigdor, G. Zosi (DISTO collaboration)
Phys. Rev. C. **69** *(2004) 064003*

26. **Production of ϕ mesons in Au+Au collisions at 11.7 A GeV/c**
B.B. Back, R.R. Betts, J. Chang, W.C. Chang, C.Y. Chi, Y.Y. Chu, J.B. Cumming, J.C. Dunlop, W. Eldredge, S.Y. Fung, R. Ganz, E. Garcia, A. Gillitzer, G. Heintzelman, W.F. Henning, D.J. Hofman, B. Holzman, J.H. Kang, E.J. Kim, S.Y. Kim, Y. Kwon, D. McLeod, A.C. Mignerey, M. Moulson, V. Nanal, C.A. Ogilvie, R. Pak, A. Ruangma, D.E. Russ, R.K. Seto, P.J. Stanskas, G.S.F. Stephans, H.Q. Wang, F.L.H. Wolfs, A.H. Wuosmaa, H. Xiang, G.H. Xu, H.B. Yao, C.M. Zou (BNL-E917 Collaboration)
Phys. Rev. C **69** *(2004) 054901*

27. **Precision spectroscopy of pionic 1s states of Sn nuclei and evidence for partial restoration of chiral symmetry in the nuclear medium**
K. Suzuki, M. Fujita, H. Geissel, H. Gilg, A. Gillitzer, R.S. Hayano, S. Hirenzaki, K. Itahashi, M. Iwasaki, P. Kienle, M. Matos, G. Münzenberg, T. Ohtsubo, M. Sato, M. Shindo, T. Suzuki, H. Weick, M. Winkler, T. Yamazaki, and T. Yoneyama
Phys. Rev. Lett. **92** *(2004) 072302*

28. **Axial observables in $\vec{d}\vec{p}$ breakup and the three-nucleon force**
H.O. Meyer, T.J. Whitaker, R.E. Pollock, B.v. Przewoski, T. Rinckel, J. Doskow, J. Kuros-Zolnierczuk, P. Thörngren-Engblom, P.V. Pancella, T. Wise, B. Lorentz, F. Rathmann
Phys. Rev. Lett. **93** *(2004) 112502*

29. **Analyzing powers and spin correlation coefficients for p+d elastic scattering at 135 and 200 MeV**
B.v. Przewoski, H.O. Meyer, J.T. Balewski, W.W. Daehnick, J. Doskow, W. Haeberli, R. Ibald, B. Lorentz, R.E. Pollock, P.V. Pancella, F. Rathmann, T. Rinckel, Swapan K. Saha, B. Schwartz, P. Thörngren-Engblom, A. Wellinghausen, T.J. Whitaker, T. Wise, H. Witala
Phys. Rev. C, accepted for publication

30. **Conceptual design and simulation of the PANDA detector**
J. Ritman
Nucl. Instrum. Meth. B **214** *(2004) 201*

31. **A method to polarize stored antiprotons to a high degree**
F. Rathmann, P. Lenisa, E. Steffens, M. Contalbrigo, P.F. Dalpiaz, A. Kacharava, A. Lehrach, B. Lorentz, R. Maier, D. Prasuhn, H. Ströher,
Phys. Rev. Lett. **94** *(2005) 014801*

2. Theory

32. **Accessing transversity via J/Ψ production in polarized $p\bar{p}$ interactions**
Anselmino, M.; Barone, V.; Drago, A.; Nikolaev, N. N.
Phys. Lett. B **594** *(2004) 97*

33. **Evidence that the a_0(980) and f_0(980) are not elementary particles**
Baru, V.; Haidenbauer, J.; Hanhart, C.; Kalashnikov, Yu.; Kudryavtsev, A.
Phys. Lett. B **586** *(2004) 53*

34. **The role of the nucleon recoil in low-energy meson nucleus reactions**
Baru, V.; Hanhart, C.; Kudryavtsev, A. E.; Meißner, U. G.
Phys. Lett. B **589** *(2004) 118*

35. **Flatte-like distributions and the a_0(980)/f_0(980) mesons**
Baru, V.; Haidenbauer, J.; Hanhart, C.; Kudryavtsev, A.; Meißner, U. G.
Eur. Phys. J. A **23**, *(2005) 523*

36. **Theory of the Trojan-horse method**
Baur, G.; Typel, S.
Prog. Theor. Phys. Suppl. **154** *(2004) 333*

37. **Radiative neutron beta-decay in effective field theory**
Bernard, V.; Gardner, S.; Meißner, U.-G.; Zhang, C.
Phys. Lett. B **593** *(2004) 105*

38. **Cutoff schemes in chiral perturbation theory and the quark mass expansion of the nucleon mass**
Bernard, V.; Hemmert, T. R.; Meißner, U.-G.
Nucl. Phys. A **732** *(2004) 149*

39. **Infrared regularization for spin-1 fields**
Bruns, P. C.; Meißner, U.-G.
Eur. Phys. J. C, in print [arXiv:hep-ph/0411223]

40. **Improving the convergence of the chiral expansion for nuclear forces I: Peripheral phases**
Epelbaum, E.; Glöckle, W.; Meißner, U.-G.
Eur. Phys. J. A **19** *(2004) 125*

41. **Improving the convergence of the chiral expansion for nuclear forces II: Low phases and the deuteron**
Epelbaum, E.; Glöckle, W.; Meißner, U.-G.
Eur. Phys. J. A **19** *(2004) 401*

42. **The two-nucleon system at next-to-next-to-next-to-leading order**
Epelbaum, E.; Glöckle, W.; Meißner, U.-G.
Nucl. Phys. **A 747** *(2005) 362*

43. **Isospin dependence of the three-nucleon force**
Epelbaum, E.; Meißner, U.-G.; Palomar, J. E.
Phys. Rev. C **71** *(2005) 024001*

44. **Chiral extrapolations of baryon masses for unquenched three-flavor lattice simulations**
Frink, M.; Meißner, U.-G.
JHEP **07** *(2004) 028*

45. **Survey of charge symmetry breaking operators for $dd \to \alpha\pi^0$**
Gardestig, A.; Horowitz, C. J.; Nogga, A.; Fonseca, A. C.; Hanhart, C.; Miller, G. A.; Niskanen, J. A.; van Kolck, U.
Phys. Rev. C **69** *(2004) 044606*

46. **Radiative tritium β-decay and the neutrino mass**
Gardner, S.; Bernard, V.; Meißner, U.-G.
Phys. Lett. B **598** *(2004) 188*

47. **How to extract the ΛN scattering length from production reactions**
Gasparyan, A.; Haidenbauer, J.; Hanhart, C.; Speth, J.
Phys. Rev. C **69** *(2004) 034006*

48. **Near threshold production of a_0(980)-mesons in the reaction $pp \to dK^+\bar{K}^0$**
V.Yu. Grishina, L.A. Kondratyuk, M. Büscher, W. Cassing
Eur. Phys. J. A **21** *(2004) 507*

49. **On the pion cloud of the nucleon**
Hammer, H.-W.; Drechsel, D.; Meißner, U.-G.
Phys. Lett. B **586** *(2004) 291*

50. **Updated dispersion-theoretical analysis of the nucleon electromagnetic form factor**
Hammer, H.-W.; Meißner, U.-G.
Eur. Phys. J. A **20** *(2004) 469*

51. **How to measure the parity of the Θ^+ in $\vec{p}\vec{p}$ collisions**
C. Hanhart, M. Büscher, W. Eyrich, K. Kilian, U.-G. Meißner, F. Rathmann, A. Sibirtsev, and H. Ströher
Phys. Lett. B **590** *(2004) 39*

52. **Meson production in nucleon-nucleon collisions close to the threshold**
Hanhart, C.
Phys. Rep. **397** *(2004) 155*

53. **On the determination of the parity of the Θ^+**
Hanhart, C.; Haidenbauer, J.; Nakayama, K.; Meissner, U. G.
Phys. Lett. B **606** *(2005) 67*

54. **Comment on "Photoproduction of η mesic ^{3}He"**
Hanhart, C.
Phys. Rev. Lett. **94** *(2005) 049101*

55. **A cluster version of the GGT sum rule**
Hencken, K.; Baur, G.; Trautmann, D.
Nucl. Phys. A **733** *(2004) 200*

56. **Production of QED pairs at small impact parameter in relativistic heavy ion collisions**
Hencken, K.; Trautmann, D.; Baur, G.
Phys. Rev. C **69** *(2004) 054902*

57. **Parity nonconserving observables in thermal neutron capture on a proton**
Hyun, C.H.; Lee, S.J.; Haidenbauer, J.; Hong, S.W.
Eur. Phys. J. A, in print [arXiv:nucl-th/0411102]

58. **Improved analysis of coherent neutral pion electroproduction on deuterium in chiral perturbation theory**
Krebs, H.; Bernard, V.; Meißner, U.-G.
Eur. Phys. J. A **22** *(2004) 503*

59. **Orthonormalization procedure for chiral effective nuclear field theory**
Krebs, H.; Bernard, V.; Meißner, U.-G.
Ann. Phys. **316** *(2005) 160*

60. **Lifetime of kaonium**
Krewald, S.; Lemmer, R. H.; Sassen, F. P.
Phys. Rev. D **69** *(2004) 016003*

61. **Spectrum and decays of kaonic hydrogen**
Meißner, U.-G.; Raha, U.; Rusetsky, A.
Eur. Phys. J. C **35** *(2004) 349*

62. **Evolution of high-mass diffraction from the light quark valence component of the Pomeron**
Nikolaev, N. N.; Schäfer, W.; Zakharov, B. G.; Zoller, V. R.
JETP Lett. **80** *(2004) 6, 371*

63. **Four-boson system with short-range interactions**
Platter, L.; Hammer, H.-W.; Meißner, U.-G.
Phys. Rev. A **70** *(2004) 052101*

64. **Universal properties of the four-boson system in two dimensions**
Platter, L.; Hammer, H.-W.; Meißner, U.-G.
Few-Body Systems **35** *(2004) 169*

65. **On the correlation between the binding energies of the triton and the alpha-particle**
Platter, L.; Hammer, H.-W.; Meißner, U.-G.
Phys. Lett. **B 607** *(2005) 254*

66. **The η-^{3}He scattering length revisited**
Sibirtsev, A.; Haidenbauer, J.; Hanhart, C.; Niskanen, J.
Eur. Phys. J. A **22** *(2004) 495*

67. **New results on the limit for the width of the exotic Θ^+ resonance**
Sibirtsev, A.; Haidenbauer, J.; Krewald, S.; Meißner, U.-G.
Phys. Lett. B **599** *(2004) 230*

68. **Bounds on the bound η-^{3}He system**
Sibirtsev, A.; Haidenbauer, J.; Niskanen, J.; Meißner, U.-G.
Phys. Rev. C **70** *(2004) 047001*

69. **Systematic analysis of charmonium photoproduction**
Sibirtsev, A.; Krewald, S.; Thomas, A. W.
Jour. Phys. G **30** *(2004) 1427*

70. **Analysis of Θ^+ production in K^+Xe collisions**
Sibirtsev, A.; Haidenbauer, J.; Krewald, S.; Meißner, U.-G.
Eur. Phys. J. **A 23** *(2005) 491*

71. **Near threshold enhancement of the $p\bar{p}$ mass spectrum in J/Ψ decay**
Sibirtsev, A.; Haidenbauer, J.; Krewald, S.; Meißner; U.-G., Thomas, A.W.;
Phys. Rev. D, in print [arXiv:hep-ph/0411386]

72. **Extended theory of finite Fermi systems: collective vibrations in closed shell nuclei**
Speth, J.; Kamerdzhiev, S.; Spethand, J.; Tertychny, G.
Phys. Rep. **393** *(2004) 1*

73. **Effective-range approach and scaling laws for electromagnetic strength in neutron-halo nuclei**
Typel, S.; Baur, G.
Phys. Rev. Lett. **93** *(2004) 142502*

74. **Nucleon-nucleon potential in finite nuclei**
Yakhshiev, U. T.; Meißner, U.-G.; Wirzba, A.; Rakhimov,A. M.; Musakhanov, M. M.
Phys. Rev. C, in print [arXiv:nucl-th/0409002]

3. Accelerator

75. **Achieving 99.9% proton spin-flip efficiency at higher energy with a small rf-dipole**
Leonova,M. A., Krisch,A. D., Morozov,V. S., Raymond,R. S., Wong,V. K., Gebel,R., Lehrach,A., Lorentz,B., Maier,R., Prasuhn,D., Schnase,A., Stockhorst,H., Eversheim,D. P., Hinterberger,F., Ulbrich,K.
Phys. Rev. Lett. **93** *(2004) 224801*

76. **Ion sources and low energy beam transport for the new superconducting injector linac for COSY/Jülich**
Gebel,R., Felden,O., von Rossen,P.
Rev. of Sci. Instr. **75** *(2004) 5, 1860*

77. **Instability phenomena of electron-cooled ion beams at COSY**
Kamerdzhiev,V., Dietrich,J., Maier,R., Meshkov,I., Mohos,I., Prasuhn,D., Sidorin,A., Stein,H. J., Stockhorst,H.
Nucl. Instr. and Meth. A **532** *(2004) 1/2, 285*

78. **Stripping injection at synchrotrons with electron cooling**
Meshkov,I. N., Sidorin,A. O., Stein,J., Dietrich,J., Kamerdzhiev,V.
Phys. of Part. and Nucl. **120** *(2004) 3, 4*

79. **Spin manipulation of 1.94 gev/c polarized protons stored in the COSY Cooler Synchrotron**
Morozov,V. S., Krisch,A. D., Leonova,M. A., Raymond,R. S., Wong,V. K., Yonehara,K., Bechstedt,U., Gebel,R., Lehrach,A., Lorentz,B., Maier,R., Prasuhn,D., Schnase,A., Stockhorst,H., Eversheim,D. P., Hinterberger,F., Rohdjeß,H., Ulbrich,K.
Phys. Rev., Accelerators and Beams **7** *(2004) 024002*

80. **Spin-flipping polarized deuterons at COSY**
Yonehara,J. C., Krisch,A. D., Morozov,V., Raymond,R. S., Wong,V. K., Bechstedt,U., Gebel,R., Lehrach,A., Lorentz,B., Maier,R., Prasuhn,D., Schnase,A., Stockhorst,H., Eversheim,D. P., Hinterberger,F., Rohdjess,H., Ulbrich,K., Scobel,W.
Inters. of Part. and Nucl. Phys. 8th Conf. 0-7354-0169-1. - 763 - 766

81. **Separatrix formalism applied to linacs accelerating particles with different charge to mass ratio**
Bogdanov,A., Maier,R., Senichev,Y
Proc. EPAC, Lucerne, CH, (2004) 92-9083-231-2. - 1252 - 1254

82. **Delta-T procedure for superconducting linear accelerator**
Bogdanov,A., Maier,R., Senichev,Y.
Proc. EPAC, Lucerne, CH, (2004) 92-9083-231-2. - 1249

83. **Beam position monitor development for the iThemba LABS cyclotron beamlines**
Dietrich,J., Mohos,I., Botha,A. H., Conradie,J. L., Delsink,J. L. G., Rohwer,P. F
Proc. EPAC, Lucerne, CH, (2004) 92-9083-231-2. - 2589 - 2591

84. **Luminosity considerations for internal and external experiments at COSY**
Lehrach,A., Bechstedt,U., Dietrich,J., Eichhorn,R., Gebel,R., Lorentz,B., Maier,R., Prasuhn,D., Schneider,H., Stassen,R., Stockhorst,H., Tölle,R.
Proc. EPAC, Lucerne, CH, (2004) 92-9083-231-2. - 1255 - 1257

85. **Status of the Cooler Synchrotron COSY-Jülich**
Lorentz,B., Bechstedt,U., Dietrich,J., Eichhorn,R., Gebel,R., Lehrach,A., Maier,R., Prasuhn,D., Schnase,A., Schneider,H., Stassen,R., Stockhorst,H., Tölle,R.
Proc. EPAC, Lucerne, CH, (2004) 92-9083-231-2. - 1246 - 1248

86. **High field gradient cavity for J-PARC 3 GeV RCS**
Ohmori,C., Anami,S., Ezura,E., Hara,K., Hashimoto,Y., Takagi,A., Toda,M., Yoshii,M., Nomura,M., Schnase,A., Tamura,F., Yamamoto,M.
Proc. EPAC, Lucerne, CH, (2004) 92-9083-231-2. - 123 - 125

87. **Methods and instrumentation for measurement of low ion beam currents at the cryring**
Paal,A., Källberg,A., Simonsson,A., Dietrich,J., Mohos,I.
Proc. EPAC, Lucerne, CH, (2004) 92-9083-231-2. - 2748 - 2749

88. **Lattice design study for HESR**
Senichev,Y., An,S., Bongardt,K., Eichhorn,R., Lehrach,A., Maier,R., Martin,S., Prasuhn,D., Stockhorst,H., Tölle,R.
Proc. EPAC, Lucerne, CH, (2004) 92-9083-231-2. - 653 - 655

89. **First results of pulsed superconducting half-wave resonators**
Stassen,R., Eichhorn,R., Esser,F. M., Laatsch,B., Maier,R., Schug,G., Tölle,R.
Proc. EPAC, Lucerne, CH, (2004) 92-9083-231-2. - 1258 - 1260

90. **Space charge problem in low energy super-conducting accelerators**
Vasyukhin,N. E., Maier,R., Senichev,Y.
Proc. EPAC, Lucerne, CH, (2004) 92-9083-231-2. - 1999 - 2001

91. **Dual harmonic acceleration with broadband ma Cavities in J-PARC RCS**
Yamamoto,M., Anami,S., Ezura,E., Hara,K., Hashimoto,Y., Ohmori,C., Takagi,A., Yoshii,M., Nomura,M., Schnase,A., Tamura,F.
Proc. EPAC, Lucerne, CH, (2004) 92-9083-231-2. - 1318 - 1320

92. **Triple-spoke cavities in FZJ**
Zaplatin,E., Braeutigam,W., Maier,R., Pap,M., Skrobucha,M., Stassen,R., Tölle,R.
Proc. EPAC, Lucerne, CH, (2004) 92-9083-231-2. - 1261 - 1263

4. Others

93. **Detection characteristics of Ge detectorsl with microstructured amorphous Ge contacts**
    Protic,D., Krings,T.
    IEEE Trans. on Nuc. Sci., 51 (2004), 1129 - 1133

94. **Time scales involved in emergent market coherence**
    Kwapien, J.; Drozdz, S.; Speth, J.
    Physica A **337** *(2004) 231 - 242*

95. **Zur Dämpfung der Globalisierung**
    Otto W.B. Schult
    Die Neue Ordnung **58** *(2004) 264 - 279*

D Beam Time at COSY 2004

Date	Experiment	Duration	Reaction
16.01.04–09.02.04	ANKE	3 weeks	$pp \rightarrow pp\phi$
13.02.–08.03.	ANKE	3 weeks	$pn \rightarrow da_0/f_0$
08.03.–16.03.	ANKE	1 week	$pA \rightarrow \Theta^+ X$
09.03.–29.03.	ENSTAR	1 week	*detector tests*
02.04.–19.04.	TOF	2 weeks	$\vec{p}p \rightarrow pp\omega$
23.04.–03.05.	SPIN@COSY	1 week	*spin manipulation*
21.05.–07.06.	PISA	2 weeks	$pA \rightarrow$spallation
25.06.–19.07.	HIRES	3 weeks	$pp \rightarrow pK^+\Lambda$
19.07.–04.08.	JESSICA	2 weeks	$pA \rightarrow$spallation
06.08.–30.08.	COSY-11	3 weeks	$pn \rightarrow pn\eta'$
03.09.–13.09.	JESSICA	1 week	$pA \rightarrow$spallation
17.09.–27.09.	TRIC	1 week	$\vec{p}p \rightarrow pp$
15.10.–29.11.	TOF	6 weeks	$pp \rightarrow pK^0\Sigma^+$
03.12.–13.12.	GEM	1 week	$\vec{d}d \rightarrow {}^4He\eta$
13.12.–20.12.	SPIN@COSY	1 week	*spin manipulation*
Total ’04		31 weeks	

E List of Authors

Abdel-Bary, M., 113–115
Abdel-Samad, S., 113–115
Ackens, A., 120
Adam, H.-H., 20
Anagnostopoulos, D.F., 42

Böge, H.G., 91
Böhme, C., 83
Büscher, M., 5–8, 38, 110
Balalykin, N.I., 83
Balasubramanyamz, J., 56
Baru, V., 53
Baur, G., 67–70
Bayer, N., 32–34
Bechstedt, U., 40, 41, 87, 89
Belov, A.S., 93
Berchem, C., 119
Bernard, V., 58, 72, 73
Birx, P., 89
Bollini, V., 32–34
Bongers, N., 88
Borgs, W., 110
Borsch, H., 89, 95
Boucard, S., 43
Bräutigam, W., 91
Brings, R., 91
Brinkmann, K.-Th., 26
Bruns, P.C., 57
Bubak, A., 32–34
Bukharov, A., 110
Bykovsky, V., 83

Chernetsky, V., 110
Chernyshev, V., 38, 110
Chernyshev, V.P., 6
Chiladze, D., 9
Clemens, U., 120
Conrad, H., 32–34
Covita, D., 42, 43
Czyzykiewicz, R., 16, 18

D'Imperio, N.L., 104
Dahmen, B., 88
Deepak, P.N., 55, 56
Deliege, C., 88
Derissen, W., 94
Dietrich, J, 83
Dietrich, J., 78, 79
Dolfus, G., 87, 89
Dolfus, N., 119
dos Santos, J.M.F., 42, 43
Dreyer, U., 67
Dschemuchadse, S., 26
Dutz, H., 112
Dzyuba, A., 5, 8

Eichhorn, R., 96–98
Ejiri, H., 50
Enge, R., 87
Engels, R., 10, 109
Epelbaum, E., 61, 62
Erkes, B., 87
Ernst, W., 119
Erven, W., 27, 120
Esser, F., 40, 41, 97, 98
Eversheim, D., 77

Faber, P., 87
Fedorets, P., 5, 6, 38, 110
Felden, O., 91, 93, 95, 107
Ferguson, P.D., 32–34
Fest, T., 89
Filges, D., 32–34
Fiori, G., 116
Frink, M., 59, 60
Fuhrmann, H., 42, 43

Göbbels, J., 95
Gad, N., 91
Gallmeier, F.X., 32–34
Gardner, S., 72, 73
Garsparyan, A.M., 47
Gebel, R., 77, 91, 93
Gehsing, D., 88
GEM, 28
Gillitzer, A., 100
Glöckle, W., 61
Glückler, H., 40, 41
Goldenbaum, F., 32–34, 40, 41
Gorke, H., 120
Gotta, D., 42, 43, 120
Grigoryev, K., 10, 109
Grishina, V., 6, 7, 38
Gruber, A., 42, 43
Grzonka, D., 21, 40, 41, 100
Gussen, A., 10
Gutschmidt, H., 120

Haberzettl, H., 50, 51
Haidenbauer, J., 46–49, 52, 53, 55, 71
Hammer, H.-W., 63–65
Hanhart, C., 47, 53, 55
Hansen, G., 40, 41
Hartmann, M., 3, 4
Hecker, R., 89
Heckmann, J., 112
Hejny, V., 38
Hencken, K., 67, 68
Henn, K., 88, 89
Hess, Ch., 112
Hinterberger, F., 77, 94
Hirtl, A., 42, 43

Hull, L., 118

Indelicato, P., 42, 43
Ishiwatari, T., 42
Iverson, E.B., 32–34

Jäkel, R., 26
Jahn, R., 94
Jansen, P., 10, 109
Janusz, M., 17, 35–37

Kacharava, A., 9
Kamerdzhiev, V., 78, 79, 83
Karsch, L., 26
Kemmerling, G., 120
Keshelashvili, I., 3, 4, 8
Khoukaz, A., 20
Kieven, A., 91
Kilian, K., 27, 100, 113–115
Klaja, P., 15, 35–37
Kleber, V., 5, 6, 8, 38
Klehr, F., 10, 109
Klein, F., 112
Kleines, H., 10, 109, 120
Koch, R., 8
Kondratyuk, L., 6, 7, 38
Koptev, V., 5, 6, 8
Korotaev, Yu., 78
Korotaev1, Yu., 79
Kozlov, V., 27
Krafft, K., 95
Kravtsov, P., 10
Krebs, H., 58
Krewald, S., 7, 8, 48, 49, 71
Krings, T., 116–118
Krisch, A.D., 77
Krol, G., 87
Kruck, K., 89, 94
Kudryavtsev, A., 38, 53
Kudryavtsev, A.E., 6
Kuhlmann, E., 23
Kulikov, S., 32–34

Lvenich, H.-W., 120
Laatsch, B., 97, 98
Lang, N., 20
Langenberg, G., 87
Le Bigot, E.-O., 42, 43
Lehrach, A., 77, 82, 103–105
Lensing, B., 32–34
Leonova, M.A., 77
Lesiak, M., 94
Lorentz, B., 10, 77
Luccio, A.U., 104, 105

Mckelburg, D., 120
Machner, H., 94
Maeda, Y., 3, 4, 8
Maier, R., 77–79, 94, 102
Majewski, J., 120
Martin, S., 40, 41
Mazerath, T., 32–34
Meißner, U.-G., 7, 46, 48, 49, 52–54, 57–66, 71–73
Mersmann, T., 20
Meshkov, I.N., 78, 79, 83
Metz, H., 116
Meyer, W., 112
Mikirtichyants, S., 8
Mikirtytchiants, M., 109
Mohos, I., 27, 83, 117
Morozov, V.S., 77
Morsch, P., 44
Moskal, P., 13, 16–19
Moskal,P., 35–37
Musakhanov, M.M., 66
Mussgiller, A., 11

Nünighoff, K., 32–34
Nakayama, K., 50, 51
Nekhipelov, M., 42
Nekipelov, M., 5, 8
Nellen, R., 27, 119
Ninaus, W., 32–34
Niskanen, J., 52

Oelert, W., 35–37, 40, 41, 100, 120
Ohm, H., 120
Orfanitski, S., 27

Pütz, H., 87
Palomar, J.E., 62
Parfenov, A.N., 83
Paul, N., 32–34
PISA, 29–31
Piskor-Ignatowicz, 19
Platter, L., 63–65
Pohl, Ch., 32–34
Polinder, H., 46
Prasuhn, D., 32–34, 77–79, 82, 103
Protić, D., 116–118
Przerwa, J., 14, 35–37
Pysz, K., 32–34

Raccanelli, A., 112
Radtke, E., 112
Raha, U., 54
Rakhimov, A.M., 66
Ramachandran, G., 56
Rathmann, F., 9, 10, 109
Raymond, R.S., 77
Reicherz, G., 112
Richert, A., 89
Richter, P., 89
Ritman, J., 100, 113–115
Roderburg, E., 24, 25
Rohdjeß, H., 77
Rossen, P.v., 91, 93, 94
Rotert, N., 91

Rozek, T., 21
Ruhrig, D., 89
Rusetsky, A., 54

Sagefka, T., 40, 41, 87
Sakardi, J., 119
Santo, R., 20
Sarkadi, J., 10, 109
Sassen, F.P., 7
Schaal, H., 32–34
Scheiba, F., 87
Scheller, I., 59
Schiffer, H., 119
Schleichert, R., 120
Schmid, P., 42, 43
Schmitz, J., 89
Schnase, A., 77, 86
Schneider, H., 89
Schug, G., 97, 98
Schulte-Wissermann, M., 26
Schwill, K., 116
Sefzick, T., 27, 40, 41, 100, 119
Semenov, A., 110
Seyfarth, H., 10, 109
Sibirtsev, A., 7, 48, 49, 52, 71
Sidorin, A., 78, 79
Simon, M., 88, 89
Simons, L.M., 42, 43
Singer, H., 96–98
Siudak, R., 94
Sivers, D.W., 77
Smirnov, A., 32–34
Smyrski, J., 12, 19
Soltner, H., 32–34, 40, 41
Spillmann, U., 117
Stöhlker, Th., 117
Stassen, R., 96–98
Stein, H.J., 78, 79
Stelzer, H., 32–34
Stengelin, L., 43
Stockhorst, H., 77–80
Stockmanns, T., 101
Ströher, H., 8
Sun, G.Y., 26

Täschner, A., 20
Tölle, R., 94
Tarasov, V.E., 6
Thomas, A.W., 71
Tietze-Jaensch, H., 32–34
Titov, A. I., 50
Trassinelli, M., 42, 43
Trautmann, D., 67, 68
Typel, S., 68–70

Ucar, A., 27
Uehlemann, J., 113–115
Ulbrich, K., 77
Ullrich, W., 26

Vashegyi, T., 88
Vassiliev, A., 109
Veloso, J.F.C.A., 42, 43
Venkataraya, 56
Vetter, K., 118
Vidyay, M.S., 56

Wüstner, P., 27
Wstner, P., 120
Wasser, A., 43
Weis, T., 83
Wilkin, C., 9
Winter, P., 22
Wintz, P., 27
Wirzba, A., 66
Wohlmuther, M., 32–34
Wong, V.K., 77

Yakhshiev, U.T., 66
Yonehara, K., 77

Zens, H., 88
Zhang, C., 73
Zhang, Z., 40, 41
Zimmermann, J., 120
Zlomanczuk, J., 35–37
Zmeskal, J., 42, 43
Zupranksi, P., 44
Zupranski, P., 25
Zwoll, K., 27, 120
Zychor, I., 8